frontiers | Research Topics

Understanding soil wind erosion and control practices in arid and semiarid environments

Edited by
Huawei Pi, Brandon L. Edwards and Bailiang Li

Published in
Frontiers in Environmental Science

ISSN 1664-8714
ISBN 978-2-83251-653-9
DOI 10.3389/978-2-83251-653-9

About Frontiers

Frontiers is more than just an open access publisher of scholarly articles: it is a pioneering approach to the world of academia, radically improving the way scholarly research is managed. The grand vision of Frontiers is a world where all people have an equal opportunity to seek, share and generate knowledge. Frontiers provides immediate and permanent online open access to all its publications, but this alone is not enough to realize our grand goals.

Frontiers journal series

The Frontiers journal series is a multi-tier and interdisciplinary set of open-access, online journals, promising a paradigm shift from the current review, selection and dissemination processes in academic publishing. All Frontiers journals are driven by researchers for researchers; therefore, they constitute a service to the scholarly community. At the same time, the *Frontiers journal series* operates on a revolutionary invention, the tiered publishing system, initially addressing specific communities of scholars, and gradually climbing up to broader public understanding, thus serving the interests of the lay society, too.

Dedication to quality

Each Frontiers article is a landmark of the highest quality, thanks to genuinely collaborative interactions between authors and review editors, who include some of the world's best academicians. Research must be certified by peers before entering a stream of knowledge that may eventually reach the public - and shape society; therefore, Frontiers only applies the most rigorous and unbiased reviews. Frontiers revolutionizes research publishing by freely delivering the most outstanding research, evaluated with no bias from both the academic and social point of view. By applying the most advanced information technologies, Frontiers is catapulting scholarly publishing into a new generation.

What are Frontiers Research Topics?

Frontiers Research Topics are very popular trademarks of the *Frontiers journals series*: they are collections of at least ten articles, all centered on a particular subject. With their unique mix of varied contributions from Original Research to Review Articles, Frontiers Research Topics unify the most influential researchers, the latest key findings and historical advances in a hot research area.

Find out more on how to host your own Frontiers Research Topic or contribute to one as an author by contacting the Frontiers editorial office: frontiersin.org/about/contact

Understanding soil wind erosion and control practices in arid and semiarid environments

Topic editors

Huawei Pi — Henan University, China

Brandon L. Edwards — New Mexico State University, United States

Bailiang Li — Xi'an Jiaotong-Liverpool University, China

Citation

Pi, H., Edwards, B. L., Li, B., eds. (2023). *Understanding soil wind erosion and control practices in arid and semiarid environments*. Lausanne: Frontiers Media SA.

doi: 10.3389/978-2-83251-653-9

Table of contents

04 Editorial: Understanding soil wind erosion and control practices in arid and semiarid environments
Huawei Pi, Brandon L. Edwards and Bailiang Li

06 Effect of Grazing Exclusion and Rotational Grazing on Soil Aggregate Stability in Typical Grasslands in Inner Mongolia, China
Lei Dong, Ying Zheng, Vegard Martinsen, Cunzhu Liang and Jan Mulder

13 Temporal Variation of Airborne Dust Concentrations in the Mogao Grottoes, Dunhuang, China
Guobin Zhang, Lihai Tan, Weimin Zhang, Hongtao Zhan and Fei Qiu

24 Vertical Sand Flux Density and Grain-Size Distributions for Wind-Blown Sand Over a Gobi Surface in Milan, Southern Xinjiang, China
Lihai Tan, Kai Zhang, Hongtao Wang, Zhishan An and Tao Wang

33 Protective Efficiency of Railway Arbor-Shrub Windbreak Forest Belts in Gobi Regions: Numerical Simulation and Wind Tunnel Tests
Kai Zhang, Jianjun Qu, Xingxin Zhang, Liming Zhao and Sheng Li

48 Aerodynamic Properties and Shelter Effects of a Concrete Plate-Insert Sand Fence Along the Lanzhou-Xinjiang High-Speed Railway in Gobi Regions Under Strong Winds
Tao Wang, Jianjun Qu, Qinghe Niu, Zhishan An, Yang Gao, Hongtao Wang and Baicheng Niu

60 Microtopographic reconstruction improves soil erosion resistance and vegetation characteristics on the slopes of large dump sites in semi-arid areas
Xiumin Tian, Ruiping Yin, Jian Wang, Lei Dong, Bo Cheng, Hu Liu and Nan Ge

73 Comparison of the characteristics of six salt crusts
Boshi Xu, Chengzhi Li and Zhaoti Li

81 Effect of tillage management on the wind erosion of arable soil in the Chinese Mollisol region
Shuai Chen, Xingyi Zhang, Jianye Li, Mingming Guo and Wei Hu

92 Phytoliths in particulate matter released by wind erosion on arable land in La Pampa, Argentina
Roger Funk, Jaqueline Busse, Nicole Siegmund, Michael Sommer, Laura A. Iturri, Juan E. Panebianco, Fernando Avecilla and Daniel E. Buschiazzo

frontiers | Frontiers in Environmental Science

TYPE Editorial
PUBLISHED 30 January 2023
DOI 10.3389/fenvs.2023.1119742

OPEN ACCESS

EDITED AND REVIEWED BY
Xingwu Duan,
Yunnan University, China

*CORRESPONDENCE
Brandon L. Edwards,
bedwar4@nmsu.edu
Bailiang Li,
bailiang.li@xjtlu.edu.cn

†These authors have contributed equally to this work

SPECIALTY SECTION
This article was submitted to Drylands, a section of the journal Frontiers in Environmental Science

RECEIVED 09 December 2022
ACCEPTED 20 January 2023
PUBLISHED 30 January 2023

CITATION
Pi H, Edwards BL and Li B (2023), Editorial: Understanding soil wind erosion and control practices in arid and semiarid environments.
Front. Environ. Sci. 11:1119742.
doi: 10.3389/fenvs.2023.1119742

Editorial: Understanding soil wind erosion and control practices in arid and semiarid environments

Huawei Pi[1,2†], Brandon L. Edwards[3*†] and Bailiang Li[4*†]

[1]Collaborative Innovation Center for Yellow River Civilization, Key Research Institute of Yellow River Civilization and Sustainable Development, Henan University, Kaifeng, China , [2]Xinjiang Institute of Ecology and Geography, Chinese Academy of Sciences, Urumqi, China, [3]Jornada Experimental Range, New Mexico State University, Las Cruces, NM, United States, [4]Department of Health and Environmental Sciences, Xi'an Jiaotong-Liverpool University, Suzhou, China

KEYWORDS

land management practice, airborne dust concentration, phytolith, wind tunnel, dust emission

Editorial on the Research Topic
Understanding soil wind erosion and control practices in arid and semiarid environments

Soil wind erosion is a serious problem in arid and semiarid regions globally because of removal of nutrients and finer soil particles from the soil surface, reduction of soil productivity, suppression of crop growth by sandblasting seedlings, damage to infrastructure, and impacts on air quality, human health, and visibility from dust emission, among other negative consequences. In this Research Topic, wind erosion is studied by various approaches such as field observations, wind tunnel testing, and laboratory measurements. Here, we present a brief review and summary of these articles.

Dong et al., Tan et al., Tian et al., and Chen et al. conducted field experiments to test how land management practices influence wind erosion parameters or reduce erosion in the field. Dong et al. present long-term observations that indicate both rotational grazing and long-term grazing exclusion can significantly enhance soil aggregate stability and analyze and discuss the relative effectiveness of these management practices. Tian et al. present results from a field experiment to explore effective slope management practices to control soil erosion from large mine dumps, which is a serious environmental problem for their study region and others. They found that microtopography modifications and vegetation treatments provided sufficient protection to prevent erosion of soils with added benefits of increasing soil organic matter content and biodiversity. Similarly, Chen et al. conducted a field experiment to test how different tillage practices reduce wind erosion in the corn belt, northern China. Similar to previous studies such as Sharratt and Feng (2009, https://doi.org/10.1002/esp.1812), they found wind erosion from no-tillage (NT) treatment significantly lower than that from conventional tillage (CT) treatments. However, their observations suggested direct creep was a dominant process for the corn belt landscape rather than suspension or saltation. Xu et al. present a laboratory experiment to test how salt crust character was influenced by salt type and content. Soil crust is an important limiting factor for wind erosion, and salt crusts can be prevalent in dry areas because of strong evaporation and high salt concentrations of irrigation water. They found that $CaCl_2$ produced crusts with greater compressive strength than did other salts, whereas Na_2SO_4 appeared to reach the maximum strength earlier than other salts with a smaller increase of salt content. They concluded that, because of their compressive strength and toughness,

crusts of KCl, $CaCl_2$, NaCl, and Na_2SO_4 could be useful to control wind erosion as long as their content was around 3%.

Like other geomorphologic processes, wind erosion is also characterized by high spatiotemporal variability among regions. Tan et al., Zhang et al., and Funk et al. report on observations of wind erosion and dust emissions in different regions and found differing results from previous studies. Tan et al. measured wind-blown sand over a Gobi surface. Transport below 0.6 m accounted for >99 per cent of the total amount, suggesting direct saltation may be a much more important process for Gobi surfaces than suspension or creep. Zhang et al. monitored airborne dust concentrations in the Mogao Grottoes, Northwest China, and indicated that particulate matter less than 10 μm (PM10) dominated total suspended particle (TSP) concentrations with a mean ratio (PM10/TSP) of 0.82. Maximum TSP real-time concentrations (16,000–21,000 μg m^{-3}) observed from the Mogao Grottoes were greater than the concentrations observed from Kennewick, WA (600 μg m^{-3}) and most hotspot dust source areas of China (10,000 μg m^{-3}), comparable to the concentrations observed from Israel, and Inland Delta region of Mali, but smaller than from Sahara, North Africa, or Tel Aviv, Israel (Ganor and Foner, 2001, https://doi.org/10.1029/2000JD900535). Generally, the composition in PM observed in the air is different from that in soil, but few studies have identified phytoliths in the PM. Funk et al. used Scanning Electron Microscopy and Energy Dispersive X-Ray analysis (SEM-EDX) to investigate the existence of phytoliths in the observed dust. They found that the fraction of phytoliths in the PM was up to 8.3%, and the fraction of organic origin was up to 25%. In contrast, the fraction of phytoliths in the soil varied from 0.01% to 3%. As an important plant nutrient and source of Silicon (Si), a sink for organic carbon (Schaller et al., 2021, https://doi.org/10.3390/plants10020295), and a reliable indicator in palaeovegetation and palaeoenvironment reconstruction (An et al., 2015, https://doi.org/10.1038/srep15523), loss of phytoliths should be highlighted in land management practices.

Wind tunnels are a useful tool in wind erosion studies because they allow researchers to control conditions. Wang et al. evaluate a Concrete Plate-Insert Sand Fence in decreasing sediment transport from a Gobi surface along the Lanzhou-Xinjiang High-Speed Railway under various wind conditions. Although the fences adequately reduced wind velocity, considerable sand may be deposited gradually on both leeward and windward sides of the sand fence because of the two wide row spacing between the double-row fences and porosity of the sand fences. As a result, the sand fences along Railway may lose their transport-limiting capacity as more sand is deposited. Risks in potential sand deposition on the Railway should be considered alongside fence effectiveness by managers to avoid losses due to sand transport in the future. Plant-based sand prevention is another popular mitigating practice. Zhang et al. test the performance of windbreak forest belts in controlling sand transport from the Gobi Desert surface along the Lan-Xin Railway, Northwest China. While sand was also deposited on both leeward and windward sides of the windbreak forest belts, the three shelterbelt rows appeared to perform better than the concrete sand fence, with an efficiency up to 90% compared to <72% efficiency of the sand fence.

This Research Topic aimed to advance our understanding of soil wind erosion and control practices in arid and semiarid environments. As a research community, we have made significant progress in understanding wind erosion processes and impacts over the last few decades. Despite this progress, wind erosion continues to be a national, regional, and international problem, especially in the context of uncertainty associated with global climate change. Future research employing a variety of approaches—including field observations, wind tunnel and laboratory experiments, remote sensing, and modeling—will continue to be needed to meet the challenges of mitigating negative impacts of soil wind erosion into an uncertain future.

Author contributions

All authors listed have made a substantial, direct, and intellectual contribution to the work and approved it for publication.

Conflict of interest

The authors declare that the research was conducted in the absence of any commercial or financial relationships that could be construed as a potential conflict of interest.

Publisher's note

frontiers in Environmental Science

ORIGINAL RESEARCH
published: 11 February 2022
doi: 10.3389/fenvs.2022.844151

Effect of Grazing Exclusion and Rotational Grazing on Soil Aggregate Stability in Typical Grasslands in Inner Mongolia, China

Lei Dong[1,2], *Ying Zheng*[1,2], *Vegard Martinsen*[3], *Cunzhu Liang*[4] *and Jan Mulder*[3]*

[1]Yinshanbeilu Grassland Eco-hydrology National Observation and Research Station, China Institute of Water Resources and Hydropower Research, Beijing, China, [2]Institute of Water Resources for Pastoral Area Ministry of Water Resources, Hohhot, China, [3]Faculty of Environmental Sciences and Natural Resource Management, Norwegian University of Life Sciences, Aas, Norway, [4]School of Ecology and Environment, Inner Mongolia University, Hohhot, China

Soil aggregate is extremely important for soil health and sustainable land management. Overgrazing has caused serious degeneration of grassland in the past decades and how to restore the degraded soil through grazing management is urgently needed. In this research, we investigated effects of long-term grazing exclusion and short-term rotational grazing with different grazing intensities on aggregate stability in the upper 10 cm of soil at two grazing sites in Xilinhot, Inner Mongolia. Treatments included long-term (34 years) exclusion, moderate-term (21 years) exclusion, and continuous grazing at adjacent reference plots. In addition, effects of rotational grazing under different grazing intensity [*i.e.*, no grazing (0 days/month), light grazing (3 days/month), moderate grazing (6 days/month) and high grazing (12 days/month)] were investigated after 5 years. Stability of aggregate fractions were determined using wet sieving. Our results showed that the stable aggregates fraction were significantly increased under grazing exclusion for both fine (0.25–1 mm) and coarse (1–2 mm) size fractions. At the rotational grazing site, stability of fine aggregates was significantly enhanced under grazing compared with no grazing, while there was little influence on stability of coarse aggregates. Our results showed that grazing exclusion significantly increased soil aggregate stability and the peak appeared in moderate-term exclusion, meanwhile, rotational grazing had little influence on aggregate stability. We suggest that rotational grazing rather than long-term grazing exclusion is a better way for soil aggregate stability and soil health, and current grazing prohibition policies may need to be adjusted.

Keywords: aggregation, grazing management, long-term exclusion, steppe, suitability

OPEN ACCESS

Edited by:
Huawei Pi,
Henan University, China

Reviewed by:
Xiaoyu Meng,
Henan University, China
Baicheng Niu,
Northwest Institute of Eco-Environment and Resources (CAS), China

***Correspondence:**
Jan Mulder
jan.mulder@nmbu.no

Specialty section:
This article was submitted to Drylands, a section of the journal Frontiers in Environmental Science

Received: *27 December 2021*
Accepted: *19 January 2022*
Published: *11 February 2022*

Citation:
Dong L, Zheng Y, Martinsen V, Liang C and Mulder J (2022) Effect of Grazing Exclusion and Rotational Grazing on Soil Aggregate Stability in Typical Grasslands in Inner Mongolia, China. Front. Environ. Sci. 10:844151. doi: 10.3389/fenvs.2022.844151

INTRODUCTION

The steppe in arid and semi-arid of northern China is among the largest remaining natural grassland in the world (Kawamura et al., 2005). However, overgrazing has caused serious grassland soil deterioration in the past decades (Tong et al., 2004). Researchers have shown that grazing exclusion is effective to restore the degraded grassland soil (Mekuria et al., 2007; Cheng et al., 2011). Recently, several policies (*e.g.*, Prohibiting Grazing Policy and Returning Grazing Lands to Grasslands) were implemented to restore the degraded grassland in northern China. When grazing is excluded, as the

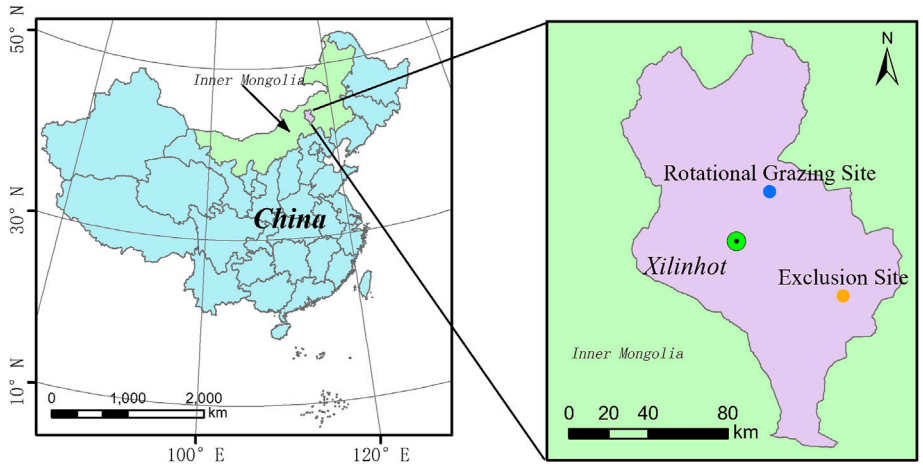

FIGURE 1 | Location of the two experimental sites.

input of organic matter increases, it may have a beneficial effect on soil organic carbon (SOC) and physical structure, but excessive litter accumulation on the surface soil immobilizes organic carbon (Reeder and Schuman, 2002) and inhibits plant growth (Xiong and Nilsson, 1999; Dong et al., 2021). So, long-term absence of grazing may inhibit important ecosystem functions. The positive effects of controlled livestock grazing and prohibiting grazing on grassland ecosystems are widely reported, however, its potential negative effects on soil quality is rarely mentioned in Inner Mongolia.

Rotational grazing, also known as multi-paddock grazing, has been proposed as a potential alternative grazing management option to maintain ecosystem sustainability and enhance grassland productivity (Sanjari et al., 2010; Teague et al., 2011). Compared with continuous grazing, rotational grazing provides a short period of high intensity grazing, followed by a long recovery period, which is particularly important for herbs (Teague et al., 2011), and which could supply higher forage production (Gourlez et al., 2018). Rotational grazing has been well studied in Oceania and North America and was found to be valuable in practice (Sovell et al., 2000; Chan et al., 2010; Sanjari et al., 2010). In Inner Mongolia, however, previous studies are more focused on continuous grazing or seasonal grazing (*e.g.*, Steffens et al., 2008; Kölbl et al., 2011; Reszkowska et al., 2011). The influence of rotational grazing has received little attention resulting in limited information about the effects of rotational grazing on soil in Inner Mongolia. Aggregate stability is of special importance for soil health and the stability of the SOC pool (Herrick et al., 2001), as it determines soil's resistance to degradation and erosion (Six et al., 2000). Moreover, increased aggregate stability reduces SOC loss by hindering microbe accessibility and increasing interaction between mineral surfaces and SOC (Wu et al., 2012).

In this study, we assess the impact of 1) 34- and 21-years grazing exclusion vs ambient grazing and 2) 5 years rotational grazing with different grazing intensities on grasslands soils of Inner Mongolia on aggregate stability. The goal of this research is to evaluate the effect of grazing exclusion and rotational grazing on soil aggregate stability. We hypothesize that rotational grazing enhances aggregate stability, while both long-term grazing exclusion and continuous grazing tend to exert negative effects. This research will provide theoretical basis for grassland management and grazing system arrangements.

METHOD AND MATERIALS

Site Description and Experimental Design

The Exclusion Site and Rotational Grazing Site are both located in Xilinhot, Inner Mongolia (**Figure 1**). The climatic condition is a semiarid temperate continental climate, with more than 60% of precipitation occurring from July to September. Soils are classified as Kastanozem (IUSS Working Group, 2014).

The Exclusion Site (ES) is located near the Inner Mongolia Grassland Ecosystem Research Station (IMGERS, 43°38′ N, 116°42′ E). The mean annual precipitation and mean annual temperature are about 343 mm and 0.7°C, respectively (Steffens et al., 2008). In 1983, a fenced area of 24 ha was set up to exclude grazing (long-term exclusion, LTE). In 1996, an additional fenced area of 2 ha was established adjacent to the former (medium-term exclusion, MTE). The area outside the fences had continuous free grazing by sheep from local herdsmen (ambient grazing, AG) (Kölbl et al., 2011). The grassland was moderately to heavily degraded. At the time of sampling, in autumn 2017, the plots had been enclosed 34 and 21 years, respectively.

The Rotational Grazing Site (RGS) is located at the Xilinhot National Climate Observatory (44°08′ N, 116°20′ E). The mean annual precipitation and mean annual temperature are about 281 mm and 2.4°C, respectively. For the rotational grazing experiment, fenced plots with four treatments according to grazing gradients were set up in 2012, with three replications for each treatment. Since 2013, the grazing experiment has been conducted in growing season (*i.e.*, from June to September). Each plot covers an area of 1.44 ha (120 m × 120 m) where 28 sheep grazed for 0 days (no grazing, NG), 3 days (light grazing, LG),

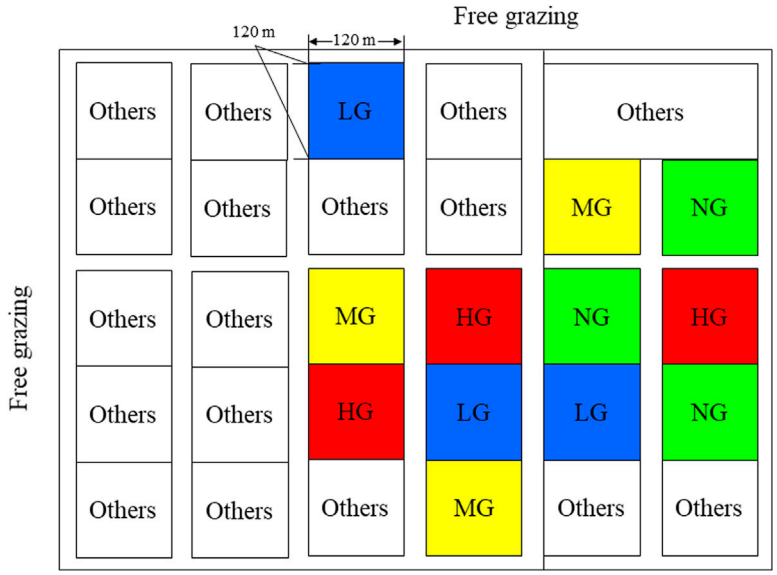

FIGURE 2 | Experimental design at the rotational grazing site (NG: No grazing. LG: Light grazing. MG: Moderate grazing. HG: High grazing. Others: Other experiments which were not relevant to this research. Ambient grazing: Free ambient grazing).

TABLE 1 | Vegetation and soil characteristics (0–20 cm) at grazing exclusion sites and rotational grazing sites.

	Exclusion site				Rotational grazing site				
	Long-term exclusion	Medium-term exclusion	Ambient grazing	Ref	No grazing	Light grazing	Medium grazing	High grazing	Ref
Belowground biomass (g/m^2)	1,386.69 A	1,459.88 A	1,299.32 B	Shi, (2016)	1,366.0 b	1,594.0 a	1,229.7 b	1,311.2 b	Shi, (2016)
Bulk density (g/cm^3)	1.20 B	1.23 B	1.43 A	Wang, (2010)	1.22	—	—	—	Xie, (2018)
SOC (g/kg)	16.6 B	18.6 A	12.2 C	Liu, (2016)	17.91 a	17.85 a	16.98 a	18.22 a	

Note: Different letters represent significant differences at $p < .05$.

6 days (moderate grazing, MG) and 12 days per month (high grazing, HG), respectively (**Figure 2**). The unfenced (free grazing) area keeps continuous free grazing with low intensity. Soil samples were collected in July 2017, the 5th year of grazing experiment.

An overview of belowground biomass and soil characteristics tested by related researchers at the same experimental plots is shown in **Table 1**.

Soil Sampling and Pretreatment

At each plot, five points were chosen randomly and the distance between each two points was greater than 15 m. About 250 g soil from 0 to 10 cm was sampled at each point using a small spade and the five soil samples were bulked prior to drying and further treatment. After air-drying for 2 weeks, the soil samples were sieved at 2 mm. All samples were stored at room temperature until analysis.

Aggregate Stability

About 200 g air-dried soil was added to a set of nested sieves with sieve openings of 1 and 0.25 mm, respectively, to obtain aggregate fractions of 1–2 mm (coarse aggregates), 0.25–1 mm (fine aggregates).

The aggregate content was calculated according to:

$$\%A = \frac{m_a}{m} \quad (1)$$

where %A is the percentage of coarse/fine aggregate in bulk soil, m_a is the mass of coarse/fine aggregate, m is the total mass of all size fractions.

Aggregate stability of the coarse and fine aggregate fractions was determined using wet sieving (Five Star Scientific, Twin Falls, United States). Both aggregate size classes (4 g), placed on the sieve (mesh 0.25 mm), were pre-moistened with distilled water for 5 min. Next, the sieve moved up and down for 3 min (stroke is 1.3 cm, at about 34 strokes/min), while immersed in a container with 80 ml distilled water. Unstable aggregates disintegrated and were collected in the container. Subsequently, the container with distilled water was replaced with a container having 80 ml dispersing solution ($2\ g\ L^{-1}$ sodium hexametaphosphate $(NaPO_3)_6$). The material remaining on the sieve was wet-sieved, while immersed in $(NaPO_3)_6$ solution, until only roots

TABLE 2 | Percentage of aggregate content at grazing exclusion site and rotational grazing site.

	Exclusion site			Rotational grazing site			
	Long-term exclusion	Medium-term exclusion	Ambient grazing	No grazing	Light grazing	Medium grazing	High grazing
Fine aggregate/% of bulk soil	39.13 C	43.46 B	50.74 A	12.97 a	14.72 a	15.07 a	14.43 a
Coarse aggregate/% of bulk soil	15.18 A	15.32 A	11.84 B	4.07 b	5.51 a	4.43 ab	4.20 b

Note: Different letters represent significant differences at p < .05.

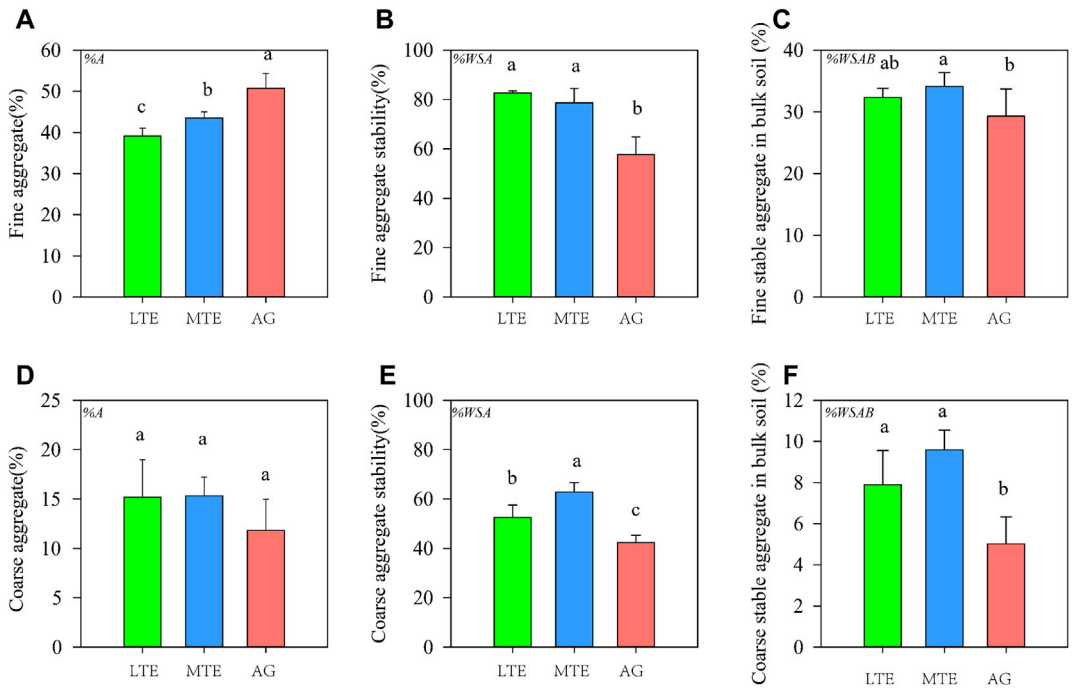

FIGURE 3 | Aggregate content and aggregate stability (mean ± SD) in response to grazing exclusion in the fine fraction **(A–C)** and the coarse fraction **(D–F)**. Different letters represent significant differences at $p < .05$. NOTE: LTE: Long-term exclusion; MTE: Medium-term exclusion; AG: Ambient grazing. %A: the percentage of coarse/fine aggregate in bulk soil; %WSA: the percentage of water stable aggregate in coarse/fine aggregate size fractions; %WSAB: the percentage of coarse/fine water stable aggregate in bulk soil.

and mineral particles >0.25 mm were left on the sieve. The $(NaPO_3)_6$ container (with accumulated sediment from the stable aggregates, now disintegrated in the $(NaPO_3)_6$ solution) and the distilled water container (with unstable aggregates) were dried in an oven (at 65°C, for about 20 h) after which, the weights were determined. More details about the procedure are presented in Kemper and Rosenau (1986).

The aggregate stability of both the coarse and fine fractions was calculated according to:

$$\%WSA = \frac{w_s}{w_s + w_{us}} \times 100\% \quad (2)$$

where %WSA is the percentage of water stable aggregate in coarse/fine aggregate size fractions, w_s is the mass of coarse/fine stable aggregate, w_{us} is the mass of coarse/fine unstable aggregate.

The percentage of both the coarse and fine water stable aggregate in bulk soil was calculated according to:

$$\%WSAB = \%WSA \times \%A \quad (3)$$

where %WSAB is the percentage of coarse/fine water stable aggregate in bulk soil.

Statistics

Statistical analyses were done using R version 3.4.5. To compare the significance of differences between different treatments, Duncan's multiple comparison (significance level $p < .05$) was calculated using *Agricolae* package (De Mendiburu, 2014).

RESULTS

At the exclusion site, after 34- and 21-years grazing exclusion, the fraction of coarse aggregate was significantly greater in the exclusion than under ambient grazing. On the contrary, the

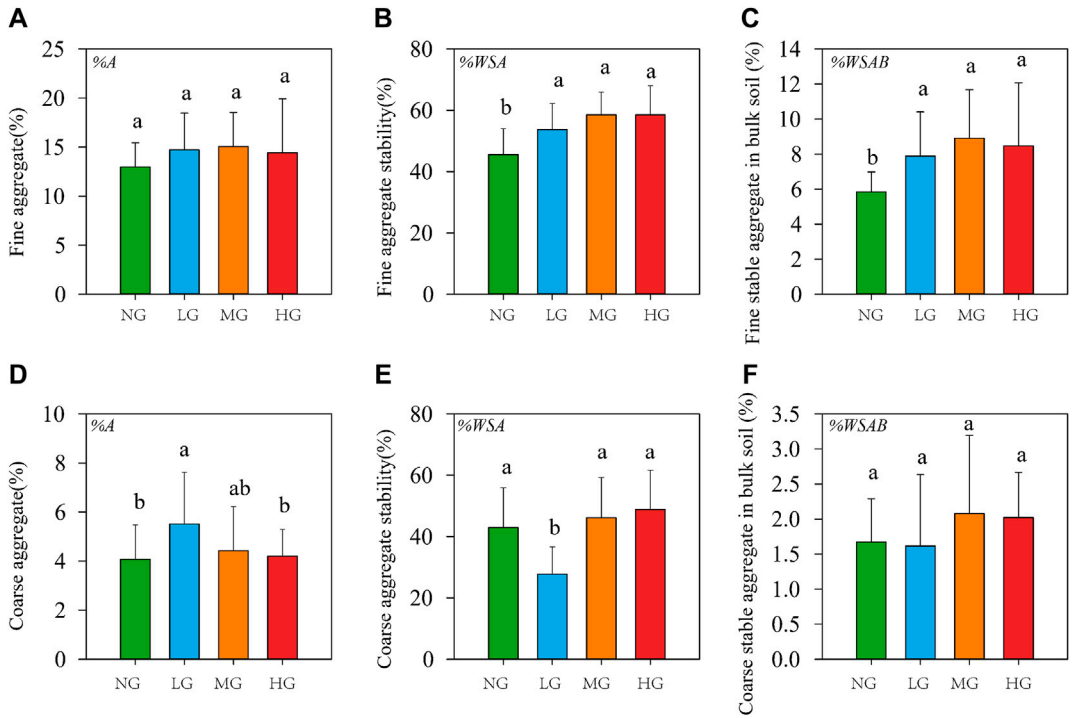

FIGURE 4 | Aggregate content and aggregate stability (mean ± SD) in response to rotational grazing in the fine fraction **(A–C)** and the coarse fraction **(D–F)**. Different letters represent significant differences at $p < .05$. NOTE: NG: No grazing; LG: Light grazing; MG: Medium grazing; HG: High grazing. %A: the percentage of coarse/fine aggregate in bulk soil; %WSA: the percentage of water stable aggregate in coarse/fine aggregate size fractions; %WSAB: the percentage of coarse/fine water stable aggregate in bulk soil.

fraction of fine aggregates decreased significantly by 22.89 and 14.34%, respectively, compared with ambient grazing (**Table 2**; **Figure 3A**). Rotational grazing had little influence on aggregate content except that light grazing enhanced the content of coarse aggregate (**Table 2**; **Figure 4A**).

Aggregate stability of both size fractions increased significantly after 34- and 21-years of grazing exclusion as compared to continuous grazing (**Figures 3B,E**). There was no significant difference in the percentage of stable aggregates (*i.e.*, %WSA) in the fine size fractions between long-term exclusion and medium-term exclusion (**Figures 3B,C**). Yet, the stability of the coarse fraction was significantly greater under medium-term than under long-term grazing exclusion (**Figure 3E**). Meanwhile, the difference between the percentage of stable aggregates (*i.e.*, %WSAB) in the coarse fractions was not significant (**Figure 3F**).

Relative to no grazing, rotational grazing significantly enhanced the fine aggregate stability (*i.e.*, %WSA) irrespective of grazing density (**Figure 4B**) and further increased the proportion of fine stable aggregates (*i.e.*, %WSAB) in the bulk soil (**Figure 4C**). On the other hand, in the coarse size fraction, the aggregate stability (*i.e.*, % WSA) decreased significantly under light grazing compared to no grazing (**Figure 4E**), however, light grazing enhanced the percentage of coarse aggregate in the bulk soil (*i.e.*, %A), as a result, the proportion of coarse stable aggregates in the bulk soil (*i.e.*, % WSAB) did not change (**Figure 4F** and **Eq. 3**).

DISCUSSION

Effect of Grazing Exclusion on Grassland Soil

Our results showed that, both medium-term and long-term grazing exclusion significantly increased the number of soil aggregates and the soil aggregate stability. Grassland soil is tightly related to plant productivity (Wang, 2010). Increased above- and belowground biomass, mainly functioning as plant litter inputs, may have multiple beneficial effects on soil physical and chemical properties (McSherry and Ritchie, 2013) in semi-arid grassland (Steffens et al., 2011). Previous researches showed that aggregate stability was highly related to root activity (Obia et al., 2016), and that soil organic matter (SOM) might function as a binding agent in the formation of aggregates (Bronick and Lal, 2005). Belowground biomass and SOC at long-term and medium-term exclusion were significantly higher than that at ambient grazing at the end of the 2016 growing season (**Table 1**). Higher primary productivity produces more root exudates (Wilson et al., 2018) and enhances aggregate stability. Combined with destruction of soil structure by livestock trampling in ambient grazing, which resulted in a negative effect on soil physical and chemical properties (*i.e.*, higher bulk density, lower aggregate stability and SOC content; **Table 1**) (Steffens et al., 2008).

It is worth to note that, although livestock exclusion is commonly found to be positive to soil aggregate stability in Inner Mongolia (Su

et al., 2005; Steffens et al., 2008; Kölbl et al., 2011), our results suggest that coarse aggregate stability shows a non–linear response to the length of exclusion period (**Figure 3E**). Specifically, we found that there was a peak in coarse aggregate stability after medium-term exclusion, whereas these properties declined in long-term exclusion experiments. Wu et al. (2008) found that aboveground biomass and SOC were the highest after 24 years of grazing exclusion (although not significant when compared with 28 years grazing exclusion and ambient grazing). This was because excess litter accumulating on the ground might influence plant growth, and litter accumulation decreased rainfall infiltration resulting in reduced soil water availability (Wu et al., 2008). In addition, Reeder and Schuman (2002) suggested that the accumulation of litter on the soil surface might restrict litter decomposition and thus C cycling and nutrient turnover in the ecosystem. Lower SOC content in long-term exclusion site [See (Dong et al., 2021)] decreased aggregate stability, and lower proportions of aggregate-occluded SOC in turn enhanced the risk of organic matter degradation and further decreased the aggregate stability (Wu et al., 2012).

Effect of Rotational Grazing on Grassland Soil

Our results showed that rotational grazing significantly increased the fine aggregate stability but had little influence on stability of coarse aggregates with the exception of a significant reduction under light grazing (**Figure 4E**). Due to the increased belowground biomass (see **Table 1**), light grazing significantly increased the total content of coarse aggregates in bulk soil, but it had little influence on the percentage of coarse stable aggregates in the bulk soil (**Figure 4F**). The reason might be that light grazing increased the unstable coarse aggregates rather than stable coarse aggregates, then, the percentage of coarse stable aggregates was relatively decreased (**Figure 4E**). By contrast, medium and high grazing did not increase the percentage of coarse aggregates (**Table 2** and **Figure 4D**). This might be because higher grazing pressure under medium and high grazing also accompanied by more disturbances especially trampling, which could crush the aggregates. As a result, medium and high grazing offset the increased aggregates stimulated by grazing. Our result is consistent with Wang et al. (2020) who also found light grazing promoted the formation of coarse aggregates and higher grazing intensity caused the disintegration of soil aggregates. Our results also showed that coarse aggregate stability was lower than fine aggregate stability (**Figures 3B,E**, **Figures 4B,E**). Puget et al. (1998) showed that coarse aggregates (>1 mm) were more sensitive to grazing interference. As a result, more coarse aggregates were crushed by trampling, which might offset the enhancement of belowground biomass increase and lead to no increase in coarse aggregate stability (Wu et al., 2012).

In addition, rotational grazing did not result in significant differences between grazing intensities. Badgery et al. (2017) found that rotational grazing supported 7–22% higher stocking rate compared with continuous grazing. This was supported by Fang and Xie's earlier findings at the same study site suggesting that rotational grazing had a slight influence on aggregates and organic C content (Fang, 2017; Xie, 2018). Considering that grassland had higher capacity under rotational grazing than continuous grazing of herbivores (Gourlez et al., 2018), even high grazing in this study was still within the carrying capacity of the ecosystem. This may suggest that grassland under rotational grazing has a higher resistance to the impact of grazing. In general, our results provided some evidence that rotational grazing, at least in a short-term, has little, if not positive, influence on aggregate stability.

CONCLUSION

Our results showed that grazing exclusion significantly increased soil aggregate stability, compared with continuous grazing. However, the peak appeared in moderate-term exclusion, whereas long-term exclusion tended to decrease these indicators compared with moderate-term exclusion (although the differences were not significant in some indicators). To restore the degenerated grassland, 2 decades of grazing exclusion was the best period. Five years of rotational grazing increased fine aggregate stability. Rotational grazing intensities had slight impact on soil. We suggest that a sustainable utilization (*e.g.*, rotational grazing) rather than long-term exclusion is a better way to maintain soil health and livelihoods of the local herdsmen.

DATA AVAILABILITY STATEMENT

The original contributions presented in the study are included in the article/Supplementary Material, further inquiries can be directed to the corresponding author.

AUTHOR CONTRIBUTIONS

Conceived the ideas: LD, VM, CL and JM. Analysis and interpretation of data: LD and YZ. Drafting of the manuscript: LD and YZ. Critical revision of the manuscript for important intellectual content: JM and VM.

FUNDING

This study was funded by the Special Project of Basic Scientific Research Business Expenses of China Institute of Water Resources and Hydropower Research (MK 2021J11), the National Key Research and Development Plan of China (2016YFC0500503) and SIU project UTF-2016-long-term/10089.

ACKNOWLEDGMENTS

The authors are indebted to the members of the Inner Mongolia Grassland Ecosystem Research Station (IMGERS) and Xilinhot National Climate Observatory (XNCO) who helped collect the samples. We also thanks laboratory engineers at the soil science laboratory of the *Norwegian University of Life* for help with lab work. LD also thanks the China Scholarship Council (CSC) for fellowship support.

REFERENCES

Badgery, W. B., Millar, G. D., Michalk, D. L., Cranney, P., and Broadfoot, K. (2017). The Intensity of Grazing Management Influences Lamb Production from Native Grassland. *Anim. Prod. Sci.* 57, 1837–1848. doi:10.1071/An15866

Bronick, C. J., and Lal, R. (2005). Soil Structure and Management: a Review. *Geoderma* 124, 3–22. doi:10.1016/j.geoderma.2004.03.005

Chan, K. Y., Oates, A., Li, G. D., Conyers, M. K., Prangnell, R. J., Poile, G., et al. (2010). Soil Carbon Stocks under Different Pastures and Pasture Management in the Higher Rainfall Areas of South-Eastern Australia. *Soil Res.* 48, 7–15. doi:10.1071/Sr09092

Cheng, J., Wu, G. L., Zhao, L. P., Li, Y., Li, W., and Cheng, J. M. (2011). Cumulative Effects of 20-year Exclusion of Livestock Grazing on above- and Belowground Biomass of Typical Steppe Communities in Arid Areas of the Loess Plateau, China. *Plant Soil Environ.* 57, 40–44. doi:10.17221/153/2010-Pse

De Mendiburu, F. (2014). Agricolae: Statistical Procedures for Agricultural Research. *R Package version1.2*–8. Available at: https://CRAN.R-project.org/package=agricolae.

Dong, L., Martinsen, V., Wu, Y., Zheng, Y., Liang, C., Liu, Z., et al. (2021). Effect of Grazing Exclusion and Rotational Grazing on Labile Soil Organic Carbon in north China. *Eur. J. Soil Sci.* 72, 372–384. doi:10.1111/ejss.12952

Fang, J. (2017). *Effects of Grazing on Productivity, Nutrient Content and Ecological Stoichiometry Feature of the Typical Grassland Communities*. (In Chinese with English abstract). Inner Mongolia University, 13–20.

Gourlez de la Motte, L., MamadouMamadou, O., Beckers, Y., Bodson, B., Heinesch, B., and Aubinet, M. (2018). Rotational and Continuous Grazing Does Not Affect the Total Net Ecosystem Exchange of a Pasture Grazed by Cattle but Modifies CO2 Exchange Dynamics. *Agric. Ecosyst. Environ.* 253, 157–165. doi:10.1016/j.agee.2017.11.011

Herrick, J. E., Whitford, W. G., De Soyza, A. G., Van Zee, J. W., Havstad, K. M., Seybold, C. A., et al. (2001). Field Soil Aggregate Stability Kit for Soil Quality and Rangeland Health Evaluations. *Catena* 44, 27–35. doi:10.1016/S0341-8162(00)00173-9

Iuss Working Group, W. (2014). *World Reference Base for Soil Resources 2014 International Soil Classification System for Naming Soils and Creating Legends for Soil Maps*. Rome: FAO.

Kawamura, K., Akiyama, T., Yokota, H.-o., Tsutsumi, M., Yasuda, T., Watanabe, O., et al. (2005). Quantifying Grazing Intensities Using Geographic Information Systems and Satellite Remote Sensing in the Xilingol Steppe Region, Inner Mongolia, China. *Agric. Ecosyst. Environ.* 107, 83–93. doi:10.1016/j.agee.2004.09.008

Kemper, W., and Rosenau, R. (1986). *Aggregate Stability and Size Distribution*.

Kölbl, A., Steffens, M., Wiesmeier, M., Hoffmann, C., Funk, R., Krümmelbein, J., et al. (2011). Grazing Changes Topography-Controlled Topsoil Properties and Their Interaction on Different Spatial Scales in a Semi-arid Grassland of Inner Mongolia, P.R. China. *Plant Soil* 340, 35–58. doi:10.1007/s11104-010-0473-4

Liu, J. (2016). "Research on Nitrogen Froms and Microbial Community Structure of Grassland Soil in Inner Mongolia," in *Chinese with English Abstract)* (Zhejiang University), 16–17.

McSherry, M. E., and Ritchie, M. E. (2013). Effects of Grazing on Grassland Soil Carbon: a Global Review. *Glob. Change Biol.* 19, 1347–1357. doi:10.1111/gcb.12144

Mekuria, W., Veldkamp, E., Haile, M., Nyssen, J., Muys, B., and Gebrehiwot, K. (2007). Effectiveness of Exclosures to Restore Degraded Soils as a Result of Overgrazing in Tigray, Ethiopia. *J. Arid Environments* 69, 270–284. doi:10.1016/j.jaridenv.2006.10.009

Obia, A., Mulder, J., Martinsen, V., Cornelissen, G., and Børresen, T. (2016). *In Situ* effects of Biochar on Aggregation, Water Retention and Porosity in Light-Textured Tropical Soils. *Soil Tillage Res.* 155, 35–44. doi:10.1016/j.still.2015.08.002

Puget, P., Angers, D. A., and Chenu, C. (1998). Nature of Carbohydrates Associated with Water-Stable Aggregates of Two Cultivated Soils. *Soil Biol. Biochem.* 31, 55–63. doi:10.1016/S0038-0717(98)00103-5

Reeder, J. D., and Schuman, G. E. (2002). Influence of Livestock Grazing on C Sequestration in Semi-arid Mixed-Grass and Short-Grass Rangelands. *Environ. Pollut.* 116, 457–463. doi:10.1016/S0269-7491(01)00223-8

Reszkowska, A., Krümmelbein, J., Peth, S., Horn, R., Zhao, Y., and Gan, L. (2011). Influence of Grazing on Hydraulic and Mechanical Properties of Semiarid Steppe Soils under Different Vegetation Type in Inner Mongolia, China. *Plant Soil* 340, 59–72. doi:10.1007/s11104-010-0405-3

Sanjari, G., Ghadiri, H., Yu, B., and Ciesiolka, C. (2010). "Increase in Ground Cover under a Paddock Scale Rotational Grazing experiment in South-East Queensland," in *Proceedings of the 19th World Congress of Soil Science: Soil Solutions for a Changing World* (International Union of Soil Sciences (IUSS), 52–55.

Shi, Y. (2016). Effects of Grazing on Underground Biomass and Individual Plant Root Traits of a Typical Grassland Community (In Chinese with English Abstract). *Inner Mongolia Universituy*, 12–17.

Six, J., Elliott, E. T., and Paustian, K. (2000). Soil Macroaggregate Turnover and Microaggregate Formation: a Mechanism for C Sequestration under No-Tillage Agriculture. *Soil Biol. Biochem.* 32, 2099–2103. doi:10.1016/S0038-0717(00)00179-6

Sovell, L. A., Vondracek, B., Frost, J. A., and Mumford, K. G. (2000). Impacts of Rotational Grazing and Riparian Buffers on Physicochemical and Biological Characteristicsof southeastern Minnesota, USA, Streams. *Environ. Manage.* 26, 629–641. doi:10.1007/s002670010121

Steffens, M., Kölbl, A., Schörk, E., Gschrey, B., and Kögel-Knabner, I. (2011). Distribution of Soil Organic Matter between Fractions and Aggregate Size Classes in Grazed Semiarid Steppe Soil Profiles. *Plant Soil* 338, 63–81. doi:10.1007/s11104-010-0594-9

Steffens, M., Kölbl, A., Totsche, K. U., and Kögel-Knabner, I. (2008). Grazing Effects on Soil Chemical and Physical Properties in a Semiarid Steppe of Inner Mongolia (P.R. China). *Geoderma* 143, 63–72. doi:10.1016/j.geoderma.2007.09.004

Teague, W. R., Dowhower, S. L., Baker, S. A., Haile, N., DeLaune, P. B., and Conover, D. M. (2011). Grazing Management Impacts on Vegetation, Soil Biota and Soil Chemical, Physical and Hydrological Properties in Tall Grass Prairie. *Agric. Ecosyst. Environ.* 141, 310–322. doi:10.1016/j.agee.2011.03.009

Tong, C., Wu, J., Yong, S., Yang, J., and Yong, W. (2004). A Landscape-Scale Assessment of Steppe Degradation in the Xilin River Basin, Inner Mongolia, China. *J. Arid Environments* 59, 133–149. doi:10.1016/j.jaridenv.2004.01.004

Wang, H. (2010). "The Study of Soil Physical Properties and Infiltration Capacity of Typical Grassland," in *Chinese with English Abstract* (Inner Mongolia University), 17–23.

Wang, J., Zhao, C., Zhao, L., Wen, J., and Li, Q. (2020). Effects of Grazing on the Allocation of Mass of Soil Aggregates and Aggregate-Associated Organic Carbon in an alpine Meadow. *Plos one* 15, e0234477. doi:10.1371/journal.pone.0234477

Wilson, C. H., Strickland, M. S., Hutchings, J. A., Bianchi, T. S., and Flory, S. L. (2018). Grazing Enhances Belowground Carbon Allocation, Microbial Biomass, and Soil Carbon in a Subtropical Grassland. *Glob. Change Biol.* 24, 2997–3009. doi:10.1111/gcb.14070

Wu, H., Wiesmeier, M., Yu, Q., Steffens, M., Han, X., and Kögel-Knabner, I. (2012). Labile Organic C and N Mineralization of Soil Aggregate Size Classes in Semiarid Grasslands as Affected by Grazing Management. *Biol. Fertil. Soils* 48, 305–313. doi:10.1007/s00374-011-0627-4

Wu, L., He, N., Wang, Y., and Han, X. (2008). Storage and Dynamics of Carbon and Nitrogen in Soil after Grazing Exclusion in Leymus Chinensis Grasslands of Northern China. *J. Environ. Qual.* 37, 663–668. doi:10.2134/jeq2007.0196

Xie, D. S. (2018). *Study on the Change Process of Soil Aggregates and Organic Carbon under Different Grazing Gradient in Typical Steppe*. (In Chinese with English abstract). Inner Mongolia University.

Xiong, S., and Nilsson, C. (1999). The Effects of Plant Litter on Vegetation: a Meta-Analysis. *J. Ecol.* 87, 984–994. doi:10.1046/j.1365-2745.1999.00414.x

Yong-Zhong, S., Yu-Lin, L., Jian-Yuan, C., and Wen-Zhi, Z. (2005). Influences of Continuous Grazing and Livestock Exclusion on Soil Properties in a Degraded sandy Grassland, Inner Mongolia, Northern China. *Catena* 59, 267–278. doi:10.1016/j.catena.2004.09.001

Conflict of Interest: The authors declare that the research was conducted in the absence of any commercial or financial relationships that could be construed as a potential conflict of interest.

frontiers | Frontiers in Environmental Science

ORIGINAL RESEARCH
published: 13 April 2022
doi: 10.3389/fenvs.2022.878466

Temporal Variation of Airborne Dust Concentrations in the Mogao Grottoes, Dunhuang, China

Guobin Zhang[1], *Lihai Tan*[2,3]*, *Weimin Zhang*[2,3], *Hongtao Zhan*[1] *and Fei Qiu*[1]

[1]Dunhuang Research Academy, Dunhuang, China, [2]Key Laboratory of Desert and Desertification, Northwest Institute of Eco-Environment and Resources, Chinese Academy of Sciences, Lanzhou, China, [3]Dunhuang Gobi Desert Research Station, Northwest Institute of Eco-Environment and Resources, Chinese Academy of Science, Dunhuang, China

Dust storms bring a large quantity of dust aerosols from arid and semi-arid regions of the Earth. However, real-time dust concentration data for dust storms in arid regions, important for wind erosion studies, are still limited. Here, temporal variation of airborne dust concentrations in the Mogao Grottoes, Northwest China, during the monitoring period from February to October 2012 and typical dust storms under different wind directions were analyzed. Results reveal that the monthly mean total suspended particle (TSP), particulate matter less than 10 μm (PM10), and particulate matter less than 2.5 μm (PM2.5) concentrations gradually decreased from February to October. The daily mean dust concentrations fluctuated with the day, with extreme values occurring mainly on February, March, and April. The daily mean PM10/TSP ratio ranged from 0.67 to 0.98 (mean of 0.82), and the PM2.5/PM10 ratio ranged from 0.31 to 0.73 (mean of 0.55), indicating PM10 dominated in TSP. In typical dust storms, the maximum real-time concentrations can reach 16, 000–21, 000 μg TSP m^{-3}, ~11, 000 μg PM10 m^{-3}, and 3000–3500 μg PM2.5 m^{-3}, and extreme real-time dust concentrations of 50358.03 μg TSP m^{-3}, 33100.86 μg PM10 m^{-3}, and 7502.59 μg PM2.5 m^{-3} were recorded. Coincidence of the dry climate and windy season and sufficient dust sources in the surrounding environment contributed to the high dust concentrations in the Mogao Grottoes. To achieve the goal of minimizing the damage of falling dust to the murals and statues, establishing a dust storm early warning system and improving the existing sand control system are recommended.

Keywords: dust storms, particulate matter, dust concentration, temporal variation, dust hazards, Mogao Grottoes

OPEN ACCESS

Edited by:
Huawei Pi,
Henan University, China

Reviewed by:
Zhongju Meng,
Inner Mongolia Agricultural University, China
Lishuai Xu,
Shanxi Agricultural University, China

***Correspondence:**
Lihai Tan
tanlihai09@lzb.ac.cn

Specialty section:
This article was submitted to Drylands, a section of the journal Frontiers in Environmental Science

Received: *18 February 2022*
Accepted: *28 March 2022*
Published: *13 April 2022*

Citation:
Zhang G, Tan L, Zhang W, Zhan H and Qiu F (2022) Temporal Variation of Airborne Dust Concentrations in the Mogao Grottoes, Dunhuang, China. Front. Environ. Sci. 10:878466. doi: 10.3389/fenvs.2022.878466

INTRODUCTION

Dust storms raise large quantities of dust from arid and semi-arid regions on Earth, which contributes more than half of the total global aerosol burden, and the dust can be transported over 1000s of kilometers and deposited downwind by wet and dry processes (Choobari et al., 2014). Mineral dust affects the Earth and Mars systems through a large variety of interactions (Kok et al., 2012). As an important kind of catastrophic weather, dust storms not only cause great losses to industrial and agricultural production and people's lives and property, but also pollute the environment and have an important impact on climate change (Goudie, 2009; Choobari et al., 2014). In China, dust storms are common, especially in north and north-west regions (Zhang et al., 1997; Wang X. et al., 2008) and mainly in spring (Zhou and Wang, 2002), which is one of significant global dust sources. For example, from March 14 to 16, 2021, an

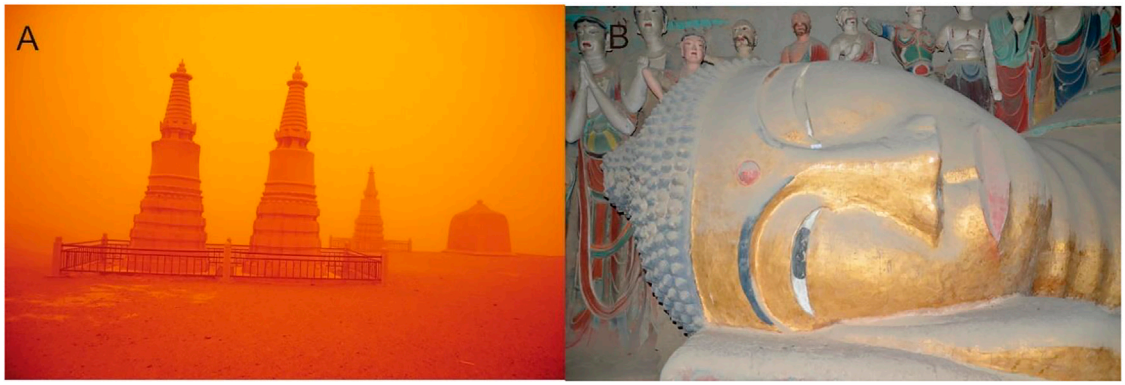

FIGURE 1 | A severe dust storm in the Mogao Grottoes **(A)** and the painted sculptures in caves are covered by falling dust particles **(B)**.

extremely strong dust storm occurred in the northern region of China, with a distribution area of more than 3.8 million km^2, and the peak concentration of PM10 reached over 5000 $\mu g\ m^{-3}$ in many areas of northern China (Yang et al., 2021; Zhang et al., 2022). In addition to Mongolia, the northern and northwestern sandy regions of China are also important dust sources (Liu et al., 2022). As estimated, an annual dust quantity of approximately 800 Tg Chinese desert dust was injected into the atmosphere, and it was almost as much as half of the global production of dust (Zhang et al., 1997).

Much recent advances have been made in our understanding of global dust sources, transport paths, their impacts both on humans and the environment, and their mass concentration, chemical composition, and optical properties (Goudie, 2009), of which the variation characteristics of airborne dust concentrations during dusty weathers is very important in aeolian research, which can help to identify dust source areas (Goudie and Middleton, 2006). However, limited studies have examined the variation of dust concentrations during dusty weathers in arid regions (Gillies et al., 1996; Ganor and Foner, 2001; Shen et al., 2004; Rashki et al., 2012; Dahmardeh Behrooz et al., 2017). Furthermore, due to the limitation of dust concentration measuring instruments, the data of dust concentrations, particularly the real-time monitoring data in northwest of China during dust storm episodes was scarce, especially in dust source areas (Wang Y. Q. et al., 2008). For example, vacuum pump-based devices or high volume samplers (HVS), which can collect the total range of particles in the air, were usually used to measure dust concentrations in wind erosion studies; however, data of dust concentrations are time-integrated over the total sampling period, while real-time dust concentrations cannot be provided by these instruments (Baddock et al., 2014). As a whole, the real-time dust concentrations data during dust storms in arid regions of the world are still limited.

The Mogao Grottoes, Dunhuang, China, one of Buddhism's most revered shrines (Stone, 2008), and surrounded by Sandy and Gobi Deserts, is a typical study area of extremely arid regions where dust storms are common and severe (**Figure 1A**). Furthermore, dust hazards caused by dust storms have threatened the protection of murals and statues in the caves. The falling dust particles cause serious discoloration and crispness of murals, which seriously affects their artistic effects. The extremely fine dust particles are easy to invade the gaps of murals and plastic pigments (**Figure 1B**), which are difficult to be removed without damaging the murals. Dust storms are the dominant source of falling dust in the grottoes. As a famous cultural heritage in China and even in the world, dust hazards have become an urgent and severe problem in the protection of Mogao Grottoes murals. Preliminary studies have been performed on the size and mineral composition of falling dust (Qu et al., 1992), TSP concentration (Wang et al., 2006), and the composition of water-soluble ions of aeolian dust in the Mogao Grottoes (Zhang et al., 2007). However, the monitoring data of dust concentrations during dust storms in the Mogao Grottoes district are limited, and at present, studies regarding aeolian research in the Mogao Grottoes mainly focus on aeolian transport over gobi (Zhang et al., 2014; Liu et al., 2011b; Tan et al., 2013, 2016) and dynamic processes of pyramid dunes atop the Mogao Grottoes (Liu et al., 2011a). Consequently, characteristics of the temporal variation of dust (TSP, PM10, and PM2.5) concentrations in the Mogao Grottoes, especially during dust storms, and the controlling factors are still poorly understood.

This study conducted continuous and synchronous observations of wind speeds and total suspended particle (TSP), particulate matter less than 10 μm (PM10), and particulate matter less than 2.5 μm (PM2.5) concentrations from February to October 2012. Temporal variation characteristics of airborne dust concentrations during the monitoring period (monthly and daily means) and typical dust storms with different wind directions (real-time values) in the Mogao Grottoes were analyzed. Factors influencing dust concentrations in the Mogao Grottoes have also been discussed.

MATERIALS AND METHODS

Aeolian Environment

The Mogao Grottoes is located approximately 25 km southeast of Dunhuang City, which is an important way station of the ancient

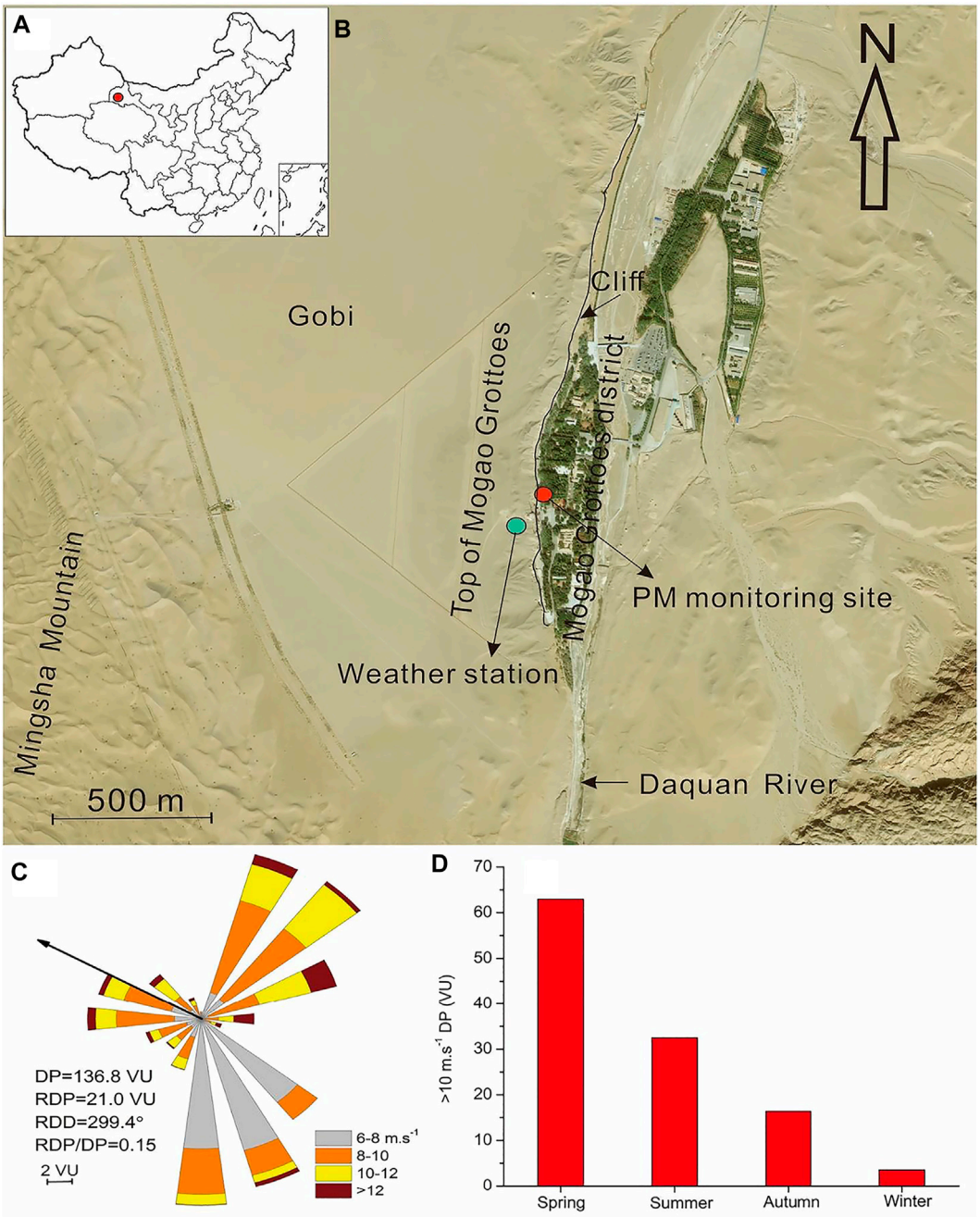

FIGURE 2 | Location of the study areas **(A,B)**, the average sand drift potential during 2005–2007 **(C)**, and the seasonal DP over 10 m s^{-1} **(D)**.

Silk Road in western China (Stone, 2008). The 492 decorated caves with 45,000 square meters of murals were excavated on the vertical cliff surface of the alluvial fan terrace on the west bank of the Daquan River in a length of 1680 m between the 4th and 14th centuries C.E., which are also called the "Museum on the Wall." The Mogao Grottoes was designated as a World Cultural Heritage site by UNESCO in 1987.

The Mogao Grottoes is adjacent to Sanwei Mountain in the east, Mingsha Mountain in the west, Daquan River in the south, and the open gobi in the north (**Figure 2 A, B**). The grottoes were built on the west bank of the Daquan River, the length of the cliff body was approximately 1680 m, and the height of the cliff body was generally 10–45 m (**Figure 2B**). The average annual precipitation in Dunhuang City was 37.9 mm, with an average annual potential evaporation of 2087.3 mm (Ba and Wang, 2010). The multi-year average number of dust days in Dunhuang City was 46.5 days, which mainly occurred in spring (Zhou and Wang, 2002). Gobi and mega-dunes are two main landforms in the

FIGURE 3 | The Metstn weather station on the top of the Mogao Grottoes **(A)** and Thermo Scientific™ Partisol™ 2025i Sequential Air Sampler in front of the Grotto 72 **(B)**.

surrounding area of the Mogao Grottoes. Mingsha Mountain, composed of huge and complex mega-dunes, is located to the west side atop the grottoes, and it is the main sand source threatening the grottoes.

The annual sand drift potential (DP) was calculated using the method proposed by Fryberger and Dean (1979), and the average annual DP on the top of the Mogao Grottoes in 2005–2007 was 136.8 vector units (VU), indicating a low wind energy environment (**Figure 2C**) (Tan, 2015). There were three main wind directions atop the Mogao Grottoes, that is, easterly, westerly, and southerly winds. Among them, the DP of westerly winds (W, WSW, WNW, and NW) was 28.3 VU, the DP of easterly winds (NNE, NE, ENE, and E) was 48.8 VU, and the DP of southerly winds was 51.5 VU, accounting for 20.7, 35.7, and 37.6% of the annual DP, respectively. The average annual compound sand drift potential (RDP) at the top of the Mogao Grottoes was 21.0 VU, the compound sand drift direction (RDD) was 299.4°, and the RDP/DP value was 0.15, which was a compound wind regime. However, though the southerly winds have the largest frequency, they were mainly in the speed range of 6–10 m s^{-1}. In the speed range of >10 m s^{-1}, the DP of easterly and westerly winds accounted for 57.9 and 24.3% of the total DP in this speed range, respectively, indicating that easterly winds had the strongest power, and the second was westerly winds. Westerly and easterly winds are two main strong winds that cause dust storms dominating in the spring of each year. The largest DP over 10 m s^{-1} occurred in spring, accounting for 54.6% of the total DP over 10 m s^{-1}, and it was followed by summer, accounting for 28.2% of the total DP over 10 m s^{-1} (**Figure 2D**).

Instrumentation

A Metstn weather station on the top of the Mogao Grottoes (**Figure 2B**) was used to measure wind velocity/direction at a height of 2 m above the ground and precipitation (**Figure 3A**), which were logged synchronously with data of dust concentrations.

Dust concentrations were measured using the Thermo Scientific Partisol 2025i Sequential Air Sampler (**Figure 3B**), which was sited in front of Grotto 72 (**Figure 2B**). The Partisol 2025i was configured to sample a wide range of ambient PM sizes, including TSP, PM10, and PM2.5. The Partisol has a fully automatic filter exchange mechanism that provides unattended monitoring for up to 16 consecutive days for 24-h sampling prior to filter change, and quartz fibre filters have been used for the collection of particulate matter (Charron et al., 2004). Dust concentration data were logged in 2 min, and the pumping inlet of the Air Sampler was mounted at a height of 1.2 m above the ground. Dust concentrations in front of Grotto 72 during February 2012 to October 2012 were continuously monitored. Unfortunately, due to the harsh aeolian environment and strong dust storms in the study area, the Partisol 2025i Sequential Air Sampler malfunctioned and could not continue to work after October 2012.

TABLE 1 | The monthly average dust concentrations in the Mogao Grottoes.

Month	Monthly average dust concentrations (μg.m^{-3})		
	TSP	PM10	PM2.5
February	544.63	477.92	234.61
March	371.71	316.18	197.97
April	117.83	90.42	53.24
May	45.54	34.56	17.56
June	35.80	29.15	16.51
July	25.63	20.59	10.91
August	17.47	13.60	6.53
September	7.44	6.43	4.00
October	4.90	4.29	2.78

RESULTS

Temporal Variation of the Mean Dust Concentrations During the Monitoring Period

Monthly Variation

The monthly mean TSP, PM10, and PM2.5 concentrations during the monitoring period were 4.90–544.63 μg m^{-3},

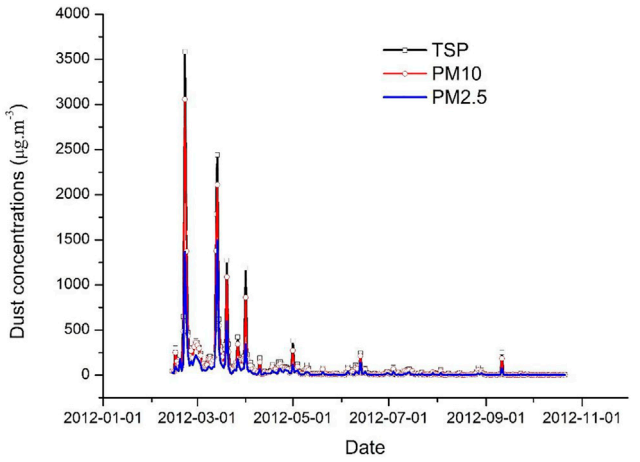

FIGURE 4 | Variation of daily mean dust concentrations in the Mogao Grottoes.

4.29–477.92 μg m^{-3}, and 2.78–234.61 μg m^{-3}, respectively (**Table 1**). The monthly mean value of dust concentrations gradually decreased from February to October, and showed a maximum in February, with TSP, PM10, and PM2.5 concentrations of 544.63, 477.92, and 234.61 μg m^{-3}. The second high concentration value occurred in March, with the TSP, PM10, and PM2.5 concentrations of 371.71, 316.18, and 197.97 μg m^{-3}. In April, the third high concentration value occurred, and the concentration values of TSP, PM10, and PM2.5 were 117.83, 90.42, and 53.24 μg m^{-3}, respectively. Zhou and Wang (2002) revealed that severe dust storms in northwest China usually occurred in spring, especially in April, and winter was the second high season. Cao et al. (2013) showed that the seasonal variation of PM10 concentration at the Dunhuang station during 2007–2011, and it indicated that the PM10 concentration was the highest in spring, lowest in autumn. The monthly mean dust concentrations in the Mogao Grottoes were consistent with this conclusion, and dust concentrations in summer and autumn significantly decreased compared with those in spring.

Daily Variation

The daily variations of TSP, PM10, and PM2.5 concentrations show fluctuation with the day, with extreme peaks on certain days (**Figure 4**). The extreme values of dust concentrations occurred mainly on February, March, and April, when dusty days were common in the Mogao Grottoes district. The daily mean TSP, PM10, and PM2.5 concentrations were in the range of 2.36–3585.53, 1.95–3056.88, 0.69–1368.60 μg m^{-3}, respectively. However, the daily mean background concentration values of TSP, PM10, and PM2.5 were 14.74, 11.99, and 6.12 μg m^{-3}, respectively. Thus, the maximum daily dust concentration values in dusty days could reach approximately 70 times of those during dust-free days. The maximum daily concentration values occurred in February, while the minimum values in October. Furthermore, the maximum daily mean dust concentrations deceased with each month. For example, the maximum daily mean TSP, PM10, and PM2.5 concentrations in February were 3585.53, 3056.88, 1368.60 μg m^{-3}, respectively, while in March they deceased to 2442.60, 2111.78, and 1495.91 μg m^{-3}, and in April, they decreased to 1185.84, 861.77, and 344.69 μg m^{-3}. Based on daily observations from air quality monitoring stations, Filonchyk et al. (2019) analyzed the PM10 and PM2.5 concentrations in typical cities of the northwest China during winter-spring period of dust storms in 2014–2017, and it showed that the peak daily average PM10 and PM2.5 concentrations exceeded 380 and 150 μg m^{-3}, respectively, and the extreme PM10 concentration value of 977 μg m^{-3} was recorded on 23 April 2014 in Lanzhou, and in Urumqi, the PM10 concentrations reached to 400 μg m^{-3}. Obviously, the daily mean PM10 concentrations in the Mogao Grottoes district were larger than those values in these cities during dusty days, while the daily dust concentrations in this study were comparable with those during dust storms in Iran, such as Zabol, located in the Sistan basin of southeast Iran (Dahmardeh Behrooz et al., 2017) and Ahvaz, southwestern Iran (Shahsavani et al., 2012).

Correlation Among the Mean Concentrations of TSP, PM10, and PM2.5

The relationship among the daily mean concentrations of TSP, PM10, and PM2.5 shows that there was a significant positive correlation between TSP, PM10, and PM2.5, that is, PM10 = 0.84TSP, PM2.5 = 0.42TSP, and M2.5 = 0.50PM10, with a determination coefficient R^2 over 0.93 (**Figure 5**). The PM10/TSP ratio ranged from 0.67 to 0.98 with a mean value of 0.82, and the PM2.5/PM10 ratio ranged from 0.31 to 0.73 (mean of 0.55). This result indicates that PM10 is the main component of TSP, and PM2.5 is dominant in PM10 in the Mogao Grottoes. Gholampour et al. (2016) reported that the daily mean PM10/TSP ratios at two sampling sites in Urmia Lake, Northwest Iran, the second great saline lake in the world, ranged from 0.38 to 0.90 and 0.57 to 0.96, respectively, with mean values of 0.64 and 0.75, which was consistent with the ratios in this study. Dahmardeh Behrooz et al. (2017) analyzed TSP and PM10 concentrations in dust events in Zabol, Southeastern Iran and revealed that the PM10/TSP ratio ranged from 0.27 to 0.99 with a mean of 0.37, indicating that particles above 10 μm were dominant in TSP, which were coarser than those in this study. They attributed the higher fraction of coarse particles to the influence of soil-crust material on the airborne samples.

Variation Characteristics of Real-Time Dust Concentrations in Typical Dust Weathers

A Typical Dust Storm Under Westerly Winds

Westerly and easterly winds are two main strong winds that cause dust storms in the Mogao Grottoes district. An episode of dust storms under westerly winds occurring at 11:50–18:10 on 1 April 2012 in the Mogao Grottoes was selected to show the variation characteristics of real-time dust concentrations (**Figure 6**). During this dust storm, the average wind

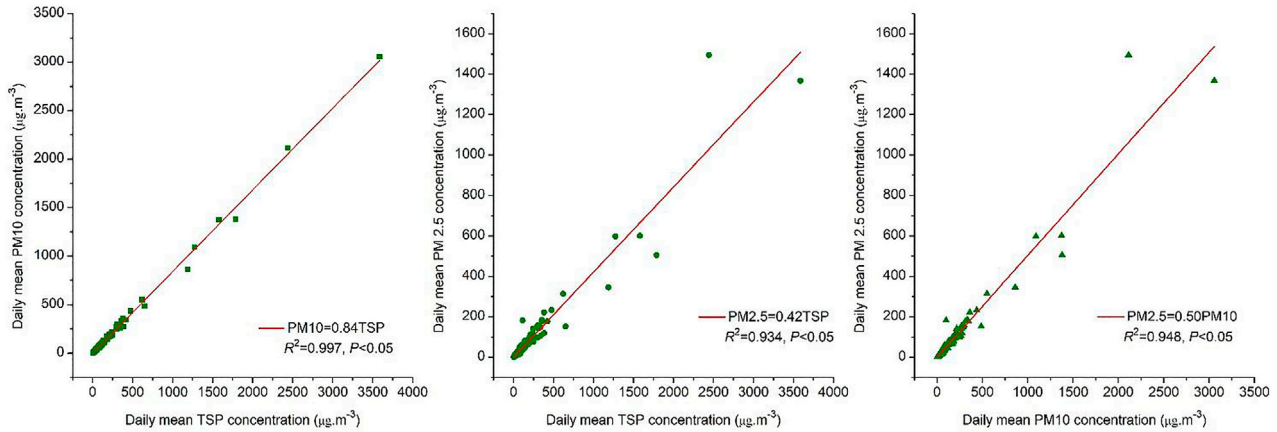

FIGURE 5 | Correlation among the mean concentrations of TSP, PM10, and PM2.5.

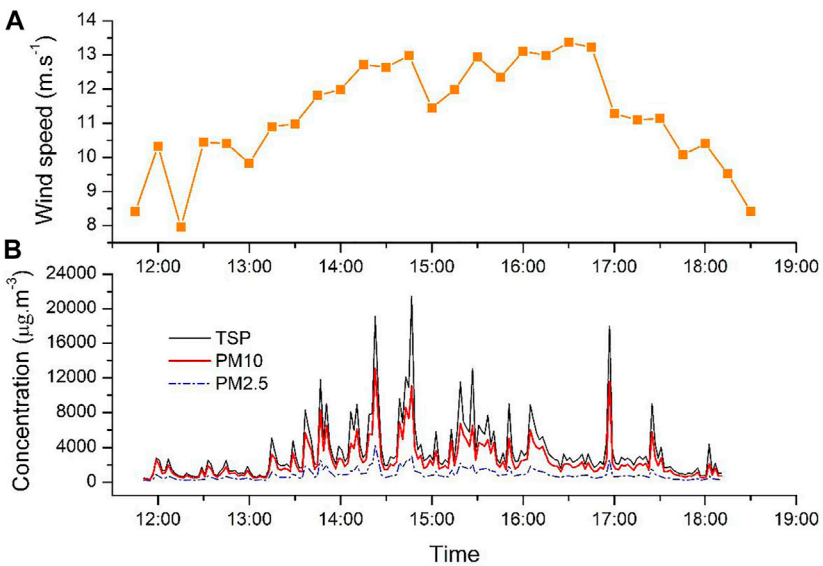

FIGURE 6 | Wind speeds at the height of 2 m atop the Mogao Grottoes **(A)** and the corresponding dust concentrations **(B)** changing with time under a typical dust storm of westerly winds on 1 April 2012.

direction at 2 m above the ground was 286.2°, belonging to WNW winds. The average wind speed at 2 m above the ground was 11.11 m s^{-1}, and the maximum wind speed was 13.37 m s^{-1} (**Figure 6A**). When converting it into the wind speed at 10 m according to the wind profile, the maximum wind speed was 15.78 m s^{-1}, indicating that it reached moderate gale. The average TSP, PM10, and PM2.5 concentrations were 3528.81, 2465.49, and 869.22 μg m^{-3}, respectively. Among them, the average ratio of PM10 to TSP concentration was 0.70, and that of PM2.5 to PM10 concentration was 0.35, implying that PM10 was the main composition of TSP during dust storms of westerly winds. The maximum dust concentrations were 21483.32 μg TSP m^{-3}, 11085.17 μg PM10 m^{-3}, and 3028.08 μg PM2.5 m^{-3} (**Figure 6B**).

A Typical Dust Storm Under Easterly Winds

A dust storm under easterly winds occurred at 14:00–19:00 on 13 March 2012 in the Mogao Grottoes, and the variation characteristics of real-time dust concentrations during this period were shown in **Figure 7**. During this dust storm, the average wind direction at 2 m above the ground was 85.4°, belonging to E winds. The average wind speed at 2 m above the ground was 11.33 m s^{-1}, and the maximum wind speed was 14.09 m s^{-1} (**Figure 7A**). The corresponding maximum wind speed at 10 m was 16.93 m s^{-1}, and thus it reached the level of moderate gale. The average TSP, PM10, and PM2.5 concentrations were 5002.71, 3745.33, and 1297.48 μg m^{-3}, respectively. Among them, the average PM10/TSP ratio was 0.75, and the average PM2.5/PM10 ratio was 0.35, showing

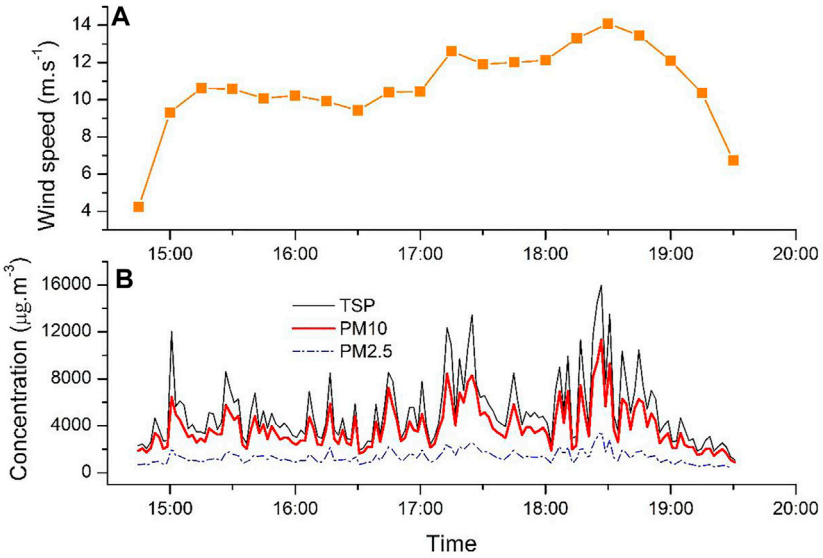

FIGURE 7 | Wind speeds at the height of 2 m atop the Mogao Grottoes **(A)** and the corresponding dust concentrations **(B)** changing with time under a typical dust storm of easterly winds on 13 March 2012.

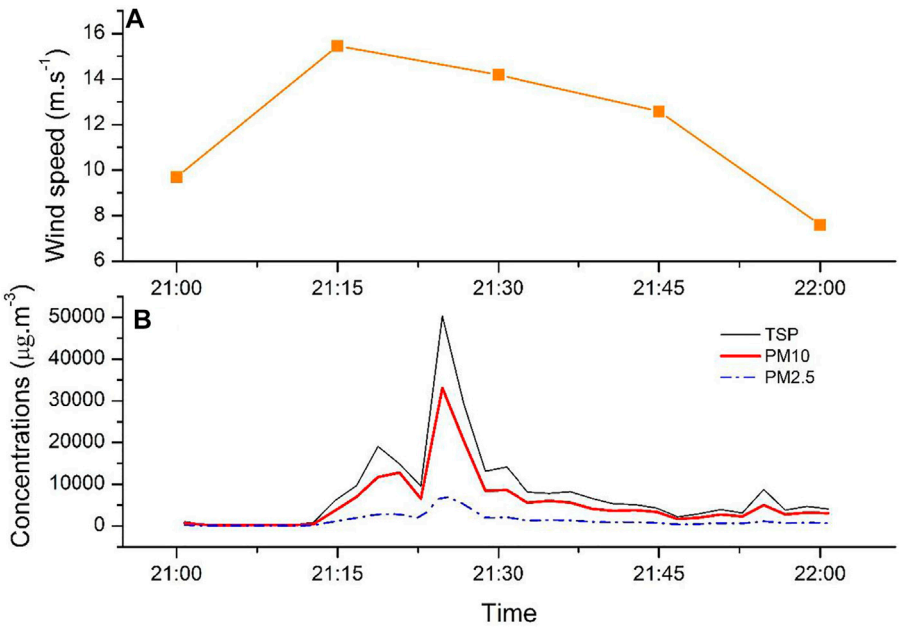

FIGURE 8 | Wind speeds at the height of 2 m **(A)** and dust concentrations **(B)** changing with time in an extreme dust episode on 21 February 2012.

that PM10 was also dominant in dust storms of easterly winds. The maximum dust concentrations in this episode were 15959.97 μg TSP m^{-3}, 11363.59 μg PM10 m^{-3}, and 3591.52 μg PM2.5 m^{-3} (**Figure 7B**).

A severe dust storm under easterly winds occurred at 21:00–22:00 on 21 February 2012. During this dust storm, the maximum wind speed at 2 m was 15.46 m s^{-1} (**Figure 8A**), which was the maximum wind speed in the whole measurement period. The corresponding wind speed at 10 m was 18.75 m s^{-1}, and it reached the level of fresh gale. The extreme dust concentrations reached 50358.03 μg TSP m^{-3}, 33100.86 μg PM10 m^{-3}, and 7502.59 μg PM2.5 m^{-3} (**Figure 8B**). The data of real-time dust concentrations during dust storm episodes in China was scarce due to the limitation of PM concentration measuring instruments. The recorded extreme values of TSP concentration over 20,000 μg m^{-3} and PM10 over 10,000 μg m^{-3} in dust storms on Earth was relatively limited in the

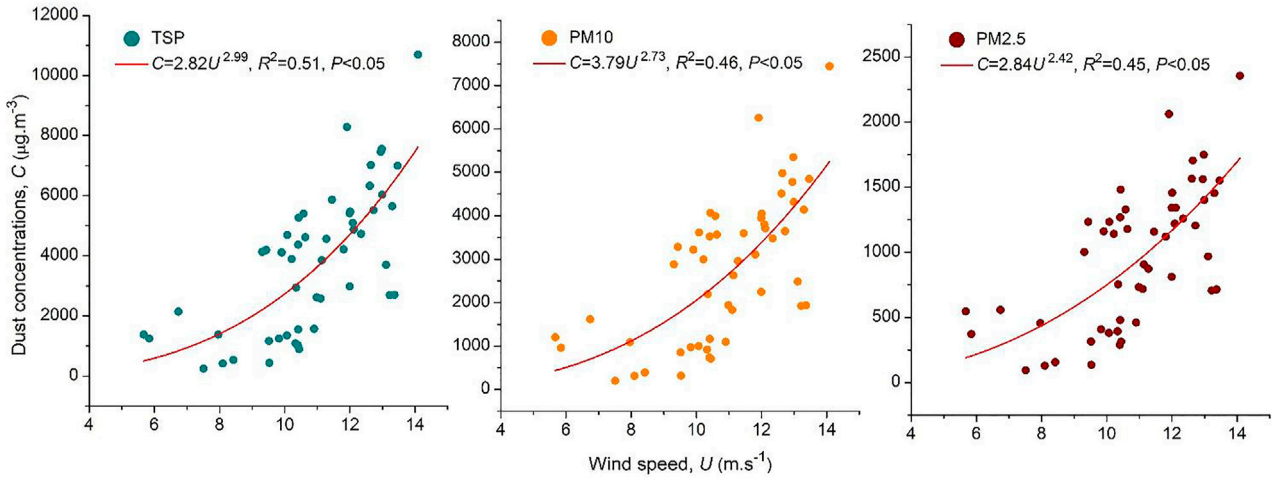

FIGURE 9 | The relationship between the concentrations of TSP, PM10 and PM2.5 and wind speed during dust storms.

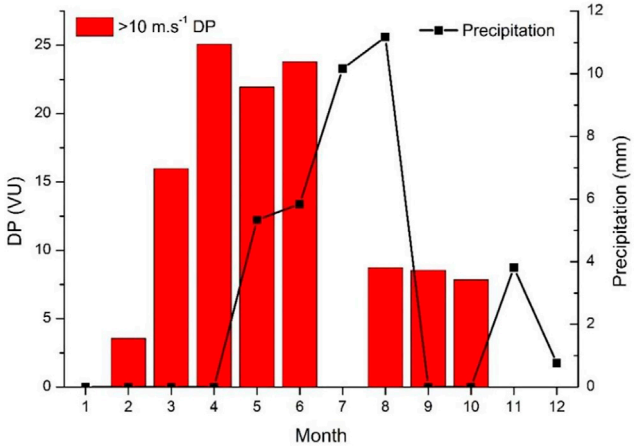

FIGURE 10 | Monthly DP (>10 m s^{-1}) and precipitation in the Mogao Grottoes district in 2012.

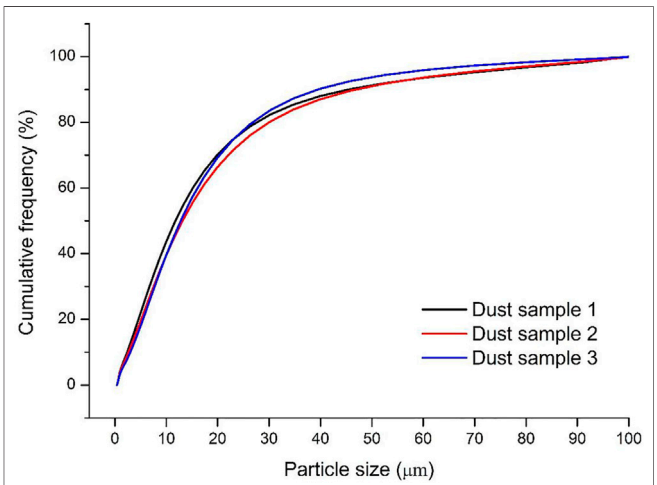

FIGURE 11 | The size composition of falling dust particles in the caves of the Mogao Grottoes.

literature. Ganor and Foner (2001) reported one dust storm in Tel Aviv when a TSP concentration of 24,000 μg m^{-3} was recorded. Gillies et al. (1996) reported a measured peak dust concentration 13735 μg m^{-3} during an intense dust plume in the Inland Delta region of Mali. Dahmardeh Behrooz et al. (2017) revealed that an extreme daily TSP concentration could reach 10780 μg m^{-3} over Sistan, Iran during the summer dusty period. Thus, the dust concentrations reported in this study were comparable to those previously obtained in dust storm events over other arid regions in the literature.

DISCUSSION

The Mogao Grottoes is located in the extremely arid region, surrounded by Gobi and Sandy Deserts, and suffered from severe dust storms. Due to the harsh aeolian environment and instrument limitation, real-time dust concentration data in dust storm episodes in the Mogao Grottoes were not easy to obtain. In this study, synchronous observations of wind speeds and concentrations of TSP, PM10, and PM2.5 were performed in the Mogao Grottoes from February to October 2012 using a Partisol 2025i Sequential Air Sampler. This study provides significant real-time concentration data of TSP, PM10, and PM2.5 in a typical dust source area of northwest China, which is important for wind erosion research in arid regions. Meanwhile, the monitoring period is representative because in the latest 10 years the variation of the occurrence frequency of dust storms in Dunhuang, northwest China is limited (Luo et al., 2021). In the following Discussion section, the main factors influencing airborne dust concentrations in the Mogao Grottoes have been discussed.

Factors Influencing Dust Concentrations in the Mogao Grottoes District

Wind Speed

Wind speed is a dynamic factor influencing dust concentrations. The relationship between the concentrations of TSP, PM10, and PM2.5 and wind speed at 2 m can be expressed by a power function (**Figure 9**):

$$C = au^b$$

Where C is dust concentrations (μg m^{-3}), u is wind speeds at a height of 2 m above the ground (m s^{-1}), and a and b are regression coefficients. Under the two dust storms, the power exponents in the power functions for TSP, PM10, and PM2.5 were 2.99, 2.73, and 2.42, respectively. Ta et al. (2003) analyzed the relationship between TSP concentration and wind speed in seven cities of Gansu Province, China and concluded that TSP concentration increased with wind speed. Wang and Zhang (2021) revealed that the PM10 concentration during a dust storm over a gobi surface was positively correlated with wind speed, and compared with that near the surface the correlation at the heights of 60 and 200 cm was weakened by the PM10 from non-local sources. These results are consistent with the results in this study.

Coincidence of Dry Climate and Windy Season

The area of the Mogao Grottoes is under an extremely dry climate, and the annual precipitation in 2012 was 37.1 mm (**Figure 10**). Meanwhile, the precipitation was mainly concentrated in summer (August, July and June), accounting for 73.3% of the total value. Spring was the driest season in a year, and there was no precipitation recorded in March and April of the study period. Furthermore, the frequency and strength of wind in these months were the highest (**Figure 10**). As a result, dust concentrations under dust storms in these months are usually the largest, contributing to the falling dust particles in the caves.

Sufficient Dust Sources

The landforms atop the Mogao Grottoes are of four types, namely, sandy gobi, gravel gobi, flat sand sheets, and mega-dunes (Zhang et al., 2014). Mingsha Mountain is composed of huge and complex mega-dunes, located to the west side atop the grottoes, and it is the main sand source threatening the grottoes. Dust particles (<63 μm) can account for 1.5 and 8.1% in mass percentage for sand dunes and gobi surfaces, respectively (Tan, 2015). Under westerly winds, these landforms atop the Mogao Grottoes supply abundant dust particles to the caves. While in the upwind of easterly winds, sandy gobi is the main landform, and during dust storms of easterly winds, it is the main source for falling dust in the caves. The falling dust in the caves mainly comes from the short distance transport of dust in Mingsha Mountain (Qu et al., 1992) and sandy gobi atop the Mogao Grottoes (Zhang et al., 2014). In addition, aeolian dust transported in a long distance within dust storms from southern Xinjiang and Inner Mongolia partly contributes to aeolian dust in the Mogao Grottoes (Gao et al., 2010).

Implications and Strategies for Grotto Dust Hazards Control

The falling dust particles in the caves have threatened to the protection of murals and statues. Dust storms are the main sources for these falling dust. In the Mogao Grottoes district, dust storms are mainly caused by westerly and easterly winds (Zhang et al., 2014). In order to control dust hazards, first, the dust storm monitoring and warning system should be established to realize the early warning. A suggestion is that making full use of the resources of the local meteorological department and providing professional real-time forecast services for the dust disaster early warning system in the Mogao Grottoes. Once the dust storm comes, as the concentration of the dust in the caves reaches a certain threshold, the caves should be closed in time. According to the wind speed monitoring at the top of the Mogao Grottoes, when the wind reaches the level of moderate gale and lasts for 30 min, it can usually be identified as a dust storm process, which takes 2–20 h to complete. According to this study, the real-time PM10 concentration in front of Cave 72 reaching 6000 μg m^{-3} (mean of peak real-time dust concentrations) can be used as the threshold for dust storm warning, and the caves should be closed at this moment. Second, the falling dust in the caves was mainly composed of particles in size of 10–30 μm, accounting for 70–75% of the total falling dust, and this coarse dust particles also indicate the proximity of dust sources (**Figure 11**). To achieve the goal of minimizing the damage of falling dust to the Mogao Grottoes, improving the existing sand control system is the right thing to do. The previous wind tunnel study showed that the artificial gobi surface with 30% coverage and 30-mm-high gravels was optimal for sand drift control engineering atop the Mogao Grottoes (Zhang et al., 2014). This technique is suggested to control dust emission from gobi surrounding the Mogao Grottoes, especially for gobi in upwind of easterly winds. Besides, further building sand fences and straw checkerboards atop the Mogao Grottoes to control dust emission from mega-dunes is also recommended.

CONCLUSIONS

Continuous and synchronous observations of wind speeds and dust concentrations in the Mogao Grottoes were performed from February to October 2012, and temporal variation characteristics of dust concentrations have been analyzed. The following conclusions can be drawn:

(1) The monthly mean TSP, PM10, and PM2.5 concentrations during the monitoring period gradually decreased from February to October. The daily mean TSP, PM10, and PM2.5 concentrations in the Mogao Grottoes area are in the range of 2.36–3585.53, 1.95–3056.88, 0.69–1368.60 μg m^{-3}, respectively, and the maximum daily mean dust concentrations occur mainly on February, March, and April.
(2) PM10 is the main particle size composition of TSP in dust storms of the Mogao Grottoes. The PM10/TSP ratio ranges from 0.67 to 0.98 with a mean value of 0.82, and the PM2.5/PM10 ratio ranges from 0.31 to 0.73 with a mean value of 0.55.

(3) The average TSP, PM10, and PM2.5 concentrations in a dust storm of westerly winds are 3528.81, 2465.49, and 869.22 μg m^{-3}, respectively, with a maximum dust concentration of 21483.32 μg TSP m^{-3}, 11085.17 μg PM10 m^{-3}, and 3028.08 μg PM2.5 m^{-3}. During a dust storm of easterly winds, the average TSP, PM10, and PM2.5 concentrations are 5002.71, 3745.33, and 1297.48 μg m^{-3}, respectively, and the maximum dust concentrations are 15959.97 μg TSP m^{-3}, 11363.59 μg PM10 m^{-3}.

(4) Coincidence of the driest and windy season of spring and sufficient dust sources, such as Mingsha Mountain and the surrounding sandy gobi contribute to the high dust concentrations in the Mogao Grottoes.

(5) A dust storm monitoring and warning system in the Mogao Grottoes should be established to realize the early warning. As the PM10 concentration in front of Cave 72 during dust storms reaches the threshold of 6000 μg m^{-3}, the caves should be closed to prevent dust hazards. Improving the existing sand control system to control dust emission from mega-dunes and sandy gobi is also recommended.

DATA AVAILABILITY STATEMENT

The original contributions presented in the study are included in the article/Supplementary Material, further inquiries can be directed to the corresponding author.

AUTHOR CONTRIBUTIONS

GZ and LT designed the experiment and wrote the manuscript. WZ, HZ, and FQ conducted statistical analysis. All authors contributed to the writing-reviewing and editing.

FUNDING

This work was founded by the National Natural Science Foundation of China (41871018), Key Research and Development Program of Gansu Province (20YF8WF016), and Scientific Research Project of Dunhuang Research Academy (2020-KJ-YB-12).

REFERENCES

Ba, J., and Wang, X. (2010). Analysis of Climate Character in Dunhuang in Recent 56 Years. *J. Arid Meteorology* 28, 304–308. (in Chinese).

Baddock, M. C., Strong, C. L., Leys, J. F., Heidenreich, S. K., Tews, E. K., and McTainsh, G. H. (2014). A Visibility and Total Suspended Dust Relationship. *Atmos. Environ.* 89, 329–336. doi:10.1016/j.atmosenv.2014.02.038

Cao, L., Cao, H., Yu, H., Yang, Q., Wang, K., and Wang, X. (2013). Concentration Distribution Characteristics of PM10 and the Relation with Meteorological Element in Extreme Arid Areas of the West Part in Hexi Corridor. *Ecol. Environ. Sci.* 22 (11), 1807–1813. (in Chinese).

Charron, A., Harrison, R. M., Moorcroft, S., and Booker, J. J. A. E. (2004). Quantitative Interpretation of Divergence between PM10 and PM2.5 Mass Measurement by TEOM and Gravimetric (Partisol) Instruments. *Atmos. Environ.* 38 (3), 415–423. doi:10.1016/j.atmosenv.2003.09.072

Choobari, O. A., Zawar-Reza, P., and Sturman, A. (2014). The Global Distribution of Mineral Dust and Its Impacts on the Climate System: A Review. *Atmos. Res.* 138, 152–165. doi:10.1016/j.atmosres.2013.11.007

Dahmardeh Behrooz, R., Esmaili-Sari, A., Bahramifar, N., and Kaskaoutis, D. G. (2017). Analysis of the TSP, PM10 Concentrations and Water-Soluble Ionic Species in Airborne Samples over Sistan, Iran during the Summer Dusty Period. *Atmos. Pollut. Res.* 8 (3), 403–417. doi:10.1016/j.apr.2016.11.001

Filonchyk, M., Yan, H., Shareef, T. M. E., Yang, S. J. T., and Climatology, A. (2019). Aerosol Contamination Survey during Dust Storm Process in Northwestern China Using Ground, Satellite Observations and Atmospheric Modeling Data. *Theor. Appl. Climatology* 135 (1), 119–133. doi:10.1007/s00704-017-2362-8

Fryberger, S. G., and Dean, G. (1979). "Dune Forms and Wind Regime," in *A Study of Global Sand Seas*. Editor E. D. McKee, 1052, 137–169. USGS Professional Paper.

Ganor, E., and Foner, H. A. (2001). Mineral Dust Concentrations, Deposition Fluxes and Deposition Velocities in Dust Episodes over Israel. *J. Geophys. Res.* 106 (D16), 18431–18437. doi:10.1029/2000JD900535

Gao, Z., Shao, L., and Li, G. (2010). Characteristics Analysis of the Sand-Dust Weather in Dunhuang Area. *J. Arid Meteroology* 28 (1), 59–64. (in Chinese).

Gholampour, A., Nabizadeh, R., Hassanvand, M. S., Taghipour, H., Rafee, M., Alizadeh, Z., et al. (2016). Characterization and Source Identification of Trace Elements in Airborne Particulates at Urban and Suburban Atmospheres of Tabriz, Iran. *Environ. Sci. Pollut. Res.* 23 (2), 1703–1713. doi:10.1007/s11356-015-5413-7

Gillies, J. A., Nickling, W. G., and McTainsh, G. H. (1996). Dust Concentrations and Particle-Size Characteristics of an Intense Dust Haze Event: Inland delta Region, Mali, West Africa. *Atmos. Environ.* 30 (7), 1081–1090. doi:10.1016/1352-2310(95)00432-7

Goudie, A. S., and Middleton, N. J. (2006). *Desert Dust in the Global System*. Springer Science & Business Media.

Goudie, A. S. (2009). Dust Storms: Recent Developments. *J. Environ. Manage.* 90 (1), 89–94. doi:10.1016/j.jenvman.2008.07.007

Kok, J. F., Parteli, E. J. R., Michaels, T. I., and Karam, D. B. (2012). The Physics of Wind-Blown Sand and Dust. *Rep. Prog. Phys.* 75 (10), 106901. doi:10.1088/0034-4885/75/10/106901

Liu, B., Peng, W., Liu, S., and Yang, T. (2022). Estimation on the Dust Lift Amount and Source Contribution of the Heavy Dust Weather in Mid-march 2021 over Central East Asia. *J. Desert Res.* 42 (13), 79–86. (in Chinese).

Liu, B., Qu, J., Zhang, W., and Qian, G. (2011a). Numerical Simulation of Wind Flow over Transverse and Pyramid Dunes. *J. Wind Eng. Ind. Aerodynamics* 99 (8), 879–888. doi:10.1016/j.jweia.2011.06.007

Liu, B., Zhang, W., Qu, J., Zhang, K., and Han, Q. (2011b). Controlling Windblown Sand Problems by an Artificial Gravel Surface: A Case Study over the Gobi Surface of the Mogao Grottoes. *Geomorphology* 134 (3), 461–469. doi:10.1016/j.geomorph.2011.07.028

Luo, X., Li, Y., Yan, Z., Yang, M., and Nie, X. (2021). Evolution Characteristics of Sandstorm and Meteorological Influence Factors in Hexi Corridor in Recent 60 Years. *Reserch of Soil and Water Conversation* 28 (5), 254–267. (in Chinese).

Qu, J., Ling, Y., Zhang, W., and Wang, X. (1992). Preliminary Studies of Atmopheric Dustfall in Mogao Cave, Duhuang. *Sci. Conversation Archeoglogy* 4 (2), 19–24. (in Chinese).

Rashki, A., Kaskaoutis, D. G., Rautenbach, C. J. d., Eriksson, P. G., Qiang, M., and Gupta, P. (2012). Dust Storms and Their Horizontal Dust Loading in the Sistan Region, Iran. *Aeolian Res.* 5, 51–62. doi:10.1016/j.aeolia.2011.12.001

Shahsavani, A., Naddafi, K., Jaafarzadeh Haghighifard, N., Mesdaghinia, A., Yunesian, M., Nabizadeh, R., et al. (2012). Characterization of Ionic Composition of TSP and PM10 during the Middle Eastern Dust (MED) Storms in Ahvaz, Iran. *Environ. Monit. Assess.* 184 (11), 6683–6692. doi:10.1007/s10661-011-2451-6

Shen, Y. B., Shen, Z. B., Du, M. Y., and Wang, W. F. (2004). Studies on Dust Emission in Gobi and Oasis of Northwest China. *China Environ. Sci.* 24 (4), 390–394.

Stone, R. (2008). Shielding a Buddhist Shrine from the Howling Desert Sands. *Science* 321 (5892), 1035. doi:10.1126/science.321.5892.1035

Ta, W., Xiao, Z., Qu, J., Yang, G., and Wang, T. (2003). Characteristics of Dust Particles from the desert/Gobi Area of Northwestern China during Dust-Storm Periods. *Env Geol.* 43 (6), 667–679. doi:10.1007/s00254-002-0673-1

Tan, L. (2015). *Aeolian Sand/dust Flux over Near-Surface Gobi: A Case Study Atop the Mogao Grottoes*. Beijing: Doctoral thesis, University of Chinese Academy of Sciences. (in Chinese).

Tan, L., Zhang, W., Qu, J., Wang, J., An, Z., and Li, F. (2016). Aeolian Sediment Transport over Gobi: Field Studies Atop the Mogao Grottoes, China. *Aeolian Res.* 21, 53–60. doi:10.1016/j.aeolia.2016.03.002

Tan, L., Zhang, W., Qu, J., Zhang, K., An, Z., and Wang, X. (2013). Aeolian Sand Transport over Gobi with Different Gravel Coverages under Limited Sand Supply: A mobile Wind Tunnel Investigation. *Aeolian Res.* 11, 67–74. doi:10.1016/j.aeolia.2013.10.003

Wang, W., Wang, T., Shen, Z., Xie, J., and Xing, J. (2006). Pollution Status of Harmful Components to Frescos in Dunhuang Mogao Grottoes. *Plateau Meteroology* 25 (1), 164–168. (in Chinese).

Wang, X., Xia, D., Wang, T., Xue, X., and Li, J. (2008). Dust Sources in Arid and Semiarid China and Southern Mongolia: Impacts of Geomorphological Setting and Surface Materials. *Geomorphology* 97 (3–4), 583–600. doi:10.1016/j.geomorph.2007.09.006

Wang, X., and Zhang, C. (2021). Field Observations of Sand Flux and Dust Emission above a Gobi Desert Surface. *J. Soils Sediments* 21 (4), 1815–1825. doi:10.1007/s11368-021-02883-5

Wang, Y. Q., Zhang, X. Y., Gong, S. L., Zhou, C. H., Hu, X. Q., Liu, H. L., et al. (2008). Surface Observation of Sand and Dust Storm in East Asia and its Application in CUACE/Dust. *Atmos. Chem. Phys.* 8, 545–553. doi:10.5194/acp-8-545-2008

Yang, X., Zhang, Q., Ye, P., Qin, H., Xu, L., Ma, L., et al. (2021). Characteristics and Causes of Persistent Sand-Dust Weather in Mid-march 2021 over Northern China. *J. Desert Res.* 41 (3), 245–255. (in Chinese).

Zhang, E., Cao, J., Wang, X., Zhang, G., Zhang, Z., Du, N., et al. (2007). Apreliminary Study of Characterizationof Indoor and Outdoor Airquality inDunhuang Mogao Grottoes. *J. Graduate Sch. Chin. Acad. Sci.* 24 (5), 612–618. (in Chinese).

Zhang, W., Tan, L., Zhang, G., Qiu, F., and Zhan, H. (2014). Aeolian Processes over Gravel Beds: Field Wind Tunnel Simulation and its Application Atop the Mogao Grottoes, China. *Aeolian Res.* 15, 335–344. doi:10.1016/j.aeolia.2014.07.001

Zhang, X. Y., Arimoto, R., and An, Z. S. (1997). Dust Emission from Chinese Desert Sources Linked to Variations in Atmospheric Circulation. *J. Geophys. Res.* 102 (D23), 28041–28047. doi:10.1029/97jd02300

Zhang, X., Zhao, S., Mei, H., Zou, Y., Zhou, Z., Zhang, X., et al. (2022). Analysis of Airport Risk Propagation in Chinese Air Transport Network. *J. Adv. Transportation* 2022 (5), 1–13. (in Chinese). doi:10.1155/2022/9958810

Zhou, Z., and Wang, X. (2002). Analysis of the Severe Group Dust Storms in Eastern Part of Northwest China. *J. Geographical Sci.* 12, 357–362. (in Chinese).

Conflict of Interest: The authors declare that the research was conducted in the absence of any commercial or financial relationships that could be construed as a potential conflict of interest.

Publisher's Note: All claims expressed in this article are solely those of the authors and do not necessarily represent those of their affiliated organizations, or those of the publisher, the editors and the reviewers. Any product that may be evaluated in this article, or claim that may be made by its manufacturer, is not guaranteed or endorsed by the publisher.

frontiers | Frontiers in Environmental Science

ORIGINAL RESEARCH
published: 25 April 2022
doi: 10.3389/fenvs.2022.859631

Vertical Sand Flux Density and Grain-Size Distributions for Wind-Blown Sand Over a Gobi Surface in Milan, Southern Xinjiang, China

Lihai Tan[1,2]*, *Kai Zhang*[1,2,3], *Hongtao Wang*[1,2], *Zhishan An*[1,2] and *Tao Wang*[1,2]

[1]Key Laboratory of Desert and Desertification, Northwest Institute of Eco-Environment and Resources, Chinese Academy of Sciences, Lanzhou, China, [2]Dunhuang Gobi Desert Research Station, Northwest Institute of Eco-Environment and Resources, CAS, Lanzhou, China, [3]School of Civil Engineering, Lanzhou Jiaotong University, Lanzhou, China

Vertical sand flux density and grain-size distributions of wind-blown sand over gobi are an essential way for examining the complex grain-bed collisions over gobi surfaces and then understanding aeolian saltation dynamics. However, compared with sand surfaces, relatively few studies have reported regarding how sand flux density and grain size vary with elevation for wind-blown sand over gobi, especially in a field scale. Here, vertical sand flux density and grain-size distributions for wind-blown sand over a typical gobi surface during three transport events were revealed. The results show that the sand flux density exponentially decreased with elevation, which is different from the previous wind tunnel studies, and 99% of the sand transport amount was concentrated in the near-surface layer of 0.6 m. The mean grain size (D_m) first increased with elevation until an inflection in grain-size trends occurred at 0.175 m or 0.285 m above the ground, and then D_m decreased with height, which is significantly different from the vertical grain-size profile patterns of sand surfaces. The grain-bed collision process of medium sand over the gobi surface caused the increase of the mean grain size with height. Sorting was dominated by moderately sorted, skewness by symmetrical or fine skewed, and kurtosis by mesokurtic. The results of this study are significant for future numerical modeling studies of aeolian saltation over rough surfaces on Earth and even on Mars.

Keywords: gobi, wind-blown sand, sand flux density, grain-size distribuition, saltation

OPEN ACCESS

Edited by:
Brandon L. Edwards,
New Mexico State University,
United States

Reviewed by:
Liang Zhou,
Jiangsu Normal University, China
Helena Granja,
University of Minho, Portugal

***Correspondence:**
Lihai Tan
tanlihai09@lzb.ac.cn

Specialty section:
This article was submitted to Drylands, a section of the journal Frontiers in Environmental Science

Received: *21 January 2022*
Accepted: *07 April 2022*
Published: *25 April 2022*

Citation:
Tan L, Zhang K, Wang H, An Z and Wang T (2022) Vertical Sand Flux Density and Grain-Size Distributions for Wind-Blown Sand Over a Gobi Surface in Milan, Southern Xinjiang, China. Front. Environ. Sci. 10:859631. doi: 10.3389/fenvs.2022.859631

1 INTRODUCTION

The vertical distribution of sand flux density and grain-size for wind-blown sand has always been a hot spot in aeolian research, because it is essential for modeling aeolian saltation, especially for grain trajectory calculations (Sherman and Ellis, 2021). Over the past 80 years, many studies on the vertical distribution of sand flux density and grain-size for wind-blown sand, especially for sand surfaces, have been performed not only by field observations (e.g., Greeley et al., 1996; Arens et al., 2002; Farrell et al., 2012; Rotnicka, 2013; Swann et al., 2021), but by wind tunnel experiments (e.g., Dong et al., 2006; Xing, 2007; Li et al., 2008; Tan et al., 2014; Yang et al., 2019). Generally, the sand flux density decreases exponentially with height (e.g., Greeley et al., 1996; Dong et al., 2002; Namikas, 2003; Farrell et al., 2012; Rotnicka, 2013). The main grain-size profile patterns for wind-blown sand over sand surfaces can be summarized as the following three types. The first one is that grain size

decreases with increasing elevation (e.g., Chen et al., 1995; Arens et al., 2002; Li et al., 2008). The second is that the particle size increases with increasing height (e.g., Bagnold, 1941; Greeley et al., 1996; Van der Wal, 2000). The third is that the mean grain-size first decreases with increasing height, and then increases, with a maximum occurring at a finite height, approximately several or dozens of centimeters above the ground (e.g., Farrell et al., 2012; Tan et al., 2014; Zhang et al., 2017; Yang et al., 2019), which is a dominant vertical profile pattern of grain-size distribution in recent studies. However, compared with sand surfaces, fewer studies have reported the vertical grain-size profiles of wind-blown sand over gobi.

Gobi is a regional name of stone pavements in central Asia (Livingstone and Warren, 1996), and the stone pavements are defined by Cooke and Warren (1973) as "armored" surfaces, and usually comprise gravels or boulders in the thickness of only one or two stones, underlain by deposits of sand, silt, or clay. Gobi is widely distributed in northwest China. It covers an area of approximately 661,000 km^2, and accounts for 6.9% of the total land area, which is roughly equal with the area of sand surfaces in China (Zhang et al., 2014). This kind of surfaces are common on Earth and even ubiquitous on Mars (Lancaster et al., 2010). Aeolian saltation processes over gobi surfaces, however, are more complex than those of sand surfaces (e.g., Zhang et al., 2014; Tan et al., 2020). The presence of nonerodible gravels creates a nearly elastic collision between them and sand grains (Qu et al., 2005), and the sand flux profiles show a nonmonotonic curve pattern, with a maximum flux density occurring a specific height above the ground (e.g., Dong et al., 2004; Qu et al., 2005; Tan et al., 2013; Zhang et al., 2014). However, these results have usually been investigated by wind tunnel experiments. Due to the harsh natural conditions in gobi areas, field studies on the vertical distribution of the sand flux density and grain size for wind-blown sand over gobi are still limited. Sharp (1964) conducted field observations on characteristics of wind-blown sand over a bouldery alluvial plain in Coachella Valley, California, United States, and it revealed that the mean grain size achieved a maximum at heights of 0.25–1 m above the ground; however, it was the cumulative results of several events of aeolian transport. Zhang and Dong (2014) showed that the grain-size distribution of aeolian transport over an artificial gravel bed presented a monotonically deceasing pattern, while they used only four traps at a height range of 0.25–2 m. In contrast, field observation results of aeolian transport over gobi atop the Mogao Grottoes revealed that grain size first increased from the surface and then decreased after the occurrence of a maximum at heights of 0.22–0.24 m above the ground (Tan et al., 2016), while the saltation trap could only examine the grain size distribution of 0.5 m above the gobi surface. Thus, there is still no consensus regarding what the vertical distribution pattern of the grain size of wind-blown sand over gobi should be. Revealing the vertical profiles of sand flux density and grain size is an effective way to understand the collision process between saltating sand grains and the gobi bed, which is helpful to further reveal the dynamic mechanism for aeolian saltation over gobi or similar rough surfaces.

In this work, based on arrays of Big Spring Number Eight (BSNE) traps, vertical distributions of sand flux density and grain-size for wind-blown sand over a typical gobi surface in southern Xinjiang, China under three transport events were examined. The main purpose of this paper was to examine the vertical structures of the sand flux density and grain size for wind-blown sand over gobi, and then to shed light on the processes of aeolian saltation of mix-sized grains. The results of this study can also provide insights into the dynamics of aeolian saltation over gobi or similar rough surfaces.

2 MATERIALS AND METHODS

2.1 Study Area

Field measurements were performed in the gobi region of Milan, Southern Xinjiang, China (39°8.062′N, 88°59.967′E) (**Figures 1A, B**). The gobi surface was located on a plain of alluvial-proluvial gobi in northern front of the Altun Mountains. The gobi surface has a gravel coverage rate ranging from 40 to 50%, and is composed mainly of fine gravels (<6 cm), underlain mainly by fine sand (median grain size d_{50} 202 μm) (**Figure 1C**). The main sand-driving wind directions in the study area were ENE and E, and the annual sand drift potential (DP) in 2018 reached 1,160 vector units, indicating a high wind-energy environment. Detailed information on the aeolian environment has been described in Tan et al. (2020).

2.2 Instrumentation

Sand particles in wind-blown sand over gobi during the three transport events were collected by a vertical array of Big Spring Number Eight (BSNE) traps (Fryrear, 1986), including seven traps at different heights (**Figure 1D**). The seven BSNE sand traps were placed at mid-inlet heights of 0.025, 0.175, 0.285, 0.585, 1.16, 1.79, and 3 m, and the direction of the spanwise layout was NW-SE, which was almost orthogonal to the main sand-driving wind direction (ENE) in the study area (Tan et al., 2020). Wind data used in this study were obtained from a meteorological observation tower with three 2D ultrasonic anemometers at heights of 2, 6, and 10 m, and recorded as 1 min averages, located approximately 150 m west of the saltation observation site.

2.3 Methods

All grain-size data of wind-blown sand samples in this study were measured by a Malvern Mastersizer-2000 grain-size analyzer. Grain-size statistics of mean, sorting, skewness, and kurtosis were calculated using the method of Folk and Ward (1957). Friction velocity u_* was computed from the logarithmic slope between the two instruments at the heights of 2 and 10 m using the following equation (Martin et al., 2013).

$$u_* = \frac{k(u_2 - u_1)}{\ln(z_2/z_1)} \quad (1)$$

where u_1 and u_2 were the wind velocities at the heights of 2 m (z_1) and 10 m (z_2).

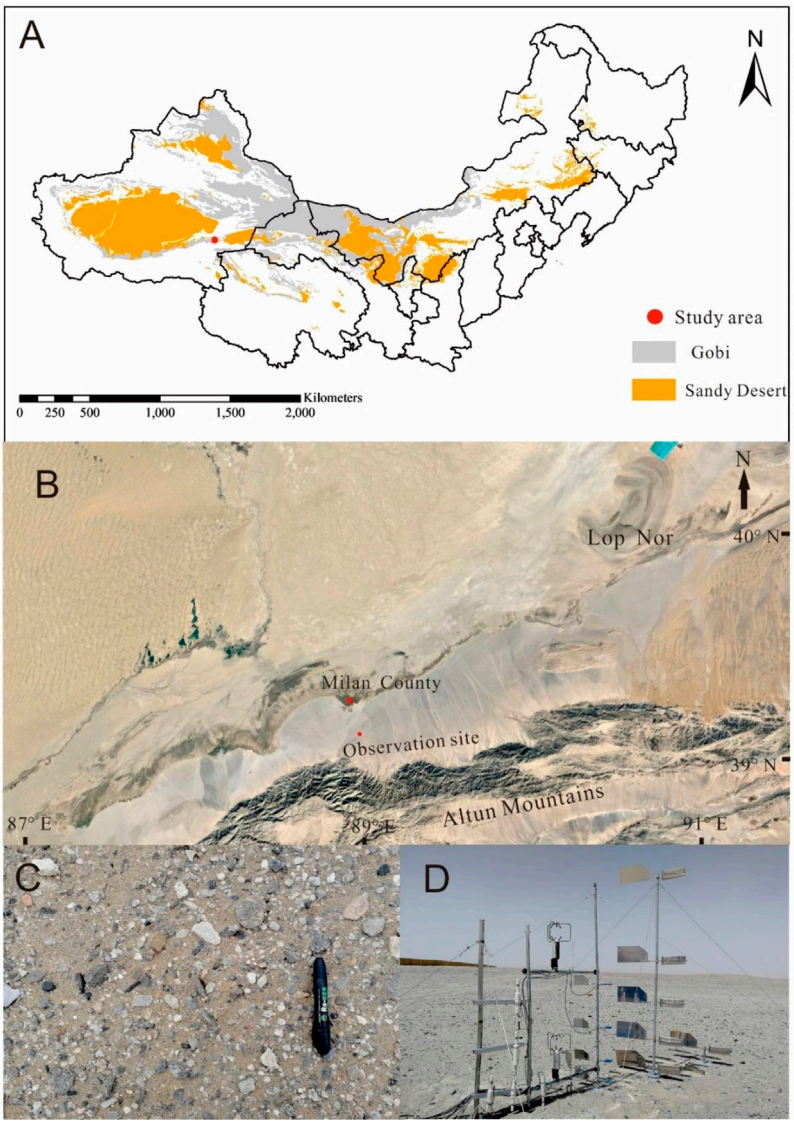

FIGURE 1 | (A) The gobi distribution map of Northwest China [this figure is revised from Zhang et al. (2019)]. **(B)** Location map for the study site (the regional map is from Google Earth). **(C)** Typical gobi surface in the study site. **(D)** *In-situ* field layout of instrument.

3 RESULTS

3.1 Sand Transport Events

Three sand transport events (20180502, 20180504, and 20180507, all the following descriptions regarding the three transport events are in this order) were observed during the fieldwork from 1 May 2018 to 8 May 2018. The variation of wind speed and direction at 10 m above the ground with time is shown in **Figure 2**. The measurement duration fell in between 110 and 420 min. The values of wind speed at a height of 10 m for the three transport events ranged from 8.35 to 19.27 m s^{-1}, 8.28–19.82 m s^{-1}, and 11.90–23.55 m s^{-1}, respectively, and the corresponding average wind speeds were 13.92, 13.70, and 18.78 m s^{-1}. At the same time, the values of wind direction at a height of 10 m for the three transport events ranged from 54.2° to 91.2°, 40.5° to 97.0°, and 19.5° to 75.3°;, respectively. The corresponding average wind directions were 80.6°, 69.7°, and 54.9°, which belonged to E, ENE, and NE winds, respectively. During the three transport events, the values of friction velocity u_* ranged from 0.11 to 0.79 m s^{-1}, 0.01–0.72 m s^{-1}, and 0.10–1.28 m s^{-1}, respectively, and the corresponding average values of u_* were 0.40, 0.28, and 0.66 m s^{-1} (**Figure 2**). The measured threshold friction velocity for sand entrainment u_{*t} was 0.30 m s^{-1} in the study area. During the transport event 20180504, the average u_* was smaller than u_{*t}, and intermittent aeolian sand transport occurred, especially in the period of 13:00–16:59 (Tan et al., 2020). In contrast, during the transport event 20180507, almost all the values of u_* were over u_{*t} in the whole measurement period,

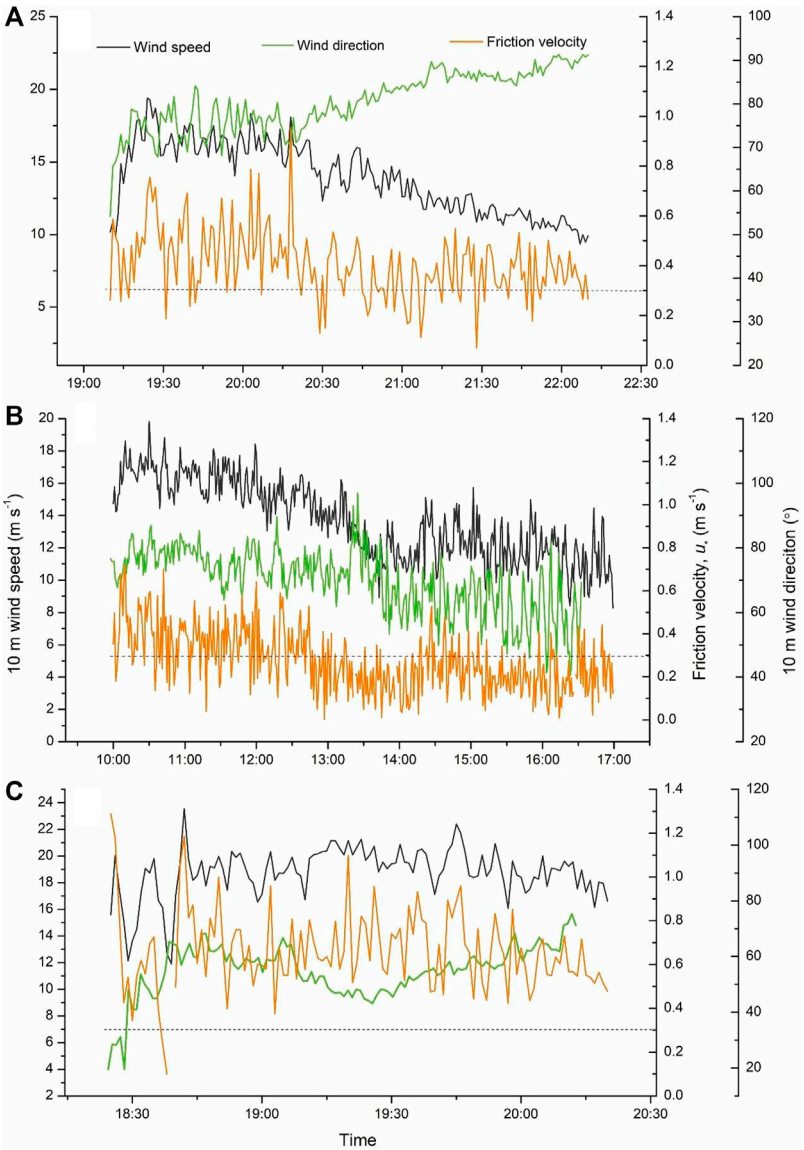

FIGURE 2 | Variation of wind speed and direction at a height of 10 m and friction velocity with time during the three transport events. **(A)** 20180502 event, **(B)** 20180504 event, and **(C)** 20180507 event. The dash line refers to the threshold friction velocity u*t (0.30 m s^{-1}).

and strong aeolian sand transport occurred (see **Figure 3A** in the next part).

3.2 Sand Flux Profiles of Wind-Blown Sand Over Gobi

Vertical sand flux profiles show that the sand flux density decreased exponentially with increasing height during the three transport events (**Figure 3A**). The proportions of the transported sand particles caught at the lowest trap (with a mid-inlet height of 0.025 m) were 40.04, 36.14, and 34.39% for the three transport events, respectively. 90% of the total sand flux for the three transport events was concentrated within layers of 0.20, 0.23, and 0.25 m above the ground, respectively. The sand particles caught within a height of 0.585 m above the surface accounted for less than 1% of the total, and thus, 99% of the sand particles in wind-blown sand over gobi were transported in the layer of 0–0.585 m (**Figure 3B**).

3.3 Vertical Grain Size Distribution of Wind-Blown Sand Over Gobi

3.3.1 Vertical Grain-Size Frequency Distribution

To ensure the accuracy of data, we excluded samples with altitudes higher than 0.585 m in the analysis of grain-size distribution. The variation of the grain-size frequency of blown sand samples with height is shown in **Figure 4**. The results show that the variation trend of the mode grain size

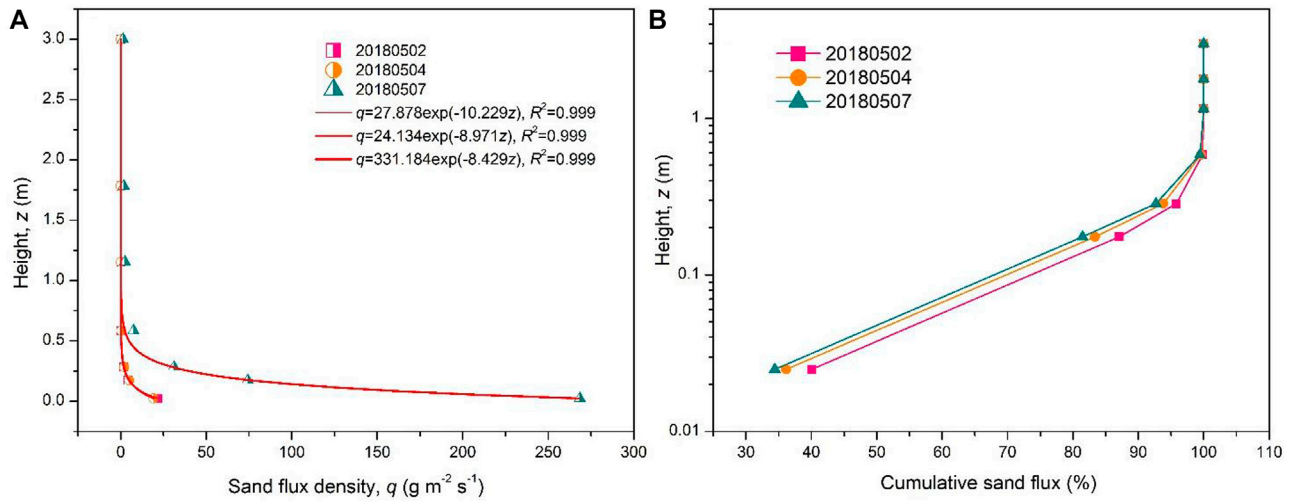

FIGURE 3 | Variation of the sand flux density **(A)** and cumulative sand flux **(B)** with height above the ground during the three transport events.

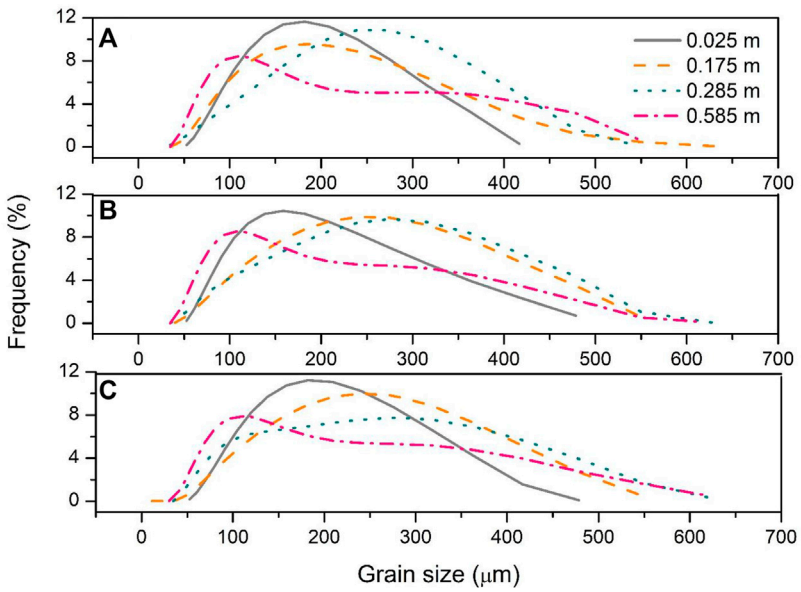

FIGURE 4 | The grain-size frequency of wind-blown sand samples changing with height in the three transport events. **(A)** 20180502 event, **(B)** 20180504 event, and **(C)** 20180507 event.

(the grain size which corresponded to the maximum grain-size frequency) as a function of height was consistent among the three transport events, that is, the mode grain size first increased with height then decreased. At 0.025 m, the values of the mode grain size in the three transport events were 182, 158, and 182 μm, respectively, and the corresponding frequencies were 11.65, 10.44, and 11.23%, respectively. At 0.175 m, the values of the mode grain size in the three transport events were 182, 240, and 240 μm, respectively, and the corresponding frequencies were 9.58, 9.89, and 10.02%, respectively. At 0.285 m, all mode grain size increased to 275 μm, and the corresponding frequencies were 10.84, 9.69, and 7.74%, respectively. However, as the height increased to 0.585 m, all mode grain size decreased to 105 μm, and the corresponding frequencies changed to 8.46, 8.57, and 7.91%, respectively.

3.3.2 Grain-Size Statistics

3.3.2.1 Mean Grain Size

The vertical profile patterns of the mean grain size of wind-blown sand over gobi were consistent among the three measured transport events, that is, D_m first increased almost linearly with elevation until a reversal in grain-size trends occurred,

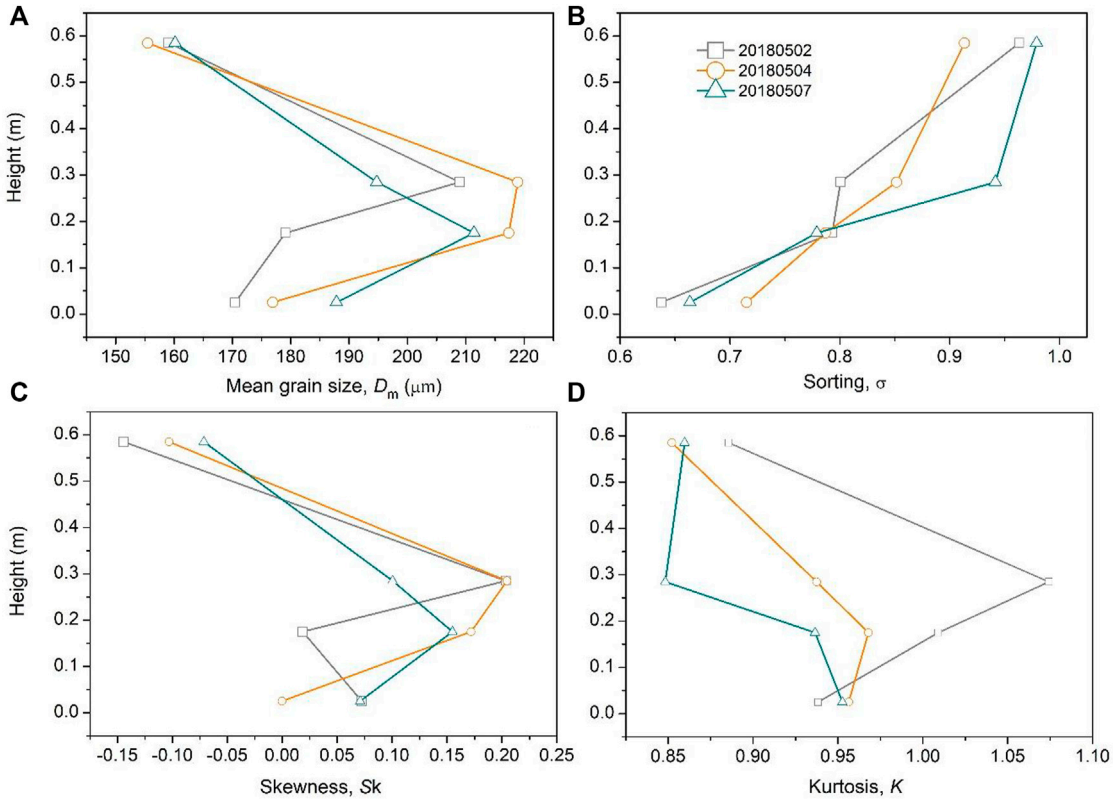

FIGURE 5 | Variation of the grain-size statistics with height during the three transport events. **(A)** Mean grain size, **(B)** Sorting, **(C)** Skewness, **(D)** Kurtosis.

and then D_m decreased, with a maximum occurring at a finite height above the ground (**Figure 5A**). Specifically, the inflection points in the vertical mean grain size profile occurred at a height of 0.175 m or 0.285 m above the ground during the three transport events, with D_m values ranging from 200 to 221 μm.

3.3.2.2 Sorting

For the three transport events, sorting values increased with increasing height within the layer of 0–0.585 m, which ranged from 0.64 to 0.98 (**Figure 5B**), and they changed from moderately well sorted to moderately sorted with increasing height according to the categorization of Folk and Ward (1957).

3.3.2.3 Skewness

The pattern of skewness changing as a function of height was similar to that of the mean grain size. *Sk* first increased with elevation until a reversal in grain-size trends occurred, and then *Sk* decreased, with a maximum occurring at a finite height above the ground (**Figure 5C**). According to the categorization of Folk and Ward (1957), the skewness changed from symmetrical on the surface to fine skewed with increasing height to 0.285 m, and then changed back to symmetrical or coarse skewed at the height of 0.585 m.

3.3.2.4 Kurtosis

The kurtosis increased with the increase of height above the ground, with values ranging from 0.85 to 1.07 (**Figure 5D**), and they belonged to the category of mesokurtic according to Folk and Ward (1957) at the lower three traps, while it changed to platykurtic for the sand trap at the height of 0.585 m.

4 DISCUSSION

4.1 The Saltation Flux Profile Pattern for the Gobi Surface

Many previous studies, mostly through wind tunnel tests, show that the sand flux density varies with height in a non-monotonic curve, with a maximum occurring at a certain height above the ground (e.g., Dong et al., 2004; Qu et al., 2005; Tan et al., 2013; Zhang et al., 2014). In contrast, this study shows that sand flux density decreases exponentially with increasing height among all the three measured transport events. Furthermore, the field study of Tan et al. (2016) also reveals that the sand flux density decreases exponentially with increasing height, which is different from the results of previous wind tunnel studies. Meanwhile, the recent field study of Tan et al. (2021) shows that the particle flux density of wind-blown sand over gobi decreases exponentially with height, which is consistent with the exponential decay model of the sand flux density against height determined using BSNE traps. The difference in results of wind tunnel tests and field observation can be attributed to the fact that the blocking effect of gravels on sand transport near the gobi surface is not as pronounced in the field as that in the wind tunnel. The scale of

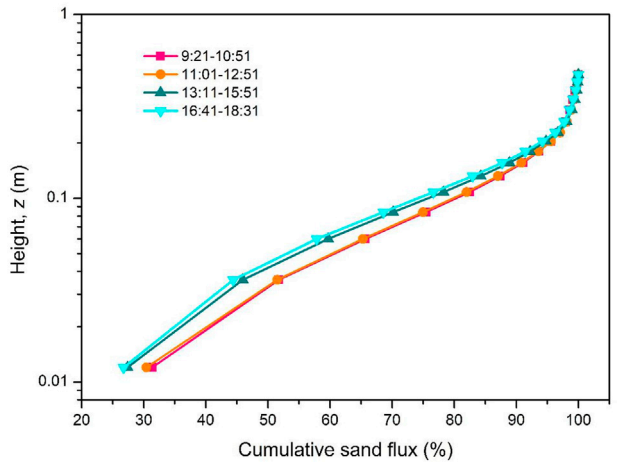

FIGURE 6 | Variation of the cumulative sand flux with height above the gobi surface atop the Mogao Grottoes during the transport event 20130417 (Tan et al., 2016).

gravels cannot be reduced in wind tunnel tests, which, in turn, increases their blocking effect, while in the field, the relief of the terrain makes the function of gravels in inhibiting near-surface wind-blown sand less obvious than that in the wind tunnel.

This study shows that 99% of the sand transport amount over gobi is concentrated in the near-surface layer of 0.6 m. Comparatively, it shows that 99% of the sand transport amount over gobi atop the Mogao Grottoes is concentrated in the near-surface layer of 0.3 m (**Figure 6**), and thus the height of the saltation layer in this study is nearly two times of that atop the Mogao Grottoes. However, in the Hundred Miles windy area along the Lanzhou-Xinjiang High-Speed Railway, 99% of sand particles are transported in the layer of 3 m above the gobi surface (Wang et al., 2022). This can be attributed to the difference in the wind speed and grain size, and Zhang et al. (2017) revealed that the cumulative sand flux is controlled more by the mean grain size of sand surfaces than wind speed. For example, the maximum mean grain size of wind-blown atop the Mogao Grottoes is 150 μm, while that of in this study is 220 μm, and larger saltating particles can reach higher in the process of aeolian saltation over gobi. In contrast, sand transport on sand surfaces is mainly concentrated in a height range of 0–0.2 m. This indicates that the grain-bed collision over gobi facilitates aeolian saltation by increasing saltation heights, in which sand particles can retain a higher proportion of their impact energy. In addition, Nield and Wiggs (2011) revealed that compared with dry, rippled sand surfaces, the saltation cloud height increased over slightly damper and harder sand surfaces.

4.2 Vertical Distributions of Grain-Size Statistics for Wind-Blown Sand Over Gobi

Vertical mean grain-size profiles of gobi wind-blown sand show that the mean grain size increases with height above the ground until a reversal occurs, and then the mean grain size decreases with height. It indicates that the coarsest grains are found at a finite height above the ground rather than on the surface. The field work atop the Mogao Grottoes also revealed a reversal in the variation of grain size with height, with an inflection occurring at 0.22 and 0.24 m for the two transport events of 20130415 and 20130417, respectively (Tan et al., 2016). Below the inflection, the mean grain size also increased with height; however, above the inflection, it showed a linear decrease in mean grain size with height, in which only 0.3 m above the inflection had been measured, while in this study an approximate 0.6 m transport layer had been considered (**Figure 5A**). The reason is that the study area of Mogao Grottoes belongs to a low wind-energy environment (Zhang et al., 2014), while the study areas in this study indicates a high wind-energy environment (Tan et al., 2020), resulting in a relatively thicker saltation layer in this study. Zhang and Dong (2014) also used BSNE traps to examine characteristics of grain-size distribution for an artificial gobi bed; however, only four traps at 0.25, 0.5, 1, and 2 m above the ground had been used. As a result, they showed that the mean grain size decreased monotonically with height, yet the change in mean grain size with height could not be examined below 0.25 m. The field study of Sharp (1964) revealed that the mean grain size for wind-blown sand over a bouldery alluvial plain in Coachella Valley, California, United States, achieved a maximum at heights ranging from 0.25 to 1 m above the ground. Wang et al. (2022) revealed that the inflection point in the vertical median grain size profile of wind-blown sand over a gobi surface in the Hundred Miles windy area, China reached 2 m above the ground surface. The heights where the inflection occurred in these two studies were larger than those of this study. This may be caused by the difference in wind power and the grain-size composition of sand sources for wind-blown sand over the rough surface.

Apparently, the vertical mean grain-size profile over gobi is significantly different from those of sand surfaces, in which the dominant profile pattern is grain size first decreases till to an inflection and then increases with elevation. This can be attributed to the difference in grain-bed collisions between gobi beds and sand surfaces. The collision between saltating particles and gravels on the gobi surface is nearly elastic, and thus, saltating sand particles will rebound and maintain a higher proportion of momentum; however, those of sand surfaces will transport momentum to new particles and the momentum has been consumed mainly on bed deformation. Liu et al. (2021) reveals that for the same gobi bed and at the same experimental particle speed, the larger the sand particle size, the higher the bounce height of sand particles after colliding with gravels. This is because gravity and the drag of the wind are the main influencing factors for the trajectory of rebounding sand particles, and as grain size increases, the ratio of inertia to drag force becomes larger. As a result, larger grains can travel in higher and farther trajectories than smaller grains. **Figure 7** shows the variation of frequencies for three grain-size groups (very fine, fine, and medium sand) with height in the three transport events. The results demonstrate that below the height of the inflection point, both the frequencies of very fine and fine sand in the three transport events decreased with height (**Figures 7A, B**), while that of the medium sand increased with height (**Figure 7C**), resulting in the increase of the mean grain size with height. In contrast, above the inflection points, the frequency of very fine sand increased (**Figure 7A**), while that of the medium sand decreased (**Figure 7C**), resulting the decrease of the mean grain size with height. This indicates that larger grains like medium sand particles

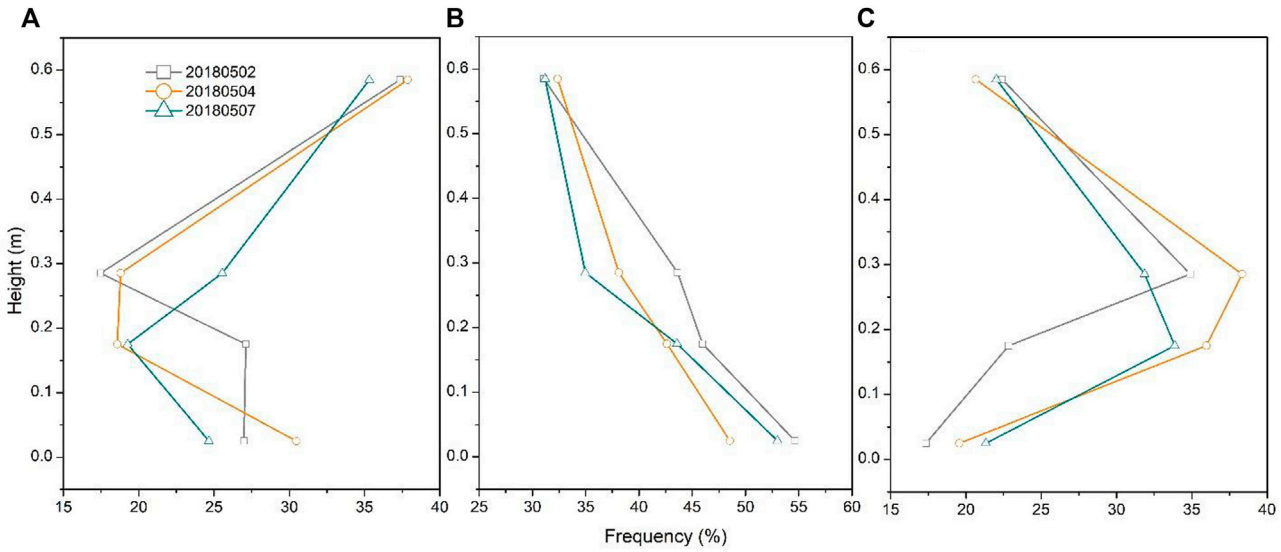

FIGURE 7 | Variation of frequencies for three grain-size groups with height in the three transport events. **(A)** very fine sands (63–125 μm), **(B)** fine sands (125–250 μm), and **(C)** medium sands (250–500 μm).

participate in the grain-bed collision process over gobi and the rebound medium sand particles can reach a higher layer. Comparatively, very fine sand is more notably affected by turbulence, and the frequency only increases in the upper saltation layer where wind momentum is less affected by saltating particles. However, in regard to sand surfaces, bed deformation consumes more energy of saltating grains, resulting in the reduction in the available energy for grain ejection. Larger grains are relatively more difficult than smaller grains to reach the same launch speed, and thus larger particles will move close to the bed in reptation rather than saltation (e.g., Rice et al., 1995; Farrell et al., 2012). Consequently, the coarse fraction of the transport sand population is distributed within near-bed elevations, while the finer fraction is at higher elevations. Thus, the mean grain size decreased with height in the saltation layer over sand surfaces.

Studies of quantifying the variation of sorting, skewness, and kurtosis with height are relatively few for sand surfaces. Williams (1964), Li et al. (2008), and Farrell et al. (2012) found that sorting improved with height. Zhang et al. (2017) revealed that sorting of sand surfaces composed of fine or medium sands improved with increasing height, while both profile patterns of sorting improving and declining with height presented for coarse sand surfaces. However, the sorting of gobi wind-blown sand in this study shows a decreasing trend with increasing height, which is consistent with the result of Tan et al. (2016).

5 CONCLUSION

Vertical flux density and grain-size profiles of wind-blown sand over a typical gobi surface during three transport events were measured using arrays of BSNE traps. The results show that in contrast with the nonmonotonic flux profiles over gobi beds measured in wind tunnel studies, the sand flux density decreased exponentially with elevation in the field. 90% of sand transport amount is concentrated in the height range of 0.22–0.27 m, while 99% of saltating sand particles are transported in the near-surface layer of 0.6 m. The mean grain size (D_m) first increased with elevation until a reversal in grain-size trends occurred, and then D_m decreased, with a maximum occurring at a finite height above the ground (0.175 or 0.285 m). In the whole saltation layer, sorting mainly belongs to moderately sorted, skewness is symmetrical or fine skewed, and kurtosis is mesokurtic.

This study provides grain-size data of wind-blown sand over gobi to the modeling community for saltating grain trajectories and also sheds light on the complex grain-bed collision on gobi surfaces, which is helpful for understanding aeolian saltation dynamics over gobi.

DATA AVAILABILITY STATEMENT

The original contributions presented in the study are included in the article/Supplementary Material, further inquiries can be directed to the corresponding author.

AUTHOR CONTRIBUTIONS

LT designed the field observation and wrote the manuscript. KZ and HW conducted statistical analysis. ZA and TW performed the observation and collected data. All authors contributed to the writing-reviewing and editing.

FUNDING

This work was founded by the Third Xingjiang Expedition and Research (2021xjkk030503), China Postdoctoral Science

Foundation (2021M703466), the Natural Science Foundation of Gansu Province, China (20JR10RA231), the Science and Technology Research and Development Program of China Railway Corporation (2017G004-E), and the Science and Technology Research Project of China Railway First Survey and Design Institute Group Co., Ltd. (2019-10).

REFERENCES

Arens, S. M., van Boxel, J. H., and Abuodha, J. O. Z. (2002). Changes in Grain Size of Sand in Transport over a Foredune. *Earth Surf. Process. Landforms* 27 (11), 1163–1175. doi:10.1002/esp.418

Bagnold, R. A. (1941). *The Physics of Wind Blown Sand and Desert Dunes*. London: Methuen.

Chen, W., Yang, Z., and Dong, Z. (1995). Vertical Distribution of Grain-Size Parameters of Drifting Particles during Sand Storms in the Taklamakan Desert, Central Asia. *Phys. Geogr.* 16 (6), 503–523.

Cooke, R. U., and Warren, A. (1973). *Geomorphology in Deserts*. London: Batsford.

Dong, Z., Liu, X., Wang, H., Zhao, A., and Wang, X. (2002). The Flux Profile of a Blowing Sand Cloud: a Wind Tunnel Investigation. *Geomorphology* 49 (s 3–4), 219–230.

Dong, Z., Qian, G., Luo, W., and Wang, H. (2006). Analysis of the Mass Flux Profiles of an Aeolian Saltating Cloud. *J. Geophys. Res. Atmospheres* 111 (D16), 1984–2012. doi:10.1029/2005jd006630

Dong, Z., Wang, H., Liu, X., and Wang, X. (2004). A Wind Tunnel Investigation of the Influences of Fetch Length on the Flux Profile of a Sand Cloud Blowing over a Gravel Surface. *Earth Surf. Process. Landforms* 29 (13), 1613–1626. doi:10.1002/esp.1116

Farrell, E. J., Sherman, D. J., Ellis, J. T., and Li, B. (2012). Vertical Distribution of Grain Size for Wind Blown Sand. *Aeolian Res.* 7, 51–61. doi:10.1016/j.aeolia.2012.03.003

Folk, R. L., and Ward, W. C. (1957). Brazos River Bar [Texas]; a Study in the Significance of Grain Size Parameters. *J. Sediment. Res.* 27 (1), 3–26. doi:10.1306/74d70646-2b21-11d7-8648000102c1865d

Fryrear, D. (1986). A Field Dust Sampler. *J. Soil Water conservation* 41 (2), 117–120.

Greeley, R., Blumberg, D. G., and Williams, S. H. (1996). Field Measurements of the Flux and Speed of Wind-Blown Sand. *Sedimentology* 43 (1), 41–52. doi:10.1111/j.1365-3091.1996.tb01458.x

Lancaster, N., Nickling, W. G., and Gillies, J. A. (2010). Sand Transport by Wind on Complex Surfaces: Field Studies in the McMurdo Dry Valleys, Antarctica. *J. Geophys. Res.* 115 (F3), F03027. doi:10.1029/2009jf001408

Li, Z., Feng, D., Wu, S., Borthwick, A., and Ni, J. (2008). Grain Size and Transport Characteristics of Non-uniform Sand in Aeolian Saltation. *Geomorphology* 100 (3), 484–493. doi:10.1016/j.geomorph.2008.01.016

Liu, B., Wang, Z., Niu, B., and Qu, J. (2021). Large Scale Sand Saltation over Hard Surface: a Controlled experiment in Still Air. *J. Arid Land* 13 (6), 599–611. doi:10.1007/s40333-021-0104-3

Livingstone, I., and Warren, A. (1996). *Aeolian Geomorphology: An Introduction*. Addison Wesley Longman Ltd.

Martin, R. L., Barchyn, T. E., Hugenholtz, C. H., and Jerolmack, D. J. (2013). Timescale Dependence of Aeolian Sand Flux Observations under Atmospheric Turbulence. *J. Geophys. Res. Atmos.* 118 (16), 9078–9092. doi:10.1002/jgrd.50687

Namikas, S. L. (2003). Field Measurement and Numerical Modelling of Aeolian Mass Flux Distributions on a sandy beach. *Sedimentology* 50 (2), 303–326. doi:10.1046/j.1365-3091.2003.00556.x

Nield, J. M., and Wiggs, G. F. S. (2011). The Application of Terrestrial Laser Scanning to Aeolian Saltation Cloud Measurement and its Response to Changing Surface Moisture. *Earth Surf. Process. Landforms* 36 (2), 273–278. doi:10.1002/esp.2102

Qu, J., Huang, N., Ta, W., Lei, J., Dong, Z., Liu, X., et al. (2005). Structural Characteristics of Gobi Sand-Drift and its Significance. *Adv. Earth Sci.* 20 (1), 19–23.

Rice, M. A., Willetts, B. B., and McEwan, I. K. (1995). An Experimental Study of Multiple Grain-Size Ejecta Produced by Collisions of Saltating Grains with a Flat Bed. *Sedimentology* 42 (4), 695–706. doi:10.1111/j.1365-3091.1995.tb00401.x

Rotnicka, J. (2013). Aeolian Vertical Mass Flux Profiles above Dry and Moist sandy beach Surfaces. *Geomorphology* 187, 27–37. doi:10.1016/j.geomorph.2012.12.032

Sharp, R. P. (1964). Wind-driven Sand in Coachella valley, California. *Geol. Soc. America Bull.* 75 (9), 785–804. doi:10.1130/0016-7606(1964)75[785:wsicvc]2.0.co;2

Sherman, D. J., and Ellis, J. T. (2021). "Sand Transport Processes☆," in *Reference Module in Earth Systems and Environmental Sciences*. Elsevier).

Swann, C., Lee, D., Trimble, S., and Key, C. (2021). Aeolian Sand Transport over a Wet, sandy beach. *Aeolian Res.* 51, 100712. doi:10.1016/j.aeolia.2021.100712

Tan, L., An, Z., Zhang, K., Qu, J., Han, Q., and Wang, J. (2020). Intermittent Aeolian Saltation over a Gobi Surface: Threshold, Saltation Layer Height, and High-Frequency Variability. *J. Geophys. Res. Earth Surf.* 125 (1), e2019JF005329. doi:10.1029/2019JF005329

Tan, L., Qu, J., Wang, T., Zhang, K., and An, Z. (2021). Field Observation Evidence for Kink Points in the Vertical Kinetic Energy Flux Profiles of Wind-Blown Sand over Gobi and its Significance. *Geophys. Res. Lett.* 48 (3), e2020GL091224. doi:10.1029/2020GL091224

Tan, L., Zhang, W., Qu, J., Du, J., Yin, D., and An, Z. (2014). Variation with Height of Aeolian Mass Flux Density and Grain Size Distribution over Natural Surface Covered with Coarse Grains: A mobile Wind Tunnel Study. *Aeolian Res.* 15, 345–352. doi:10.1016/j.aeolia.2014.06.008

Tan, L., Zhang, W., Qu, J., Wang, J., An, Z., and Li, F. (2016). Aeolian Sediment Transport over Gobi: Field Studies Atop the Mogao Grottoes, China. *Aeolian Res.* 21, 53–60. doi:10.1016/j.aeolia.2016.03.002

Tan, L., Zhang, W., Qu, J., Zhang, K., An, Z., and Wang, X. (2013). Aeolian Sand Transport over Gobi with Different Gravel Coverages under Limited Sand Supply: A mobile Wind Tunnel Investigation. *Aeolian Res.* 11, 67–74. doi:10.1016/j.aeolia.2013.10.003

Van der Wal, D. (2000). Grain-size-selective Aeolian Sand Transport on a Nourished beach. *J. Coastal Res.*, 896–908.

Wang, T., Qu, J., Tan, L., Gao, Y., Zhang, K., and Shi, B. (2022). Aeolian Sediment Transport over the Gobi with High Gravel Coverage under Extremely strong Winds in the Hundred Miles Windy Area along the Lanzhou-Xinjiang High-Speed Railway. *J. Wind Eng. Ind. Aerodynamics* 220, 104857. doi:10.1016/j.jweia.2021.104857

Williams, G. (1964). Some Aspects of the Eolian Saltation Load. *Sedimentology* 3 (4), 257–287. doi:10.1111/j.1365-3091.1964.tb00642.x

Xing, M. (2007). The Harmonious Character in Equilibrium Aeolian Transport on Mixed Sand Bed. *Geomorphology* 86 (3), 230–242. doi:10.1016/j.geomorph.2006.08.015

Yang, Y., Liu, L., Li, X., Shi, P., Zhang, G., Xiong, Y., et al. (2019). Aerodynamic Grain-Size Distribution of Blown Sand. *Sedimentology* 66 (2), 590–603. doi:10.1111/sed.12497

Zhang, K., Qu, J., Yu, Y., Han, Q., Wang, T., An, Z., et al. (2019). Progress of Research on Wind-Blown Sand Prevention and Control of Railways in China. *Adv. Earth Sci.* 34 (6), 573–583.

Zhang, W., Tan, L., Zhang, G., Qiu, F., and Zhan, H. (2014). Aeolian Processes over Gravel Beds: Field Wind Tunnel Simulation and its Application Atop the Mogao Grottoes, China. *Aeolian Res.* 15, 335–344. doi:10.1016/j.aeolia.2014.07.001

Zhang, Z., Dong, Z., and Qian, G. (2017). Field Observations of the Vertical Distribution of Sand Transport Characteristics over fine, Medium and Coarse Sand Surfaces. *Earth Surf. Process. Landforms* 42 (6), 889–902. doi:10.1002/esp.4045

Zhang, Z., and Dong, Z. (2014). The Characteristics of Aeolian Transport Particle Size Distribution over the Pebble Artificial Surfaces. *J. Desert Res.* 34 (3), 639–644.

Conflict of Interest: The authors declare that the research was conducted in the absence of any commercial or financial relationships that could be construed as a potential conflict of interest.

Publisher's Note: All claims expressed in this article are solely those of the authors and do not necessarily represent those of their affiliated organizations, or those of the publisher, the editors and the reviewers. Any product that may be evaluated in this article, or claim that may be made by its manufacturer, is not guaranteed or endorsed by the publisher.

frontiers | Frontiers in Environmental Science

ORIGINAL RESEARCH
published: 29 April 2022
doi: 10.3389/fenvs.2022.885070

Protective Efficiency of Railway Arbor-Shrub Windbreak Forest Belts in Gobi Regions: Numerical Simulation and Wind Tunnel Tests

Kai Zhang[1,2], *Jianjun Qu*[1]*, *Xingxin Zhang*[2], *Liming Zhao*[2] *and Sheng Li*[2]

[1]Key Laboratory of Desert and Desertification/Dunhuang Gobi and Desert Research Station, Northwest Institute of Eco-Environment and Resources, Chinese Academy of Sciences, Lanzhou, China, [2]College of Civil Engineering, Lanzhou Jiaotong University, Lanzhou, China

The railways in the Gobi area have serious sand hazards. To prevent these hazards and ensure operational safety, plant-based sand prevention is a fundamental measure for the prevention and control of railway wind-sand hazards. This study considers the protective windbreak forest belts along the Lan-Xin Railway, Northwest China as the study area and evaluates its protective benefits from the perspectives of windproof efficiency and sand control efficiency using numerical simulations and wind tunnel testing. Our results show that the disrupting effect of the three shelterbelt rows on the airflow was significantly enhanced, and the wind velocity profile began to change at 2H. As the airflow continued to move forward, the wind velocity profile gradually deviated from the logarithmic law, and an obvious turning point appeared at 13H behind the forest belt. Under different incoming wind velocities, the maximum wind protection efficiency of the three shelterbelt rows appeared at 5H on the leeward side. The maximum wind protection efficiencies in the numerical simulation were 95.1, 90.4, and 88.6%, respectively. The minimum value appeared at 15H on the leeward side, and the minimum wind protection efficiencies were 58.3, 53.1, and 47.1%, respectively. The maximum wind protection efficiencies in the tunnel test were 94.3, 90.1, and 86.5%, and the minimum value appeared at 15H on the leeward side. As the wind velocity increased, the efficiency of wind protection tended to decrease. The sand control efficiencies of the shelterbelt were 93.8, 91.6, and 88.1%, and as the wind velocity increased, the sand control efficiency continued to decrease. In general, the forest belt had a significant effect on reducing the sand flux density, especially below the forest belt height, which can effectively control the wind and sand disasters in some Gobi areas along the Lan-Xin Railway.

Keywords: railway, gobi, wind-blown sand, shelterbelt, protective benefit

OPEN ACCESS

Edited by:
Bailiang Li,
Xi'an Jiaotong-Liverpool University, China

Reviewed by:
Jie Zhang,
Lanzhou University, China
Yukun Liu,
University of Oxford, United Kingdom

***Correspondence:**
Jianjun Qu
qujianj@lzb.ac.cn

Specialty section:
This article was submitted to Drylands, a section of the journal Frontiers in Environmental Science

Received: *27 February 2022*
Accepted: *11 April 2022*
Published: *29 April 2022*

Citation:
Zhang K, Qu J, Zhang X, Zhao L and Li S (2022) Protective Efficiency of Railway Arbor-Shrub Windbreak Forest Belts in Gobi Regions: Numerical Simulation and Wind Tunnel Tests. Front. Environ. Sci. 10:885070. doi: 10.3389/fenvs.2022.885070

1 INTRODUCTION

Aeolian sand is a typical sand transport method in desert areas, which has a profound impact on desert topography and landform formations (Huang et al., 2020). Sand transported by wind is a process of lifting and spreading from the ground, and finally depositing back to the ground (Baniamerian and Mehdipour, 2019). Severe wind-sand hazards have brought great trouble to

the construction, development, and safe operation of railways in sandy areas (Zhang et al., 2010; Wang et al., 2018; Zhang et al., 2020). In recent decades, scholars have summarized three types of sand control measures in the engineering practice of sand prevention and control: mechanical, chemical, and plant measures. Among them, plant measures are one of the most fundamental, economical, and effective methods for controlling sand disasters.

As an important part of plant-based sand prevention measures, windbreak forest belts are widely installed on the windward side of transportation facilities, such as railways and highways. By increasing the wind-sand flow resistance, enhancing energy consumption, and promoting sand deposition, they can intercept the passing wind-sand flows. Different types of protective windbreak forest belts have different effects in sand-wind prevention. For permeable protection forest belt, multiple "ventilation holes" are formed inside the forest belt, which make it easy for quicksand to penetrate the protection forest belt and cause sand damage. For tight protection forest belt, the quicksand is blocked as far as possible at the edge of the protection forest belt and cannot penetrate it, which is effective in preventing sandstorms. Field observations (Tuzet and Wilson, 2007; Amichev et al., 2015; Li et al., 2016), theoretical analyses (Takahashi et al., 1998; Ucar and Hall, 2001) and wind tunnel tests (Schwartz et al., 1995; Judd et al., 1996; Lee et al., 2002) have always been effective means to evaluate the benefits of the wind and sand resistance of forest belts. With recent advances in computer technology, numerical simulations have become widely used in the field of fluid dynamics owing to their high efficiency, accuracy, and convenience. For example, based on numerical simulation, Wang et al. (2003) developed the numerical model and simulation procedure systematically to describe the influence of the permeability, width, and direction of the incoming wind of the shelterbelt on the flow field, and to explain the relationship between the structure of the shelterbelt and the wind choke effect. Santiago et al. (2007) used three different turbulence models to analyze the flow characteristics of the airflow on the leeward side of the shelterbelt on a flat surface, and then selected an appropriate numerical model to analyze the optimum permeability of the shelterbelt as 35%. Zhan et al. (2017) using a two-dimensional Computational Fluid Dynamics (CFD) model numerically simulated and evaluated the impact of sand-fixing windbreak forests on wind-sand flows.

However, in these studies, there are two main limitations. First, the numerical simulations are limited to two spatial dimensions, ignoring the structural changes in the shelterbelt along the spanwise dimension. For windbreak forest belts composed of different tree species, the canopy has strong heterogeneity and complexity, making the spanwise dimension an important parameter that should not be neglected when describing the aerodynamic characteristics of the shelterbelt (Zhou et al., 2005; Bourdin and Wilson, 2008; Rosenfeld et al., 2010). Second, the research area is mostly concentrated on the sandy surface, with relatively little research under the Gobi surface. This has always been a weak link in this field. Compared with general desert areas, sand particles have a large initial velocity, large bounce angle, and high jump height under the Gobi surface. The sand particles can fully move due to the energy of the airflow, and the wind-sand flow often presents an unsaturated transport state (Dong et al., 2004; Zhang et al., 2011; Tan et al., 2016), making it difficult to fully visualize the wind-sand flow field around the vegetation using wind tunnel tests. Additionally, the Gobi area is uninhabited, with harsh natural conditions and heavy traffic restrictions, making field observations very difficult. Therefore, it is necessary to use three-dimensional numerical simulation technology to study the protective benefits of Gobi forest belts.

The Lan-Xin Railway crosses the Gobi Desert in Northwest China, with plant protection measures installed in some sections to prevent wind and sand hazards and ensure driving safety. Shelterbelts along the Lan-Xin Railway consist of trees and shrubs, which are *Populus bolleana* Lauche approximately 12 m high, and *Haloxylon ammodendron* approximately 3 m high, respectively, with a total of three rows and a row spacing of 72 m. In this study, numerical simulations are used to construct a three-dimensional physical model of the shelterbelt to study the change law of the wind velocity profile and wind resistance efficiencies at different positions of the shelterbelt. This study aims to make an effective scientific assessment of the wind and sand resistance effect of the shelterbelt. Additionally, the results of the numerical simulation were verified through wind tunnel tests, and the sand flux density and sand blocking effect of the shelterbelt were studied. The research results provide theoretical support for the wide application of windbreak forest belts and are of great significance to the application of plant protection measures along the railway in the Gobi area.

2 MATERIAL AND METHODS

2.1 Numerical Simulation

2.1.1 Governing Equation

In the numerical simulation, a steady-state method was used to solve the problem. The solution model used the standard k–ε model, and the airflow at the inlet was an incompressible airflow. During the solution process, the continuity equation, RANS equation, and two standard k-ε turbulence closed equations were solved. The control equation is as follows:

$$\frac{\partial \mathrm{u}_j}{\partial \mathrm{x}_j} = 0 \tag{1}$$

$$\frac{\partial u_i}{\partial t} + u_j\frac{\partial u_i}{\partial x_j} = -\frac{1}{\rho}\frac{\partial p}{\partial x_i} + \frac{\mu}{\rho}\frac{\partial^2 u_i}{\partial x_i \partial x_j} - \frac{\partial}{\partial x_j}\overline{u_i' u_j'} + g_i \tag{2}$$

$$\rho\frac{\partial k}{\partial t} + \rho u_i\frac{\partial (k)}{\partial x_i} = \frac{\partial}{\partial x_j}\left[\left(\mu + \frac{\mu_t}{\sigma_k}\right)\frac{\partial k}{\partial x_j}\right] + G_k - \rho\varepsilon \tag{3}$$

$$\rho\frac{\partial \varepsilon}{\partial t} + \rho u_i\frac{\partial (\varepsilon)}{\partial x_i} = \frac{\partial}{\partial x_j}\left[\left(\mu + \frac{\mu_t}{\sigma_\varepsilon}\right)\frac{\partial \varepsilon}{\partial x_j}\right] + C_{1\varepsilon}G_k\frac{\varepsilon}{k} - C_{2\varepsilon}\rho\frac{\varepsilon^2}{k} \tag{4}$$

where u_i and u_j are the components of the velocity along the i and j directions, respectively; t is time; ρ is the air density; k is the turbulent kinetic energy; ε is the turbulent dissipation rate; μ is the dynamic viscosity; μ_t is the turbulent viscosity; g_i is the gravitational acceleration along the i directions; G_k is the

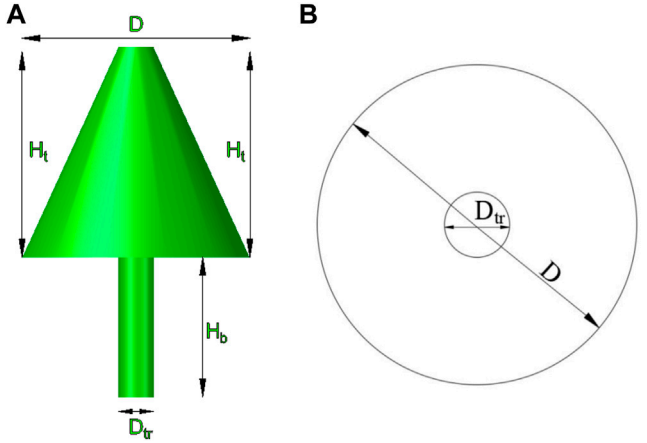

FIGURE 1 | Simplified schematic diagram of plant. **(A)**: The size of plant, **(B)**: Trunk diameter.

turbulent kinetic energy produced by the average velocity gradient of the air phase; σ_k and σ_ε are the Trump constants corresponding to the turbulent kinetic energy and its dissipation rate, respectively, $\sigma_k = 1.0$, $\sigma_\varepsilon = 1.3$; and C_μ, $C_{1\varepsilon}$, and $C_{2\varepsilon}$ are the empirical constants, $C_\mu = 0.09$, $C_{1\varepsilon} = 1.44$, $C_{2\varepsilon} = 1.92$.

2.1.2 Porous Media Model

Forest belts are usually composed of multiple rows of trees; thus, the shelterbelt area was regarded as a porous medium area in the numerical simulation. In ANSYS Fluent, the porous medium model adds a source term to the momentum equation to simulate the resistance of the porous area to the fluid flow. The governing equation is as follows:

$$S_i = -\left(\frac{\mu}{\alpha}u_i + C_2\frac{1}{2}\rho|u|u_i\right) \tag{5}$$

$$C_2 = \frac{k_r}{W} \tag{6}$$

Where α is the permeability; C_2 is the coefficient of inertial resistance; u is the overall velocity; W is the width of the windbreak forest; and k_r is the pressure loss coefficient.

2.1.3 Geometric Modeling

To ensure modeling accuracy, the SCDM 2019R3 software, which has an intelligible interface for Fluent, was used to establish a three-dimensional solid model of the shelterbelt plants. The layout method used was high in the front and low in the back, arranged in a "product" shape, with a belt spacing of 72 m ($6H_B$, $H_B = 12$ m). The overall layout consisted of regions with one belt and two rows (referred to as a row), two belts and four rows (referred to as two rows), and three belts and six rows (referred to as three rows). Through reasonable trial calculations, the size of the calculation domain was determined to be X × Y × Z = 360, 432, and 504 m (30, 36, and $42H_B$) × 84 m ($7H_B$) × 72 m ($6H_B$), and the model was set at 120 m ($10H_B$) from the entrance. To avoid backflow, the distance from the model to the outlet was 240 m ($20H_B$). In the model, the canopy was simplified into a truncated cone, and the trunk was simplified into a cylinder (**Figure 1**); a schematic diagram of the 3D finite element model of the three rows of windbreak forest belts in the numerical simulation is shown in **Figure 2**. The distance between A (B) plants is 6 m in spanwise dimension, and the distance between plant trunks is 9 m in X dimension. **Table 1** shows the characteristic dimensions of the simplified model of the two plants in the numerical simulation simultaneously.

2.1.4 Meshing

To ensure the full development of airflow in the flow field, the model was set 120 m ($10H_B$) away from the entrance. Owing to the complex structure of the model, it is difficult to generate structured grids; therefore, the Tetrahedrons method in Workbench Mesh was used for unstructured meshing of the entire computational basin. To improve the calculation efficiency, the size control method is used to locally encrypt the cells near the model, and 10 boundary layers were set along the bottom wall and the surface of the model, and the growth rate was set to 1.2. In the end, the total number of single-, double-, and triple-row shelterbelt units were 2.58, 3.36, and 4.02 million, respectively. The maximum inclination rate of the grid was controlled below 0.7, and the quality of the grid was good, which could meet the accuracy requirements of the calculation.

2.1.5 Boundary Conditions

The boundary conditions of the numerical simulations are listed in **Table 2**. A user-defined function (UDF) was used at the entrance and a C language self-compiled function was embedded, so that the wind velocity profile was in logarithmic form conforming to wind tunnel test, the wind velocity at the axis was 8, 12, 16 m s^{-1}, respectively, and the wind velocity profile form was:

$$v(z) = \frac{v}{k}\ln\frac{z}{z_0} \tag{7}$$

where $v(z)$ represents the velocity at z height, in m·s^{-1}; v represents the frictional wind velocity, in m·s^{-1}; k represents

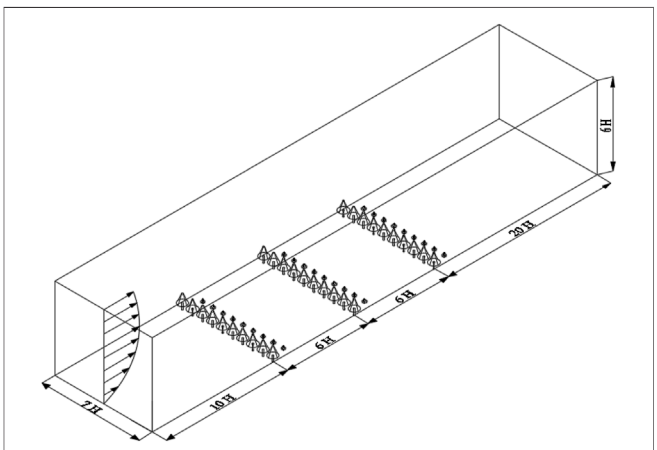

FIGURE 2 | Schematic diagram of the 3D finite element model of the shelterbelt.

TABLE 1 | Plant characteristic size in numerical simulation.

Plant type	$H_{A\backslash B}$ (Plant height)	H_b (Height of plant trunk)	D (Crown width)	D_{tr} (trunk diameter)
A plant	3 m (H_A)	1.2 m	3 m	0.5 m
B plant	12 m (H_B)	4.8 m	7.8 m	1.2 m

TABLE 2 | Computational domain boundary conditions.

Location	Boundary condition
Inflow boundary	Velocity $v(z) = \frac{v}{k}\ln(z/z_0)$
Downstream boundary	Fully developed outflow $\frac{\partial}{\partial x}(u_i, u_y, u_z, k, \varepsilon) = 0$
Upper face of computational domain	Free slip, $\frac{\partial}{\partial z}(u_i, u_j, k, \varepsilon) = 0$, w = 0
Ground surface boundary	Wall, K_S = 0.017 m, C_S = 0.5, z_0 = 0.00087 m

the von Karman coefficient, k = 0.4; z represents the height, in m; and z_0 is the roughness length, in m.

2.1.6 Solution

The entire solution domain is a fluid domain, in which the canopy area of the shelterbelt plants was set as a porous medium area, with porosity set to 30.17%. The velocity in the simulation was much lower than that of sound, and air was regarded as an incompressible fluid. The pressure solver was used for the steady-state solution, the finite volume method was used for solution control, the solution method was SIMPLE (Wang and Takle, 1995; Mahgoub and Ghani, 2021), the momentum used the second-order upwind style, and the turbulence energy and turbulent dissipation rate used the first-order upwind style. The convergence standard of the residual was set to 10^{-6}. When the residual was less than 10^{-6}, the accuracy requirement was met, and the calculations were terminated.

2.2 Wind Tunnel Tests

2.2.1 Test Design

The wind tunnel used in this test was a direct current downward blowing wind tunnel with a total length of 38.9 m, of which the test section was 16.0 m long, the cross-sectional size was 1.2 m × 1.2 m, the boundary layer thickness was 0.5 m, and the test wind velocity range was adjustable between approximately 4 and 35 m s^{-1}. This test included two parts: a flow field test and a sediment transport test. The flow field test used a 10-channel Pitot tube to measure the wind velocity profile at different positions. The sand transport test was conducted at a position 1.0 m downwind from the entrance of the test section. A sand bed

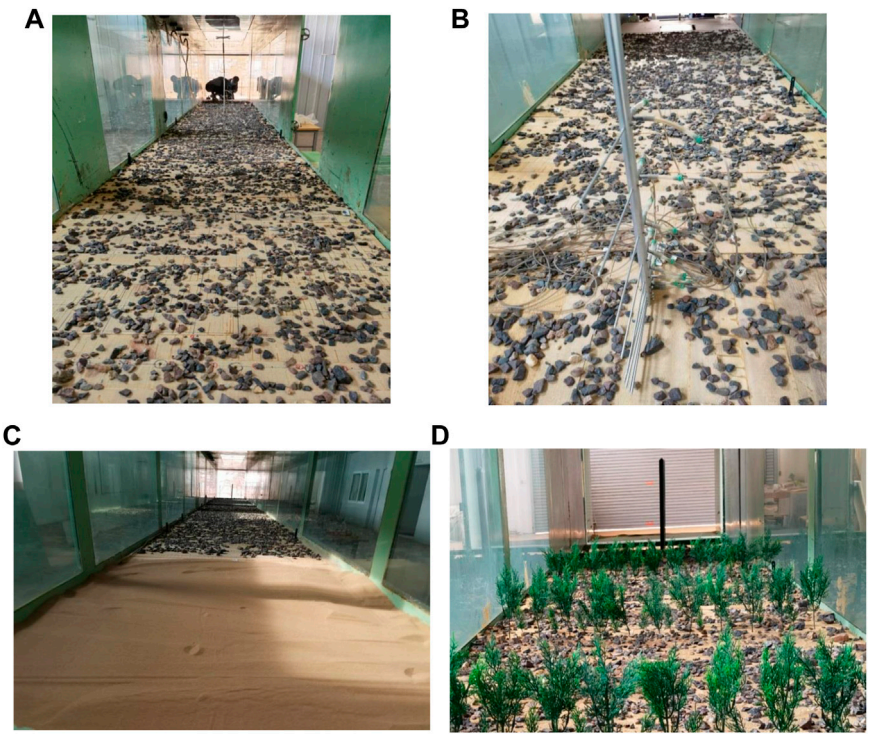

FIGURE 3 | The layout of Gobi surface, sand beds, and plants in the wind tunnel test. **(A)**: Gobi bed, **(B)**: Flow field test, **(C)**: Sand bed, **(D)**: Sediment transport test.

TABLE 3 | Selection table of plant parameters.

Type	Plant height	Crown width	Height of plant trunk	Branch angle	Branch length
A plant	5 cm (H_1)	5 cm × 5 cm	2 cm	30°–40°	3–4 cm
B plant	20 cm (H_2)	13 cm × 13 cm	8 cm	30°–40°	14–15 cm

The height of the plant is the height above the bed.

with a width of 1.2 m, a length of 4.0 m, and a thickness of 5.0 cm was laid. The particle size was between 0.075 and 0.500 mm, the sand source was supplemented, and the sand surface was leveled before each test to ensure sufficient sand source supply. The test site is shown in **Figure 3**.

In this wind tunnel test, two plants, A and B, were selected (**Table 3** for detailed plant parameters). The arrangement method was high in the front and low in the back, arranged in the shape of "product," with a total of three belts and six rows (referred to as three rows). The plant spacing was 10 cm ($0.5H_2$, H_2 = 20 cm), the belt spacing was 120 cm ($6H_2$). The forest belt permeability was estimated by using an unsupervised classification analysis of crown photographs using the software ERDAS IMAGINE 9.2 (Tntergraph, United States). The forest belt permeability was 30.17% (Ma et al., 2019). To simulate the surface of the Gobi, a layer of gravel with a length of 12.0 m and a width of 1.2 m was laid in the wind tunnel. The gravel surface was composed of natural Gobi gravel with a diameter of 0.5–5.0 cm. Additionally, the selected test wind velocities were 8, 12, and 16 m s^{-1} in the wind tunnel test.

2.2.2 Similarity Criterion

The reliability of wind tunnel test results primarily depends on the degree of similarity between experimental and field conditions. To ensure the accuracy of the test results, the wind tunnel test must meet three similarity conditions: geometric similarity, similar motion, and similar dynamics (White, 1996). For geometric similarity, to avoid wall interference, it is generally required that the ratio of the turbulent boundary layer of the wind tunnel to the ground-attached boundary layer does not exceed 6% of obstruction. In this experiment, the ratio of the plant model to the actual field was 1:60, which satisfied the geometric similarity. Motion similarity primarily considers two aspects: the flow state and the wind velocity profile form. The test verified that the wind velocity profile form conformed to the logarithmic distribution law (**Figure 4**), indicating that the wind tunnel test meets the motion similarity. As long as the Reynolds number in the wind tunnel is sufficiently large, a self-simulation zone independent of the Reynolds number can be formed (Ma et al., 2019). Three wind velocities of 8, 12, and 16 m s^{-1} were selected for this experiment. Under the three test wind velocities, the Reynolds number was 6.75 × 10^5–1.35×10^6 (Re = ρvl/μ_1, ρ: air density, equal to 1.205 kg m^{-3}; v: the characteristic velocity of the flow field; l: the characteristic length at 0.98 m; μ_1: the kinematic viscosity

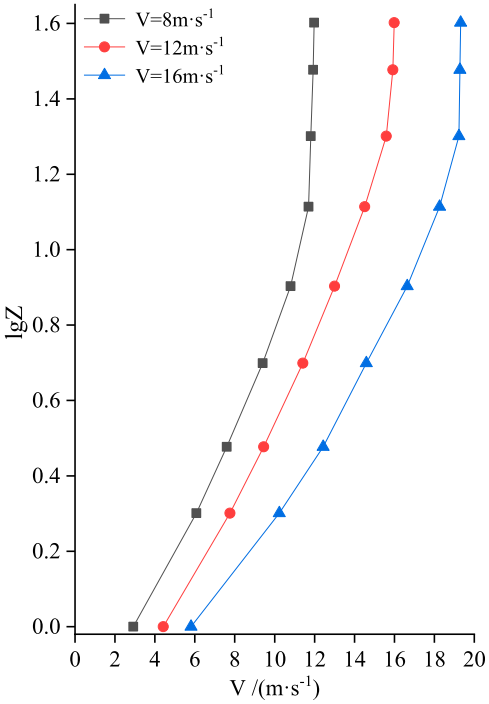

FIGURE 4 | The change law of the wind velocity profile of the cavity under different test wind velocities.

of air, equal to 1.4 × 10^{-5} m^2 s^{-1}), which is much larger than 1 × 10^5. The dynamic similarity is satisfied.

2.2.3 Data Processing

In this wind tunnel test, a Pitot tube was used to measure the wind velocities at different locations in the forest belt (**Figure 3B**). The measured heights of the Pitot tube were 1, 2, 3, 5, 8, 13, 20, 30, and 40 cm, and the collection frequency was 0.5 s, the collection time of each wind velocity was 60 s, and the average value was taken as the actual wind velocity at that point. The wind protection efficiency near the forest belt was calculated using the following formula:

$$\varphi_{(x,z)} = \left(1 - \frac{V_{(x,z)}}{V'_{(x,z)}}\right) \times 100\% \quad (8)$$

where $\varphi_{(x,z)}$ is wind protection efficiency, x is the horizontal position of the test point (m), z is the height of the test point (cm),

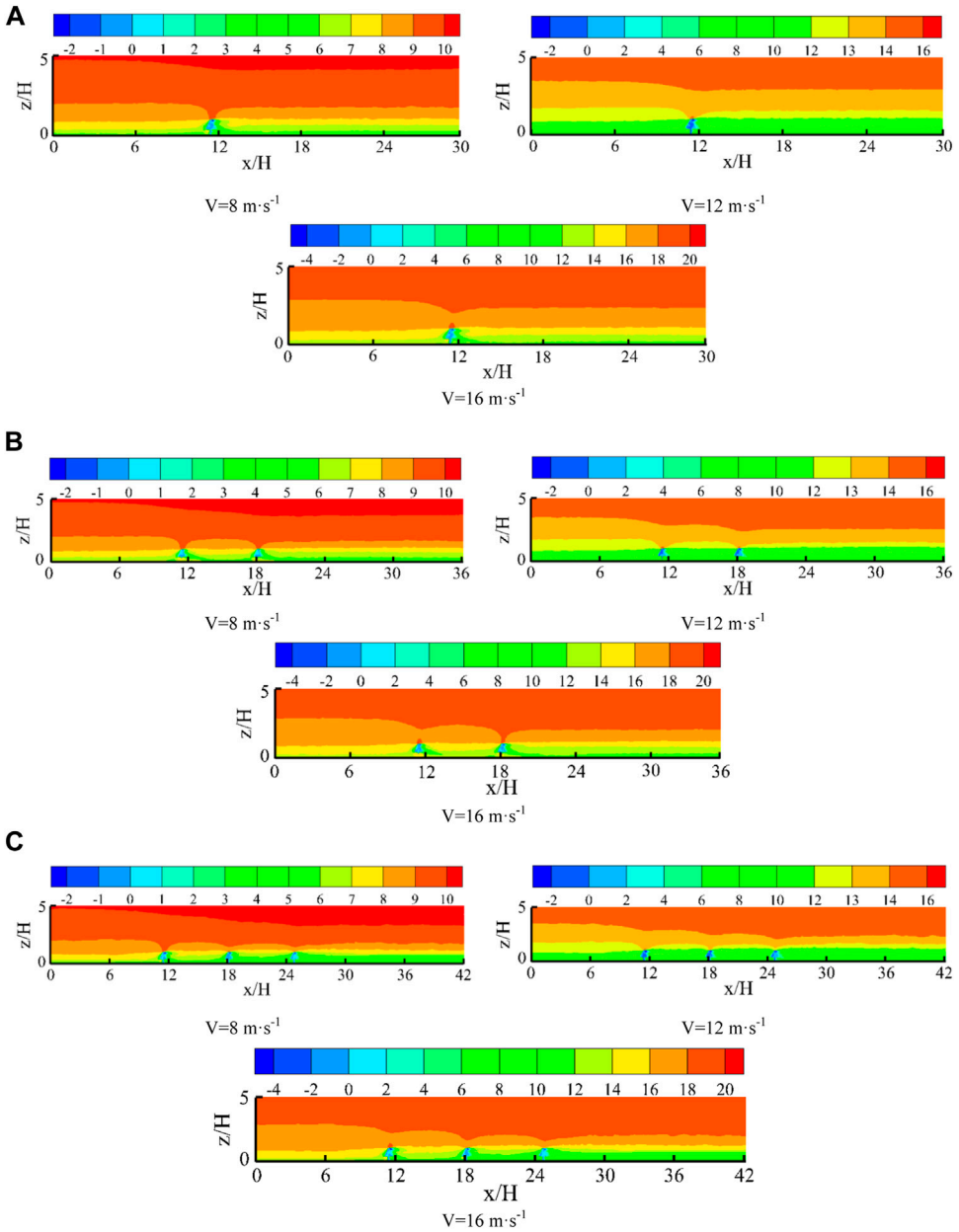

FIGURE 5 | Distribution characteristics of flow field near forest belts. **(A)**: Single row of forest belts, **(B)**: Two rows of forest belts, **(C)**: Three rows of forest belts.

$V_{(x,z)}$ is the horizontal wind velocity at the point (x, z), m·s^{-1}, and $V'_{(x,z)}$ is the horizontal wind velocity when the windward side of the forest belt is undisturbed (m·s^{-1}).

A vertical gradient sand collector was used to test sediment transport. The height of the sand collector was 50 cm, and the cross-sectional size of each sand collector was 2 cm × 2 cm. At test wind velocities of 8, 12, and 16 m s^{-1}, the sand collection times were 3, 2, and 1 min, respectively. The collected sand was weighed in the sandbox at different heights with high-precision electronic peace, and its weight was represented with q. The sand flux density at different heights can be obtained by dividing the area and collection time of a single sand collection port by q. Q was the sand transport rate through unit spanwise scale (total sum of q*dz). The sand blocking efficiency near the forest belt was calculated using the following formula:

$$\delta = \left(1 - \frac{Q}{Q'}\right) \times 100\% \tag{9}$$

where δ is the efficiency of preventing sand, Q is the sand transport rate at $10H_2$ behind the forest belt (kg·m^{-1}·min^{-1}), and Q' is the sand transport rate without forest belt (kg·m^{-1}·min^{-1}).

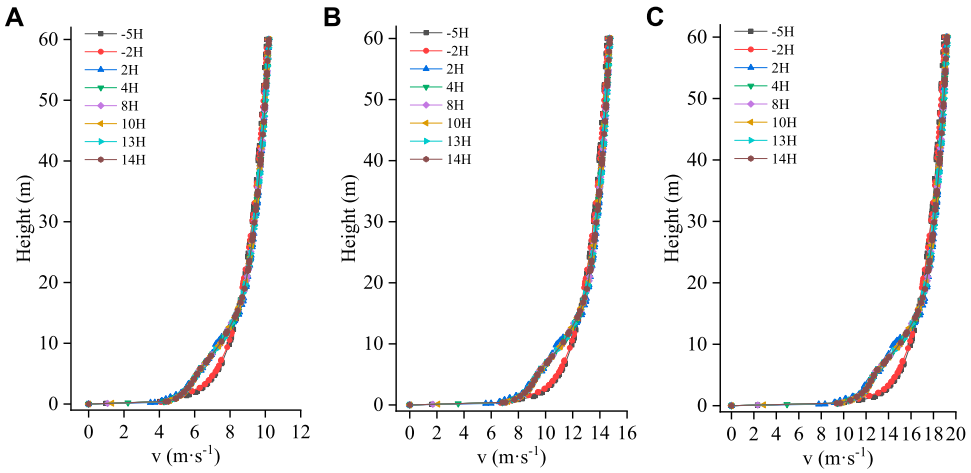

FIGURE 6 | Wind velocity profile variations at different positions of single-row forest belt under different incoming wind velocities. **(A)**:V = 8 m·s^{-1}, **(B)**: V = 12 m·s^{-1}, **(C)**: V = 16 m·s^{-1}.

3 RESULTS

3.1 Numerical Simulation

3.1.1 Flow Field

Figure 5 shows the distribution characteristics of the flow field near different rows of windbreak forest belts under different incoming wind velocities. It can be seen from the figure that under different incoming wind velocities, the distribution characteristics of the flow field near the windbreak forest belts were basically the same, and there were obvious partition characteristics near the forest belts. A zone of low airflow occurred. When the windbreak forest belts were arranged in multiple rows, the blocking effect on the airflow was more obvious, and an obvious low-speed airflow area occurred between the forest belts. Compared with the single-row forest belt, the area of the low-speed area on the leeward side of the double-row and three-row windbreak forest belts was significantly larger. When the windbreak forest belts were arranged in three rows, the area of the leeward side deceleration area was the largest, and the purification effect on the wind and sand flow was the strongest. In addition, it can also be found that when the windbreak forest belts were arranged in multiple rows, the low-speed area of airflow between the windbreak forest belts and that on the leeward side tended to be integrated.

3.1.2 Variation Law of Wind Velocity Profile

Figures 6–8 show the broken line diagrams of the wind velocity profile changes under the single-, double-, and triple-row forest belts. The first row of windbreak forest belts is used as a reference point for each position on the figure. As seen in **Figures 6–8**, the wind velocity profile shows similar changes under different wind velocities. At $2H_B$ and $5H_B$ before the forest belt, the airflow was not disturbed by the forest belt, and the wind velocity profile changed logarithmically; however, the change pattern of the wind velocity profile at different positions inside the forest belt and on the leeward side was different from that in front of the forest belt. The wind velocity profiles under the single- and double-row windbreak forest belts were less disturbed, with relatively gentle changes, and no obvious turning point. When the forest belt was arranged in three rows, the disturbing effect on the airflow was enhanced, and variations in the wind velocity profile began at $2H_B$. As the airflow moved forward, the wind velocity profile gradually deviated from following a logarithmic law, with a turning point observed at $13H_B$ behind the forest belt. Compared with the wind velocity profile at the front edge of the forest belt, the horizontal wind velocity decreased notable below the height of plant A. Additionally, there were two wind velocity turning points in the disturbed wind velocity profile, first at approximately 3 m high, which is the top of plant A, then at approximately 12 m high, which is the top of plant B. Between the two wind velocity turning points, the airflow velocity decreased significantly, and the attenuation amplitude of the airflow decreased as height increased. Above the height of plant B, the obstructive effect of the forest belt was lost, and the airflow velocity slowly recovered.

3.1.3 Windproof Efficiency

Figure 9 shows the windbreak efficiencies at different positions at a height of 60 cm on the leeward side of the forest belt with different incoming wind velocities in the numerical simulation. Each position in the figure is based on the last row of forest belts, where DLT_{1HB} is 1H away from the leeward side of the third row of forest belts. Overall, under different incoming wind velocities, the windbreak efficiencies of different windbreak forest belts rows showed a trend of increasing and then decreasing. Among them, at the DLT_{5HB} position, the wind protection efficiency reached the maximum, then the wind protection efficiency decreased to a minimum at the DLT_{15HB}position behind the forest belt. As the number of windbreak forest belts increased, the windbreak efficiencies of the windbreak forest belts increased significantly. When the forest belt was arranged in three rows belt under the three inlet wind velocities, the wind protection efficiency was the best at the DLT_{5HB} position, and the maximum wind protection efficiencies were 95.1, 90.4, and 88.6%,

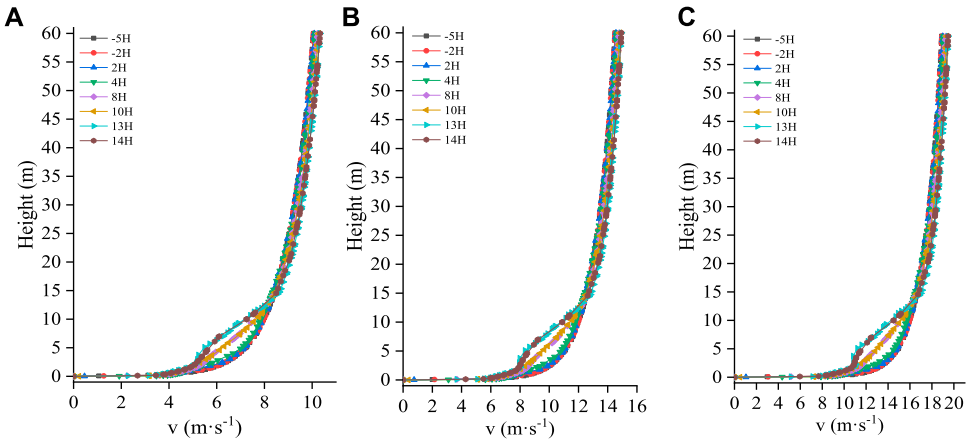

FIGURE 7 | Wind velocity profile variations at different positions of double-row forest belt under different incoming wind velocities. **(A)**:V = 8 m·s^{-1}, **(B)**: V = 12 m·s^{-1}, **(C)**: V = 16 m·s^{-1}.

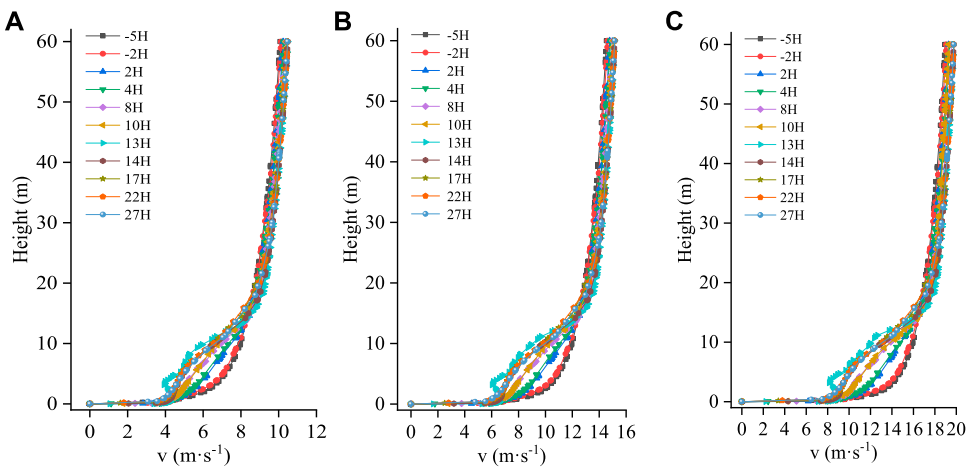

FIGURE 8 | Wind velocity profile variations at different positions of three rows of windbreak forest belts under different incoming wind velocities. **(A)**:V = 8 m·s^{-1}, **(B)**: V = 12 m·s^{-1}, **(C)**: V = 16 m·s^{-1}.

respectively. Compared with the single-row arrangement, the maximum wind protection efficiency increased by 23.7, 22.1, and 23.9%, respectively. Compared with the double-row arrangement, the maximum wind protection efficiency increased by 5.7, 4.2, and 3.0%, respectively. At the same time, as the incoming wind velocity continued to increase, the wind protection efficiency at the same location showed a decreasing trend.

3.2 Wind Tunnel Tests

3.2.1 Airflow Field Characteristics

The characteristics of the airflow field around the three rows of windbreak forest belts under different incoming wind velocities are shown in **Figure 10**. Each position in the figure is based on the first row of windbreak forest belts as a reference point. Generally, when the airflow encounters obstacles near the forest belt, airflow deceleration zones, acceleration zones, and vortex zones are formed. In this study, the airflow produced clear zoning characteristics near the forest belt, and the changes in the airflow field were basically the same under different airflows. When the airflow moved to the vicinity of the forest belt, it was blocked by the forest belt, and the airflow velocity decreased, forming a windward side deceleration zone at the front edge of the forest belt, and some sand particles in the sand-carrying airflow were deposited here. Part of the airflow crossed the tree canopy and rose when obstructed, forming a high-speed area of airflow between 0.5 and 1.5H_2 above the canopy. The airflow continued to move forward and was hindered by the forest belt twice, continually decreasing the kinetic energy and forming a large deceleration zone on the leeward side of the forest belt. Ma et al. (2019) studied the flow field characteristics of windbreak forest belts through wind tunnel tests. The results show that under different incoming wind velocities, a local acceleration zone was formed above the shelterbelt, and there were large

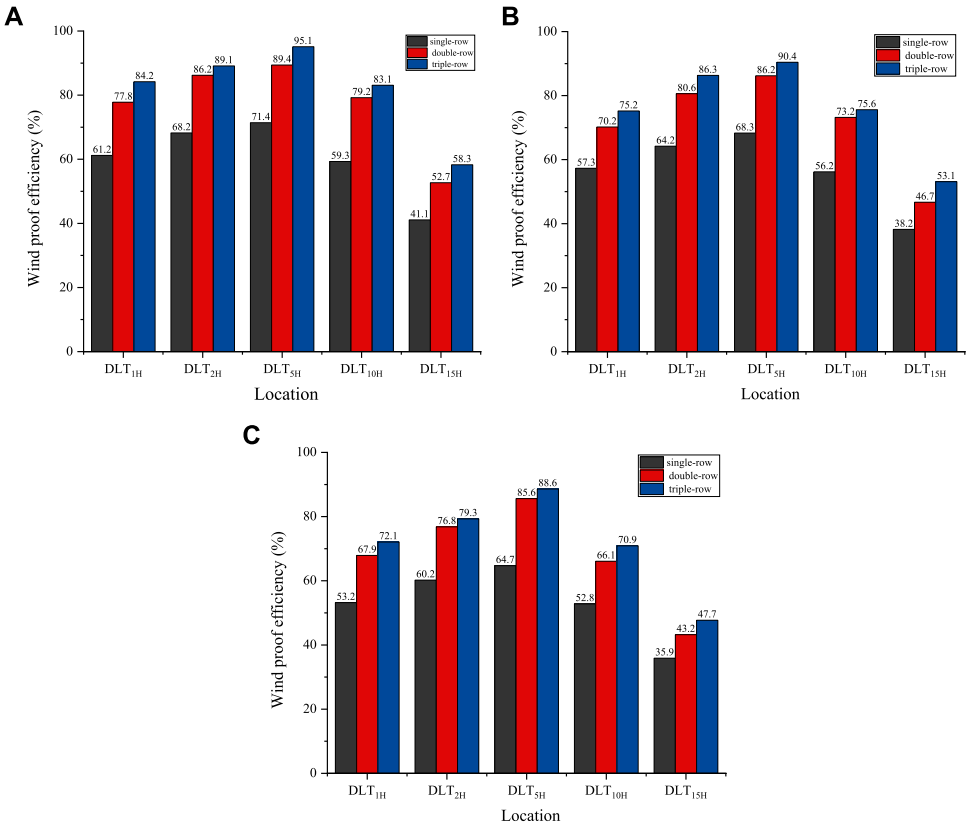

FIGURE 9 | The relationship between windbreak efficiency and forest belt downwind distance under different incoming wind velocities. **(A)**:V = 8 m·s^{-1}, **(B)**: V = 12 m·s^{-1}, **(C)**: V = 16 m·s^{-1}.

deceleration zones between the windbreak forest belts and on the leeward side. We drew the same conclusions as Ma et al. (2019) during our study; however, They mentioned that there was also a local acceleration area inside the forest belts, while almost all the windbreak forest belts were deceleration zones in this study, which was caused by the difference between the line and the belt spacing in the experiment. Finally, with the continuous increase in the incoming wind velocity, the range of the deceleration zone on the leeward side of the forest belt tended to gradually shrink, which agrees with the results of them.

We also observed that the streamlines between the windbreak forest belts and on the leeward side of the windbreak forest belts were curved rather than smooth. The streamline showed an upward curve directly above the forest belt, and there was a downward bending trend between the forest belts, which showed that the airflow velocity between the windbreak forest belts was greatly attenuated, forming a low-speed airflow area (Dong et al., 2007). Here, the sand-carrying capacity of the airflow was greatly reduced, the velocity of sand particles was reduced below the starting wind velocity, and most of the sand particles were deposited in the forest belts.

3.2.2 Wind Velocity Profiles

The wind velocity profile changes at different positions of the three rows of windbreak forest belts in the wind tunnel test are shown in **Figure 11**. The first row of windbreak forest belts is used as a reference point for each position in the figure. As shown in **Figure 11**, at $2H_2$ and $5H_2$ up the forest belt, the forest belt has no clear influence on the wind velocity, and the wind velocity profile obeys the logarithmic distribution law; however the airflow disturbance by the forest belt stops following the logarithmic distribution in the lower wind direction of the forest belt. Below the forest belt height, the airflow resistance decreased, especially above the height of plant A and below the height of plant B, the air velocity was significantly reduced, and the decrease in the air velocity reached a maximum at approximately $22–27H_2$ in the downwind direction of the forest belt. Above the height of plant B, without the obstacle of the forest belt, the airflow velocity began to increase, and then the airflow slowly returned to the incoming wind velocity. The change law of the wind velocity profile in the wind tunnel test was basically the same as that of the three rows of windbreak forest belts in the numerical simulation; however, the air velocity of the forest belt downwind above the height of plant B in the wind tunnel test was slightly lower than that in the numerical simulation. This is because the wind tunnel test is a scaled test, which has certain restrictions compared with the prototype test. Additionally, the presence of collection equipment such as Pitot tubes in the wind tunnel test will also have a certain impact on the airflow. Therefore, it is necessary to compare the numerical simulation results and the wind tunnel test results with each other and verify each other to enhance the accuracy and rigor of the results.

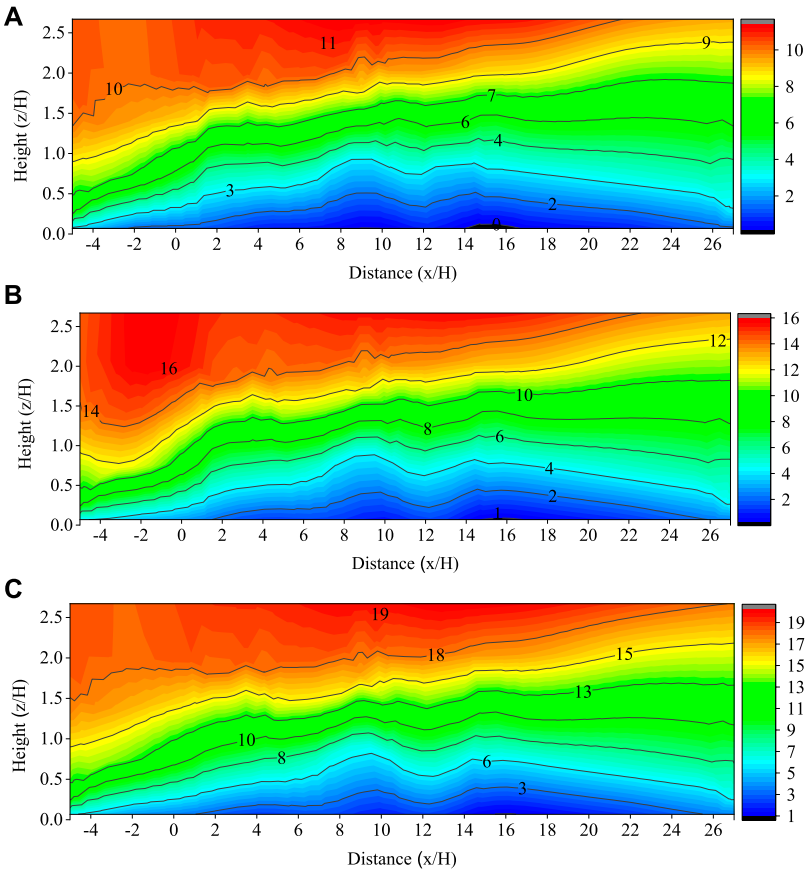

FIGURE 10 | The characteristics of the airflow field around the three rows of windbreak forest belts under different incoming wind velocities. The units in parenthesis for all figures are m·s^{-1}. **(A)**:V = 8 m·s^{-1}, **(B)**: V = 12 m·s^{-1}, **(C)**: V = 16 m·s^{-1}.

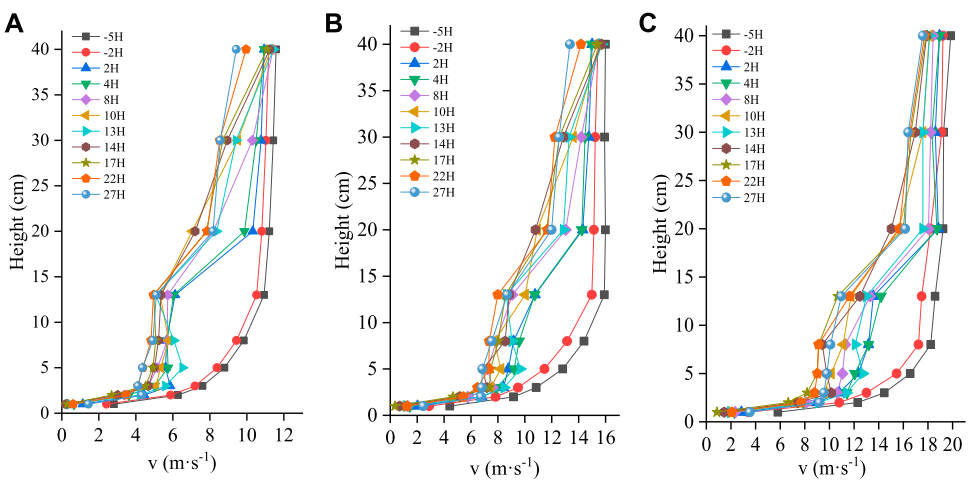

FIGURE 11 | Variation law of wind velocity profile at different positions of three rows of windbreak forest belts under different incoming wind velocities. **(A)**: V = 8 m·s^{-1}, **(B)**: V = 12 m·s^{-1}, **(C)**: V = 16 m·s^{-1}.

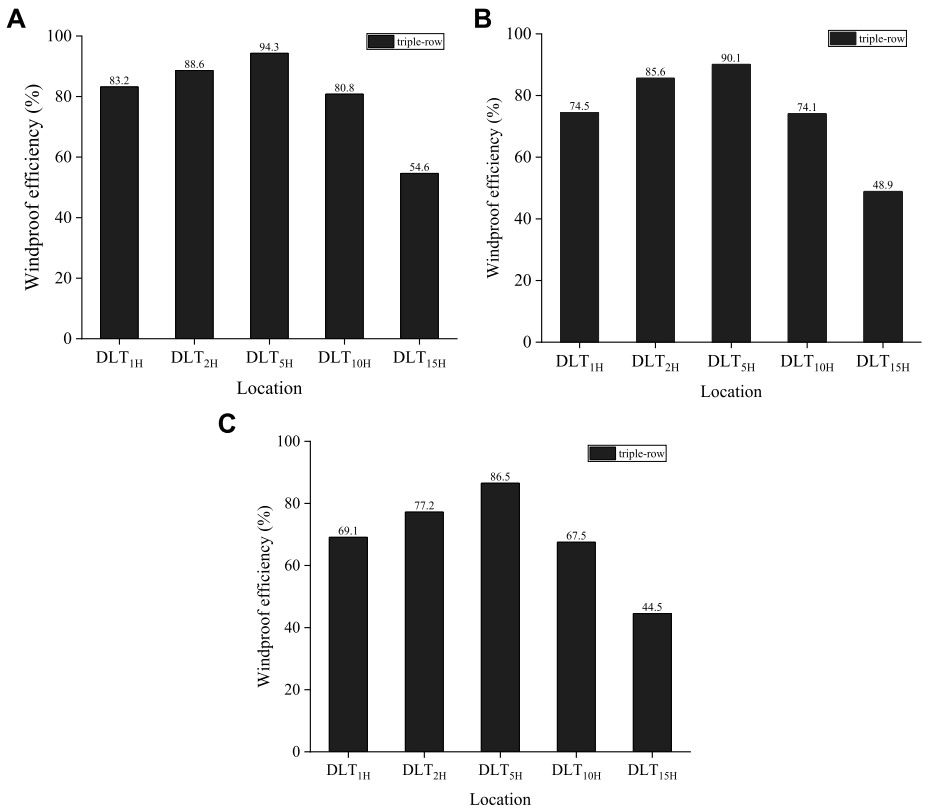

FIGURE 12 | The relationship between windbreak efficiency and forest belt downwind distance under different incoming wind velocities. **(A)**: V = 8 m·s^{-1}, **(B)**: V = 12 m·s^{-1}, **(C)**: V = 16 m·s^{-1}.

3.2.3 Windproof Efficiency

Figure 12 shows the wind protection efficiencies at different locations at a height of 1 cm on the leeward side of the forest belt with different incoming wind velocities in the wind tunnel test. Each position in the figure is based on the last row of windbreak forest belts as a reference point, where DLT_{1H2} is $1H_2$ from the leeward side of the third row of forest belts. As shown in **Figure 11**, when the wind velocity was 8, 12, and 16 m s^{-1}, the wind protection efficiency changed, respectively. As the wind velocity increased, the efficiency of wind protection tended to decrease. Additionally, when the wind velocity was 8, 12, and 16 m s^{-1}, the maximum windbreak efficiencies of windbreak forest belts occurred at $5H_2$, which were 94.3, 90.1, and 86.5%, respectively, while the minimum windbreak efficiencies all occurred at $15H_2$, which were 54.6, 48.9, and 44.5%, respectively.

4 DISCUSSION

4.1 Comparison of Wind Tunnel Test and Numerical Simulation Results

Figure 13 shows a comparison of the horizontal wind velocities at different heights from the ground surface between the three rows of windbreak forest belts in the numerical simulation and wind tunnel test under different incoming wind velocities. The x-axis is normalized by plant height B, and the y-axis is normalized by the incoming wind velocity, V_0. The curve represents the predicted value of the numerical simulation, and the data points represent the actual measured values of the wind tunnel test. As shown in **Figure 13**, at Z/H = 0.15 and Z/H = 0.25, when the airflow moved to the vicinity of the forest belt, it encountered resistance and decelerated, greatly reducing the velocity. Later, affected by the acceleration zone, three peaks were formed near the forest belt, and the airflow gradually stabilized after passing through the forest belt. At Z/H = 0.40 and Z/H = 0.65, the airflow decelerated when encountering obstacles, and the velocity quickly decayed to zero near the forest belt. Affected by the deceleration zone, three clear depressions were formed near the forest belt, and the airflow slowly reached equilibrium after passing through the forest belt.

Additionally, **Figure 13** shows that the numerical simulation results are in good agreement with the measured results in the wind tunnel test, which can prove the accuracy of the numerical simulation results to a certain extent. To quantify the error between the numerical simulation results and the wind tunnel test results, and enhance the accuracy and rigor of the numerical simulation results, the statistical model performance indicators proposed by Chang and Hanna (2004) were used to compare the results of the numerical simulation and the wind tunnel test, its calculation formulae are as follows:

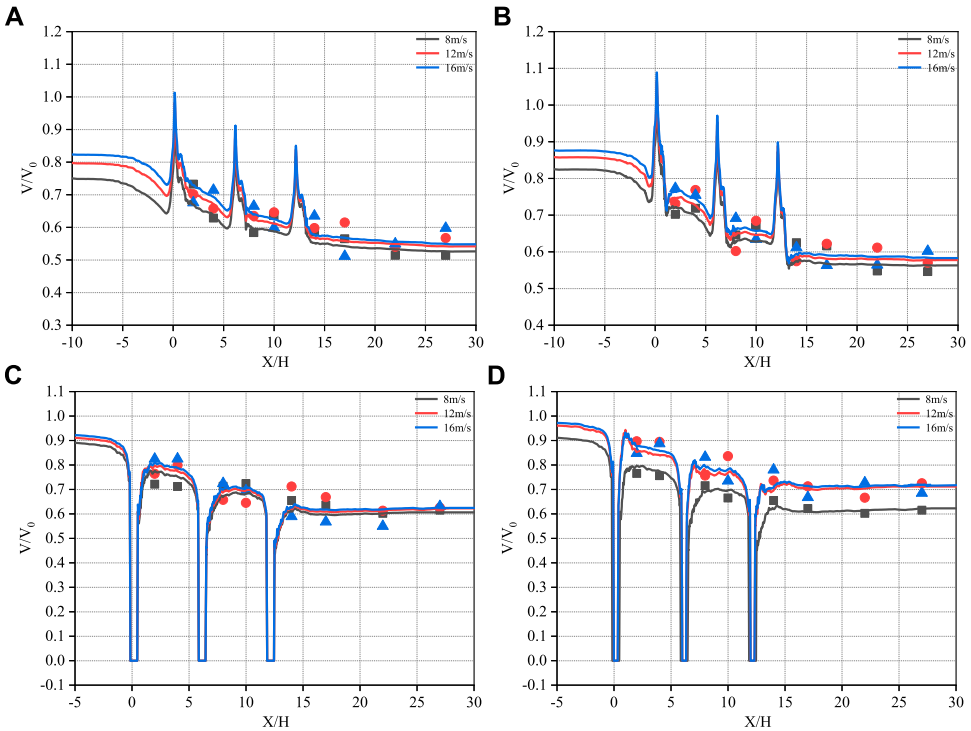

FIGURE 13 | Comparison of numerical simulation and wind tunnel test results under different incoming wind velocities. **(A)**: Z/H = 0.15, **(B)**: Z/H = 0.25, **(C)**: Z/H = 0.40, **(D)**: Z/H = 0.65.

$$FB = \frac{\overline{C_o} - \overline{C_p}}{0.5\left(\overline{C_o} + \overline{C_p}\right)} \tag{10}$$

$$MG = \exp\left(\overline{\ln C_o} - \overline{\ln C_p}\right) \tag{11}$$

$$NMSE = \frac{\overline{\left(C_o - C_p\right)^2}}{\overline{C_o}\,\overline{C_p}} \tag{12}$$

$$VG = \exp\left[\overline{\left(\ln C_o - \ln C_p\right)^2}\right] \tag{13}$$

$$R = \frac{\overline{\left(C_o - \overline{C_o}\right)\left(C_p - \overline{C_p}\right)}}{\sigma_{C_p}\sigma_{C_o}} \tag{14}$$

where FB is the score deviation, MG is the geometric mean deviation, NMSE is the normalized mean square deviation, VG is the geometric variance, R is the correlation coefficient, C_p is the predicted value of the numerical simulation, C_o is the measured value of the wind tunnel test, $\bar{C}$ is the average value of the dataset, and σ_c is the standard deviation of the data set. When the values of FB and NMSE were closer to 0, the values of MG, VG, and R were inversely closer to 1, indicating that the results of the wind tunnel test and numerical simulation are more consistent.

Table 4 compares the results of the numerical simulation and wind tunnel test, and calculates the specific values of FB, MG, NMSE, VG, and R using **Eqs 10–14**. From the calculation results in **Table 4**, under the three incoming wind velocities, the maximum deviation of FB is 0.1244, the maximum deviation of MG is 0.1174, the maximum deviation of NMSE is 0.0181, the maximum deviation of VG is 0.0391, and the maximum deviation of the correlation coefficient R is 0.3860. Comprehensive analyses of these five statistical performance indicators show that the results of the numerical simulation and the wind tunnel test are in agreement, and the results of the numerical simulation are reliable.

TABLE 4 | Numerical simulation results and wind tunnel test error analysis table.

Location	Velocity	FB	MG	Deviation NMSE	VG	R
Z/H = 0.15	8	0.0313	1.0286	0.0051	1.0046	0.8426
	12	0.0339	1.0355	0.0017	1.0031	0.8879
	16	0.1012	1.0112	0.0031	1.0061	0.7277
Z/H = 0.25	8	0.0351	0.9737	0.0079	1.0094	0.7254
	12	0.0263	0.9910	0.0029	1.0077	0.8641
	16	0.0399	1.0565	0.0042	1.0391	0.8938
Z/H = 0.40	8	0.0134	1.0189	0.0071	1.0078	0.7644
	12	0.0118	1.0157	0.0068	1.0113	0.6140
	16	−0.0113	1.0369	0.0022	1.0248	1.0774
Z/H = 0.65	8	−0.1244	0.8826	0.0181	1.0186	0.8321
	12	0.0079	1.0065	0.0023	1.0034	0.8521
	16	−0.0086	0.9565	0.0038	1.0194	0.7218

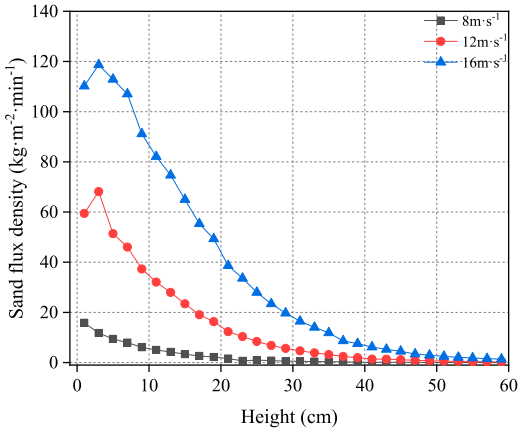

FIGURE 14 | Variation law of sand flux density on Gobi gravel bed under different incoming wind velocities.

4.2 Comparison of Related Research Results of Protection Benefits

Compared with the results of the three rows of windbreak forest belts in the numerical simulation, the windproof efficiency in the wind tunnel test was slightly lower. The position with the largest difference was $15H_2$ away from the forest belt, the deviation was 4.2%, and the deviation of the other positions was within 4%. Ma et al. (2019) studied the wind protection efficiency of windbreak forest belts composed of different plant types through the technical means of wind tunnel tests. The results show that when the incoming wind velocity was 7 m s^{-1}, the maximum windproof efficiency of the product glyph shelterbelt was approximately 80%. In this study, when the incoming wind velocity was 8 m s^{-1}, the maximum windproof efficiency of the shelterbelt was 95.1%. This difference was caused by the distance between forest belts. The distance between windbreak forest belts as reported by them was 40H, while the distance in this study was 6H, resulting in a higher windproof efficiency obtained in this study. Lin et al. (2020) conducted wind tunnel tests on *Caragana korshinskii* shrubs with different spacings, and the results showed that when the incoming wind velocity was 10 m s^{-1} and the forest belt spacing was 6H, the average windbreak efficiency on the leeward side of the forest belt was 73.3%. When the incoming wind velocity was 12 m s^{-1}, the average windbreak efficiency on the leeward side of the forest belt was 76.1%. The results of them are consistent with those of this study.

Figures 14, **15** show the variations in the sand transport rate with height at $10H_2$ behind the Gobi gravel bed and three rows of windbreak forest belts under different incoming wind velocities, respectively. As shown in the figures, under the Gobi gravel bed, the sand flux density showed a negative exponential change with the height, and with an increase in the incoming wind velocity, the sand flux density continued to increase, similar to the results obtained by Wang et al. (2017), Wang et al. (2020). The results of the cave tests are consistent. The forest belt has a significant effect on reducing the sand flux density, especially below the height of the forest belt. Additionally, an interesting point is that when the incoming wind velocity was 12 and 16 m s^{-1}, the sand flux density reached a maximum at 4 cm high, and then gradually decreased. This is the unique "elephant effect" of the wind-sand flow structure in the Gobi area proposed by Qu et al. (2005). On the surface of quicksand, the sand flux density generally reached its maximum at a height of 2 cm from the surface, while the peak sand flux density in this study appeared 4 cm from the surface. This is due to the high hardness, rich gravel, and large surface roughness of the Gobi surface. There was less energy loss due to sand-gravel collisions, and the bounce height of sand particles increased, so that the position of the saturation layer of the wind-sand flow moved up. Lv et al. (2016) studied the changing laws of sand flux density under different ground surfaces, and the results showed that the maximum sand flux density under the Gobi surface appeared at approximately 2–4 cm, which is the same as the results of this study. Notably, this unique elephant effect only occurs under the Gobi gravel bed, but is not present under the

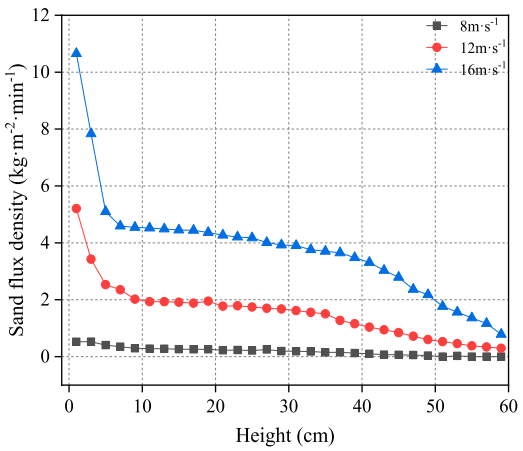

FIGURE 15 | Changes of sand flux density at $10H_2$ after three rows of windbreak forest belts under different incoming wind velocities.

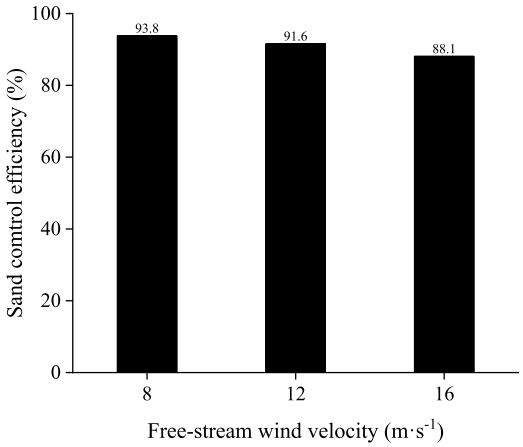

FIGURE 16 | Histogram of sand control efficiency at $10H_2$ behind the three rows of windbreak forest belts under different incoming wind velocities.

forest belt. This is because the forest belt has a strong interception effect on the sand particles in the sandstorm, so that the sandstorm on the leeward side of the forest belt is completely in a state of unsaturated transport. Therefore, there is no unique elephant effect under the forest belt.

Figure 16 shows that when the incoming wind velocities are 8, 12 and 16 m s^{-1}, the sand control efficiencies at $10H_2$ on the leeward side of the forest belt were 93.8, 91.6, and 88.1%, respectively. The efficiency of sand control was inversely proportional to the incoming wind velocity; that is, the higher the incoming wind velocity, the lower the corresponding sand control efficiency.

Gillies et al. (2017) tested the sand control efficiencies of multiple sand barriers in California, United States. The results of the study show that when the distance between the sand barriers was 7H, the sand control efficiency reached a balance at 27H behind the barrier. At this time, the sand control efficiency at 50H on the leeward side of the sand barrier was reduced by 91.0%. When the distance between the sand barriers was 10H, the sand transport reached equilibrium at the 93H position, and the sand transport at the 50H position on the leeward side of the sand barrier was reduced by 50.0%. Zhang et al. (2020) set up three sand barriers, and when the distance between the sand barriers was 20H, the sand control efficiency was 89.6%. From this, it can be observed that when the incoming wind velocity was 8 and 12 m s^{-1}, compared with the three sand barriers, the forest belt sand control efficiency in this study increased by 4.2 and 2.0%, respectively. The results show that the protection benefit of the forest belt is better than that of the three-row sand barriers with a spacing of 20H, which can effectively control the wind and sand hazards along the railway and is suitable for wind and sand protection in the Gobi area of the Lan-Xin Railway. Additionally, we found that when the incoming wind velocity was 16 m s^{-1}, the sand control efficiency of the shelterbelt was 88.1%, which was slightly less than the sand control efficiency of the three sand barriers. This is because Gillies et al. (2017) studied the surface of quicksand, while this study focused on the surface of the Gobi. When the incoming wind velocity was too high, the initial velocity of the sand jump was high, the jump angle was high, and some of the sand jumped over the shelterbelt, which led to a decrease in the sand control efficiency of the shelterbelt.

5 CONCLUSION

To evaluate the protective benefits of the protective windbreak forest belts in the Gobi area of some sections of the Lan-Xin Railway, this study used numerical simulations and wind tunnel tests to study the protective windbreak forest belts composed of different numbers of belts. It analyzed the change characteristics of the flow field around the shelterbelt and the change law of the wind velocity profile, and conducted a comprehensive evaluation of its protection benefits from the perspectives of windproof efficiency and sand control efficiency. The following conclusions were obtained:

1) Affected by the forest belt, the wind velocity profile on the leeward side of the forest belt no longer followed a logarithmic change. Below the height of plant B, the airflow velocity was significantly reduced, and above the B plant height, the airflow velocity was slowly restored without the obstacle of the forest belt.
2) Under different incoming wind velocities, the maximum windproof efficiency on the leeward side of the forest belt appeared at $5H_2$. The maximum windproof efficiency was approximately 90%, and the minimum windproof efficiency was approximately 50%. With an increase in wind velocity, the wind windproof efficiency showed a decreasing trend.
3) In the vicinity of the forest belt, airflow encountered obstacles to generate velocity zones, forming airflow deceleration zones and airflow high-speed zones. The streamlines between the windbreak forest belts bent downwards, the airflow decreased significantly, and the sand velocity dropped below the starting wind velocity, causing most of the sand falls and deposits.
4) The forest belt had a significant effect on reducing the sand flux density. When the incoming wind velocity was 12 and 16 m s^{-1}, a unique "elephant effect" appeared at a height of 4 cm on the Gobi gravel bed. As the wind-sand flow on the leeward side of the forest belt was in a saturated transport state, the "trunk effect" disappeared.
5) Under the three test wind velocities, the sand control efficiency of the forest belt was approximately 90%, which can effectively alleviate the wind and sand hazards along the railway. The protection forest belt can play an important role in the prevention and control of wind and sand disasters along railways.

DATA AVAILABILITY STATEMENT

The original contributions presented in the study are included in the article/Supplementary Material, further inquiries can be directed to the corresponding author.

AUTHOR CONTRIBUTIONS

KZ, JQ, XZ, LZ, and SL contributed to conception and design of the study. KZ organized the database. XZ performed the statistical analysis. KZ wrote the first draft of the manuscript. JQ, XZ, LZ, and SL wrote sections of the manuscript. All authors contributed to manuscript revision, read, and approved the submitted version.

FUNDING

This research was financially supported by the fellowship of the China Postdoctoral Science Foundation (2021M703466), the Basic Research Innovation Group Project of Gansu Province, China (21JR7RA347), the Natural Science Foundation of Gansu Province, China (20JR10RA231).

REFERENCES

Amichev, B. Y., Bentham, M. J., Cerkowniak, D., Kort, J., Kulshreshtha, S., Laroque, C. P., et al. (2015). Mapping and Quantification of Planted Tree and Shrub Shelterbelts in Saskatchewan, Canada. *Agroforest Syst.* 89, 49–65. doi:10.1007/s10457-014-9741-2

Baniamerian, Z., and Mehdipour, R. (2019). A New Approach in Reducing Sand Deposition on Railway Tracks to Improve Transportation. *Aeolian Res.* 41, 100537. doi:10.1016/j.aeolia.2019.07.003

Bourdin, P., and Wilson, J. D. (2008). Windbreak Aerodynamics: Is Computational Fluid Dynamics Reliable? *Bound. Lay. Meteorol.* 126 (2), 181–208. doi:10.1007/s10546-007-9229-y

Chang, J. C., and Hanna, S. R. (2004). Air Quality Model Performance Evaluation. *Meteorol. Atmos. Phys.* 87 (1-3), 167–196. doi:10.1007/s00703-003-0070-7

Dong, Z. B., Luo, W. Y., Qian, G. Q., and Wang, H. T. (2007). A Wind Tunnel Simulation of the Mean Velocity Fields Behind Upright Porous Fences. *Agric. For. Meteorol.* 146 (1–2), 82–93. doi:10.1016/j.agrformet.2007.05.009

Dong, Z., Wang, H., Liu, X., and Wang, X. (2004). A Wind Tunnel Investigation of the Influences of Fetch Length on the Flux Profile of a Sand Cloud Blowing Over a Gravel Surface. *Earth Surf. Process. Landforms* 29, 1613–1626. doi:10.1002/esp.1116

Gillies, J. A., Etyemezian, V., Nikolich, G., Glick, R., Rowland, P., Pesce, T., et al. (2017). Effectiveness of an Array of Porous Fences to Reduce Sand Flux: Oceano Dunes, Oceano CA. *J. Wind Eng. Ind. Aerodyn.* 168, 247–259. doi:10.1016/j.jweia.2017.06.015

Huang, N., He, P., and Zhang, J. (2020). Large-Eddy Simulation of Sand Transport under Unsteady Wind. *Geomorphology* 358, 107105. doi:10.1016/j.geomorph.2020.107105

Judd, M. J., Raupach, M. R., and Finnigan, J. J. (1996). A Wind Tunnel Study of Turbulent Flow Around Single and Multiple Windbreaks, Part I: Velocity fields. *Bound. Lay. Meteorol.* 80 (1), 127–165. doi:10.1007/bf00119015

Lee, S.-J., Park, K.-C., and Park, C.-W. (2002). Wind Tunnel Observations about the Shelter Effect of Porous Fences on the Sand Particle Movements. *Atmos. Environ.* 36 (9), 1453–1463. doi:10.1016/s1352-2310(01)00578-7

Li, F.-R., Liu, J.-L., Sun, T.-S., Ma, L.-F., Liu, L.-L., and Yang, K. (2016). Impact of Established Shrub Shelterbelts Around Oases on the Diversity of Ground Beetles in Arid Ecosystems of Northwestern China. *Insect Conserv. Divers.* 9 (2), 135–148. doi:10.1111/icad.12152

Lin, X. G. (2020). Study on Windproofing Effect of Korshinskii Shrub with Different Distribution Patterns. Master Dissertation. Beijing, China: Beijing Forestry University.

Lv, P., Dong, Z. B., and Ma, X. M. (2016). Aeolian Sand Transport above Three Desert Surfaces in Northern China with Different Characteristics (Shifting Sand, Straw Checkerboard, and Gravel): Field Observations. *Environ. Earth Sci.* 75 (7), 577. doi:10.1007/s12665-016-5361-7

Ma, R., Li, J. R., Ma, Y. J., Shan, L. S., Li, X. L., and Wei, L. Y. (2019). A Wind Tunnel Study of the Airflow Field and Shelter Efficiency of Mixed Windbreaks. *Aeolian Res.* 41 (3), 80–88. doi:10.1016/j.aeolia.2019.100544

Mahgoub, A. O., and Ghani, S. (2021). Numerical and Experimental Investigation of Utilizing the Porous media Model for Windbreaks CFD Simulation. *Sustain. Cities Soc.* 65, 102648. doi:10.1016/j.scs.2020.102648

Qu, J. J., Huang, N., Tuo, W. Q., Lei, J. Q., Dong, Z. B., Liu, X. W., et al. (2005). Structural Characteristics of Gobi Sand-Drift and its Significance. *Adv. Earth Sci.* 20 (01), 19–23. doi:10.11867/j.issn.1001-8166.2005.01.0019

Rosenfeld, M., Marom, G., and Bitan, A. (2010). Numerical Simulation of the Airflow across Trees in a Windbreak. *Boun. Lay. Meteorol.* 135 (1), 89–107. doi:10.1007/s10546-009-9461-8

Santiago, J. L., Martín, F., Cuerva, A., Bezdenejnykh, N., and Sanz-Andrés, A. (2007). Experimental and Numerical Study of Wind Flow Behind Windbreaks. *Atmos. Environ.* 41 (30), 6406–6420. doi:10.1016/j.atmosenv.2007.01.014

Schwartz, R. C., Fryrear, D. W., Harris, B. L., Bilbro, J. D., and Juo, A. S. R. (1995). Mean Flow and Shear Stress Distributions as Influenced by Vegetative Windbreak Structure. *Agric. For. Meteorol.* 75 (1-3), 1–22. doi:10.1016/0168-1923(94)02206-y

Takahashi, S., Du, M., Wu, P., Maki, T., and Kawashima, S. (1998). Three Dimensional Numerical Simulation of the Flow over Complex Terrain with Windbreak Hedge. *Environ. Model. Softw.* 13 (3/4), 257–265. doi:10.1016/s1364-8152(98)00026-7

Tan, L., Zhang, W., Qu, J., Wang, J., An, Z., and Li, F. (2016). Aeolian Sediment Transport over Gobi: Field Studies Atop the Mogao Grottoes, China. *Aeolian Res.* 21, 53–60. doi:10.1016/j.aeolia.2016.03.002

Tuzet, A., and Wilson, J. D. (2007). Measured Winds about a Thick Hedge. *Agric. For. Meteorol.* 145 (3-4), 195–205. doi:10.1016/j.agrformet.2007.04.013

Ucar, T., and Hall, F. R. (2001). Windbreaks as a Pesticide Drift Mitigation Strategy: a Review. *Pest Manag. Sci.* 57 (8), 663–675. doi:10.1002/ps.341

Wang, H., and Takle, E. S. (1995). A Numerical Simulation of Boundary-Layer Flows Near forest Belts. *Bound. Lay. Meteorol.* 75 (1-2), 141–173. doi:10.1007/bf00721047

Wang, H., Takle, E. S., and Shen, J. M. (2003). Forest Belts and Windbreaks: Mathematical Modeling and Computer Simulations of Turbulent Flows. *Annu. Rev. Fluid Mech.* 33 (1), 549–586. doi:10.1146/annurev.fluid.33.1.549

Wang, T., Qu, J., Ling, Y., Liu, B., and Xiao, J. (2018). Shelter Effect Efficacy of Sand Fences: A Comparison of Systems in a Wind Tunnel. *Aeolian Res.* 30 (30), 32–40. doi:10.1016/j.aeolia.2017.11.004

Wang, T., Qu, J., Ling, Y., Xie, S., and Xiao, J. (2017). Wind Tunnel Test on the Effect of Metal Net Fences on Sand Flux in a Gobi Desert, China. *J. Arid Land* 9 (6), 888–899. doi:10.1007/s40333-017-0068-5

Wang, T., Qu, J., and Niu, Q. (2020). Comparative Study of the Shelter Efficacy of Straw Checkerboard Barriers and Rocky Checkerboard Barriers in a Wind Tunnel. *Aeolian Res.* 43, 100575. doi:10.1016/j.aeolia.2020.100575

White, B. R. (1996). Laboratory Simulation of Aeolian Sand Transport and Physical Modeling of Flow Around Dunes. *Ann. Arid Zone* 35 (3), 187–213.

Zhan, K., Liu, S., Yang, Z., Fang, E., Zhou, L., and Huang, N. (2017). Effects of Sand-Fixing and Windbreak Forests on Wind Flow: a Synthesis of Results from Field Experiments and Numerical Simulations. *J. Arid Land* 9, 1–12. doi:10.1007/s40333-016-0058-z

Zhang, K. C., Qu, J. J., Liao, K. T., Niu, Q. H., and Han, Q. J. (2010). Damage by Wind-Blown Sand and its Control along Qinghai-Tibet Railway in China. *Aeolian Res.* 1 (3), 143–146. doi:10.1016/j.aeolia.2009.10.001

Zhang, K., Zhao, P. W., Zhao, J. C., and Zhang, X. X. (2020). Protective Effect of Multi-Row HDPE Board Sand Fences: A Wind Tunnel Study. *Int. Soil Water Conservation Res.* 9 (2), 103–115. doi:10.1016/j.iswcr.2020.08.006

Zhang, W., Wang, T., Wang, W., and Liu, B. (2011). Wind Tunnel Experiments on Vertical Distribution of Wind-Blown Sand Flux and Change of the Quantity of Sand Erosion and Deposition above Gravel Beds under Different Sand Supplies. *Environ. Earth Sci.* 64 (4), 1031–1038. doi:10.1007/s12665-011-0921-3

Zhou, X. H., Brandle, J. R., Mize, C. W., and Takle, E. S. (2005). Three-Dimensional Aerodynamic Structure of a Tree Shelterbelt: Definition, Characterization and Working Models. *Agroforest Syst.* 63 (2), 133–147. doi:10.1007/s10457-004-3147-5

Conflict of Interest: The authors declare that the research was conducted in the absence of any commercial or financial relationships that could be construed as a potential conflict of interest.

frontiers | Frontiers in Environmental Science

ORIGINAL RESEARCH
published: 02 May 2022
doi: 10.3389/fenvs.2022.861063

Aerodynamic Properties and Shelter Effects of a Concrete Plate-Insert Sand Fence Along the Lanzhou-Xinjiang High-Speed Railway in Gobi Regions Under Strong Winds

Tao Wang[1,2,3], *Jianjun Qu*[1,2,3], *Qinghe Niu*[1,2,3]*, *Zhishan An*[1,2,3], *Yang Gao*[1,2,3], *Hongtao Wang*[1,2,3] *and Baicheng Niu*[4]

[1]Key Laboratory of Desert and Desertification, Northwest Institute of Eco-Environment and Resources, Chinese Academy of Sciences, Lanzhou, China, [2]Dunhuang Gobi and Desert Ecology and Environment Research Station, Northwest Institute of Eco-Environment and Resources, Chinese Academy of Sciences, Dunhuang, China, [3]Research Station of Gobi Desert Ecology and Environment in Dunhuang of Gansu Province, Dunhuang, China, [4]Academy of Plateau Science and Sustainability, Qinghai Normal University, Xining, China

OPEN ACCESS

Edited by:
Huawei Pi,
Henan University, China

Reviewed by:
Yaping Shen,
Southwest Jiaotong University, China
Andreas Baas,
King's College London, United Kingdom
Yongcheng Zhao,
Xinjiang Institute of Ecology and Geography (CAS), China

***Correspondence:**
Qinghe Niu
niuqh@lzb.ac.cn

Specialty section:
This article was submitted to Drylands, a section of the journal Frontiers in Environmental Science

Received: *24 January 2022*
Accepted: *07 April 2022*
Published: *02 May 2022*

Citation:
Wang T, Qu J, Niu Q, An Z, Gao Y, Wang H and Niu B (2022) Aerodynamic Properties and Shelter Effects of a Concrete Plate-Insert Sand Fence Along the Lanzhou-Xinjiang High-Speed Railway in Gobi Regions Under Strong Winds. Front. Environ. Sci. 10:861063. doi: 10.3389/fenvs.2022.861063

The Lanzhou-Xinjiang High-Speed Railway runs through high-wind areas in the Gobi Desert, and disasters arising from the effects of blown sand critically endanger the safety of railway operations. To prevent sand deposition on the rail bed, double rows of sand fences composed of concrete columns and plates are installed on the windward side of the railway line. However, the aerodynamic properties and sheltering effects of these fences remain unclear. In this study, the effects of sand fences on boundary wind patterns and sand transport were investigated in the field and in a wind tunnel. The following results were obtained: 1) The wind velocity was efficiently reduced on the leeward side of the first and second rows of fences by 78% and 87%, respectively. Nevertheless, owing to large openings in the fence, the sand-trapping efficiencies of the first and second rows of fences on the leeward sides were only 72 and 63%, respectively. 2) The effective shelter distance (D_s) of the fence is 10 times the height of the fence; however, the horizontal distance between the two rows of fences is much larger than the D_s of the fence. This allows the wind velocity between the fences to rise above the saltation threshold once again, thereby reducing the overall sheltering effects of the double-row of fences. This study will produce a theoretical reference for improving the design and installation of blown-sand control systems in the strong-wind regions of the Gobi.

Keywords: sand fence, wind-blown sand control, Gobi, strong winds, shelter effects

1 INTRODUCTION

The Lanzhou-Xinjiang High-Speed Railway is the first high-speed railway in China that runs through the high-wind areas of the Gobi, including the "Yandun," "Hundred Miles," "Thirty Miles," and "Dabancheng" windy areas, from east to west in Xinjiang. These areas have land surfaces characteristic of Gobi, where sand is commonly driven by strong winds, providing high kinetic energy to the transported sand particles (Tan et al., 2021; Jiang et al., 2010). The wind-blown sand seriously threatens the railway by, for example, deeply burying its tracks (**Figure 1A**), while the high-

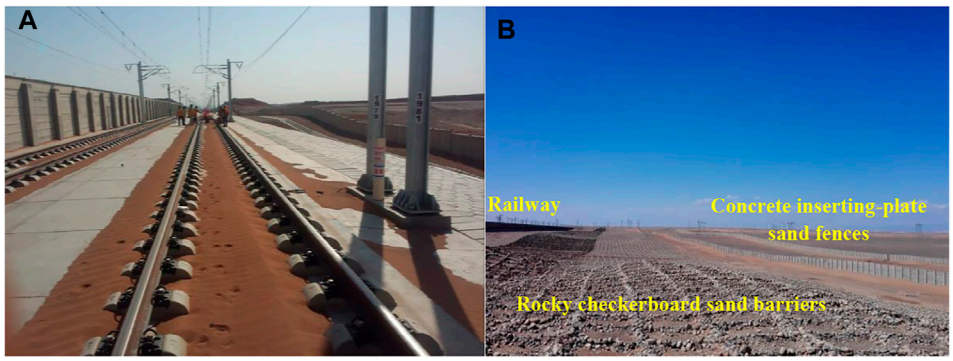

FIGURE 1 | (A) Sand deposition around the rail bed; **(B)** blown-sand control system built on the windward side of the railway (Wang et al., 2018).

energy saltating particles damage road and traffic equipment (Xiao et al., 2016). The threats from such wind-blown sand in these areas endanger the operational safety of the railway (Wang et al., 2017, 2022; Huang et al., 2019; Dun et al., 2021). To protect the tracks and road traffic equipment from damage and destruction by wind-blown sand, a mechanical system to protect against wind-blown sand was designed by the railway design department and built on the windward side of the railway (Wang et al., 2018, 2020). The most important part of this control system primarily comprises two rows of concrete pillar and plate wall sections that function as a sand fence (**Figure 1B**), hereafter referred to as the concrete plate-insert sand fence.

Sand fences are artificial structures used to control aeolian erosion and deposition and are one of the most important structures in aeolian engineering. Fences are constructed using materials including wood (Ling et al., 1984; Bofah and Al-Hinai, 1986), concrete (Zhang et al., 2010), nylon net (Wang et al., 2005), plastic (Zhang et al., 2021), metal (Wang et al., 2017, 2018), or vegetation (Dong et al., 2004), depending on the materials available in different areas. Common types of sand fence design-types include horizontal, upright, holed-plank, griddled, and wind-screened fences (Dong et al., 2007). The aerodynamic properties and sheltering effects of sand fences depend mainly on their geometric design and multiple design factors, including height, length, width, porosity, opening size/shape/distribution, and row numbers and the spacing between rows (Li and Sherman, 2015; Lima et al., 2020; Xin et al., 2021). The sheltering effect of multiple rows of sand fences is commonly considered to be more efficient than that of a single-row sand fence (Fang et al., 2018; Liu et al., 2018). Additionally, porosity, the ratio of a fence's open area to its total area, is the most important structural parameter for controlling the performance of a sand fence of any given height (Heisler and Dewalle, 1988; Cornelis and Gabriels, 2005; Mustafa et al., 2016). Porosity controls not only the wind velocity reduction efficiency and effective shelter distance of the sand fence but also determines sand trapping efficiency and the location of particle deposition. Considering the combination of both the boundary wind and sediment transport effects of sand fences, their optimum porosity ranges from 30 to 50% (Perera, 1981; Grant and Nickling, 1998; Boldes et al., 2001; Cornelis and Gabriels, 2005; Dong et al., 2006) and depends upon fence material and the size, shape, and distribution of openings (Li and Sherman, 2015). At constant porosity, increases in pore diameter increases the rate of penetration of wind and sand through a sand fence and also lowers wind reduction and sand trapping efficiencies of the fence (Savage, 1963; Manohar and Bruun, 1970). Hotta et al. (1987) suggested that the opening size of a sand fence should exceed 10 times the sand diameter. In addition, early studies indicated that sand fences with sharp edges (e.g., square holes, vertical slits, or horizontal slits) have higher sand-trapping efficiencies than those with round edges (e.g., circular holes) (Richards et al., 1984). Height is another important structural parameter of sand fences and is critical for determining sand trapping efficiency and the magnitude of dune deposition (Lima et al., 2020; Ning et al., 2020; Xin et al., 2021). To trap as many transported particles as possible, fence heights usually exceed the saltation height of the wind-blown sand (Phillips and Willetts, 1979). Studies of flow fields (van Eimern et al., 1964) and sand transport regimes (Hotta and Horikawa, 1990) have shown that the shelter zone and life span of a sand fence are proportional to its height. The impact of a sand fence on local wind regime and sand transport also depends on the environmental characteristics, including incoming flow conditions (velocity, turbulence, and direction), sedimentology, and topography (Li and Sherman, 2015). The environmental characteristics of Gobi are clearly different from desert (Pi et al., 2017a; 2017b), and aeolian sediment transport over the Gobi surface exhibits extremely different characteristics than that over sand surfaces. On the Gobi surface, an elastic collision occurs between saltating particles and gravel clasts, allowing higher energy saltating particles (Tan et al., 2021) to rebound to greater heights. The bouncing height of coarse particles over Gobi surfaces under extremely strong winds can surpass 2 m (Wang et al., 2022), far greater than that over a sand surface. Therefore, the materials and geometric design of sand fences in Gobi areas differs from that in desert areas. However, there are few theoretical studies on sand fences in Gobi regions, especially in Gobi regions experiencing extremely strong winds.

The concrete plate-insert sand fence is heavy and has a capacity for high wind-resistance. Consequently, it is widely used in the high-wind areas along the Lanzhou-Xinjiang High-Speed Railway. However, the material's properties and complex

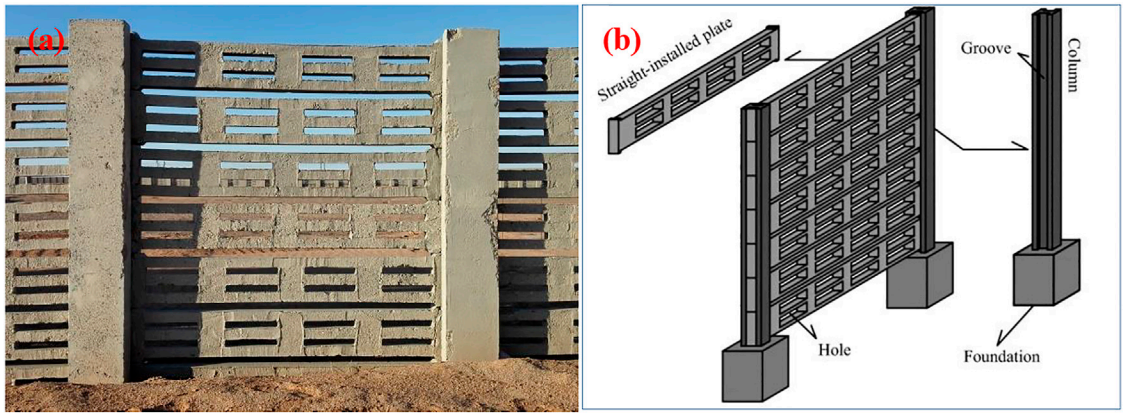

FIGURE 2 | (A) Concrete plate-insert sand fence and **(B)** schematic diagram of the fence structure (Shi et al., 2021).

construction process result in the sand fence having a large opening size and relatively low porosity (described in subsections below). Although damage to the railway by wind-blown sand has been reduced, aeolian sand particles still accumulate around the railroad. At present, the aerodynamic properties and shelter effects of the concrete plate-insert sand fence in the Gobi regions under strong winds remain unclear. In this study, the results of wind tunnel experiments were compared with field observations to investigate the wind velocity reduction efficiency, effective shelter distance, sand-trapping efficiency, and the volume of sand deposited around the sand fence. This analysis will highlight deficiencies of fence design and produce a theoretical reference for improving the design and installation of blown-sand control systems in the strong-wind regions of the Gobi.

2 MATERIALS AND METHODS

2.1 Geometric Design of the Concrete Plate-Insert Sand Fence

The height of the concrete plate-insert sand fence (CPISF) is 2 m. Each section is made of seven horizontal straight-installed plates (SIPs) (**Figures 2A,B**). The length, thickness, and height of the SIPs are 1.50, 0.05, and 0.25 m, respectively. There are eight rectangular holes uniformly distributed across each SIP, with each hole being 0.25 × 0.05 m in size. The porosity of the SIPs is 25%; however, as there are gaps between the SIPs after it is assembled as a fence, the overall porosity of the CPISF is increased to 30%. In each wall section, six gaps exist between the seven SIPs, with each gap being 1.50 × 0.05 m in size. The row spacing between the double-row CPISFs placed at the forefront of the wind-blown sand protection systems along the Lanzhou-Xinjiang High-Speed Railway is 74 m (equivalent to 37 H, where H is the fence height).

2.2 Wind Tunnel Experiments

Experiments were conducted in a wind tunnel at the State Key Laboratory of the Desertification and Aeolian Sand Disaster Combating, Gansu Desert Control Research Institute. The non-circulating blow-type wind tunnel has a total length of 38.9 m and consists of air inflow, power, stabilization, shrink, test, adjustable, and diffusion sections. The test section is 16 m long and has a cross-sectional area of 1.2 × 1.2 m. The expected wind speed in the wind tunnel ranges from 4 to 35 m s^{-1}, and the boundary layer in the test section has a maximum thickness of 0.5 m (Wang et al., 2018).

To simulate the CPISF more realistically, we used the SIPs (**Figure 3A**) as the models in our wind tunnel experiments. Two groups of models were tested: 1) a single row of SIPs and 2) a double row of SIPs with a row spacing of 9.25 m (37 H). To simulate the Gobi surface, gravels sampled from the field were spread out on the floor of the tunnel test section. Free-stream wind velocities (U) of 10, 15, 20, and 25 m s^{-1} were selected for the measurements of wind velocity profiles in this study. The wind profiles were measured using an array of pitot-static tubes at nine heights, from 1 to 40 cm, above the wind tunnel floor; the pitot-static tubes array was moved throughout the profile along the direction of inflow, and 27 measurement points were selected around the sand fences (**Figures 3B,C**). For each point where wind velocity was measured, the duration of wind data acquisition was 30.0 s, with a data acquisition interval of 0.5 s. The wind data were time-averaged and interpolated via bilinear interpolation to reconstruct the flow field around the sand fences using Origin 9.6 drawing software. The relative wind velocity (u/u_0) at each measurement point is the ratio of the wind velocity u to the reference velocity u_0, which is the inlet velocity at the corresponding height. The following equation represents the wind velocity reduction efficiency (R_w) around the sand fences:

$$R_w = \left(1 - \frac{u}{u_0}\right) \times 100\% \quad (1)$$

2.3 Field Observations

We observed the wind profiles, sand transport profiles, and shapes of the sand deposition on the windward and leeward

FIGURE 3 | (A) Horizontally aligned straight-installed plates used in the wind tunnel; **(B)** wind velocity profiles measured using pitot-static tubes; and **(C)** the positions of wind velocity measurement points.

sides of the double rows of CPISFs in the "Yandun" windy area, along the Lanzhou-Xinjiang High-Speed Railway.

The wind profiles were measured using 3-D ultrasonic anemometers (Wind Master Pro, Gill Instruments) at height, z = 1.0, 1.5, and 3.0 m above the Gobi surface. The ultrasonic anemometer array was moved throughout the profile perpendicular to the sand fences, and around the sand fences, 28 measurement points, x = −40, −30, −20, −10, −6, −4, −2, −1, 1, 2, 4, 6, 10, 20, 30, 40, 53, 63, 67, 69, 71, 72, 74, 76, 78, 80, 84, and 94 m, were selected (**Figure 4A**). Because of the placement requirements of the ultrasonic anemometer and the principle of velocity measurement, all ultrasonic anemometers were aligned in the direction of magnetic north. Therefore, the positive direction of the horizontal velocity (u) is due north, the positive direction of the vertical velocity (w) is vertically upwards, and the positive direction of the transverse velocity (v) is due west. For each measurement point, the duration of wind data acquisition was 5 min, with an acquisition interval of 1 s. A 3-D ultrasonic anemometer, installed at a height of 1 m, was used to establish a reference point at 60 m (30 H), windward of the first sand fence row. The wind velocity profiles around the sand fences were measured from 11:00 to 17:50 on 11 November 2016. The 10-min average wind velocity at a height of 2 m during the observation period varied from 9.32 to 12.15 m s^{-1}, with a mean of 10.66 m s^{-1}. The wind direction during the whole measurement period was relatively steady, and the 10-min average angles ranged from 59.33° to 76.48°, with a mean of 67.43° (ENE winds). Post-processing of data acquired from the ultrasonic anemometer conducted as described by Walker (2005). The higher acquisition frequency of 3-D ultrasonic anemometer allows the analysis of airflow turbulence, and hence, we calculated the turbulence intensity (Tu) using the following formula (Bennett and Best, 1995; Venditti and Bauer, 2005):

$$u_i' = \bar{u} - u_i \tag{2}$$

$$T_u = \frac{\left[\frac{1}{n}\sum_{i=1}^{n} u_i'^2\right]^{0.5}}{\bar{u}} = \frac{\left[\frac{1}{n}\sum_{i=1}^{n} (\bar{u} - u_i)^2\right]^{0.5}}{\bar{u}} \tag{3}$$

where u_i' is the horizontal fluctuating wind velocity, u_i is the horizontal instantaneous wind velocity, and $\bar{u}$ is the average horizontal wind velocity during the observation period.

Sand transport profiles were measured using three vertically segmented sand samplers. The height and width of the sand samplers were 2.8 m and 0.03 m, respectively, with segments at 5 cm and 10 cm intervals in the lower 1.3 m and upper 1.5 m of the samplers, respectively. The first sand sampler was located 60 m (30 H) windward of the first sand fence row (**Figure 4B**) and was used to measure the quantity of sand transported over the gravel surface without sand fences. The second and third sand samplers were located

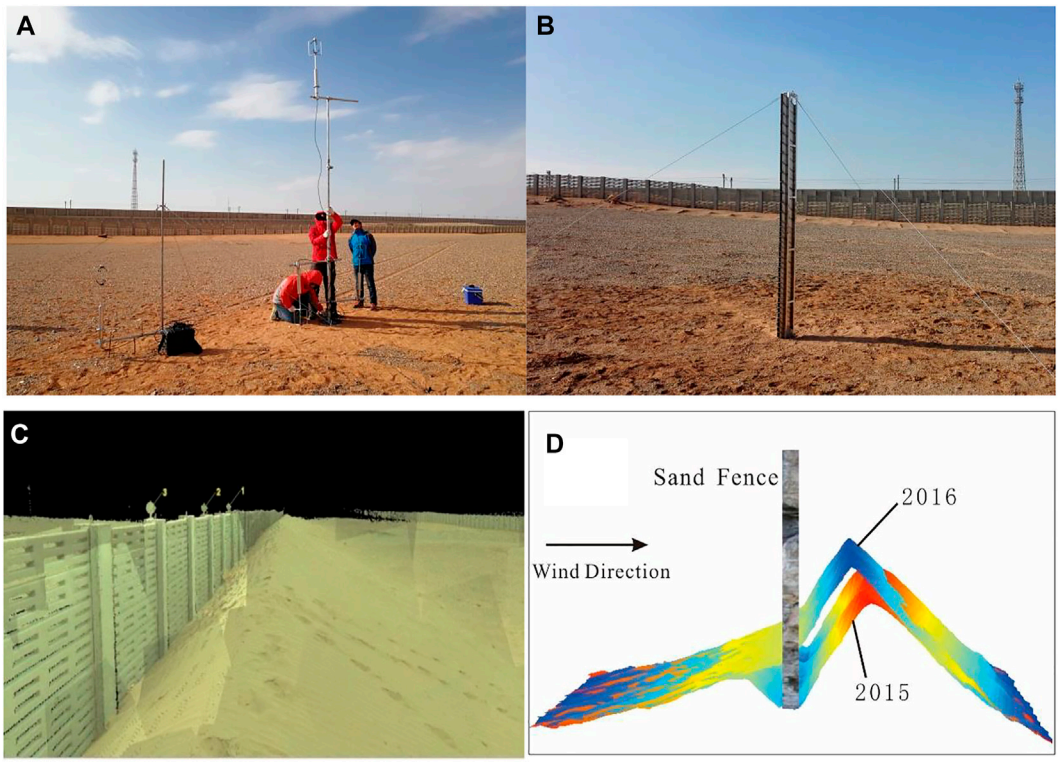

FIGURE 4 | (A) 3-D ultrasonic anemometers used to measure the wind profiles around the sand fences; **(B)** the sand sampler located windward of the first sand fence row; **(C)** scanning image of the deposited sand dune, as captured by a 3-D laser scanner; and **(D)** DEM model of the dunes deposited, depicted in ArcGIS software.

TABLE 1 | Basic information for the six sandstorms that occurred during the observation period (January to March 2016) to collect sand transport data (the wind data was obtained from a meteorological station (Gill MaxiMet GMX600), located approximately 1 km northeast of the observation site; both wind velocity and direction were measured at a height of 2.0 m).

Period (2016)	Duration	Average wind velocity (m s^{-1})	Peak gust wind velocity (m s^{-1})	Wind direction
08:30 1.03–05:40 1.04	21 h 40 min	12.66	21.17	ENE
22:20 1.23–18:40 1.24	20 h 20 min	10.42	17.66	ENE
03:50 1.25–22:20 1.25	18 h 30 min	9.13	15.17	ENE
23:20 1.26–01:10 1.29	50 h 50 min	11.99	24.54	ENE
07:30 2.18–16:30 2.18	09 h 00 min	9.66	15.34	ENE
09:10 3.14–13:50 3.16	53 h 40 min	12.90	26.53	ENE

20 m (10 H) leeward of the first and second rows of sand fences and were used to measure the quantity of sand transported over the gravel surface after interaction with the sand fences. All sand samplers were situated perpendicular to the prevailing wind direction. The sand transport profiles were measured from January to March 2016. During the observation period, there were six intense sandstorms, and the duration of each sandstorm exceeded 18 h (**Table 1**). Profiles of the rate of sand transport (Q) on the windward and leeward sides of the fences were obtained by converting the masses of sand collected at each sampling height of the sand samplers into rates (kg m^{-1}). The sand trapping efficiency (T_s) of the sand fences can be represented by the following equation:

$$T_s = \left(1 - \frac{Q_{tl}}{Q_{tw}}\right) \times 100\,\% \tag{4}$$

where Q_{tl} and Q_{tw} are the total rates of sand transport on the leeward and windward sides of the fences, respectively.

A 3-D laser scanner (Leica Scan Station C10; detailed information on this device is described in An et al., 2018) was used to obtain point-cloud data of the shapes of sand deposits on both sides of the sand fences (**Figure 4C**). Multistation scanning was performed at the surveyed sites. Sphere targets were used to

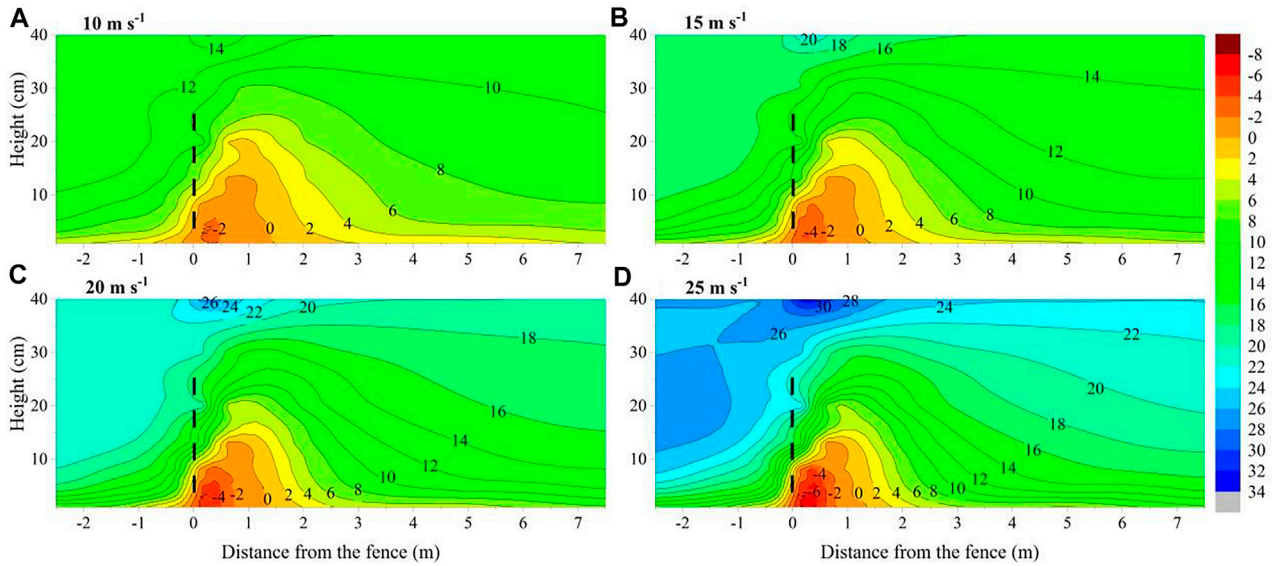

FIGURE 5 | Velocity contours (m s^{-1}) in the vicinity of the single-row straight-installed plate (SIP) under different free-stream wind velocities. The negative wind velocities represent recirculated airflow, and the dashed line shows the position of sand fences.

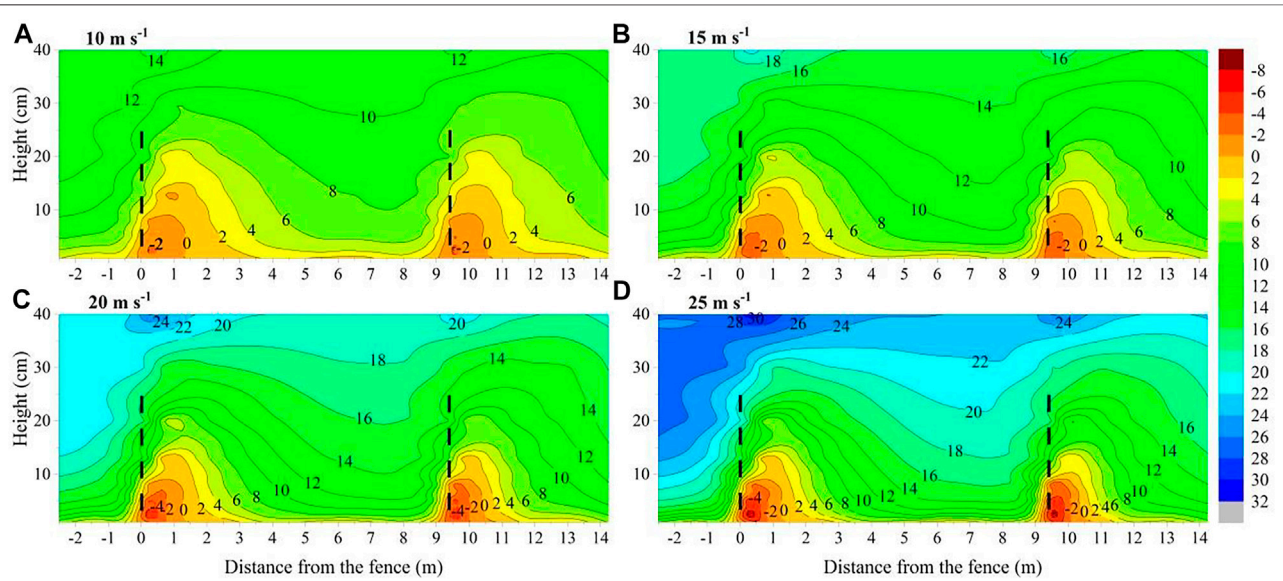

FIGURE 6 | Velocity contours (m s^{-1}) in the vicinity of the double-row straight-installed plates (SIPs) under different free-stream wind velocities. The negative wind velocities represent recirculated airflow, and the dash line shows the position of sand fences.

join and mosaic the overlapping data from multiple stations, with four sphere targets set between every two stations, limiting alignment errors to no more than 6 mm. Cyclone software was used to splice the data from different sites and eliminate the interference from point cloud data. ArcGIS software was used to establish TIN and DEM models (**Figure 4D**), and accurate data for the dynamic deposition of sand were obtained. Field operations were carried out on 15 September 2015 and 14 September 2016.

3 RESULTS

3.1 Wind Tunnel Experiments

3.1.1 Airflow Field

On the windward side of the single-row SIP fence, wind velocity decreased gradually as it approached the fence, with a deceleration zone emerging at x = −1.25–0 m (−5–0 H); the deceleration zone contained a small eddy field at x = −0.25–0 m (−1–0 H) (**Figure 5**). When airflow approached the

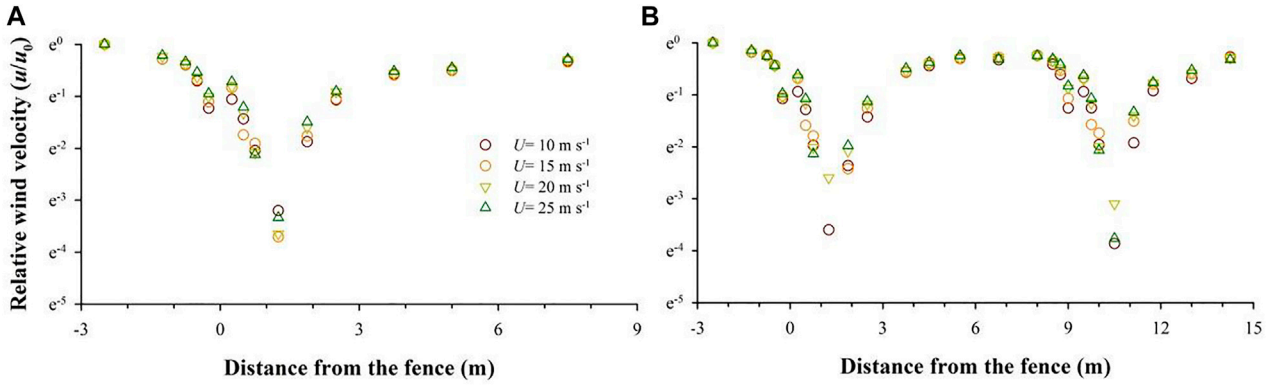

FIGURE 7 | Relative wind velocity versus distance for the **(A)** single-row straight-installed plate (SIP) and **(B)** double-row SIPs at a height of 13 cm (0.52 *H*) under different free-stream wind velocities.

fence, the blocking effect of the fence resulted in an upward vertical velocity component, and thus, an acceleration zone emerged over the top of the fence. On the leeward side of the fence, a main deceleration zone emerged below the height of the fence, located at x = 0–2.5 m (0–10 *H*). The main deceleration zone contained a larger eddy field at x = 0–1.25 m (0–5 *H*), which was 0.13 m (0.52 *H*) high. Behind the main deceleration zone (x = 2.5–7.5 m, i.e., 10–30 *H*), the upward acceleration flow reattached to the ground, and airflow velocity gradually recovered; this zone can be referred to as the restoration zone.

For double-row SIPs (**Figure 6**), airflow patterns around the first sand fence were similar to those around the single fence. For the second sand fence, wind velocity did not fully recover to the incoming wind velocity when it was first approaching the fence; hence, the eddy field leeward of the second fence was slightly smaller than that leeward of the first fence. In addition, under different free-stream wind velocities, the airflow patterns were similar around both the single- and double-row SIPs.

3.1.2 Wind Velocity Reduction and Effective Shelter Distance

Patterns in the variations in wind velocity at different heights corresponding to various distances from the fences were similar. **Figure 7** illustrates relative wind velocity, u/u_0, in the vicinity of the single- and double-row SIPs at a height of 13 cm (0.52 *H*), under different free-stream wind velocities. Variations in wind velocity at various distances from each sand fence decreased slightly on the windward side and considerably on the leeward side. The minimum velocity was close to the fence but gradually recovered as distance from the fence increased. The reduction and recovery trends were similar for different free-stream wind velocities.

For the single-row SIP (**Figure 7A**), the minimum u/u_0 appeared at x = 1.25 m (5 *H*). The average u/u_0 was 0.09, and the velocity recovered to 0.75 u_0 at x = 7.5 m (30 *H*). For the double-rows SIPs (**Figure 7B**), the minimum u/u_0 appeared at x = 1.25 m (5 *H* leeward of the first-row fence) and 10.50 m (5 *H* leeward of the second-row fence), with average u/u_0 being 0.09 and 0.11, respectively. Velocity recovered to 0.75u_0 at x = 8.0 m (32 *H* leeward of the first sand fence row) and 0.70 u_0 at x = 14.25 m (20 *H* leeward of the second sand fence row). According to **Eq. 1**, the maximum R_w on the leeward side of the single-row and double-row SIPs were 91 and 89%, respectively.

The effective shelter distance (D_s) of the sand fence is the distance within which wind velocity is reduced below the threshold wind velocity (u_t) (Dong et al., 2006), which, at a height of 13 cm over the artificial gravel surface, was 6.54 m s^{-1} in our wind tunnel experiment. The corresponding u_t/u_0 at a height of 13 cm under free-stream wind velocities of 10, 15, 20, and 25 m s^{-1} were 0.53, 0.39, 0.31, and 0.25, respectively. According to the u/u_0 at a height of 13 cm in the vicinity of the single-row SIP (**Figure 7A**), wind velocity leeward of the fence recovered to the threshold values at x = 3.75, 2.5, 1.875, and 1.875 m (15, 10, 7.5 and 7.5 *H*), under free-stream wind velocities of 10, 15, 20, and 25 m s^{-1}, respectively, with a mean of x = 2.5 m (10 *H*). Thus, the average D_s of the SIP was 10 *H*.

3.2 Field Observations

3.2.1 Variations in Airflow

Figure 8 shows variations in airflow at different heights around the CPISFs measured in the field. Patterns in the variations in wind velocity at various distances from each sand fence were similar to those tested in the wind tunnel (**Figure 8A**). The horizontal wind velocity (u) was on average reduced to 0.22 u_{ref} at x = 10 m (5 *H* leeward of the first fence), which then recovered to 0.50 u_{ref} at x = 67 m (33.5 *H* leeward of the first sand fence row). However, it was again reduced to 0.13 u_{ref} at x = 84 m (5 *H* downwind of the second sand fence row). This indicates that the maximum R_w on the leeward side of the first and second CPISF rows were 78 and 87%, respectively. The vertical wind velocity (w) accelerated considerably as the airflow approached the fence, and its upward vertical velocity increased to approximately 10 w_{ref} between the heights of 1.0 and 1.5 m and 20 w_{ref} at the height of 3.0 m at x = 1 m (0.5 *H* windward of the first fence) (**Figure 8B**). The horizontal wind direction changed to gradually become parallel to the sand fences as the wind approached the fences (on the windward sides), which indicates the occurrence of a transversal displacement flow (**Figure 8C**). Turbulence was

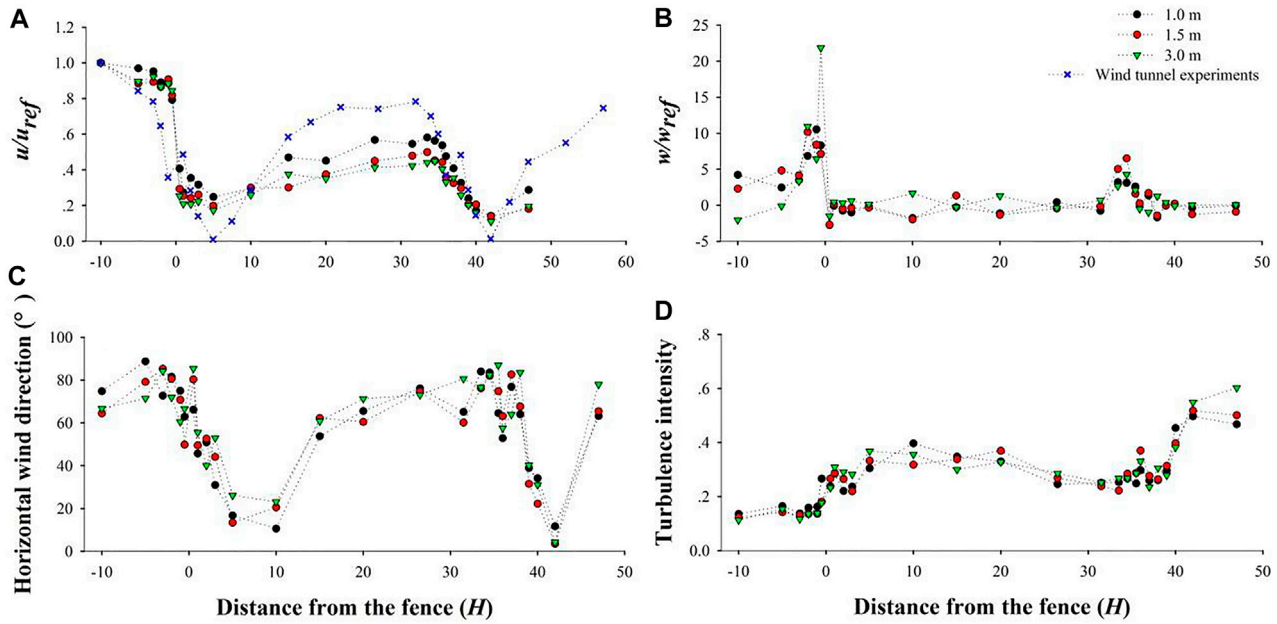

FIGURE 8 | Variations in **(A)** horizontal wind velocity, **(B)** vertical wind velocity, **(C)** horizontal wind direction, and **(D)** turbulence intensity at different heights around the concrete plate-insert sand fences (CPISFs), as measured in the field.

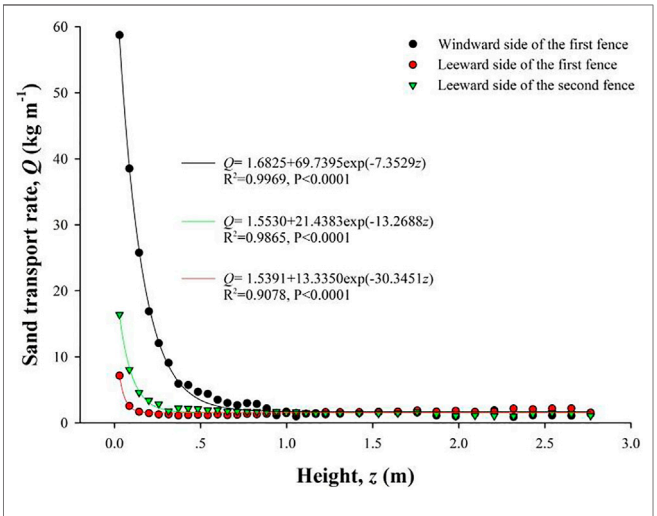

FIGURE 9 | Sand transport rate profiles upwind and downwind of the concrete plate-insert sand fences (CPISFs) during the observation period.

greatly intensified by the fences, with an average value of 0.13 when there was no fence and increased to 0.35 and 0.52 on the leeward sides of the first and second fences, respectively (**Figure 8D**).

3.2.2 Sand-Trapping Efficiency

Figure 9 shows the profiles of the rate of sand transport (Q) upwind and downwind of the CPISFs during the observation period. The profiles all obey an exponential decay function. Below the height of the sand fences, Q downwind of the sand fences was lower than that over the Gobi surface without a sand fence, whereas above the height of the sand fences, it was slightly larger than that over the Gobi surface without a sand fence. In general, Q was substantially lower downwind of sand fences. However, it was interesting that Q downwind of the first CPISF was less than that downwind of the second CPISF. According to **Eq. 4**, the T_s on the leeward side of the first and second CPISF were 72.43 and 62.97%, respectively.

3.2.3 Morphologies of Sand Depositions

Figure 10 shows the morphologies of the sand deposited on the windward and leeward sides of the first and second CPISF in 2015 and 2016; it was clear that dunes developed on both sides of the two fences. On the windward side of the first fence, sand deposition began at $x = -8$ m ($-4\ H$), the dune crest was located at $x = -2$ m ($-1\ H$), and the height of the crest was 0.7 m (0.35 H). However, on the leeward side of the first fence, sand was deposited at x = 0–7 m (0–3.5 H), the dune crest was located at x = 2 m (1 H), and the height of the crest was 1.3 m (0.65 H) in 2015, increasing to 1.5 m (0.75 H) in 2016. On windward side of the second fence, sand deposition began at $x = -6$ m ($-3\ H$), the dune crest was located at x = 0.5 m (0.25 H), and the height of the crest was 0.6 m (0.3 H). On the leeward side of the second fence, sand deposition began at x = 0–7 m (0–3.5 H), the dune crest was located at x = 1.5 m (0.75 H), and the height of the crest was 1.0 m (0.5 H). From 2015 to 2016, the incremental sand deposition volumes on the windward and leeward sides of the first and second CPISFs were 0.17 and 1.00 $m^3\ m^{-1}$ and 0.11 and 0.08 $m^3\ m^{-1}$, respectively (**Table 2**).

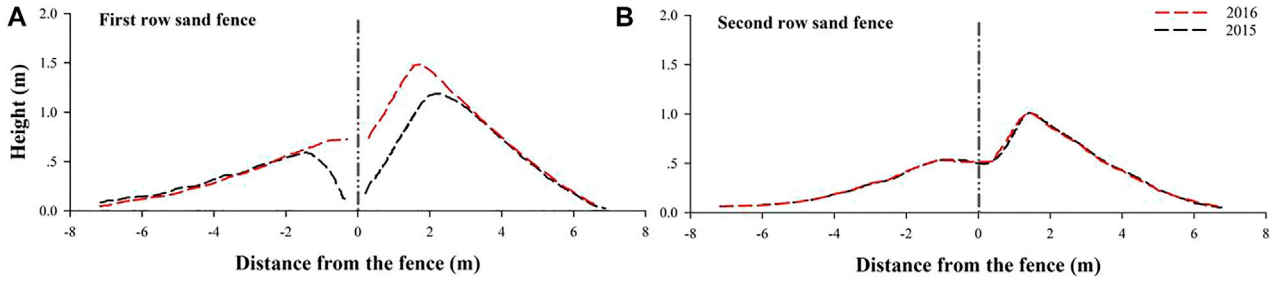

FIGURE 10 | Morphology of the deposited sand on the windward and leeward sides of the **(A)** first and **(B)** second concrete plate-insert sand fences (CPISFs) in 2015 and 2016. The red and black dashed lines show the dune shapes in 2016 and 2015, respectively.

TABLE 2 | Volume of deposited sand on the windward and leeward sides of the first and second concrete plate-insert sand fences (CPISFs) in 2015 and 2016.

Locations	Sand deposition in 2015 (volume per width, m^3 m–1)	Sand deposition in 2016 (volume per width, m^3 m–1)	Difference in sand depositions between 2016 and 2015 (m^3 m–1)
Winward of the first fence	6.46	6.63	0.17
Leeward of the first fence	8.74	9.74	1.00
Winward of the second fence	3.25	3.36	0.11
Leeward of the second fence	5.89	5.97	0.08

4 DISCUSSION

4.1 Airflow Field and Wind Shelter Effects

The airflow field in the vicinity of a sand fence determines the sand transport and deposition regime around the fence (Li and Sherman, 2015). A deceleration zone containing a small eddy field appeared in the windward airflow around the SIPs of the sand fence, while an acceleration zone emerged over the top of the fence. Additionally, a main deceleration zone with a larger eddy field appeared leeward of the fence, and a restoration zone was present behind the main deceleration zone. This was consistent with the airflow regimes identified near sand fences in previous studies (Dyunin, 1964; Plate, 1971; Judd et al., 1996; Dong et al., 2007). In theory, transported sand is deposited in deceleration zones. Our field measurements demonstrated that sand was indeed deposited in the windward and leeward deceleration zones of the double-row CPISFs and that sand dunes developed on both sides of the fences, indicating that the fences sufficiently reduced wind velocity. Eddy fields only appeared when the porosity of the sand fence was lower than 40% (Gloyne, 1954; Lee and Kim, 1999). Eddy fields appeared on both the windward and leeward sides of the SIP, which indicates that the fence induced a strong disturbance in the airflow field and that turbulence around the fence was intensified (Lee and Lee, 2012). The field observations demonstrated that turbulence was greatly intensified by the presence of the CPISFs and increased 2.7 and 4.0 times on the leeward sides of the first and second rows of the sand fence, respectively. Owing to the intense blocking effect of the low-porosity SIP, a vertical displacement flowfield was present, which formed an acceleration zone over the top of the fence. This is consistent with field observations that the upward vertical velocity increased to approximately 20 w_{ref} over the top of the CPISF. In addition, the direction of horizontal wind gradually became parallel to the sand fences as the wind approached the CPISFs, which indicates that a transverse displacement flow also appeared windward of the fences (Huang et al., 2013).

Traditionally, the wind-shelter effects of sand fences have been evaluated based on the wind velocity reduction efficiency (R_w) and effective shelter distance (D_s). The results of 3D-CFD simulations have indicated that maximum R_w decreases with increasing fence porosity (Fang et al., 2018). Our wind tunnel experiments demonstrated a limit in the maximum R_w of individual SIPs of 91%, but when they were assembled as a CPISF in the field, their maximum R_w was reduced to 78%, owing to the higher porosity of the sand fences in the final assembly. The optimal spacing between multiple rows of sand fences is determined by the D_s of the fence (Dong et al., 2006; Liu et al., 2018). Previous studies suggested that the peak value of D_s occurs with a fence porosity of 30–40%, and the optimal spacing of double-row sand fences with 30–40% porosity is approximately 5–7 H (Boldes et al., 2001; Wu et al., 2013; Fang et al., 2018). Our wind tunnel experiments demonstrated that the D_s of the SIP decreased as free-stream wind velocities increased, with an average value of 10 H. However, the spacing between the double-row CPISFs of the system installed as protection against wind-blown sand along the Lanzhou-Xinjiang High-Speed Railway is 37 H, which is much larger than the D_s of the sand fence. Consequently, the

distance between the first and second sand fence is wide enough for the wind velocity to recover to velocities above the saltation threshold velocity. The impact of the first sand fence on the second sand fence is dissipated, and the two fences function independently.

4.2 Sand-Trapping Efficiency and Dune Growth

In field observations, T_s values on the leeward side of the first and second CPISF fences were 72.43 and 62.97%, respectively. These observations raise two questions. First, why was the T_s on the leeward side of the second CPISF fence lower than that of the first? On the one hand, sand dunes developed in front of and behind the fences provided ramps for sand to blow over each fence. Furthermore, as discussed above, the spacing between the two fences is much larger than the D_s of the sand fence, allowing the wind velocity between the two fences to recover above the saltation threshold velocity. Thus, sand on the ground surface between the two fences becomes entrained by the wind and transported downwind. Because of these two effects, the rate of sand transport downwind of the second fence exceeded that downwind of the first fence. Second, why was the R_w of the CPISF high but its T_s low? Most previous studies indicate that the maximum T_s of a sand fence is obtained with a porosity of 40–50% (Manohar and Bruun, 1970; Bofah and Al-Hinai, 1986; Zhang et al., 2004), and fences that are spaced too closely will change the wind direction, causing relatively low T_s (Savage and Woodhouse, 1968). In the current study, wind velocities were adequately reduced because of the low porosities of the CPISF; however, the large size of the openings in the fences allowed more sand particles to be transported through them and reduced the T_s of the fences (Savage, 1963; Savage and Woodhouse, 1968; Manohar and Bruun, 1970; Lee and kim 1999).

Wind tunnel experiments by Hotta and Horikawa (1990) demonstrated that sand is deposited on both sides of a sand fence when its porosity exceeds 10% and that dune deposition leeward of the fence occurs more intensely than that on the windward side. In addition, sand fences with 40% porosity trap larger volumes of sand, and lower porosity sand fences are more easily buried by dunes. Our field measurements showed that dunes developed on both sides of the double-row CPISFs and that the leeward dunes were larger than the windward dunes. The leeward dunes at the first and second fences grew to 75 and 50% of the fence height in 2016, respectively, and dune deposition continued at rapid rates each year. The growth of the sand dunes around the CPISFs is expected to decrease the sand trapping efficiencies of the sand fences (Ning et al., 2020), and they may gradually lose their sand-blocking capacity once the deposited dunes grow to 80% of the height of the fence (Hotta and Horikawa, 1990).

5 CONCLUSION

We studied the aerodynamic properties and shelter effects of a CPISF along the Lanzhou-Xinjiang High-Speed Railway in Gobi regions under strong winds, using wind tunnel experiments and field observations. The main conclusions are as follows:

1) Deceleration zones appeared on the windward and leeward sides of the sand fence, and sand was deposited in corresponding deceleration zones. Eddy fields also appeared on the windward and leeward sides of the fence owing to the relative low fence porosity.
2) The R_w of the sand fence was high, and the maximum R_w values on the leeward side of the first and second fences were 78 and 87%, respectively. However, because of the large size of the openings in the sand fence, the T_s of the sand fence was low, that is, only 72 and 63% on the leeward side of the first and second fences, respectively.
3) The D_s of the sand fence was 10 H. However, the row spacing between the two sand fences constructed in the field is much larger than the D_s of the fence, which allows the wind velocity between the double-row sand fences to recover to velocities above the saltation threshold velocity. Thus, the overall shelter effects of the double-row sand fences were significantly diminished.

DATA AVAILABILITY STATEMENT

The raw data supporting the conclusion of this article will be made available by the authors, without undue reservation.

AUTHOR CONTRIBUTIONS

TW: conceptualization, investigation, data curation, writing–original draft preparation. JQ: supervision, project administration, funding acquisition. QN: methodology, investigation, writing–reviewing and editing. ZA: formal analysis. YG: formal analysis. HW: investigation. BN: investigation.

FUNDING

This work was financially supported by the National Natural Science Foundation of China (41730644 and 41901011), the Open Fund of State Key Laboratory Breeding Base of Desertification and Aeolian Sand Disaster Combating (GSDC201903), the Natural Science Foundation of Gansu Province, China (20JR10RA231), and the fellowship of China Postdoctoral Science Foundation (2021M703466).

REFERENCES

An, Z.-s., Zhang, K.-c., Tan, L.-h., Zhang, H., and Niu, B.-c. (2018). Dune Dynamics in the Southern Edge of Dunhuang Oasis and Implications for the Oasis protection. *J. Mt. Sci.* 15 (10), 2172–2181. doi:10.1007/s11629-017-4723-2

Bennett, S. J., and Best, J. L. (1995). Mean Flow and Turbulence Structure over Fixed, Two-Dimensional Dunes: Implications for Sediment Transport and Bedform Stability. *Sedimentology* 42, 491–513. doi:10.1111/j.1365-3091.1995.tb00386.x

Bofah, K. K., and Al-Hinai, K. G. (1986). Field Tests of Porous Fences in the Regime of Sand-Laden Wind. *J. Wind Eng. Ind. Aerodynamics* 23, 309–319. doi:10.1016/0167-6105(86)90051-6

Boldes, U., Colman, J., and Marañon Di Leo, J. (2001). Field Study of the Flow behind Single and Double Row Herbaceous Windbreaks. *J. Wind Eng. Ind. Aerodynamics* 89, 665–687. doi:10.1016/s0167-6105(01)00065-4

Cornelis, W. M., and Gabriels, D. (2005). Optimal Windbreak Design for Wind-Erosion Control. *J. Arid Environments* 61 (2), 315–332. doi:10.1016/j.jaridenv.2004.10.005

Dong, Z. B., Luo, W. Y., Qian, G. Q., and Wang, H. T. (2007). A Wind Tunnel Simulation of the Mean Velocity fields behind Upright Porous Fences. *Agric. For. Meteorology* 146 (1-2), 82–93. doi:10.1016/j.agrformet.2007.05.009

Dong, Z., Chen, G., He, X., Han, Z., and Wang, X. (2004). Controlling Blown Sand along the Highway Crossing the Taklimakan Desert. *J. Arid Environments* 57 (3), 329–344. doi:10.1016/j.jaridenv.2002.02.001

Dong, Z., Qian, G., Luo, W., and Wang, H. (2006). Threshold Velocity for Wind Erosion: the Effects of Porous Fences. *Environ. Geol.* 51 (3), 471–475. doi:10.1007/s00254-006-0343-9

Dun, H., Xin, G., Huang, N., Shi, G., and Zhang, J. (2021). Wind-Tunnel Studies on Sand Sedimentation Around Wind-Break Walls of Lanxin High-Speed Railway II and its Prevention. *Appl. Sci.* 11, 5989. doi:10.3390/app11135989

Dyunin, A. K. (1964). *The Analytic Determination of the Surface Wind Velocity behind Open Snow Fences*. Washington, DC: US Department of Commerce.

Fang, H., Wu, X., Zou, X., and Yang, X. (2018). An Integrated Simulation-Assessment Study for Optimizing Wind Barrier Design. *Agric. For. Meteorology* 263, 198–206. doi:10.1016/j.agrformet.2018.08.018

Gloyne, R. W. (1954). Some Effects of Shelterbelts upon Local and Micro Climate. *Forestry* 27 (2), 85–95. doi:10.1093/forestry/27.2.85

Grant, P. F., and Nickling, W. G. (1998). Direct Field Measurement of Wind Drag on Vegetation for Application to Windbreak Design and Modelling. *Land Degrad. Dev.* 9, 57–66. doi:10.1002/(sici)1099-145x(199801/02)9:1<57::aid-ldr288>3.0.co;2-7

Heisler, G. M., and Dewalle, D. R. (1988). 2. Effects of Windbreak Structure on Wind Flow. *Agric. Ecosyst. Environ.* 22-23, 41–69. doi:10.1016/0167-8809(88)90007-2

Hotta, S., and Horikawa, K. (1990). "Function of Sand Fence Placed in Front of Embankment," in Proceedings of the 22nd Conference on Coastal Engineering, July 2–6, 1990 (Delft, Netherlands: AMCE) 1 (9), 2754–2767. doi:10.9753/icce.v22.%25p

Hotta, S., Kraus, N. C., and Horikawa, K. (1987). Function of Sand Fences in Controlling Wind-Blown Sand. *Coastal Sediments* 87, 772–787.

Huang, N., Gong, K., Xu, B., Zhao, J., Dun, H., He, W., et al. (2019). Investigations into the Law of Sand Particle Accumulation over Railway Subgrade with Wind-Break wall. *Eur. Phys. J. E* 42, 145. doi:10.1140/epje/i2019-11910-0

Huang, N., Xia, X., and Tong, D. (2013). Numerical Simulation of Wind Sand Movement in Straw Checkerboard Barriers. *Eur. Phys. J. E* 36, 99. doi:10.1140/epje/i2013-13099-6

Jiang, F. Q., Li, Y., Li, K. C., Cheng, J. J., Xue, C. X., and Ge, S. C. (2010). Study on Structural Characteristics of Gobi Wind Sand Flow in 100 Km Wind Area Along Lan-Xin Railway. *J. China Railway Soc.* 32 (3), 105–110. doi:10.3969/j.issn.1001-8360.2010.03.019

Judd, M. J., Raupach, M. R., and Finnigan, J. J. (1996). A Wind Tunnel Study of Turbulent Flow Around Single and Multiple Windbreaks, Part I: Velocity fields. *Boundary-Layer Meteorology* 80 (1-2), 127–165. doi:10.1007/bf00119015

Lee, J. P., and Lee, S. J. (2012). PIV Analysis on the Shelter Effect of a Bank of Real Fir Trees. *J. Wind Eng. Ind. Aerodynamics* 110 (11), 40–49. doi:10.1016/j.jweia.2012.07.003

Lee, S.-J., and Kim, H.-B. (1999). Laboratory Measurements of Velocity and Turbulence Field behind Porous Fences. *J. Wind Eng. Ind. Aerodynamics* 80 (3), 311–326. doi:10.1016/s0167-6105(98)00193-7

Li, B., and Sherman, D. J. (2015). Aerodynamics and Morphodynamics of Sand Fences: A Review. *Aeolian Res.* 17, 33–48. doi:10.1016/j.aeolia.2014.11.005

Lima, I. A., Parteli, E. J. R., Shao, Y., Andrade, J. S., Herrmann, H. J., and Araújo, A. D. (2020). CFD Simulation of the Wind Field over a Terrain with Sand Fences: Critical Spacing for the Wind Shear Velocity. *Aeolian Res.* 43, 100574. doi:10.1016/j.aeolia.2020.100574

Ling, Y. Q., Jin, J., Zou, B. G., Cong, Z. L., and Wen, X. L. (1984). Effect of Fence Techniques in Leveling Sand Accumulation Around Sand-Breaks--Case Study in Shapotou District. *J. Desert Res.* 4 (3), 16–25.

Liu, C., Zheng, Z., Cheng, H., and Zou, X. (2018). Airflow Around Single and Multiple Plants. *Agric. For. Meteorology* 252, 27–38. doi:10.1016/j.agrformet.2018.01.009

Manohar, M., and Bruun, P. (1970). Mechanics of Dune Growth by Sand Fences. *Dock and Harbour Authority* 51, 243–252.

Mustafa, M., Xu, Y., Haritos, G., and Kenji, K. (2016). Measurement of Wind Flow Behavior at the Leeward Side of Porous Fences Using Ultrasonic Anemometer Device. *Energ. Proced.* 85, 350–357. doi:10.1016/j.egypro.2015.12.261

Ning, Q., Li, B., and Ellis, J. T. (2020). Fence Height Control on Sand Trapping. *Aeolian Res.* 46, 100617. doi:10.1016/j.aeolia.2020.100617

Perera, M. D. A. E. S. (1981). Shelter behind Two-Dimensional Solid and Porous Fences. *J. Wind Eng. Ind. Aerodynamics* 8, 93–104. doi:10.1016/0167-6105(81)90010-6

Phillips, C. J., and Willetts, B. B. (1979). Predicting Sand Deposition at Porous Fences. *J. Wtrwy., Port, Coast., Oc. Div.* 105, 15–31. doi:10.1061/jwpcdx.0000129

Pi, H., Sharratt, B., and Lei, J. (2017b). Atmospheric Dust Events in central Asia: Relationship to Wind, Soil Type, and Land Use. *J. Geophys. Res. Atmos.* 122, 6652–6671. doi:10.1002/2016jd026314

Pi, H., Sharratt, B., and Lei, J. (2017a). Windblown Sediment Transport and Loss in a Desert-Oasis Ecotone in the Tarim Basin. *Sci. Rep.* 7, 7723. doi:10.1038/s41598-017-04971-4

Plate, E. J. (1971). The Aerodynamics of Shelter Belts. *Agric. Meteorology* 8, 203–222. doi:10.1016/0002-1571(71)90109-9

Richards, P. J., Kay, E. F., Russell, D., and Wilson, G. R. C. (1984). *Porous Artificial Windbreaks in Oblique Winds*. Hastings: Paper 67/84 for Institute of Professional Engineers of New Zealand (IPENZ) Conference 10, 1–10.

Savage, R. P. (1963). *Experimental Study of Dune Building with Sand Fences*. Mexcio City: Proceedings of 8th Conference on Coastal Engineering, 380–396.

Savage, R. P., and Woodhouse, W. W. (1968). "Creation and Stabilization of Coastal Barrier Dunes," in Proceedings of 11th Conference on Coastal Engineering, September, 1968 (London, United Kingdom: US Coastal Engineering Research Center) 1 (11), 617–685. doi:10.9753/icce.v11.43

Shi, L., Wang, D., Cui, K., and Xue, C. (2021). Comparative Evaluation of concrete Sand-Control Fences Used for Railway protection in strong Wind Areas. *Rail. Eng. Sci.* 29 (2), 183–198. doi:10.1007/s40534-020-00228-5

Tan, L. H., Qu, J. J., Wang, T., Zhang, K., and An, Z. S. (2021). Field Observation Evidence for Kink Points in the Vertical Kinetic Energy Flux Profiles of Wind-Blown Sand over Gobi and its Significance. *Geophys. Res. Lett.* 48, e2020GL091224. doi:10.1029/2020gl091224

van Eimern, J., Karschon, R., Razumova, L. A., and Robertson, G. W. (1964). *Windbreaks and Shelterbelts*. Technical Note No. 59. World Meteorological Organization, 188.

Venditti, J. G., and Bauer, B. O. (2005). Turbulent Flow over a Dune: Green River, Colorado. *Earth Surf. Process. Landforms* 30, 289–304. doi:10.1002/esp.1142

Walker, I. J. (2005). Physical and Logistical Considerations of Using Ultrasonic Anemometers in Aeolian Sediment Transport Research. *Geomorphology* 68, 57–76. doi:10.1016/j.geomorph.2004.09.031

Wang, T., Qu, J., Ling, Y., Liu, B., and Xiao, J. (2018). Shelter Effect Efficacy of Sand Fences: A Comparison of Systems in a Wind Tunnel. *Aeolian Res.* 30, 32–40. doi:10.1016/j.aeolia.2017.11.004

Wang, T., Qu, J., Ling, Y., Xie, S., and Xiao, J. (2017). Wind Tunnel Test on the Effect of Metal Net Fences on Sand Flux in a Gobi Desert, China. *J. Arid Land* 9 (6), 888–899. doi:10.1007/s40333-017-0068-5

Wang, T., Qu, J., and Niu, Q. (2020). Comparative Study of the Shelter Efficacy of Straw Checkerboard Barriers and Rocky Checkerboard Barriers in a Wind Tunnel. *Aeolian Res.* 43, 100575. doi:10.1016/j.aeolia.2020.100575

Wang, T., Qu, J., Tan, L., Gao, Y., Zhang, K., and Shi, B. (2022). Aeolian Sediment Transport over the Gobi with High Gravel Coverage under Extremely strong Winds in the Hundred Miles Windy Area along the Lanzhou-Xinjiang High-Speed Railway. *J. Wind Eng. Ind. Aerodynamics* 220, 104857. doi:10.1016/j.jweia.2021.104857

Wang, W. F., Wang, T., Fan, J. S., Zhang, W. M., Qu, J. J., Agnew, N., et al. (2005). Effect of Nylon Net Fence on Preventing Blown Sand at Top of Mogao Grottoes, Dunhuang. *J. Desert Res.* 25 (5), 640–648.

Wu, X., Zou, X., Zhang, C., Wang, R., Zhao, J., and Zhang, J. (2013). The Effect of Wind Barriers on Airflow in a Wind Tunnel. *J. Arid Environments* 97, 73–83. doi:10.1016/j.jaridenv.2013.05.003

Xiao, J. H., Yao, Z. Y., Qu, J. J., and Jiang, F. Q. (2016). Characteristics and Formation Mechanism of Extreme Wind in Hundred-Li Wind Zone along Lanxin Railway. *China Railway Sci.* 37 (3), 130–136. doi:10.3969/j.issn.1001-4632.2016.03.19

Xin, G., Huang, N., Zhang, J., and Dun, H. (2021). Investigations into the Design of Sand Control Fence for Gobi Buildings. *Aeolian Res.* 49, 100662. doi:10.1016/j.aeolia.2020.100662

Zhang, K. C., Qu, J. J., Liao, K. T., Niu, Q. H., and Han, Q. J. (2010). Damage by Wind-Blown Sand and its Control along Qinghai-Tibet Railway in China. *Aeolian Res.* 1 (3), 143–146. doi:10.1016/j.aeolia.2009.10.001

Zhang, K. C., Zu, R. P., and Fang, H. Y. (2004). Simulation on Abrated Effect of Nylon Net With Different Porosities on Wind-Blown Sand in Wind Tunnel. *J. Soil Water Conservation* 18 (4), 4–7. doi:10.13870/j.cnki.stbcxb.2004.04.002

Zhang, K., Zhao, P., Zhao, J., and Zhang, X. (2021). Protective Effect of Multi-Row HDPE Board Sand Fences: A Wind Tunnel Study. *Int. Soil Water Conservation Res.* 9, 103–115. doi:10.1016/j.iswcr.2020.08.006

Conflict of Interest: The authors declare that the research was conducted in the absence of any commercial or financial relationships that could be construed as a potential conflict of interest.

Publisher's Note: All claims expressed in this article are solely those of the authors and do not necessarily represent those of their affiliated organizations or those of the publisher, the editors, and the reviewers. Any product that may be evaluated in this article, or claim that may be made by its manufacturer, is not guaranteed or endorsed by the publisher.

frontiers | Frontiers in Environmental Science

TYPE Original Research
PUBLISHED 08 August 2022
DOI 10.3389/fenvs.2022.930519

OPEN ACCESS

EDITED BY
Huawei Pi,
Henan University, China

REVIEWED BY
Zhenhong Wang,
Guizhou University, China
Jinman Wang,
China University of Geosciences, China

*CORRESPONDENCE
Jian Wang,
304406378@qq.com

SPECIALTY SECTION
This article was submitted to Drylands, a section of the journal Frontiers in Environmental Science

RECEIVED 28 April 2022
ACCEPTED 11 July 2022
PUBLISHED 08 August 2022

CITATION
Tian X, Yin R, Wang J, Dong L, Cheng B, Liu H and Ge N (2022), Microtopographic reconstruction improves soil erosion resistance and vegetation characteristics on the slopes of large dump sites in semi-arid areas. *Front. Environ. Sci.* 10:930519. doi: 10.3389/fenvs.2022.930519

Microtopographic reconstruction improves soil erosion resistance and vegetation characteristics on the slopes of large dump sites in semi-arid areas

Xiumin Tian[1,2], Ruiping Yin[1,2], Jian Wang[1,2]*, Lei Dong[1,2], Bo Cheng[1,2], Hu Liu[1,2] and Nan Ge[1,2]

[1]Yinshanbeilu Grassland Eco-Hydrology National Observation and Research Station, China Institute of Water Resources and Hydropower Research, Beijing, China, [2]Soil and Water Conservation Laboratory, Ministry of Water Resources, Research Institute of Pastoral Water Resources Science, Hohhot, China

In view of the management of slopes in large mine dumps in semi-arid regions, this study explored different methods for controlling soil erosion and improving the microenvironment of the surface of such slopes. Focusing on microtopography modifications and vegetation measures on the slopes of a large mine dump in a semi-arid region, the soil erosion resistance of the slope was continuously monitored using installed observation plots. In addition, the characteristics of plant communities that thrived on the dump were investigated. The results indicate that the soil erosion resistance, soil organic matter content, and biodiversity increased to different degrees in the large mine dump that experienced microtopography modifications and implemented vegetation measures compared with those of slopes managed only by soil cover and planting. Compared with that in the control plot, under the same vegetation restoration measures, the macroaggregate content in the four plots that implemented microtopography modifications increased by 20%, 24%, 21%, and 30%; the soil erodibility (K-factor) decreased by 7.8%, 8.5%, 10%, and 10.7%; and the soil organic matter increased by 2%, 4.5%, 3.4%, and 4.7%. Microtopography modification consisting of U-shaped blocking boards and fixed rods embedded in the slope, combined with vegetation measures, resulted in a protective effect, which in turn induced the highest diversity, evenness, and richness index values of 2.35, 0.87, and 1.94, respectively. The study results revealed that a combination of microtopography modifications and vegetation measures can be used to achieve effective vegetation restoration, prevent soil erosion, and create different microhabitats, indicating that our approach is an effective way to control critical issues affecting large mine dumps in semi-arid regions.

KEYWORDS

semi-arid region, mine dump, microtopography modification, soil erosion, species diversity

1 Introduction

Mine dumps are a necessary by-product of surface mining (Monjezi et al., 2009; Franco-Sepúlveda et al., 2019; Shi et al., 2021), and the operation and management of such dumps have a profound impact on soil erosion, surface vegetation, and landscapes (Chen et al., 2019; Blake et al., 2018; Esmali Ouri and Kateb 2020). Owing to an increasing emphasis on ecological conservation in China, the number of studies on soil erosion control and vegetation restoration techniques associated with mine dumps has increased. Previous studies have shown that the biodiversity of mine dumps depends on vegetation restoration efforts (Feng et al., 2019; Tang et al., 2022). Suitable vegetation restoration techniques improve the nutrient contents and activity in the surface soil of mine dumps (Yuan et al., 2018; Raghunathan et al., 2021). Furthermore, soil aggregates are the basic structural units of soil. They are closely related to soil erosion, and their size and stability significantly affect soil erodibility. Thus, they are an important factor for evaluating the soil erosion resistance environment (Nie et al., 2018; De Laurentiis et al., 2019). Composition and stability of soil aggregates are the main indicators of soil structure and quality (Hao Wang et al., 2018; Lehmann et al., 2020). The formation of surface soil aggregates and improvement of erosion resistance of mine dumps also require appropriate vegetation restoration (Guo et al., 2020; Ke et al., 2021; Ma et al., 2022).

Large mine dump slopes represent soil erosion and vegetation restoration sites between platforms (flat sections (steps) and step slopes), whereby soil erosion and vegetation restoration have contrasting effects of intensification and suppression of soil erosion, respectively. Slopes are key areas of vegetation restoration and soil erosion control in large mine dumps, but vegetation restoration on the slopes of mine dumps is difficult to achieve using soil and vegetation cover alone. Furthermore, these slopes are important for the ecological conservation of mining areas, and it is important to overcome chronic soil and water conservation issues in large mine dumps.

To overcome these shortcomings in soil and water conservation in mine dumps, experts and scholars have carried out theoretical and practical analyses covering various topics, such as vegetation, engineering, and soil improvement measures to manage mining wastelands (Fischer et al., 2013; Chen et al., 2018; Luo et al., 2018). Previous studies have indicated that vegetation restoration and soil improvement measures can significantly control soil erosion in mining areas (Ouyang et al., 2018; Neuenkamp et al., 2019), but relying solely on the natural restoration of soil and vegetation through natural succession to shrubs and grasses requires 15–30 years, which can extend to more than 100 years in forest communities (Groninger et al., 2017; Mander et al., 2017; Chen et al., 2020). Poorly considered measures can increase the slope erosion more than that observed on bare land (Vinci et al., 2017; Guo et al., 2019). As a result, it is important to adopt appropriate measures and methods during the ecological restoration of large mine dumps. Some studies have shown that microtopography modifications affect rainfall infiltration, control soil erosion (Prosdocimi et al., 2017; Eltner et al., 2018; Zhang et al., 2018; Caviedes-Voullième et al., 2021), improve surface habitat, and promote water and soil conservation as well as vegetation restoration (Perreault et al., 2017; Yixia Wang et al., 2018; Wang et al., 2020; Mata-González et al., 2022). Following microtopography modifications, vegetation measures can significantly increase the content of nitrogen, phosphorus, potassium, and other organic matter in the damaged soil of mining areas, which further improves the physical and chemical properties of this soil, as well its erosion resistance (Orgiazzi and Panagos 2018; Zhao et al., 2018). To date, studies on the slope management of large mine dumps tended to focus on a single vegetation restoration model, and the selection of suitable vegetation species plays an important role in these studies. Only a few studies have analyzed the effects of microtopography modifications in conjunction with appropriate vegetation restoration on the regulation of soil erosion on the slopes of mine dumps in semi-arid areas.

Based on the shortcomings in slope management of large-scale mine dumps in semi-arid areas, in the present study, we analyzed the efficacy of microtopography modifications used in combination with appropriate vegetation measures and proposed viable soil and water conservation measures to control the chronic issues faced by large surface mine dumps in semi-arid areas. The results of the present study can be used to guide the ecological restoration of soil dumps and promote the sustainable exploitation of large surface mine dumps.

2 Materials and methods

2.1 Study area overview

Our study area was the southern mine dump of the East No. 2 Shengli Surface Coal Mine in the northeast city of Xilinhot in the Inner Mongolia Autonomous Region of China (44°3′29.68″–44°3′39.36″ N and 116°14′23.75″–116°14′36.03″ E; Figure 1). The soil and water conservation area is designated as the Xilinhot Plateau Soil Conservation Ecological Maintenance Area. The original terrain of the mine dump site was relatively flat, with an altitude range of 990–1,021 m. The relative height range of the mine dump was 100–120 m, with steps every 20 m. The dumping period was 10 years. The angle of slope repose was 33°. The steps had a longitudinal slope of 8°–10° and a transverse slope of 3°–5°. The test area was a slope containing bare patches. The average thickness of the surface layer of the slope was 20 cm. In terms of physical and chemical properties of the upper soil layer (0–20 cm), the bulk density

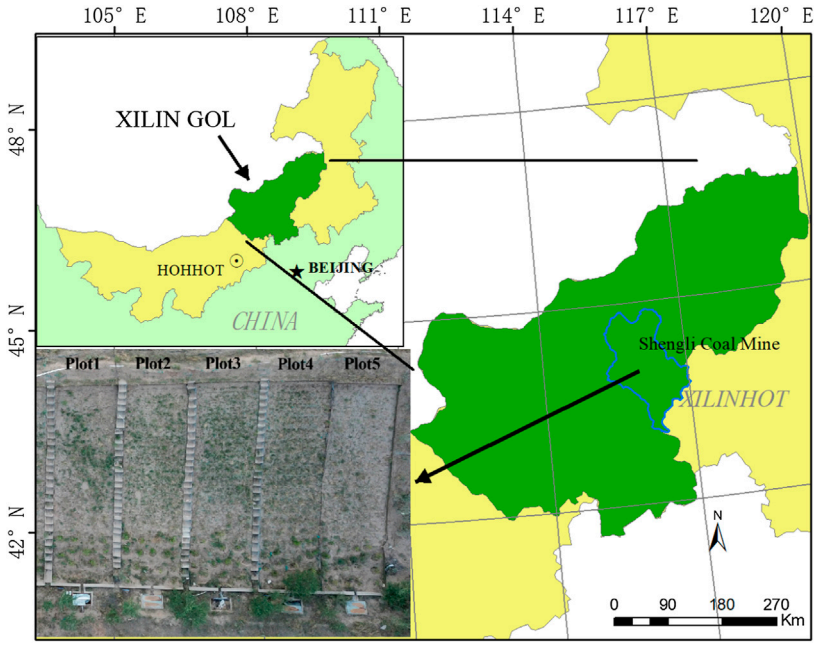

FIGURE 1
Location of the experimental site.

TABLE 1 Slope microtopography modifications in the five plots analyzed in the present study.

Runoff plot no.	Size (m × m)	Slope (°)	Microtopography modifications	Ground preparation
1	20 × 5	33	Straight blocking board	Cover with soil, hole sowing *Caragana korshinskii*, and spreading *Medicago sativa* and *Elymus dahuricus*
2	20 × 5	33	Straight blocking board + fixed rods	Cover with soil, hole sowing *Caragana korshinskii*, and spreading *Medicago sativa* and *Elymus dahuricus*
3	20 × 5	33	U-shaped blocking board	Cover with soil, hole sowing *Caragana korshinskii*, and spreading *Medicago sativa* and *Elymus dahuricus*
4	20 × 5	33	U-shaped blocking board + fixed rods	Cover with soil, hole sowing *Caragana korshinskii*, and spreading *Medicago sativa* and *Elymus dahuricus*
5 (control)	20 × 5	33	None	Cover with soil, and hole sowing *Caragana korshinskii*, and spreading *Medicago sativa* and *Elymus dahuricus*

The straight blocking board was wooden plywood, and the fixed rods were sand willow sticks (10 mm in diameter).

was 1.53 g cm^{-3}, soil particle size was mainly medium sand >0.25 mm, and soil quality was poor. Total nitrogen content in the 0–20-cm soil layer of the slope was 0.12 g kg^{-1}; available potassium content was 0.08 g kg^{-1}, available phosphorus content was 0.92 mg kg^{-1}, organic matter content was 2.0 g kg^{-1}, and pH was 8.47.

The study area was located in the hinterland of the Inner Mongolia Plateau, which is known to have a mid-temperate semi-arid climate. The mean annual precipitation was 289.2 mm, 69% of which occurred from June to August. The maximum 24 h rainfall was 85.3 mm in the past 10 years and 111.5 mm in the past 20 years. The mean annual evaporation was 1805.1 mm, which was six times higher than the mean annual precipitation. The annual dominant wind direction was southwest, mean annual wind speed was 3.5 m s^{-1}, and number of strong wind days (≥17 m/s) was 58. The zonal soil in the study area was sandy loam, and the non-zonal soil was chestnut soil. The vegetation type was typical grassland vegetation, with *Stipa krylovii* and *Leymus chinensis* as the main constructive species in the region. The vegetation coverage was 35–50%.

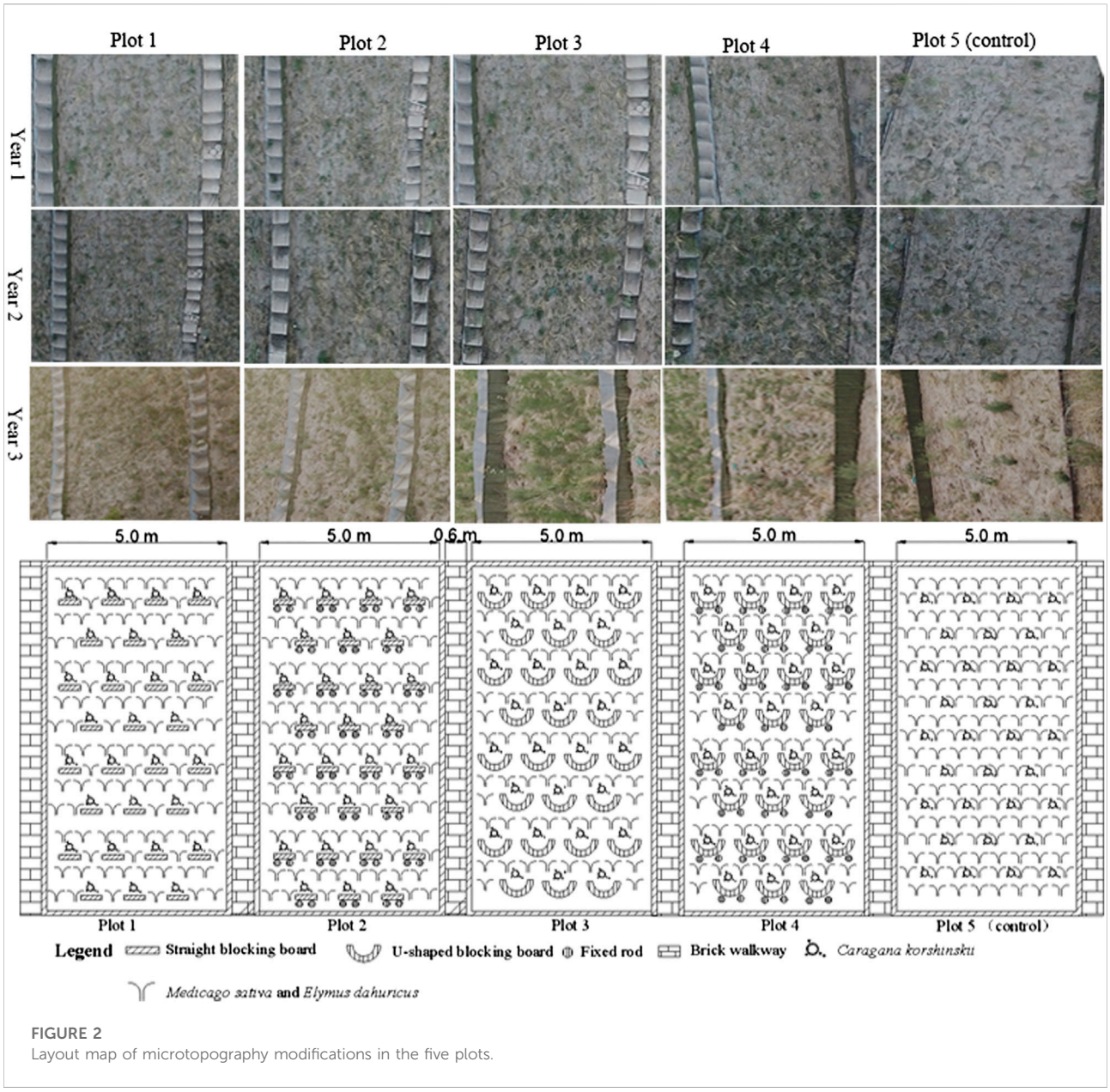

FIGURE 2
Layout map of microtopography modifications in the five plots.

2.2 Experiment installation

On the third step of the southern mine dump of the East No. 2 Shengli Surface Coal Mine, we chose the middle section, which had a uniform slope, to select five runoff plots. Plots 1, 2, 3, and 4 were microtopography modification plots, and Plot five was a control plot (see Table 1; Figure 2 for details). Each plot was laid out in sequence along the longitudinal direction of the slope, and 0.6 m wide brick walkways were created between the plots to allow observations and sampling. The size of each plot was 20 × 5 m.

The microtopography modification method of Plot one involved embedding straight blocking boards (plywood boards) on the slope surface, with blocking boards laid in a zigzag shape along the longitudinal direction of the plot. The straight blocking boards were 60 cm long, 60 cm wide, and 0.5 cm thick. The horizontal spacing of the straight blocking boards was 60 cm, and the vertical spacing was 120 cm. The blocking boards were inserted in pre-cut grooves perpendicular to the slope at a depth of 30 cm. After they were buried, we ensured that the edges of the blocking boards were levelled with the slope. The main function of the blocking boards was to reduce the downhill movement of surface soil so that plant seeds would be evenly distributed in the slope surface layer before the vegetation had an effect on soil and water conservation as

well as to avoid bare patches during the process of vegetation restoration. Once the blocking boards were in place, the open space of the plot was planted with *Caragana korshinskii* from top to bottom, with the inter-plant spacing of 120 cm and row spacing of 120 cm. The planting holes had a depth of 5 cm and radius of 5 cm, with a semi-circular cross section. The rest of the open space of the plots was scattered with a mix of *Medicago sativa* and *Elymus dahuricus* in a mixing ratio of 1:1.

The microtopography modification method of Plot two was to embed straight blocking boards and insert fixed rods in the slope. The layout positions and method of the blocking boards and the specifications were the same as those in Plot 1. The fixed rods were sand willow sticks, with a diameter of 10 mm and length of 35 cm. They were wedged into the slope along the back of the blocking boards so that their tops were flush with the edge of the boards. Once the blocking boards and rods were installed, the plot was levelled.

The microtopography modification method applied in Plot three consisted of U-shaped blocking boards (also plywood boards) arranged in a zigzag shape across the entire plot. The U-shaped blocking boards were 60 cm in length, 60 cm in width, and 0.5 cm in thickness. The layout and method of installing the U-shaped blocking boards were the same as those in Plot 1. After the blocking boards were installed, the plot was levelled.

The microtopography modification method of Plot 4 consisted of embedding U-shaped blocking boards and fixed rods in the slope. The layout positions and method of the blocking boards and the specifications were the same as those in Plot 1. The blocking board specifications were the same as those in Plot 3. The material, length, and installation method of the fixed rods were the same as those in Plot 2. Once the blocking boards and the rods were installed, the plot was levelled.

Plot 5 was the control plot. No microtopography modifications were applied to the plot, and only shrubs and grasses were planted after the topsoil was restored, which is the most common restoration method used in mine dumps. The thickness of the soil cover and the method of planting shrubs and grasses were the same as those in Plot 1. The implementation of the methods in all five plots was completed on 16 May 2019. Notably, the vegetation selection and planting methods for all the plots were the same.

2.3 Data processing

2.3.1 Soil sample collection and analysis

In this study, only the surface layer (0–20 cm) of the mine dump, which was covered with surface soil, was sampled. Below 20 cm, the lithology consisted of a mixture of clay, shale, and coal gangue; therefore, no sampling was carried out below this depth. Soil sampling were taken at the end of the plant growth season (mid to late September) in the period between 2019 and 2021. In each plot, nine soil samples of the 0–20-cm soil were randomly collected (i.e., three samples from the upper, middle, and lower parts of the slope, respectively) using a soil drill. In each plot, the samples collected from the upper, middle, and lower parts were mixed respectively and analyzed in a laboratory. The undisturbed soil was segregated into portions with diameters of 5 cm based on their structure. Plants, fine roots, stones, and other debris were removed, and the samples were placed in a ventilated place to dry naturally. After being air-dried, the soil samples from each plot were mixed, sieved, and stored in Ziplock bags for indoor analysis.

The dry sieving method was used to sort the soil according to the particle size, so that the contents of soil aggregates could be measured at all levels. One air-dried soil sample (240 g) was dry sieved, and the weight of soil aggregates in the particle sizes of 0.5, 0.1–0.25, 0.05–0.1, and <0.05-mm was measured to calculate the weight proportions for each soil aggregate particle grade. Another air-dried soil sample (50 g) were wet sieved and analyzed using an aggregate analysis meter. The water-stable aggregate content of the 0.25–0.5, 0.1–0.25, 0.05–0.1, and <0.05-mm grades were measured. After drying in an oven at a constant temperature of 4°C, the samples were weighed to calculate the percentage of water-stable aggregates in the soil for each grade.

The air-dried soil samples were sieved through a 2 mm sieve, and the samples were ground before being sieved again. The content of soil organic matter was determined using the potassium dichromate-volumetric method (external heating method).

2.3.2 Calculation methods for soil erosion resistance index

The specific formulas for calculating the mean weight diameter (MWD; mm) of soil aggregates (calculated using wet sieve aggregate size) and soil erodibility K-factor (in the case of limited soil physical and chemical properties, only the geometric mean soil particle size was considered) (van Bavel 1950; Shirazi et al., 1988) were as follows:

$$\mathrm{MWD} = \sum_{i}^{n} x_i w_i \Big/ \sum_{i}^{n} w_i \tag{1}$$

$$\mathrm{GMD} = \exp\left[\left(\sum_{i}^{n} w_i \ln x_i\right) \Big/ \sum_{i}^{n} w_i\right] \tag{2}$$

$$K = 7.954 \times \left\{0.0017 + 0.0494 \times \exp\left[-0.5 \times \left(\frac{\log\mathrm{GMD} + 1.675}{0.6986}\right)^2\right]\right\} \tag{3}$$

where x_i is the diameter of the aggregate at each particle grade level (mm), w_i is the percentage of aggregate mass, and GMD is the geometric mean diameter of the soil aggregate.

2.3.3 Plant community survey

In mid-August 2021, three quadrats (1 × 1 m) were randomly selected from the upper, middle, and lower parts of the five plots, and the individual plant height and density were measured; additionally, the cover of each plant species in each quadrat was

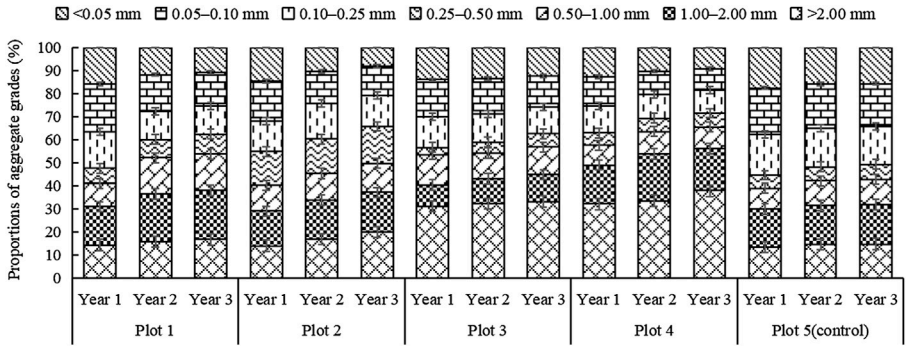

FIGURE 3
Changes in the soil aggregate grain sizes in the plots corresponding to different microtopography modifications.

measured, and the plant species present in the quadrats were recorded (Zhang 2007).

Species diversity was analyzed using three indices: Shannon–Wiener index of diversity, Pielou's evenness index, and Margalef's richness index. The calculation formulas for the indexes are given below (Clobert et al., 2018):

$$\text{Shannon} - \text{Wiener index of diversity}\,(H'):\ H' = -\sum P_i \ln P_i \tag{4}$$

$$\text{Pielou evenness index}\,(J):\ J = \frac{H'}{\ln S} \tag{5}$$

$$\text{Margalef's richness index}\,(R):\ R = \frac{S-1}{\ln N} \tag{6}$$

where P_i is the relative importance value, that is, $P_i = N/N_i$; N_i is the importance value of species i; N is the sum of importance values of species in the surveyed quadrat; and S is the number of species in the surveyed quadrat.

The calculation method of importance value (I) was calculated using the following equation:

$$I = R_C + R_F + R_D \tag{7}$$

where R_C is the relative cover, R_F is the relative frequency, and R_D is the relative density.

We analyzed the data using SPSS Statistics V22.0 (IBM. Corp., Armonk, NY, United States) and plotted the data using Microsoft Excel 2016 (Microsoft Corp., Redmond, WA, United States).

3 Results and analysis

3.1 Effects of microtopography modification on soil aggregate structure

As shown in Figure 3, in Plots 3 and 4, after 3 years of vegetation restoration, the content of aggregates larger than 2.0 mm constituted 30–40% of the soil, whereas that of aggregates larger than 2.0 mm in the other plots constituted only 15–20% of the soil. The microtopography modification method, consisting of U-shaped blocking boards and fixed rods (Plot 4), resulted in different degrees of increase in macroaggregates after vegetation restoration.

As shown in Figure 3, the trends for the content aggregates larger than 0.25 mm in plot 1 to plot 4 were basically similar, increasing year by year in each plot; however, there was no obvious trend for aggregates of grade 0–0.25 mm. Following microtopography reconstruction on the slope surface of the mine dump site and the implementation of similar vegetation measures, the order of the plots, from large to small, in terms of the content of aggregates larger than 0.25 mm was: Plot 4 > Plot 3 > Plot 2 > Plot 1 > Plot 5 (control) in the first year; Plot 4 > Plot 2 > Plot 1 > Plot 3 > Plot 5 (control) in the second year; and Plot 4 > Plot 2 > Plot 3 > Plot 1 > Plot 5 (control) in the third year. The analysis revealed that during the same vegetation restoration periods, the plots with microtopography modifications had higher contents of aggregates larger than 0.25 mm than those of the control plot (Plot 5).

3.2 Effects of microtopography modifications on the MWD of soil aggregates

As shown in Figure 4A, the MWDs of the plots with microtopography modifications as well as that of the control plot increased more slowly with increasing vegetation restoration. During the same vegetation restoration periods, the soil MWDs of the plots managed by microtopography modifications were greater than that of Plot 5. This indicated that even though we adopted the same vegetation restoration measures, microtopography modifications were more effective in gradually increasing the amounts of soil aggregates. Under the same vegetation

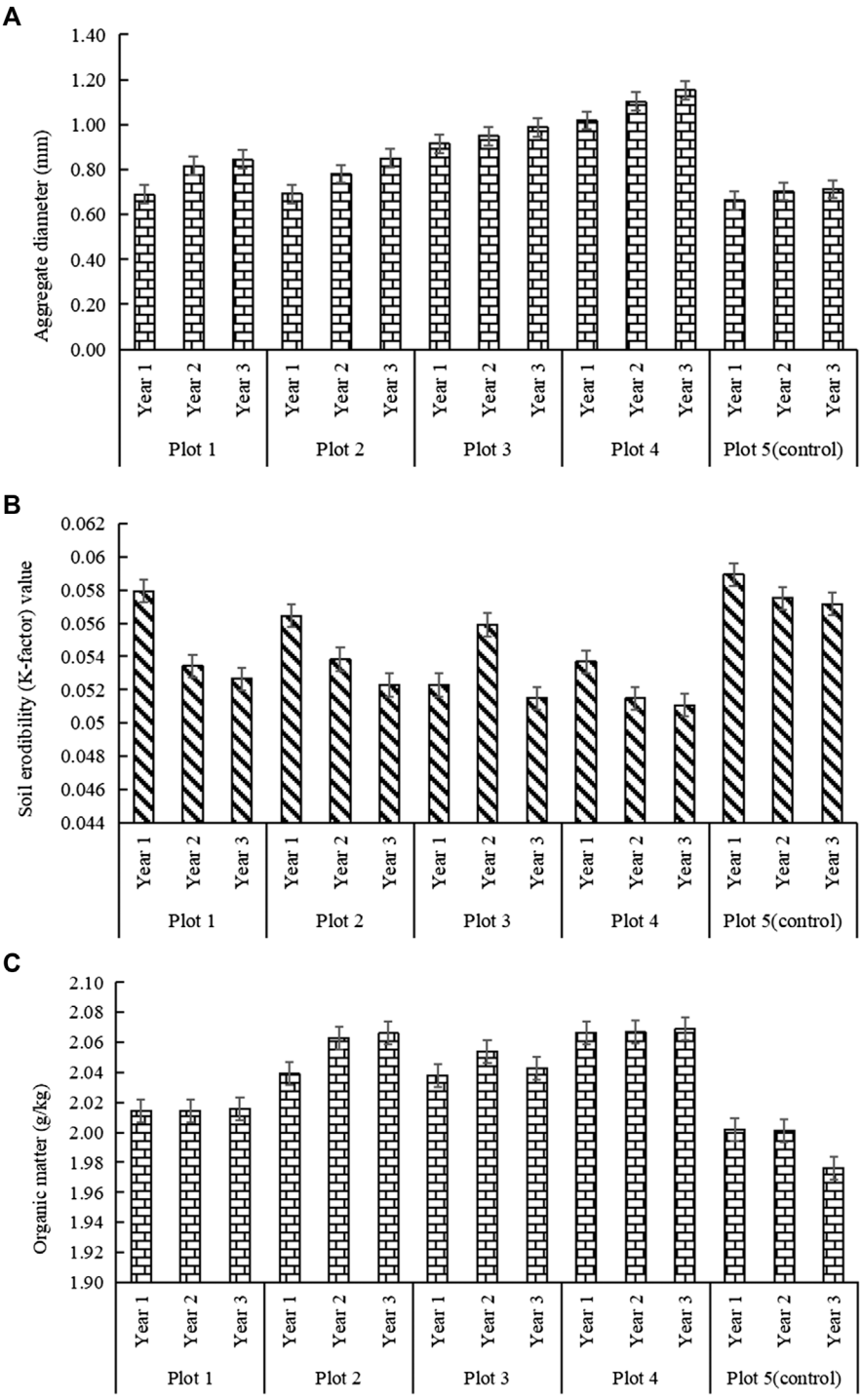

FIGURE 4
(A) Changes in mean weight diameter (MWD) of the soil aggregates in the four plots corresponding to different microtopography modifications. **(B)** Changes in soil erodibility in the plots corresponding to different microtopography modifications. **(C)** Changes in organic matter in the plots corresponding to different microtopography modifications.

restoration measures, the order of the plots, from large to small, in terms of soil MWD was: Plot 4 > Plot 3 > Plot 2 = Plot 1 > Plot 5 (control) in the first year; Plot 4 > Plot 3 > Plot 1 > Plot 2 > Plot 5 (control) in the second year; and Plot 4 > Plot 3 > Plot 2 > Plot 1 > Plot 5 (control) in the third year. Even though the vegetation restoration measures were the same, in

any given year, the U-shaped blocking boards and fixed rod modification method (Plot 4) resulted in the greatest MWD, followed by the plot that only used U-shaped blocking boards (Plot 3).

3.3 Comparison of soil erodibility of plots under different microtopography modifications

Soil erodibility (K-factor) values are used as comprehensive indicators of soil resistance to water erosion. The higher the K-factor value, the weaker the soil erosion resistance and vice versa. As shown in Figure 4B, except for the K-factor value of Plot 3, which increased and then decreased with time (after vegetation restoration), the K-factor values of the other plots gradually decreased with time (after vegetation restoration). Following vegetation restoration at the same time point, the order of K-factor values of the plots, from small to large, with respect to various microtopography modifications was: Plot 3 < Plot 4 < Plot 2 < Plot 1 < Plot 5 (control) in the first year; Plot 4 < Plot 1 < Plot 2 < Plot 3 < Plot 5 (control) in the second year; and Plot 4 < Plot 3 < Plot 2 < Plot 1 < Plot 5 (control) in the third year. After the vegetation restoration measures were implemented, the K-factor value of Plot 4 decreased at the quickest rate, decreasing by 10% in the second year and 11% in the third year compared to that of the control plot. This indicated that with respect to the same vegetation restoration measures, the K-factor value of the plot with microtopography modifications consisting of U-shaped blocking boards and fixed rods decreased gradually with time, indicating an overall increase in soil erosion resistance.

3.4 Effects of microtopography modifications on soil organic matter content

Previous studies have reported that an increase in the soil organic matter content can promote soil cementation, strengthen the adsorption between particles, and increase the amount of macroaggregates, thereby improving the soil structure, aeration and water permeability, and erosion resistance (Šimanský et al., 2019; Chung et al., 2021; Liu et al., 2021). As shown in Figure 4C, with respect to the same vegetation restoration measures, the organic matter content in the surface soil of the plots that underwent microtopography modifications was higher than that in the control plot in the second and third years. With the exception of Plots 3 and 1, the surface soil organic matter content in the modified plots had the same change trend. After vegetation restoration, the organic matter content in the soil showed a slow increasing trend, consistent with the changes in soil erosion resistance. Under the same vegetation restoration measures, the order of organic matter content of the four plots, from large to small, under various microtopography modifications was: Plot 4 > Plot 2 > Plot 3 > Plot 1 > Plot 5 (control) in the first year; Plot 4 > Plot 2 > Plot 3 > Plot 1 > Plot 5 (control) in the second year; and Plot 4 > Plot 2 > Plot 3 > Plot 1 > Plot 5 (control) in the third year. After vegetation restoration, the surface organic matter content in the soil of Plot 4 increased slowly, up 3.2% in the first year, 3.2% in the second year, and 4.7% in the third year, compared with that in the control plot. After 3 years of vegetation recovery, the implementation of microtopography modifications increased the organic matter content in the slope surface soil from 2.0 to 2.06 g/kg. This may be related to the fact that microtopography modifications created a stable environment for plant growth. Vegetation restoration increased the soil organic matter content, and the organic matter content increased the soil resistance to erosion (Fonseca et al., 2017; Herrick et al., 2018; Guo et al., 2020).

3.5 Effects of microtopography modifications on plant community diversity

Previous studies have demonstrated that appropriate microtopography modifications can enhance the effects of vegetation restoration (García-Ávalos et al., 2018; Qiu et al., 2019; Wentzell et al., 2021). Furthermore, studies have shown that microtopography modifications are closely linked to vegetation restoration status and the corresponding soil and water conservation and biodiversity (Melnik et al., 2018; Tukiainen et al., 2019). In mid-August 2021, we conducted a plant community survey in the four plots wherein we implemented microtopography modifications, as well as in the control plot. In the five plots, 15 plant species were identified, and they belonged to five families and 14 genera. The plant species and their importance values (P_i) are shown in Table 2, and the results of the species diversity index analysis are shown in Table 3.

Species diversity is a comprehensive quantitative indicator of species richness and distribution uniformity in a habitat; thus, it is a good reflection of community composition (Tonkin et al., 2017; Hubbard et al., 2018). As shown in Table 3, compared to those in the control plot (Plot 5), the number of species, diversity (H'), evenness (J), and richness (R) indexes were all higher in the four plots where we implemented microtopography modifications. Among the four modified plots, Plot 4 had the highest diversity value (2.35), while Plots 2, 3, and 1 had the second, third, and fourth highest diversity values of 2.25, 2.20, and 2.10, respectively. In general, the evenness index indicates the evenness of plant distribution in a community. In the present study, Plot 4 had the highest evenness index, with a value of 0.87, followed by Plots 2, 3, and 1, with evenness index values of 0.83, 0.82, and 0.79, respectively. Generally, the species richness index indicates the total number of species in a community. In the

TABLE 2 Importance values of plants (Pi) in the plots.

No.	Plant species	Family, genus	Plot 1	Plot 2	Plot 3	Plot 4	Plot 5 (control)
1	*Caragana korshinskii*	Fabaceae, *Caragana*	50	30	29	10	100
2	*Lespedeza davurica*	Fabaceae, *Lespedeza*	219	256	255	270	169
3	*Elymus dahuricus*	Poaceae, *Elymus*	263	308	315	324	203
4	*Chloris virgata*	Poaceae, *Chloris*	130	152	145	100	100
5	*Medicago sativa*	Fabaceae, *Medicago*	263	308	308	324	203
6	*Corispermum mongolicum*	Amaranthaceae, *Corispermum*	68	80	90	84	53
7	*Allium polyrhizum*	Amaryllidaceae, *Allium*	50	23	23	24	15
8	*Eragrostis Pilosa*	Poaceae, *Eragrostis*	130	152	200	20	150
9	*Chenopodium aristatum*	Chenopodiaceae *Chenopodium*	46	46	80	30	48
10	*Salsola collina*	Chenopodiaceae *Salsola*	70	46	60	30	70
11	*Panicum miliaceum*	Poaceae, *Panicum*	76	76	76	50	30
12	*Setaria viridis*	Poaceae, *Setaria*	76	76	90	50	150
13	*Chenopodium acuminatum*	Amaranthaceae, *Chenopodium*	15	15	50	10	60
14	*Amaranthus retroflexus*	Amaranthaceae, *Amaranthus*	23	23	45	15	-
15	*Bassia dasyphylla*	Amaranthaceae, *Bassia*	-	20	20	15	-

[a]Indicates that the plant did not appear in the surveyed quadrat.

TABLE 3 Comparison of the community diversity, evenness, and richness of the different plots.

Plot	No. of species	Diversity index (H)	Evenness index (J)	Richness index (R)
1	14	2.10 ± 0.76	0.79 ± 0.13	1.78 ± 0.43
2	15	2.25 ± 0.79	0.83 ± 0.15	1.89 ± 0.48
3	15	2.20 ± 0.75	0.82 ± 0.15	1.86 ± 0.46
4	15	2.35 ± 0.81	0.87 ± 0.24	1.94 ± 0.54
5 (control)	13	1.97 ± 0.55	0.77 ± 0.13	1.66 ± 0.40

present study, Plot 4 had the highest richness index value among the plots having microtopography modifications, with a value of 1.94, followed by Plots 2, 3, and 1, with richness index values of 1.89, 1.86, and 1.78, respectively. The Shannon–Wiener index of diversity objectively reflects the changes in species of a plant community, while taking into account any insufficiencies in species richness and evenness. Thus, it can indicate the diversity of a community more effectively than other indices. The plant community in Plot 4, which underwent microtopography modifications, had a higher species diversity than that of the other plots.

In Plot 4, we applied the microtopography modifications of U-shaped blocking boards and fixed rods. This combination prevented slope soil from slipping and additionally increased surface infiltration. The blocking boards embedded in the slope prevented the surface soil from separating from the slope, and the fixed rods reinforced the blocking boards. Thus, these modifications could provide a safe and stable environment for plant growth. They protected the slope before the vegetation measures took full effect and played an important role in improving the soil organic matter content as well as its erosion resistance. Therefore, Plot 4 had the highest plant community diversity, evenness, and richness index values.

In Plot 2, we applied straight blocking boards and fixed rods, which refined the space within the plot and ensured the initial evenness of plant species distribution. Although it prevented the surface soil from separating from the slope, the surveys revealed that it suffered more longitudinal erosion than Plot 4 did, which may have accounted for its diversity index value being lower than that of Plot 4. Plots 1 and 3 used single microtopography modification methods, and the surveys revealed that they contained bare patches ranging from 0.01 to 0.09 m^2 in area. Owing to fewer species and more bare patches, the biodiversity of Plots one and three was lower than that of Plot 4. Plot 5 (control) only had soil cover and planted vegetation, with no protection methods for the surface soil on the slope. Therefore, the slope surface soil suffered severe slippage, indicating that the vegetation measures were not effective and did not stop slope erosion; thus, the bare patches on the slope increased over the duration of the study period. This plot had bare patches ranging

from 0.5 to 1.0 m^2 in area, which increased in size each year; additionally, compared to the other plots, this plot had fewer species and the least diverse plant community. By collating the surveys from the 3 years, we concluded that the plant species in the plots were the same in 2019, consisting primarily of artificially planted species, with minimal gradation and a single-layer structure. By 2021, the number of species in Plots one to four increased, and gradation appeared, indicating that microtopography modifications can allow vegetation restoration to take effect.

4 Discussion

4.1 Effects of microtopography modifications on soil erodibility

In the plots with microtopography modifications, the amount of macroaggregates increased every year. In 2021, compared with those in the control plot, aggregates larger than 0.25 mm increased by 20, 24, 21, and 30% in plots 1, 2, 3 and 4, respectively. Plot 4 exhibited the fastest increase in the amount of aggregates larger than 0.25 mm, followed by Plot 2. Some studies have reported that the water-stable aggregate content, particularly the content of aggregates larger than 0.25 mm, is one of the best indicators of soil erodibility (Hao Wang et al., 2018; Lehmann et al., 2020). The plots with microtopography modifications have different manifestations in terms of the three indicators of MWD, erosion resistance, and mine dump surface soil organic matter content. By 2021, compared with those in the control plot, the MWD in plots 1, 2, 3, and 4 increased by 15, 16, 27, and 38%; the soil erodibility (K-factor) values decreased by 7.8, 8.5, 10, and 10.7%, and the soil organic matter content increased by 2, 4.5, 3.4, and 4.7%, respectively. The results revealed that if the values surpassed these increments, the soil organic matter increased, soil erodibility decreased, and the MWD of soil aggregates increased. Previous studies have also demonstrated that soil organic matter is an important indicator of soil quality (Šimanský et al., 2019; Chung et al., 2021). It is also a binding material that forms soil aggregates and is important for increasing soil erosion resistance. Thus, the number and characteristics of soil aggregates reflects soil erosion resistance. This was consistent with the findings of Chung et al. (2021) and Šimanský et al. (2019).

In the present study, we proposed different combinations of microtopography modification materials and methods known to have good soil and water conservation effects. However, our study was limited to soil erosion resistance studied for a period of 3 years. Therefore, it lacks long-term observations of erosion prevention and control. Future studies should focus on the quantitative analysis of vegetation restoration and soil erosion on the slopes of mine dumps following the implementation of microtopography modifications. Compared with the control plot, plot 4 with the microtopography modification method of embedding U-shaped blocking boards and fixed rods in the slope was most effective at enhancing soil erosion resistance. Our study was based on the field survey of soil erosion resistance. However, we did not consider the process of the wind erosion; hence, increased observation of the amount of wind erosion is required in the future.

4.2 Effects of microtopography modifications on biodiversity

The implementation of microtopography modifications can create conditions for vegetation restoration and enhance biodiversity (Liu et al., 2020; Miller et al., 2021). In the present study, we investigated the characteristics of plant communities and showed that compared with the control plot, Plot 4 had the highest number of species (15), along with the highest Shannon–Weiner diversity (2.35), evenness (0.87), and richness indices (1.94). All four plots with microtopography modifications showed a higher plant diversity compared to that in the control (Plot 5). This indicated that single or combined microtopography modifications can create different microhabitats on the slopes of mine dumps. Before vegetation measures have an effect on soil and water conservation, modifications provide a safe and stable environment for plant growth, creating suitable conditions for species reproduction. This was consistent with the findings of Qiu et al. (2019) and Wentzell et al. (2021). In terms of vegetation restoration, we observed a close link between microtopography combinations and biodiversity. Nevertheless, as our investigation was limited to studying plant community characteristics in mid-August 2021, during a period of vigorous plant growth, it remains unclear whether microtopography modifications promote positive succession of plant communities during the other months of the year. The order of plots, from high to low, in terms of diversity, evenness, and richness were Plot 4 > Plot 2 > Plot 3 > Plot 1 > Plot 5 (control). This result was based on a survey of only a few plant community characteristics, and future studies should consider the dynamic changes in plant communities caused by single and combined microtopography modification methods.

4.3 The practicality of microtopography modification methods

The barrier plates and fixed piles used in the present study are all wooden materials. Following the application of soil and water conservation measures, such wooden materials begin to decay and are degraded into the soil. Before the plant measures come into effect, the slope surface material can be fixed to prevent the surface soil from separating from the slope and to provide a safe and stable environment for plant growth. In the project area, a large area of the slope with conventional plant measures emerged as an exposed open space. As the surface soil of the slope declined, which made the surface soil thinner, the slope

vegetation cover decreased, and the erosion ditch density increased because there are no fixed measures for maintenance of the slope surface material, and consequently, the soil and water conservation treatment effects cannot be achieved. In the present study, the resources (1.2–1.5 fold higher) invested in the test plots were greater than those in the control plot (Plot 5). Moreover, a large amount of work was invested to address the problem of soil dump slope surface material separation; however, further studies are required to determine the quantitative transformation relationship between investment benefit and ecological benefit.

5 Conclusion

Using plot-based observation facilities, we studied the effects of microtopography modifications on the soil erosion resistance and biodiversity of a large mine dump in a semi-arid region. Our findings can serve as a reference for methodological support and production practices. The major conclusions of our study are explained below.

Soil erosion resistance and the biodiversity index under single or combined microtopography modifications, along with vegetation measures, on the slopes of the investigated large mine dump in a semi-arid region, were greater than those under soil cover and vegetation only. The combination of microtopography modifications and vegetation measures may prevented the slippage and separation of surface soil from the slope, creating a safe and stable micro-environment for plant growth. Thus, our study showed that a combination of microtopography modification measures and vegetation planting is effective at improving soil erosion and vegetation restoration along the slopes of large mine dumps.

Data availability statement

The original contributions presented in the study are included in the article/supplementary material; further inquiries can be directed to the corresponding author.

Author contributions

Conception: XT and JW. Analysis and interpretation of data: XT. Drafting of the manuscript: XT, RY, JW, LD, BC, HL, and NG.

Funding

This study was supported by the Special scientific research project of the China Institute of Water Resources and Hydropower Research (Grant number: MK 2019J11); central funds to guide local science and technology development program, “Analysis of the coupling mechanisms of water, salt, and nitrogen in drip irrigation under film in saline-alkali farmland in the Yellow River irrigation area, Inner Mongolia” (Grant number: 2021ZY0031).

Acknowledgments

The authors are indebted to the members of the Shengli Coal Mine who helped collect the samples.

Conflict of interest

The authors declare that the research was conducted in the absence of any commercial or financial relationships that could be construed as a potential conflict of interest.

Publisher’s note

References

Blake, W. H., Rabinovich, A., Wynants, M., Kelly, C., Nasseri, M., Ngondya, I., et al. (2018). Soil erosion in East Africa: An interdisciplinary approach to realising pastoral land management change. *Environ. Res. Lett.* 13, 124014. doi:10.1088/1748-9326/aaea8b

Caviedes-Voullième, D., Ahmadinia, E., and Hinz, C. (2021). Interactions of microtopography, slope and infiltration cause complex rainfall-runoff behavior at the hillslope scale for single rainfall events. *Water Resour. Res.* 57, e2020. doi:10.1029/2020WR028127

Chen, H., Zhang, X., Abla, M., Lü, D., Yan, R., Ren, Q., et al. (2018). Effects of vegetation and rainfall types on surface runoff and soil erosion on steep slopes on the Loess Plateau, China. *CATENA* 170, 141–149. doi:10.1016/j.catena.2018.06.006

Chen, F., Yang, Y., Mi, J., Liu, R., Hou, H., Zhang, S., et al. (2019). Effects of vegetation pattern and spontaneous succession on remediation of potential toxic metal-polluted soil in mine dumps. *Sustainability* 11, 397. doi:10.3390/su11020397

Chen, X., Liang, Z., Zhang, Z., and Zhang, L. (2020). Effects of soil and water conservation measures on runoff and sediment yield in red soil slope farmland under natural rainfall. *Sustainability* 12, 3417. doi:10.3390/su12083417

Chung, H., Kim, S. H., and Nam, K. (2021). Application of microbially induced calcite precipitation to prevent soil loss by rainfall: Effect of particle size and organic matter content. *J. Soils Sediments* 21, 2744–2754. doi:10.1007/s11368-020-02757-2

Clobert, J., Chanzy, A., Le Galliard, J.-F., Chabbi, A., Greiveldinger, L., Caquet, T., et al. (2018). How to integrate experimental research approaches in ecological and

environmental studies: AnaEE France as an example. *Front. Ecol. Evol.* 6, 43. doi:10.3389/fevo.2018.00043

De Laurentiis, V., Secchi, M., Bos, U., Horn, R., Laurent, A., Sala, S., et al. (2019). Soil quality index: Exploring options for a comprehensive assessment of land use impacts in LCA. *J. Clean. Prod.* 215, 63–74. doi:10.1016/j.jclepro.2018.12.238

Eltner, A., Maas, H. G., and Faust, D. (2018). Soil micro-topography change detection at hillslopes in fragile Mediterranean landscapes. *Geoderma* 313, 217–232. doi:10.1016/j.geoderma.2017.10.034

Esmali Ouri, A., and Kateb, F. (2020). Study of soil erosion potential using landscape measurements (case study: Sharif Beiglou watershed, Ardabil Province). *Hydrogeomorphology* 7, 145–164. doi:10.22034/HYD.2020.41552.1543

Feng, Y., Wang, J., Bai, Z., and Reading, L. (2019). Effects of surface coal mining and land reclamation on soil properties: A review. *Earth. Sci. Rev.* 191, 12–25. doi:10.1016/j.earscirev.2019.02.015

Fischer, L. K., Lippe, Mvd, Rillig, M. C., and Kowarik, I. (2013). Creating novel urban grasslands by reintroducing native species in wasteland vegetation. *Biol. Conserv.* 159, 119–126. doi:10.1016/j.biocon.2012.11.028

Fonseca, F., de Figueiredo, T., Nogueira, C., and Queirós, A. (2017). Effect of prescribed fire on soil properties and soil erosion in a Mediterranean mountain area. *Geoderma* 307, 172–180. doi:10.1016/j.geoderma.2017.06.018

Franco-Sepúlveda, G., Del Rio-Cuervo, J. C., and Pachón-Hernández, M. A. (2019). State of the art about metaheuristics and artificial neural networks applied to open pit mining. *Resour. Policy* 60, 125–133. doi:10.1016/j.resourpol.2018.12.013

García-Ávalos, S., Rodriguez-Caballero, E., Miralles, I., Luna, L., Domene, M. A., Solé-Benet, A., et al. (2018). Water harvesting techniques based on terrain modification enhance vegetation survival in dryland restoration. *CATENA* 167, 319–326. doi:10.1016/j.catena.2018.05.004

Groninger, J., Skousen, J., AngelAngel, P., Barton, C., Burger, J., and Zipper, C. (2017). Mine reclamation practices to enhance forest development through natural succession the forestry reclamation approach: Guide to successful reforestation of mined lands, in eds. M. B. Adams. *Gen. Tech. Rep. NRS-169* (Newtown Square, PA: United States Department of Agriculture, Forest Service, Northern Research Station), 1–7. doi:10.1016/0169-2046(89)9022-4

Guo, M., Wang, W., Shi, Q., Chen, T., Kang, H., Li, J., et al. (2019). An experimental study on the effects of grass root density on gully headcut erosion in the gully region of China's Loess Plateau. *Land Degrad. Dev.* 30, 2107–2125. doi:10.1002/ldr.3404

Guo, M., Wang, W., Wang, T., Wang, W., and Kang, H. (2020). Impacts of different vegetation restoration options on gully head soil resistance and soil erosion in loess tablelands. *Earth Surf. Process. Landf.* 45, 1038–1050. doi:10.1002/esp.4798

Hao Wang, H., Zhang, G. H., Li, N. N., Zhang, B., and Yang, H. (2018). Soil erodibility influenced by natural restoration time of abandoned farmland on the Loess Plateau of China. *Geoderma* 325, 18–27. doi:10.1016/j.geoderma.2018.03.037

Herrick, J. E., Weltz, M. A., Reeder, J. D., Schuman, C. E., and Simanton, J. R. (2018). "Rangeland soil erosion and soil quality: Role of soil resistance, resilience, and disturbance regime," in *Soil quality and soil erosion*. Editor R. Lal (Boca Raton, FL: CRC Press), 209–233.

Hubbard, C. J., Brock, M. T., Van Diepen, L. T., Maignien, L., Ewers, B. E., Weinig, C., et al. (2018). The plant circadian clock influences rhizosphere community structure and function. *ISME J.* 12, 400–410. doi:10.1038/ismej.2017.172

Ke, W., Zhang, X., Zhu, F., Wu, H., Zhang, Y., Shi, Y., et al. (2021). Appropriate human intervention stimulates the development of microbial communities and soil formation at a long-term weathered bauxite residue disposal area. *J. Hazard. Mat.* 405, 124689. doi:10.1016/j.jhazmat.2020.124689

Lehmann, J., Bossio, D. A., Kögel-Knabner, I., and Rillig, M. C. (2020). The concept and future prospects of soil health. *Nat. Rev. Earth Environ.* 1, 544–553. doi:10.1038/s43017-020-0080-8

Liu, Y., Du, J., Xu, X., Kardol, P., and Hu, D. (2020). Microtopography-induced ecohydrological effects alter plant community structure. *Geoderma* 362, 114119. doi:10.1016/j.geoderma.2019.114119

Liu, B., Xie, Y. H., Tang, C. S., Pan, X-H., Jiang, N.-J., Singh, D. N., et al. (2021). Bio-mediated method for improving surface erosion resistance of clayey soils. *Eng. Geol.* 293, 106295. doi:10.1016/j.enggeo.2021.106295

Luo, C., Deng, Y., Inubushi, K., Liang, J., Zhu, S., Wei, Z., et al. (2018). Sludge biochar amendment and alfalfa revegetation improve soil physicochemical properties and increase diversity of soil microbes in soils from a rare Earth element mining wasteland. *Int. J. Environ. Res. Public Health* 15, 965. doi:10.3390/ijerph15050965

Ma, R., Hu, F., Xu, C., Liu, J., and Zhao, S. (2022). Response of soil aggregate stability and splash erosion to different breakdown mechanisms along natural vegetation restoration. *CATENA* 208, 105775. doi:10.1016/j.catena.2021.105775

Mander, M., Jewitt, G., Dini, J., Glenday, J., Blignaut, J., Hughes, C., et al. (2017). Modelling potential hydrological returns from investing in ecological infrastructure: Case studies from the Baviaanskloof-Tsitsikamma and uMngeni catchments, South Africa. *Ecosyst. Serv.* 27, 261–271. doi:10.1016/j.ecoser.2017.03.003

Mata-González, R., Averett, J. P., Abdallah, M. A. B., and Martin, D. W. (2022). Variations in groundwater level and microtopography influence desert plant communities in shallow aquifer areas. *Environ. Manage.* 69, 45–60. doi:10.1007/s00267-021-01526-2

Melnik, K., Landhäusser, S. M., and Devito, K. (2018). Role of microtopography in the expression of soil propagule banks on reclamation sites. *Restor. Ecol.* 26, S200–S210. doi:10.1111/rec.12587

Miller, V. S., Naeth, M. A., and Wilkinson, S. R. (2021). Micro topography, organic amendments and an erosion control product for reclamation of waste materials at an arctic diamond mine. *Ecol. Eng.* 172, 106399. doi:10.1016/j.ecoleng.2021.106399

Monjezi, M., Shahriar, K., Dehghani, H., and Samimi Namin, F. (2009). Environmental impact assessment of open pit mining in Iran. *Environ. Geol.* 58, 205–216. doi:10.1007/s00254-008-1509-4

Neuenkamp, L., Prober, S. M., Price, J. N., Zobel, M., and Standish, R. J. (2019). Benefits of mycorrhizal inoculation to ecological restoration depend on plant functional type, restoration context and time. *Fungal Ecol.* 40, 140–149. doi:10.1016/j.funeco.2018.05.004

Nie, X., Li, Z., Huang, J., Liu, L., Xiao, H., Liu, C., et al. (2018). Thermal stability of organic carbon in soil aggregates as affected by soil erosion and deposition. *Soil Tillage Res.* 175, 82–90. doi:10.1016/j.still.2017.08.010

Orgiazzi, A., and Panagos, P. (2018). Soil biodiversity and soil erosion: It is time to get married: Adding an earthworm factor to soil erosion modelling. *Glob. Ecol. Biogeogr.* 27, 1155–1167. doi:10.1111/geb.12782

Ouyang, W., Wu, Y., Hao, Z., Zhang, Q., Bu, Q., Gao, X., et al. (2018). Combined impacts of land use and soil property changes on soil erosion in a mollisol area under long-term agricultural development. *Sci. Total Environ.* 613–614, 798–809. doi:10.1016/j.scitotenv.2017.09.173

Perreault, L. M., Yager, E. M., and Aalto, R. (2017). Effects of gradient, distance, curvature and aspect on steep burned and unburned hillslope soil erosion and deposition. *Earth Surf. Process. Landf.* 42, 1033–1048. doi:10.1002/esp.4067

Prosdocimi, M., Burguet, M., Di Prima, S., Sofia, G., Terol, E., Rodrigo Comino, J. R., et al. (2017). Rainfall simulation and Structure-from-Motion photogrammetry for the analysis of soil water erosion in Mediterranean vineyards. *Sci. Total Environ.* 574, 204–215. doi:10.1016/j.scitotenv.2016.09.036

Qiu, D., Yan, J., Ma, X., Luo, M., Wang, Q., Cui, B., et al. (2019). Microtopographical modification by a herbivore facilitates the growth of a coastal saltmarsh plant. *Mar. Pollut. Bull.* 140, 431–442. doi:10.1016/j.marpolbul.2019.01.066

Raghunathan, K., Marathe, D., Singh, A., and Thawale, P. (2021). Organic waste amendments for restoration of physicochemical and biological productivity of mine spoil dump for sustainable development. *Environ. Monit. Assess.* 193, 599. doi:10.1007/s10661-021-09379-2

Shi, W., Wang, J., Li, X., Xu, Q., and Jiang, X. (2021). Multi-fractal characteristics of reconstructed landform and its relationship with soil erosion at a large opencast coal-mine in the loess area of China. *Geomorphology* 390, 107859. doi:10.1016/j.geomorph.2021.107859

Shirazi, M. A., Boersma, L., and Hart, J. W. (1988). A unifying quantitative analysis of soil texture: Improvement of precision and extension of scale. *Soil Sci. Soc. Am. J.* 52, 181–190. doi:10.2136/sssaj1988.03615995005200010032x

Šimanský, V., Juriga, M., Jonczak, J., Uzarowicz, Ł., and Stępień, W. (2019). How relationships between soil organic matter parameters and soil structure characteristics are affected by the long-term fertilization of a sandy soil. *Geoderma* 342, 75–84. doi:10.1016/j.geoderma.2019.02.020

Tang, J., Liang, J., Yang, Y., Zhang, S., Hou, H., Zhu, X., et al. (2022). Revealing the structure and composition of the restored vegetation cover in semi-arid mine dumps based on LiDAR and hyperspectral images. *Remote Sens. (Basel).* 14, 978. doi:10.3390/rs14040978

Tonkin, J. D., Bogan, M. T., Bonada, N., Rios-Touma, B., and Lytle, D. A. (2017). Seasonality and predictability shape temporal species diversity. *Ecology* 98, 1201–1216. doi:10.1002/ecy.1761

Tukiainen, H., Kiuttu, M., Kalliola, R., Alahuhta, J., and Hjort, J. (2019). Landforms contribute to plant biodiversity at alpha, beta and gamma levels. *J. Biogeogr.* 46, 1699–1710. doi:10.1111/jbi.13569

van Bavel, C. H. M. V. (1950). Mean weight-diameter of soil aggregates as a statistical index of Aggregation. *Soil Sci. Soc. Am. J.* 14, 20–23. doi:10.2136/sssaj1950.036159950014000C0005x

Vinci, A., Todisco, F., Brigante, R., Mannocchi, F., and Radicioni, F. (2017). A smartphone camera for the structure from motion reconstruction for measuring soil surface variations and soil loss due to erosion. *Hydrol. Res.* 48, 673–685. doi:10.2166/nh.2017.075

Wang, G., Lv, J., Han, G., Zhu, S., Liu, X., Wang, A., et al. (2020). Ecological restoration of degraded supratidal wetland based on microtopography modification: A case study in the Yellow River delta. *Wetlands* 40, 2659–2669. doi:10.1007/s13157-020-01351-z

Wentzell, B. M., DeVito, E. D., and Shebitz, D. J. (2021). Effects of restoration strategies on vegetation establishment in retired cranberry bogs. *Plant Ecol.* 222, 897–913. doi:10.1007/s11258-021-01150-4

Yixia Wang, Y., Ran, L., Fang, N., and Shi, Z. (2018). Aggregate stability and associated organic carbon and nitrogen as affected by soil erosion and vegetation rehabilitation on the Loess Plateau. *CATENA* 167, 257–265. doi:10.1016/j.catena.2018.05.005

Yuan, Y., Zhao, Z., Niu, S., Li, X., Wang, Y., Bai, Z., et al. (2018). Reclamation promotes the succession of the soil and vegetation in opencast coal mine: A case study from *Robinia pseudoacacia* reclaimed forests, pingshuo mine, China. *CATENA* 165, 72–79. doi:10.1016/j.catena.2018.01.025

Zhang, J. E. (2007). *Common experimental research methods and techniques in ecology (in Chinese)*. Beijing, China: Chemical Industry Press.

Zhang, X., Hu, M., Guo, X., Yang, H., Zhang, Z., Zhang, K., et al. (2018). Effects of topographic factors on runoff and soil loss in Southwest China. *CATENA* 160, 394–402. doi:10.1016/j.catena.2017.10.013

Zhao, L., Hou, R., Wu, F., and Keesstra, S. (2018). Effect of soil surface roughness on infiltration water, ponding and runoff on tilled soils under rainfall simulation experiments. *Soil Tillage Res.* 179, 47–53. doi:10.1016/j.still.2018.01.009

frontiers | Frontiers in Environmental Science

TYPE Original Research
PUBLISHED 11 August 2022
DOI 10.3389/fenvs.2022.905410

OPEN ACCESS

EDITED BY
Brandon L. Edwards,
New Mexico State University,
United States

REVIEWED BY
Prabir K. Kolay,
Southern Illinois University Carbondale,
United States
Sara Mola Ali Abasiyan,
University of Maragheh, Iran

*CORRESPONDENCE
Chengzhi Li,
xdlichengzhi@xju.edu.cn

SPECIALTY SECTION
This article was submitted to Drylands, a section of the journal Frontiers in Environmental Science

RECEIVED 27 March 2022
ACCEPTED 14 July 2022
PUBLISHED 11 August 2022

CITATION
Xu B, Li C and Li Z (2022), Comparison of the characteristics of six salt crusts. *Front. Environ. Sci.* 10:905410. doi: 10.3389/fenvs.2022.905410

Comparison of the characteristics of six salt crusts

Boshi Xu[1], Chengzhi Li[1,2,3]* and Zhaoti Li[1]

[1]College of Ecology and Environment, Xinjiang University, Urumqi, China, [2]Key Laboratory of Oasis Ecology Ministry of Education, Xinjiang University, Urumqi, China, [3]Xinjiang Jinghe Observation and Research Station of Temperate Desert Ecosystem, Ministry of Education, Jinghe, Xinjiang, China

Salt crust is a soil layer formed by the cementation of soluble salt on the surface or inside of soil with soil particles. The salt crust can alter the soil's ability to resist wind erosion. To explore the characteristics of different types of salt crust, six kinds of salt ($CaCl_2$, KCl, Na_2SO_4, NaCl, Na_2CO_3, and $NaHCO_3$) were selected and six salt contents (0.2, 0.5, 1, 2, 3, and 4%) were set up to conduct the experiment of a sandy soil crust. The experiment compares the characteristics of crust appearance, compressive strength, and toughness of six selected kinds of salt crust. The results showed that Na_2SO_4 formed the subflorescence, while $CaCl_2$, KCl, NaCl, Na_2CO_3, and $NaHCO_3$ formed the efflorescences. The compressive strength and toughness of Na_2SO_4 salt crust initially increased and then decreased as the salt content increased, and both the strength and toughness reached the maximum when the salt content was 3%. At first, the compressive strength of NaCl crusts increased and then stabilized as a result of the increase in salt content. The toughness of the NaCl salt crust experienced an initial increase and then a decrease, reaching the maximum when the salt content was 3%. The compressive strength and toughness of the salt crusts of $CaCl_2$ and KCl increased as the salt content increased. There was a slight increase in the compressive strength of the crusts formed by Na_2CO_3 and $NaHCO_3$, with hardly any noticeable change even as the salt content increased, and the maximum compressive strength was only 0.03 and 0.40 MPa, respectively. The crusts of Na_2CO_3 and $NaHCO_3$ were susceptible to wind erosion, while the crusts of KCl, $CaCl_2$, NaCl, and Na_2SO_4, having high compressive strength and crust toughness, were capable of resisting wind erosion.

KEYWORDS

salt crust, crust appearance, compressive strength, crust toughness, wind erosion resistance

Introduction

Soil wind erosion is an important component of soil desertification, and its control is important to sandy soil management (Yi et al., 2006). Some kinds of soil crusts can compact the soil structure and also improve the resistance of the soil to wind erosion (Li and Shen, 2006). There are two types of soil crust: biological crust and physical crust. A biological crust is a layer formed by mosses, algae, microorganisms, etc., and their secretions cement soil particles. Biocrust formation requires a long period, but it has high resistance to wind erosion. Physical crusts are formed when fine particles clog the soil surface pores during rainfall

splashing or when fine particles adhere to large soil particles during soil water evaporation. Physical crusts are formed in a short time and are much less resistant to wind erosion than biological crusts (Langston and Neuman, 2005; Li and Shen, 2006). Salt crust is a special type of physical crust, which is a layer of soil crust formed when soluble salts in the soil cement with surface particles or internal particles (Li, 2018). The presence of salt crusts alters the structure of the soil and affects its resistance to wind erosion (Ji, 2001). In addition, salt crusts can increase the water content in the soil beneath the crusts (Zhang et al., 2010), thereby causing a further increase in the binding capacity of soil particles, which in turn improves the resistance of soil to wind erosion (Chepil, 1951; Yi et al., 2006). Where vegetation is scarce, the presence of salt crusts is of great importance to soil resistance to wind erosion.

The formation of salt crust is influenced by a variety of factors. When the brine solution evaporates in the porous medium, as evaporation proceeds, salt solubility increases and reaches the salt saturation concentration, resulting in precipitation of salt crystals. The initial salt concentration of the brine solution, temperature, and humidity affect the formation of salt crusts (Clercq et al., 2013; Rad et al., 2015; Menéndez and Petráňová, 2016; Shokri-kuehni et al., 2017a; Shokri-kuehni et al., 2017b). The higher the initial concentration of the brine solution, the higher the evaporation temperature of the evaporation surface, and the lower the humidity of air, the earlier the formation of salt crystals, and the easier it is to form salt crusts. The type of salt crust formed by different salts also varies. Na_2SO_4 forms the subflorescence at room temperature, with salt crystals crystallizing in the pores of the surface soil layer, while NaCl forms the efflorescences, with salt crystals aggregating on the soil surface (Benavente et al., 2015; Lindström et al., 2015; Desarnaud et al., 2016). The efflorescences of NaCl have two forms, "crusty" and "patchy". When the particle size of the medium material is larger, when the medium has more water-repellent particles, or the medium particles have irregular angles, it tends to form a discrete crust, which is the "patchy" crust. When the particle size of the medium material is fine, it forms a continuity crust, that is, a "crusty" crust (Eloukabi et al., 2013; Rad and Shokri, 2014). In further studies on salt crust, it was found that continuity crusts had better resistance to wind erosion and reduced water evaporation from the soil (Nield et al., 2016a; Zhang et al., 2019).

To investigate the characteristics of different types of salt crust, six salts, $CaCl_2$, KCl, Na_2SO_4, NaCl, Na_2CO_3, and $NaHCO_3$, were selected in this study to compare the crust appearance, compressive strength, and crust toughness formed by the six salts. The aim was to compare the crust characteristics formed by the six salts to provide theoretical support in the practical application of salt crust.

Materials and methods

Materials

The sandy soil used in the experiment was obtained from the dunes at the Gurbantunggut Desert in Xinjiang, China. The distribution of the particle size of the natural sandy soils is shown in Table 1. To ensure the uniformity and representativeness of the sandy soil, we selected soil with a particle size range of 100–200 μm for the experiment. To remove the interference of soluble salts in the soil, the soil was cleaned with deionized water, and the cleaned sand was placed in an oven at 105°C for drying. The salts used for the experiment were $CaCl_2$, KCl, Na_2SO_4, NaCl, Na_2CO_3, and $NaHCO_3$ (purity ≥99.99%). Six gradients of salt content were set for each salt, 0.2, 0.5, 1, 2, 3, and 4% (the value of soluble salt mass as a percentage of the soil mass). The solvent was deionized water.

Crust experiment

For the experiment, the mass of the soil was fixed at 750 g, and the corresponding mass of salt at all salt content is shown in Table 2. 100 ml of deionized water was added, stirred well, and then poured into a mold (a cylindrical plastic cup of 3.5 cm height and 4 cm radius). The surface of the mold was then smoothed, and the bulk density is 1.43 g cm^{-3}, after which the samples were placed in an oven at 75°C until all the water in the samples evaporated and the sample mass reached constant weight. Ten replicates were carried out for all salt content.

Data acquisition and processing

The dried samples were cooled to room temperature (the average temperature is 24.41°C and the average humidity is 20.85% indoor). Photographs were taken from above and on the side of the samples to observe the apparent morphological characteristics of the crusts. The process of taking pictures lasts about 2–3 min, and then the compressive strength was immediately measured. The crust compressive strength was tested with a digital electronic manometer (HANDPI, HP-1000N, accuracy: 0.1 N, range: 0–1000 N). The manometer was fixed on a holder, and the speed of the manometer probe was set to 1 mm s^{-1} and the diameter of the manometer probe is 10 mm. The stress-time curves were automatically recorded by the manometer connected to a computer. The compressive strength of a sample was the value of the maximum compressive strength on the stress-time curve of the sample. The average and standard deviation of the compressive strength of each salt content were calculated, and the average of the compressive strength was represented as the compressive strength of the samples at the same salt content. The energy absorbed by the crust per unit area is the toughness of the crust, that is, the ratio between the work done by the manometer probe and the area of the manometer probe when the compressive strength of the crust reaches its maximum.

10.3389/fenvs.2022.905410

TABLE 1 Particle size of natural wind sand.

Particle size (μm)	<50 (%)	50–100 (%)	100–200 (%)	200–300 (%)	300–500 (%)	>500 (%)
Ratios (%)	1.2	1.8	72.2	17.5	4.2	3.1

TABLE 2 Quantity of crystalline salt at different salt content.

Salt content	0.2%	0.5%	1%	2%	3%	4%
Wind-sand soil quantity (g)	750	750	750	750	750	750
Salt quantity (g)	1.5	3.75	7.5	15	22.5	30

Results

Characteristics of salt crust appearance

Figure 1 shows the appearance of the crusts of the six salts at different salt contents. As can be seen from Figure 1, there were differences in the appearance of crusts formed by the different salts. When the salt content was 0.2%, there were no macroscopic salt crystals on the surface of all six salt crusts, and the color of the crusts was brownish-red. There were a few cracks at the surface of Na_2CO_3 and $NaHCO_3$ crusts, while cracks were not seen on other salt crusts. When the salt content was 1%, macroscopic salt crystals appeared on the surface of the salt crusts, except for Na_2SO_4. The salt crusts formed by Na_2CO_3 had the largest area of salt crystals on the surface and had some fine polygonal fractures. When the salt content was 4%, the salt crystals did not appear on the surface of Na_2SO_4 salt crusts still, and the salt crystals on the surface of the other five salt crusts increased noticeably. Polygonal fractures existed on the surface of both salt crusts of Na_2CO_3 and $NaHCO_3$, and an obvious expansion could be seen in the crust formed by Na_2CO_3.

The side view photographs of Na_2CO_3 and $NaHCO_3$ crusts are shown in Figure 2. When the salt content was 0.2%, the surface of the crusts formed by Na_2CO_3 and $NaHCO_3$ had cracked but did not exhibit swelling. When the salt content was 1%, obvious swelling could be seen in the Na_2CO_3 samples, and swelling was seen only in the surface edge area in the $NaHCO_3$ samples. When the salt content was 4%, the swelling phenomenon inside both samples was further intensified, the crusts formed by Na_2CO_3 had separated from the soil thoroughly, and the internal loose sand under the crust could be seen. The crusts formed by $NaHCO_3$ were lifted noticeably from the sample.

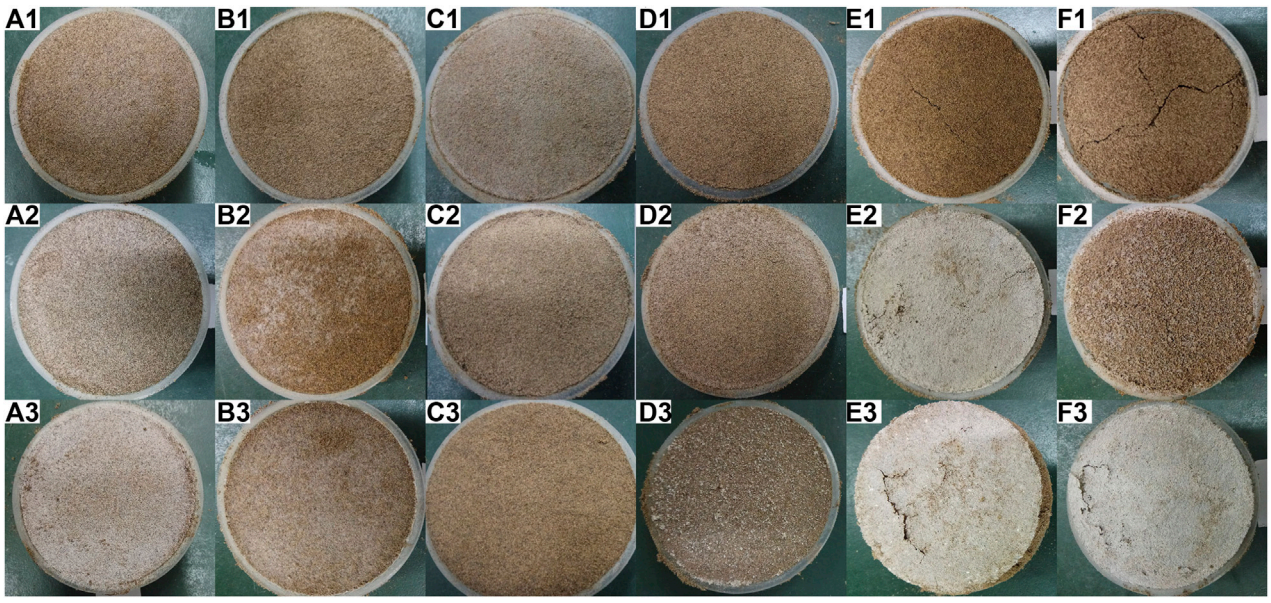

FIGURE 1
Apparent morphology of salt crusts (A, B, C, D, E, and F represent $CaCl_2$, KCl, Na_2SO_4, NaCl, Na_2CO_3, and $NaHCO_3$ six kinds of salt, respectively; 1, 2, and 3 indicate salt content of 0.2, 1, and 4% respectively).

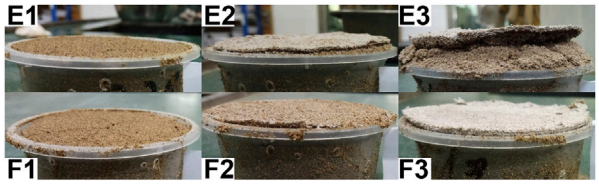

FIGURE 2
Side view photographs of Na_2CO_3 and $NaHCO_3$ salt crusts (E, F represent Na_2CO_3 and $NaHCO_3$ respectively; 1, 2, and 3 indicate salt content of 0.2, 1, and 4% respectively).

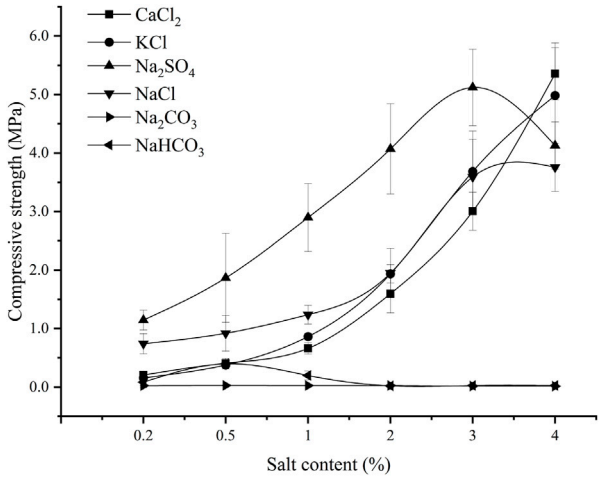

FIGURE 3
Diagram of compressive strength variation of salt crust.

Compressive strength of salt crusts

Figure 3 showed the variation of compressive strength with salt content for the six salt crusts. The compressive strength of different salt crusts varied with the salt content variation. With the increase in the salt content, the compressive strength of the Na_2SO_4 crust increased first and then decreased, reaching a maximum of 5.12 MPa at a salt content of 3%. The compressive strength of the NaCl crust increased first and then remained stable, and the compressive strength of the crust of NaCl reached 3.59 MPa when the salt content was 3% and 3.76 MPa when the salt content was 4%, which was only an increase of 4.7%. The compressive strength of KCl and $CaCl_2$ crusts increased almost exponentially with the increase of the salt content. The compressive strength of $NaHCO_3$ crusts increased slightly but then decreases, reaching a maximum at 0.5% salt content, but its compressive strength was only 0.40 MPa. The compressive strength of Na_2CO_3 crusts was almost stable, and the maximum was only 0.03 MPa.

When the salt content was ≤3%, the compressive strength of the crust formed by Na_2SO_4 was significantly higher than that of the other five salt crusts ($p < 0.05$), and the compressive strength reached 1.15 MPa when the salt content was 0.2%. When the salt content was >3%, the compressive strength of the crusts formed by $CaCl_2$ and KCl salts was higher than that of the crusts formed by Na_2SO_4. The compressive strength of $CaCl_2$ and KCl salt crusts reached 5.36 and 4.98 MPa at 4% salt content, respectively, while the compressive strength of Na_2SO_4 and NaCl was slightly less, 4.53 and 3.76 MPa, respectively.

Stress-time curve and toughness of crusts

Figure 4 showed the stress-time curves of four salts, Na_2SO_4, NaCl, $CaCl_2$, and KCl at different salt contents (the stress-time curve of Na_2CO_3 and $NaHCO_3$ crusts was not considered because the compressive strength of their crusts was very small). The energy absorbed by the crust per unit area is the toughness of the crust, and Figure 5 is the graph of the crust toughness of four salts. From Figure 4 and Figure 5, it could be seen that the crust compressive strength and crust toughness did not always have a positive correlation, and there were differences in the toughness of different salt crusts. The toughness of the Na_2SO_4 crusts and the NaCl crusts all increased and then decreased. The crust toughness of KCl and $CaCl_2$ increased gradually as the salt content increased, with the crust toughness of KCl being slightly higher than that of $CaCl_2$. When the salt content is ≤3%, the crust toughness of Na_2SO_4 was higher than that of $CaCl_2$, KCl, and NaCl, while in the range of the salt content between 2 and 3%, the difference between the crust toughness of Na_2SO_4 and NaCl was not obvious. When the salt content is 4%, the crust toughness of $CaCl_2$ and KCl was greater than that of Na_2SO_4 and NaCl.

Discussion

Salt crust surface characteristics

Under these experimental conditions, Na_2SO_4 formed the subflorescence, with most of the salt crystals distributed inside the soil and fewer salt crystals distributed on the surface of the soil, which was the same as the results of the previous studies (Espinosa et al., 2007; Shahidzdeh-bonn et al., 2010; Gentilini et al., 2012; Li et al., 2021). NaCl, $CaCl_2$, KCl, Na_2CO_3, and $NaHCO_3$ formed the efflorescences. As the salt content increased, the crystals of salts gradually increased on the surface of a sample. The crusts formed by Na_2CO_3 and $NaHCO_3$ produced the phenomena of cracks and swelling on the samples, which was related to the crystallization process of Na_2CO_3 and $NaHCO_3$. Both solutions could produce hydrate crystals. The hydrate crystals were all bigger than the crystals of

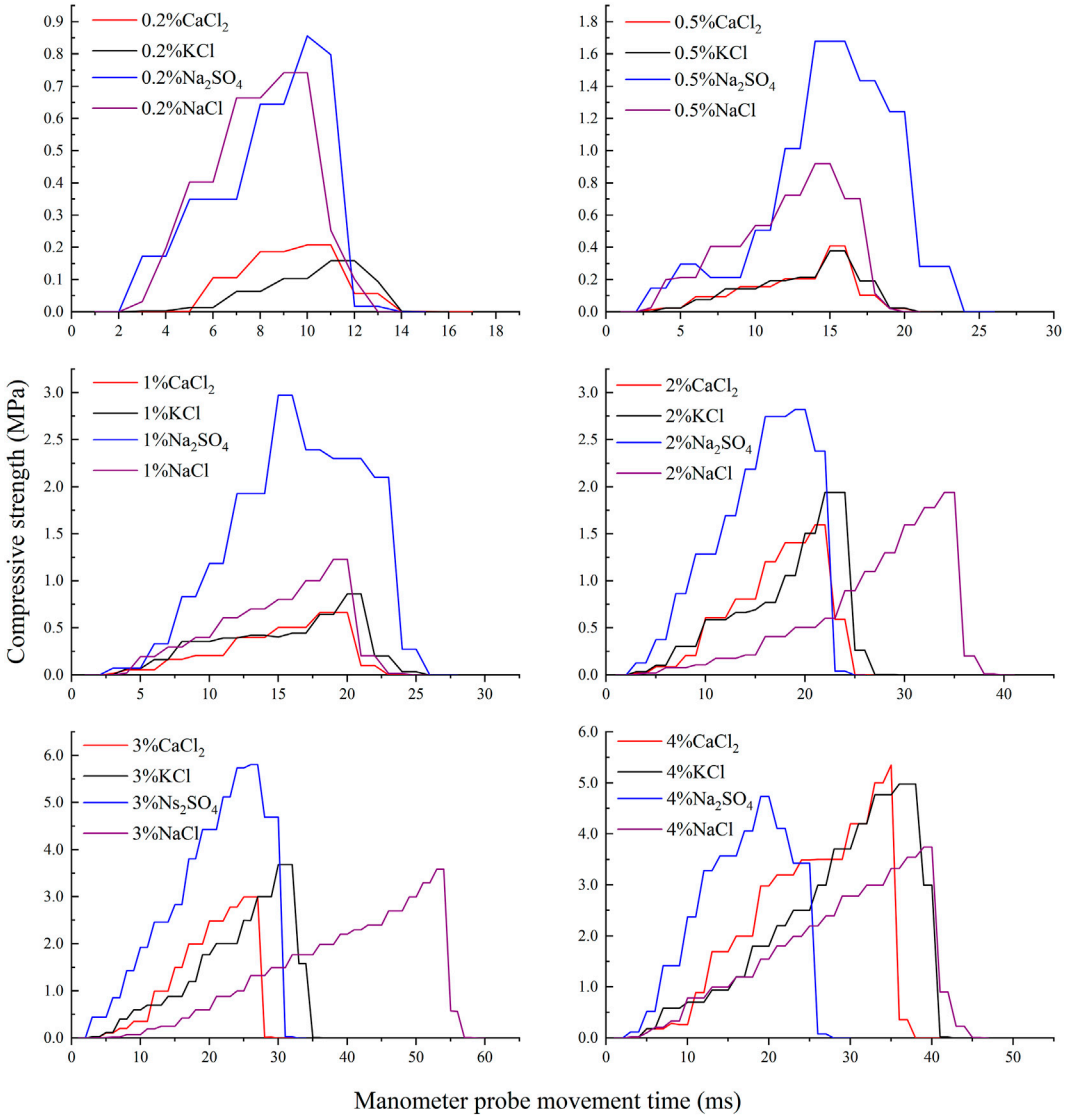

FIGURE 4
Stress-time curves of four salts with different salt content.

Na_2CO_3 and $NaHCO_3$. The saturated Na_2CO_3 solution produced Na_2CO_3-$10H_2O$ crystals, and the Na_2CO_3-$10H_2O$ crystals would increase in volume, and the formation of hydrate crystals in the soil would produce stress to the surrounding sand grains, causing the soil to swell. The crystals of Na_2CO_3-$10H_2O$ would lose water at temperatures higher than 33°C to form anhydrous Na_2CO_3 crystals. The crystals of anhydrous Na_2CO_3 decreased in volume. Crystal expansion and shrinkage resulted in soil expansion and cracking. The Na_2CO_3-$10H_2O$ crystal layer crystallized on the surface of the soil lost water and then decreased in volume, resulting in the surface crust being cracked (Rijniers et al., 2005; Liu, 2016). The $NaHCO_3$ solution had a similar phenomenon to the Na_2CO_3 solution, but the volume expansion of $NaHCO_3$-$10H_2O$ was smaller than that of the Na_2CO_3-$10H_2O$, so its cracks and expansion were smaller than those of Na_2CO_3. The swelling phenomenon of Na_2CO_3 and $NaHCO_3$ salt crusts was related to salt content. The greater the salt content, the more obvious the salt swelling phenomenon, which could be verified from Figure 2.

Compressive strength

During the evaporation of soil water, the brine in the fine pores evaporates and the salt crystallizes as the salt solution reaches saturation solubility (Rad et al., 2013; Li et al., 2021). In this experiment, the crystals of Na_2SO_4 formed the subflorescence, and

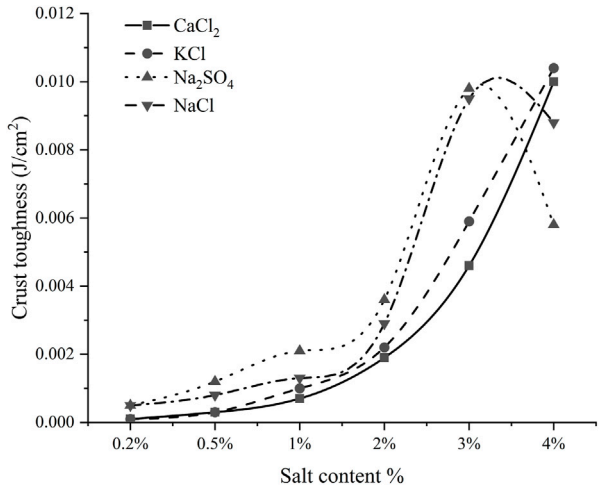

FIGURE 5
Diagram of a variation of crust toughness.

most of the salt crystals crystallized in the internal pores of the soil. When the Na_2SO_4 content was ≤3%, with the increase in salt content, the number of salt crystals crystallized in the pores gradually increased, the cementation between salt crystals and soil particles became strong, and the compressive strength of the salt crust increased. With a further increase in salt content (>3%), the crystals gradually filled the soil pores and generated salt swelling pressure, which damaged the soil structure, and the compressive strength of the salt crust formed by Na_2SO_4 decreased obviously. In these experiments, NaCl, KCl, and $CaCl_2$ formed the efflorescences, with salt crystallization occurring mainly on the soil surface. As evaporation proceeded, the salts gradually accumulated on the soil surface, and the thickness of the salt crust on the surface increased; thus, the increase in salt content only increased the number of the crystals on the surface of the soil and did not affect the internal structure of the soil. Therefore, the compressive strength of these three salts gradually increased with the increase of salt content. The compressive strength of NaCl crusts remained stable at salt content >3%, which might be due to the detachment of the salt crust of NaCl from the soil surface, which hindered water evaporation and inhibited the movement of salt ions to the soil surface (Nachshon et al., 2018). The crystallization process of Na_2CO_3 and $NaHCO_3$ salts resulted in severe salt swelling, which led to salt crust bulging. The compressive strength of the two salt crusts was extremely low, with the maximum compressive strength of the crusts of Na_2CO_3 being only 0.03 MPa and that of $NaHCO_3$ being 0.40 MPa.

Implications for wind erosion resistance

The crust strength and crust toughness of the crusts affect the wind erosion resistance of the crusts. The greater the crust strength and crust toughness, the greater the potential resistance of the crust to wind erosion, and the more potentially erosive events the soil crust can withstand (Nickling and Ecclesstone, 1981; Nield et al., 2016b). This study compared the wind erosion resistance of six salt crusts by three indicators: crust appearance, crust compressive strength, and crust toughness. The surface of the crust formed by Na_2CO_3 and $NaHCO_3$ salts had obvious swelling, exposing the loose soil beneath the crust (as shown in Figure 2), and the compressive strength of the crust was extremely low. The compressive strength of the crust formed by the two salts was far from the sand fixation strength of 1 MPa (Han et al., 2000), and the crusts formed by the two salts would be susceptible to wind erosion. The crusts formed by Na_2SO_4, NaCl, KCl, and $CaCl_2$ were flat relatively, the salt expansion was not observed, and the compressive strength of the salt crust was stronger than that of other salt crusts. These salt crusts could be used for increasing soil resistance. The compressive strength and crust toughness of the Na_2SO_4 crust both increased and then decreased with the increase of the salt content. The compressive strength could reach 1.15 MPa at the salt content of 0.2%, and the compressive strength and crust toughness reached the maximum at the salt content of 3%, with the best resistance to wind erosion. There are two stable crystalline phases during Na_2SO_4 solution crystallization, decahydrate (Na_2SO_4-$10H_2O$) and anhydrous state (Na_2SO_4); when the temperature is high, anhydrous Na_2SO_4 is generated, and as the humidity in the air increases, anhydrous Na_2SO_4 is transformed into Na_2SO_4-$10H_2O$. The solubility of Na_2SO_4-$10H_2O$ is less than that of anhydrous Na_2SO_4, resulting in super-saturation of Na_2SO_4-$10H_2O$, generating a crystallization pressure and causing damage to the medium material (Steiger and Asmussen, 2008; Saidov et al., 2015). Thus, the optimal salt content of the Na_2SO_4 crust for wind erosion resistance under field conditions still needs to be further investigated. The compressive strength of the NaCl crust increased first and then stayed stable with the increase of salt content, reaching the maximum of 3.76 MPa at the salt content of 4%. The toughness of NaCl crust increased first too and then decreased with the increase in salt content. The toughness reached its maximum at the salt content of 3%, and its compressive strength also reached 3.59 MPa, which was slightly lesser than that of 4% (about 0.16 MPa). Thus, for NaCl, the best potential resistance to wind erosion of the salt crust was the salt content of 3%. The compressive strength and crust toughness of KCl and $CaCl_2$ crusts increased gradually with the increase in salt content, and the compressive strength already reached 1.94 and 1.60 MPa, respectively, at 2% salt content, both having wind erosion resistance. For the crusts formed by Na_2SO_4, NaCl, KCl, and $CaCl_2$, the compressive strength and toughness of the crust formed by the Na_2SO_4 are higher than those of the remaining salts, and the wind erosion resistance is the best when the salt content is ≤3%; the crust

formed by $CaCl_2$ has the best wind erosion resistance when the salt content is 4%, its compressive strength is the greatest, and the crust toughness is also better.

Conclusion

In this article, Na_2SO_4, NaCl, $CaCl_2$, KCl, Na_2CO_3, and $NaHCO_3$ were selected for salt crusting experiments to investigate crust properties related to resistance to wind erosion, and the following was concluded.

1) Na_2SO_4 formed a subflorescence, and the appearance of the salt crust was not affected by the increase in the salt content. $CaCl_2$, KCl, NaCl, $NaHCO_3$, and Na_2CO_3 formed efflorescences. The area of crystals on the surface of the soil increased gradually with the increasing salt content. Soil expansion occurred with Na_2CO_3 and $NaHCO_3$ crusts as salt content increased.
2) The compressive strength of Na_2SO_4 crusts increased first and then decreased with increasing salt content, reaching the maximum at 3% salt content. The crust compressive strength of $CaCl_2$ and KCl increased continuously with increasing salt content. The compressive strength of the NaCl crust increased first and then stabilized at the salt content of 3% with increasing salt content. The crust compressive strength of Na_2CO_3 crusts was low, with a maximum of only 0.03 MPa. The compressive strength of $NaHCO_3$ crusts was low too, and the maximum was only 0.40 MPa.
3) The crust toughness of both Na_2SO_4 and NaCl increased and then decreased with increasing salt content, and the crust toughness reached the maximum at 3% salt content. While the crust toughness of both KCl and $CaCl_2$ gradually increased with increasing salt content.

The salt crust of Na_2CO_3 and $NaHCO_3$ swelled, destroying the internal structure of the soil, and the compressive strength of the crusts was low, which is not suitable for protecting wind-sand soils. The salt crust formed by Na_2SO_4, NaCl, KCl, and $CaCl_2$ had higher crust strength and better crust toughness, having the power to resist wind erosion. Under these experimental conditions, the optimum salt contents of the four salts were 3, 3, 4, and 4%, respectively. The crust formed by Na_2SO_4 has the best wind erosion resistance when the salt content is ≤3%, and the crust formed by $CaCl_2$ has the best wind erosion resistance when the salt content is 4%.

Data availability statement

The original contributions presented in the study are included in the article/Supplementary Material; further inquiries can be directed to the corresponding author.

Author contributions

Conceptualization: CL; investigation, CL and ZL; resources, CL; data curation, BX; writing—original draft preparation, BX; writing—review and editing, BX; visualization, BX; supervision, CL; project administration, CL; funding acquisition, CL. All authors have read and agreed to the published version of the manuscript.

Funding

This research was funded by the National Natural Science Foundation of China (Nos. 41761005 and 41301286).

Conflict of interest

The authors declare that the research was conducted in the absence of any commercial or financial relationships that could be construed as a potential conflict of interest.

Publisher's Note

All claims expressed in this article are solely those of the authors and do not necessarily represent those of their affiliated organizations, or those of the publisher, the editors, and the reviewers. Any product that may be evaluated in this article, or claim that may be made by its manufacturer, is not guaranteed or endorsed by the publisher.

References

Benavente, D., Brimblecombe, P., and Grossi, C. M. (2015). Thermodynamic calculations for the salt crystallisation damage in porous built heritage using PHREEQC. *Environ. Earth Sci.* 74 (3), 2297–2313. doi:10.1007/s12665-015-4221-1

Chepil, W. S. (1951). Properties of soil which influence wind erosion: IV. State of dry aggregate structure. *Soil Sci.* 72 (5), 387–402. doi:10.1097/00010694-195111000-00007

Clercq, H. D., Jovanović, M., Linnow, K., and Steiger, M. (2013). Performance of limestones laden with mixed salt solutions of Na_2SO_4–$NaNO_3$ and Na_2SO_4–K_2SO_4. *Environ. Earth Sci.* 69 (5), 1751–1761. doi:10.1007/s12665-012-2017-0

Desarnaud, J., Bonn, D., and Shahidzadeh, N. (2016). The Pressure induced by salt crystallization in confinement. *Sci. Rep.* 6, 30856. doi:10.1038/srep30856

Eloukabi, H., Sghaier, N., Nasrallah, S. B., and Prat, M. (2013). Experimental study of the effect of sodium chloride on drying of porous media: The crusty–patchy efflorescence transition. *Int. J. Heat. Mass Transf.* 56 (1–2), 80–93. doi:10.1016/j.ijheatmasstransfer.2012.09.045

Espinosa, R., Franke, L., and Deckelmann, G. (2007). Predicting efflorescence and subflorescences of salts. *MRS Proc.* 1047, 105. doi:10.1557/PROC-1047-Y04-03

Gentilini, C., Franzoni, E., Bandini, S., and Nobile, L. (2012). Effect of salt crystallisation on the shear behaviour of masonry walls: An experimental study. *Constr. Build. Mater.* 37, 181–189. doi:10.1016/j.conbuildmat.2012.07.086

Han, Z. W., Hu, Y. D., Chen, G. T., Yao, Z. Y., and Shao, G. S. (2000). The suitability of chemical engineering stabilization in controlling aeolian hazard along the highway in tarim basin. *Environ. Sci.* 05, 86–88. doi:10.13227/j.hjkx.2000.05.021

Ji, F. (2001). Preliminary study on desert types and their anti-wind erosion characteristics in tarim basin. *J. Soil Water Conservation* 01, 16–18+53. doi:10.13870/j.cnki.stbcxb.2001.01.005

Langston, G., and Neuman, C. M. (2005). An experimental study on the susceptibility of crusted surfaces to wind erosion: A comparison of the strength properties of biotic and salt crusts. *Geomorphology* 72 (1-4), 40–53. doi:10.1016/j.geomorph.2005.05.003

Li, C. Z. (2018). A review: The formation, development and prospect of soil salt crust on the view of soil erosion. *J. Xinjiang Univ. Sci. Ed.* 35 (04), 402–408+415. doi:10.13568/j.cnki.651094.2018.04.003

Li, S. H., Li, C. Z., and Fu, X. L. (2021). Characteristics of soil salt crust formed by mixing calcium chloride with sodium sulfate and the possibility of inhibiting wind-sand flow. *Sci. Rep.* 11, 9746. doi:10.1038/s41598-021-89151-1

Li, X. L., and Shen, X. D. (2006). The analysis on the mechanism of anti - wind erosion of soil crust. *J. Arid Land Resour. Environ.* 20 (2), 203–207. doi:10.3969/j.issn.1003-7578.2006.02.039

Lindström, N., Heitmann, N., Linnow, K., and Steiger, M. (2015). Crystallization behavior of $NaNO_3$–Na_2SO_4 salt mixtures in sandstone and comparison to single salt behavior. *Appl. Geochem.* 63, 116–132. doi:10.1016/j.apgeochem.2015.07.007

Liu, C. Y. N. (2016). Experimental study on the Pure Salt Expansion of silty clay and salt expansion characteristics analysis ([China (BJ)]: Beijing Jiaotong University). [master's thesis].

Menéndez, B., and Petráňová, V. (2016). Effect of mixed vs single brine composition on salt weathering in porous carbonate building stones for different environmental conditions. *Eng. Geol.* 210, 124–139. doi:10.1016/j.enggeo.2016.06.011

Nachshon, U., Weisbrod, N., Katzir, R., and Nasser, A. (2018). NaCl crust architecture and its impact on evaporation: Three-dimensional insights. *Geophys. Res. Lett.* 45 (12), 6100–6108. doi:10.1029/2018GL078363

Nickling, W. G., and Ecclesstone, M. (1981). The effects of soluble salts on the threshold shear velocity of fine sand. *Sedimentology* 28 (4), 505–510. doi:10.1111/j.1365-3091.1981.tb01698.x

Nield, J. M., Neuman, C. M., O'brien, P., Bryant, R. G., and Wiggs, G. F. (2016). Evaporative sodium salt crust development and its wind tunnel derived transport dynamics under variable climatic conditions. *Aeolian Res.* 23, 51–62. doi:10.1016/j.aeolia.2016.09.003

Nield, J. M., Wiggs, G. F., King, J., Bryant, R. G., Eckardt, F. D., Thomas, D. S., et al. (2016). Climate–surface–pore-water interactions on a salt crusted playa: Implications for crust pattern and surface roughness development measured using terrestrial laser scanning. *Earth Surf. Process. Landf.* 41 (6), 738–753. doi:10.1002/esp.3860

Rad, M. N., and Shokri, N. (2014). Effects of grain angularity on NaCl precipitation in porous media during evaporation. *Water Resour. Res.* 50 (11), 9020–9030. doi:10.1002/2014WR016125

Rad, M. N., Shokri, N., Keshmiri, A., and Withers, P. J. (2015). Effects of grain and pore size on salt precipitation during evaporation from porous media. *Transp. Porous Media* 110 (2), 281–294. doi:10.1007/s11242-015-0515-8

Rad, M. N., Shokri, N., and Sahimi, M. (2013). Pore-scale dynamics of salt precipitation in drying porous media. *Phys. Rev. E* 88 (3), 032404. doi:10.1103/PhysRevE.88.032404

Rijniers, L. A., Pel, L., Huinink, H. P., and Kopinga, K. (2005). Salt crystallization as damage mechanism in porous building materials—A nuclear magnetic resonance study. *Magn. Reson. Imaging* 23 (2), 273–276. doi:10.1016/j.mri.2004.11.023

Saidov, T. A., Pel, L., and Van Der Heijden, G. H. A. (2015). Crystallization of sodium sulfate in porous media by drying at a constant temperature. *Int. J. Heat. Mass Transf.* 83, 621–628. doi:10.1016/j.ijheatmasstransfer.2014.12.043

Shahidzdeh-bonn, N., Desarnaud, J., Bertrand, F., Chateau, X., and Bonn, D. (2010). Damage in porous media due to salt crystallization. *Phys. Rev. E* 81 (6), 066110. doi:10.1103/PhysRevE.81.066110

Shokri-kuehni, S. M. S., Rad, M. N., Webb, C., and Shokri, N. (2017). Impact of type of salt and ambient conditions on saline water evaporation from porous media. *Adv. Water Resour.* 105 (7), 154–161. doi:10.1016/j.advwatres.2017.05.004

Shokri-kuehni, S. M. S., Vetter, T., Webb, C., and Shokri, N. (2017). New insights into saline water evaporation from porous media: Complex interaction between evaporation rates, precipitation, and surface temperature. *Geophys. Res. Lett.* 44 (11), 5504–5510. doi:10.1002/2017GL073337

Steiger, M., and Asmussen, S. (2008). Crystallization of sodium sulfate phases in porous materials: The phase diagram Na_2SO_4–H_2O and the generation of stress. *Geochimica Cosmochimica Acta* 72 (17), 4291–4306. doi:10.1016/j.gca.2008.05.053

Yi, X. Y., Zhao, H. L., Zhao, X. Y., Li, Y. Q., Zuo, X. A., and Fu, Z. (2006). Erodibility of aeolian soils in moisture content. *Acta Pedol. Sin.* 43 (4), 684–687. doi:10.3321/j.issn:0564-3929.2006.04.023

Zhang, J. G., Li, H. W., Li, Y. F., Li, Y. N., Ma, Y., Tian, L. L., et al. (2019). Artificial cultivation of soil salt crust and effects of its damage rate on soil evaporation. *Trans. Chin. Soc. Agric. Eng.* 35 (13), 138–144. doi:10.11975/j.issn.1002-6819.2019.13.015

Zhang, J. G., Sun, S. G., Xu, X. W., Lei, J. Q., Wang, H. F., and Li, S. Y. (2010). Chemical characteristics and its effect on soil evaporation of soil salt crusts in the Tarim desert highway shelterbelts. *J. Arid Land Resour. Environ.* 24 (04), 174–179. doi:10.13448/j.cnki.jalre.2010.04.026

frontiers | Frontiers in Environmental Science

TYPE Original Research
PUBLISHED 02 September 2022
DOI 10.3389/fenvs.2022.954004

OPEN ACCESS

EDITED BY
Huawei Pi,
Henan University, China

REVIEWED BY
Worradorn Phairuang,
Kanazawa University, Japan
Lihai Tan,
Northwest Institute of Eco-Environment and Resources (CAS), China
Xiuqin Wu,
Beijing Forestry University, China

*CORRESPONDENCE
Wei Hu,
weihu987@163.com

SPECIALTY SECTION
This article was submitted to Drylands, a section of the journal Frontiers in Environmental Science

RECEIVED 26 May 2022
ACCEPTED 08 August 2022
PUBLISHED 02 September 2022

CITATION
Chen S, Zhang X, Li J, Guo M and Hu W (2022), Effect of tillage management on the wind erosion of arable soil in the Chinese Mollisol region.
Front. Environ. Sci. 10:954004.
doi: 10.3389/fenvs.2022.954004

Effect of tillage management on the wind erosion of arable soil in the Chinese Mollisol region

Shuai Chen[1,2], Xingyi Zhang[2], Jianye Li[2], Mingming Guo[2] and Wei Hu[2]*

[1]College of Public Administration, Chongqing Technology and Business University, Chongqing, China, [2]Key laboratory of Mollisols Agroecology, Northeast Institute of Geography and Agroecology, Chinese Academy of Sciences, Harbin, Heilongjiang, China

Wind erosion is a serious problem in agricultural regions and threatens the regional food production in Northeast China. However, limited information is available on the characteristics of wind erosion in arable soil in Northeast China. As a result, field-based research during periods of vulnerability to wind erosion is essential. This study quantified the characteristics of soil wind erosion under no-tillage (NT) and conventional tillage (CT) treatments in China's northern "corn-belt." The results determined the wind erosion transport mode of Mollisols to be generally characterized by creep and supplemented by saltation and suspension in Northeast China. The erodible particles of the creep accounted for 80.37% and 85.42% of the total wind erosion under the NT and CT treatments, respectively. During experiments with erodible particles in the saltation mode from the soil surface to 2 m, the majority of the particles were collected by the sampler at 0.5 m height, with the NT and CT treatments collecting 5.82 $kg{\cdot}m^{-2}$ and 6.93 $kg{\cdot}m^{-2}$ of erodible particles per unit area, respectively. Wind erosion on agricultural land was observed to be influenced by tillage practices, rainfall, wind speed, and soil moisture content. Average and maximum wind speeds exhibited significant positive correlations with wind erosion during April and May. Moreover, the erodible particles of each wind erosion transport mode (creep, saltation, and suspension) under CT were higher (1.73, 1.41, and 1.35 times) than those under the NT treatment. With less damage and greater protection of the surface soil, the NT treatment was able to decrease the occurrence of wind erosion and influence its outcome on farmland. Therefore, NT treatment should be encouraged as a key initiative for the reduction of wind erosion of arable soil in the Chinese Mollisol region.

KEYWORDS

tillage treatment, wind erosion, interrelationship, arable, Mollisols

Introduction

Wind erosion is the movement of coarse and fine particles by wind across a landscape (Jarrah et al., 2020) and involves three transport processes: creep, saltation, and suspension (Cornelis, 2006). It is a global environmental problem faced by many countries (Katra et al., 2016; Yildiz et al., 2017) and not only causes serious on-site problems, such as a reduction in soil and crop productivity, but also induces off-site problems (e.g., dust storms) (Blanco and Lal, 2008). Furthermore, wind erosion brings great harm to industrial and agricultural production. Therefore, the measurement and prevention of wind erosion are crucial for sustainable land use and environmental protection (Uzun et al., 2020).

The Mollisol region in Northeast China possesses fertile and productive soil and is the country's ecological security base (Liu et al., 2019). Due to highly intensive cultivation, irrational farming, and improper land use practices in the short term, the Mollisol region is easily eroded by rain, wind, freeze–thaw, snowmelt runoff, and other external agents occurring in this special geographical environment in Northeast China (Xie et al., 2019). The arable land fertility of this region is currently decreasing, which consequently threatens the grain production and food security in Northeast China (Shen et al., 2020). Numerous studies have focused on the underlying formation mechanism, influential factors, and hazards of water erosion and freeze-thaw erosion in this region (Jia et al., 2015; Yao et al., 2017; Xu et al., 2018; Shen et al., 2020). However, the wind eroded area in the Mollisol zone makes up 11.1% of the total area in Northeast China (Chi et al., 2019). Large amounts of fine-grained soil and its adsorbed organic matter are transported by wind erosion. This severely damages the productivity of the land, resulting in bare crop seeds following spring sowing and ultimately affects the seeding emergence rate (Sharratt et al., 2018). Thus, the agricultural production and ecological environment in the arable Mollisol region are seriously threatened by wind erosion, and consequently, exploring the characteristics of wind erosion on arable land is crucial for the Mollisol region in Northeast China.

As a widely promoted tillage treatment in Northeast China, no-tillage (NT) has been the focus of much research. In particular, NT is considered to have an important role in retaining soil water (Sekaran et al., 2021), controlling soil and water losses (Jia et al., 2019), improving soil structure, providing nutrients (Wang et al., 2019b), reducing straw burning, and protecting the ecological environment (Wang and Wang, 2022). Nevertheless, due to the constraints in the observation methods and research techniques, studies on the wind erosion in the arable Mollisol region in Northeast China are limited. Wind erosion is typically measured *via* wind tunnel tests and field measurements. More specifically, wind tunnel tests are employed to explore the quantitative relationships of the wind erosion influencing factors (Feizi et al., 2019). For example, Lyu et al. (2021) determined wind speed as the initiating force of wind erosion, with a positive correlation between wind speed and wind erosion intensity. Soil moisture content in arable land is reported to visually reflect the climatic state of the field and is negatively correlated with the wind erosion rate (Shahabinejad et al., 2019). Wassif et al. (2020) demonstrated the ability of straw mulching in NT to effectively reduce wind erosion efficiency, with a wind-induced soil erosion rate under NT observed to be 62.9% lower than that with conventional tillage (CT). However, compared to wind tunnel tests, field observations have the advantage of fully revealing the entire wind erosion process on arable land. The key influencing factors of wind erosion of arable land are a function of climatic conditions and tillage practices (Hong et al., 2020). These factors vary greatly across regions, and hence research on the primary controlling factors of wind erosion and the correlation between them is essential for the arable land in the Mollisol region.

The research in the current study was performed in the Mollisol region of Northeast China, a common experimental site for water erosion (Chen et al., 2019a) and freeze-thaw erosion (Chen et al., 2019b) under different tillage treatments. A revised wind erosion sampler was created by our research group to collect and measure soil particles by wind erosion, with specific applicability in Northeast China (Yang, 2018; Chen et al., 2019c). The principal aims of this study are to: 1) identify the wind erosion characteristics under NT and CT in the arable Mollisol region in Northeast China; and 2) analyze the factors influencing wind erosion under different tillage treatments and the correlation between them.

Materials and methods

Study site

The study site is located at the Hailun Monitoring and Research Station of Soil and Water Conservation, Northeast Institute of Geography and Agroecology, Chinese Academy of Sciences, Heilongjiang Province (Figure 1). It is situated in the center of the typical Mollisol zone within Northeast China (47°23′ N, 126°51′ E; 240 m altitude) (Chen et al., 2019a). The mean annual temperature is 1.5°C (34.7°F), and the mean annual precipitation is approximately 530 mm, with 65% occurring from June to August. Total annual solar radiation is 4600 MJ m^{-2}, and annual available accumulated temperature (≥10°C [50°F]) is 2,450°C (4,442°F). The soil is a loess-derived fine, mixed, superactive Oxyaquic Haplocryoll with a light silty clay texture, slightly acidic reaction, and 4.4% SOM (Table 1). The soil classification information was obtained from Liu et al. (2015) and the guidelines from the Key to Soil Taxonomy (Soil Survey Staff, 2014).

Wind erosion occurs during high wind speed events. The maximum wind speeds were measured in order to clarify the

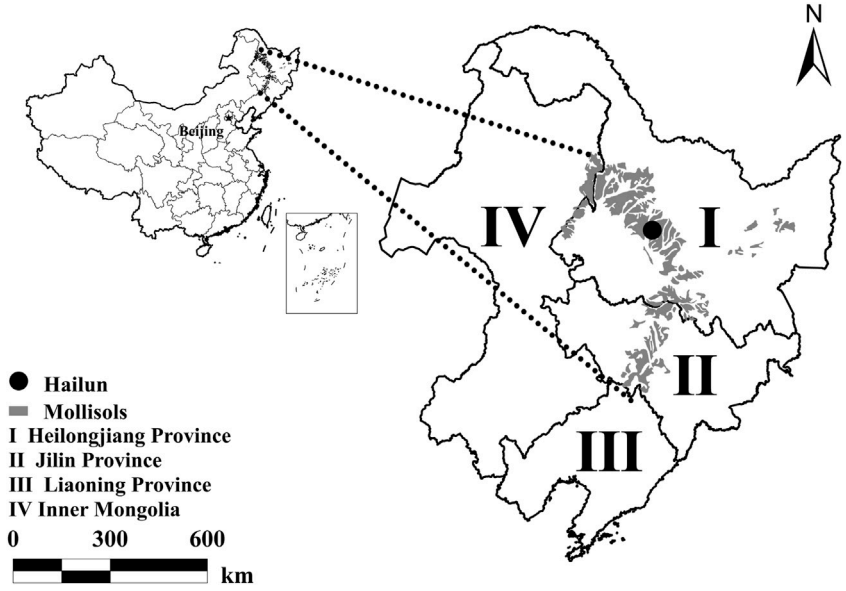

FIGURE 1
Location of the study area.

TABLE 1 Basic physical–chemical properties in the study area.

Soil texture (%)			Texture	Bulk density (g/cm^3)	SOM (g/kg)
Sand	Silt	Clay			
25.5	33.7	40.8	Loam clay	1.12	44.1

occurrence of high wind events from 2009 to 2018 occurring at the study site (Figure 2). Approximately 7% of wind speed observations exceed 14 m·s^{-1} from April to June. This period corresponds to less rainfall and field coverage in the black soil region of Northeast China compared to the rest of the year. Therefore, the subsequent field observations were performed from April to June.

Layout of the experiment

Experiments were performed under no-tillage (NT) and conventional tillage (CT) treatments in the field during 2016–2018. The size of each experiment plot was 3.2 h m^2. For the NT treatment, all biomass (with the exception of the harvested seeds) were cut and uniformly distributed across the plot in autumn. No other soil tillage practices were implemented. For the CT treatment, all aboveground biomass was removed manually and ridged via rotary tillage in the autumn. The field was ridged twice every 15 days after sowing (Chen et al., 2011).

Different field measurements were adopted to collect the erodible particles based on the three wind erosion transport modes, namely, creep, saltation, and suspension. In particular, the large-sized particles (0.5–1 mm diameter) generally creep with the rolling movement along the surface. Small-sized particles (<0.1 mm diameter) are suspended in the air for a long time, moving with the wind and subsequently falling slowly. New small particles are constantly added, and these particles move forward in a suspended state. Medium-sized particles (0.1–0.5 mm diameter) break away from the surface and make continuous leaping movements, denoted as saltation (Cornelis, 2006; Blanco and Lal, 2008; Avecilla et al., 2018). Based on the existing research and current field situation in the study area (Fryrear, 1986; Shao, 2001; Bagnold, 2012), we selected a set of devices to collect and measure the soil particles under the three transport forms (creep, saltation, and suspension) of the actual wind erosion in the field (Figure 3).

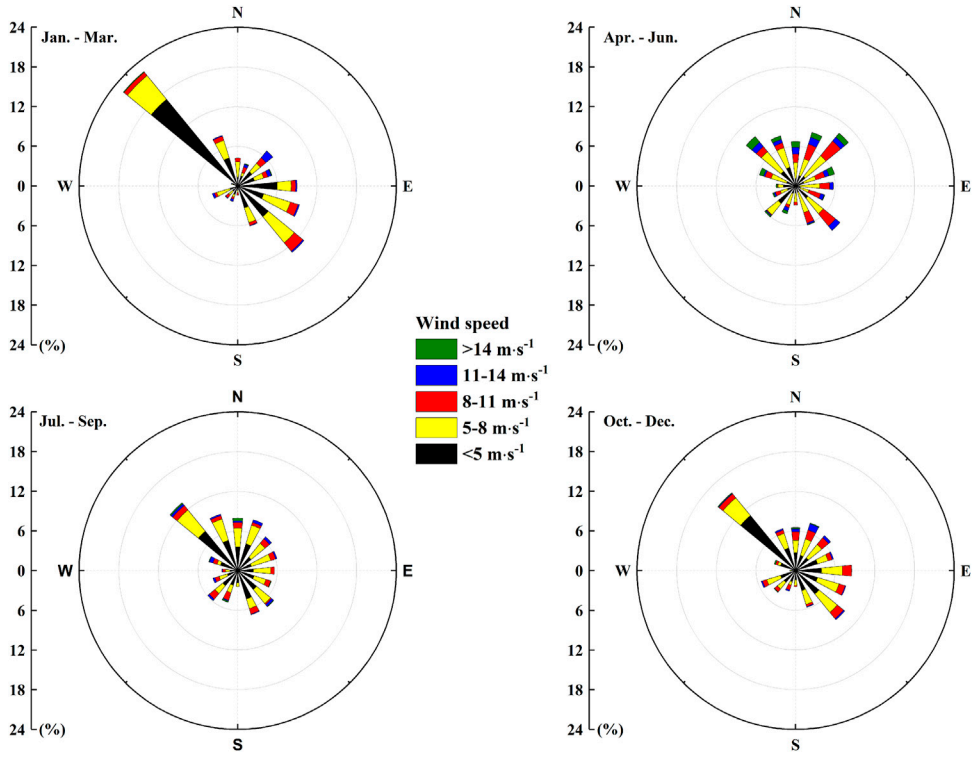

FIGURE 2
Wind rose diagrams for January–March, April–June, July–September, and October–December during 2007–2018 in the study area.

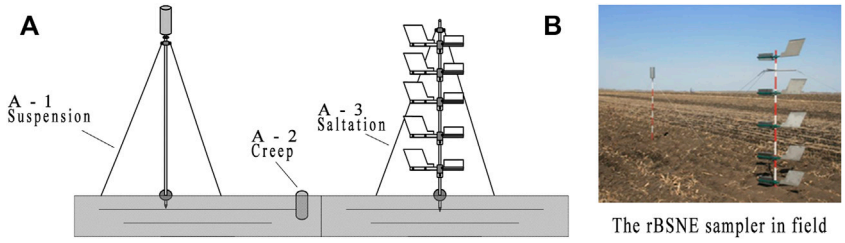

FIGURE 3
Collection system for soil erosion used in this study. (**A-1**, **A-2,** and **A-3** are the collection subsystems of soil particle by suspension, creep, and saltation, respectively; **(B)** is the rBSNE sampler in the field).

The collection system for the wind erosion particles consists of three subsystems (Yang, 2018). The suspension subsystem includes one bucket (0.2 m height, 0.16 m diameter) and one bracing piece (2 m height), and collects the deposition of suspended materials (Figure 3-A-1). The creep subsystem contains one bucket (0.2 m height, 0.16 m diameter, Figure 3-A-2), with the barrel mouth level to the ground in order to increase accuracy (Bagnold, 1941; Liu et al., 2014; Kang et al., 2017). The last collecting subsystem is the revised Big Spring Number Eight (rBSNE) sampler for collecting materials by saltation at five heights (0.2, 0.5, 1.0, 1.5, 2.0 m). This system is based on the Big Spring Number Eight (BSNE) sampler (Figure 3A-3). However, we altered the original internal baffle from a large pore screen structure to a reverse louver baffle structure. Once air enters the sampler, the air speed is reduced and the suspended soil particles settle into the collection pan. A 60-mesh screen is used as the air discharge channel. The louver baffle reduces the movement of deposited soil particles, possibly increasing the loss of fine soil particles from the top of the 60-mesh screen (Chen et al., 2019c). Wind tunnel pretests reveal the retention efficiency of the soil particles by the rBSNE sampler to be significantly higher than that of the BSNE sampler under different wind speeds, particularly for particle sizes less than 0.25 mm at wind speeds

TABLE 2 Retention rate of soil particles (%) by the BSNE sampler and rBSNE samplers for different material sizes under different wind speeds.

Wind speed (m•s^{-1})	The size of soil particles							
	0–0.075 mm		0.078–0.25 mm		0.25–0.5 mm		0.5–1 mm	
	BSNE	rBSNE	BSNE	rBSNE	BSNE	rBSNE	BSNE	rBSNE
10	89.70B	98.40A	94.27B	98.57A	99.06A	99.17A	99.25A	99.35A
12	58.80B	94.70A	90.13B	97.63A	98.22A	98.52A	98.42A	98.66A
15	47.20B	88.30A	83.10B	96.20A	96.50B	98.10A	97.71A	98.18A
20	35.90B	83.50A	71.70B	92.50A	91.90B	95.70A	94.70B	97.20B

Different uppercase letters (A–B) indicate significant differences at $p < 0.05$ between the BSNE, and rBSNE, samplers.

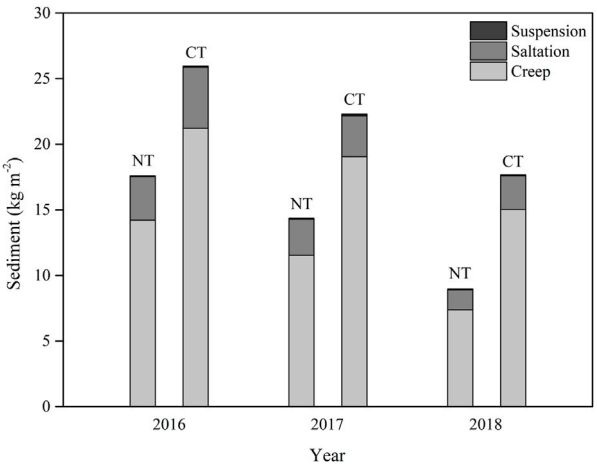

FIGURE 4
Total erodible particles (creep, saltation, and suspension) during 1st April to 1st June under different tillage treatments in Northeast China by the rBSNE sampler (2016–2018).

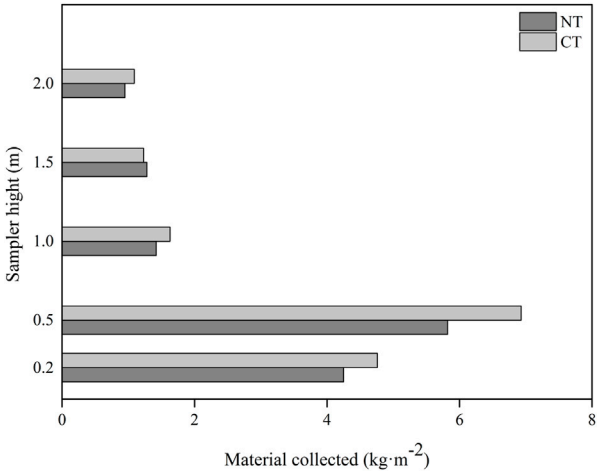

FIGURE 5
Total erodible particles (saltation) by the rBSNE sampler at different height (0.2, 0.5, 1.0, 1.5, and 2.0 m) from the ground under different tillage during 1st April to 1st June in 2017.

above 10 m·s–^{1} (Table 2). In addition, the rBSNE sampler has a tail and can be freely rotated (Figure 3A-3). Thus, it can always be freely rotated with the main wind direction and the entrance of the sampler always directly facing the erosional wind direction.

The wind erosion measurements were repeated three times for each tillage management. In order to avoid the influence of long distance transport of wind erosion on the results, each collection device was separated by a distance of 50 m. To further analyze the relationship between soil, wind erosion, and environmental factors, we measured soil water content, precipitation, and wind speed in the field during the observation period.

Statistical analysis

All statistical analyses were performed using the SPSS 16.0 (SPSS Inc., USA). Independent sample t-tests were performed to compare the retention rate of the material by the BSNE and rBSNE samplers. The correlation between the total erodible particles collected by the sampler, rainfall, average wind speed, maximum wind speed, and soil water content was also evaluated based on the linear correlation analysis. Differences were considered significant based on Tukey's multiple comparison using a 0.05 level of probability. All data were expressed as means.

Results

Characteristics of wind erosion in the field

Figure 4 presents the total amount of erodible particles (creep, saltation, and suspension) for the NT and CT treatments in Northeast China from April to June during

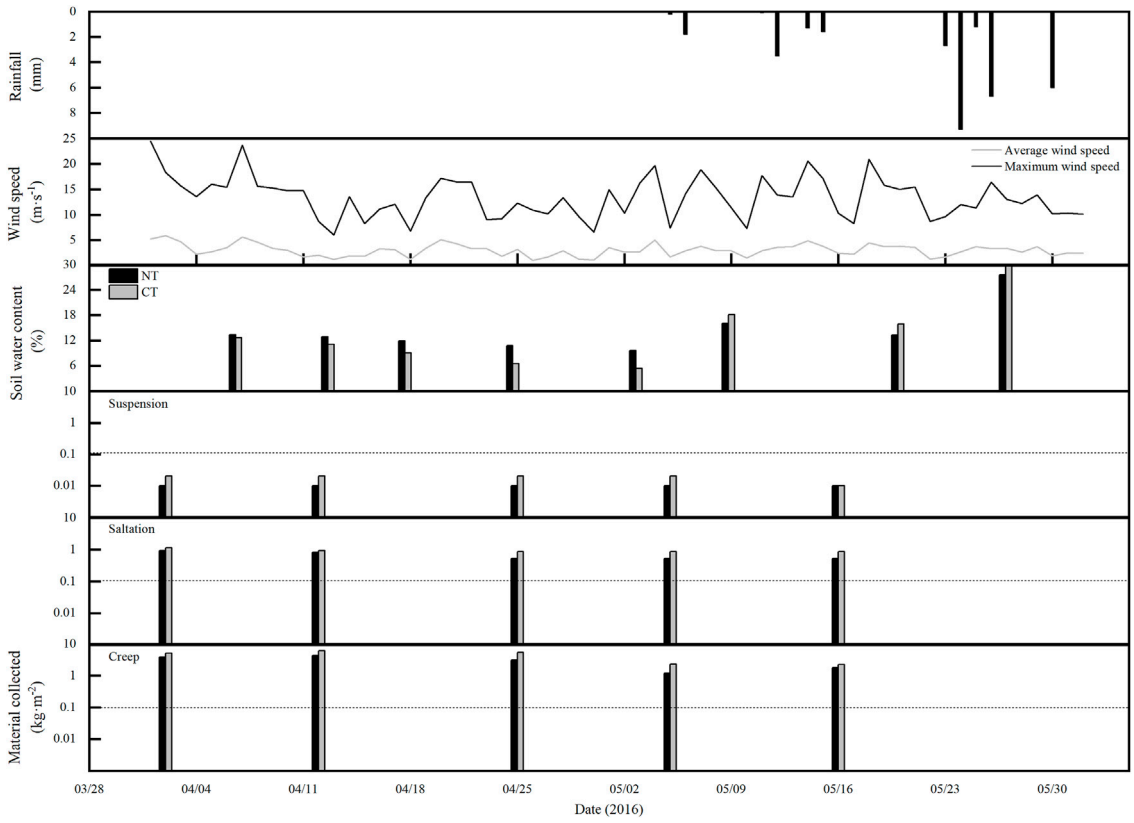

FIGURE 6
Rainfall, average wind speed, maximum wind speed, soil water content, and erodible particles (creep, saltation, and suspension) under different tillage treatment over the period from 1st April to 1st June (2016–2018).

2016–2018. Wind erosion was mainly caused by creep (81.15% and 84.07%, respectively), followed by saltation (18.30% and 15.51%, respectively), and suspension (0.55% and 0.42%, respectively).

Erodible particles in saltation mode were collected at five heights (0.2, 0.5, 1.0, 1.5, and 2.0 m) in the NT and CT treatments (Figure 5). The most erodible particles were collected by the sampler at 0.5 m height, with the NT and CT treatments collecting 5.82 kg·m^{-2} and 6.93 kg·m^{-2} of erodible particles per unit area, respectively. Above 0.5 m, the amount of erodible particles collected by the sampler was observed to decrease with increasing height.

Wind erosion under different tillage treatments

NT and CT are currently the dominant tillage practices for the Mollisol region in Northeast China. Our results reveal the erodible particles of creep, saltation, and suspension under the CT treatment to exceed those of the NT treatment by 1.73, 1.41, and 1.35 times, respectively (Figure 4). Moreover, the amount of erodible particles of saltation under the NT treatment was significantly lower than that of the CT treatment within the height range from the surface to 0.5 m (Figure 5).

Correlations between wind erosion and other factors

Figure 6 depicts the wind erosion and environmental factors observations in farmland from 2016 to 2018. The total daily precipitation from April to June was determined as 34.4, 40.6, and 51.6 mm, for 2016–2018, respectively. Due to the uncertainty of natural conditions, the distribution of rainfall and wind varied greatly from 2016 to 2018. The maximum wind speed from 2016 to 2018 ranged between 6.0-24.5 m·s^{-1}, 6.4–23.1 m·s^{-1}, and 4.0–12.3 m·s^{-1}, respectively. The soil moisture content increased with the increase in precipitation. Furthermore, more erodible particles (creep, saltation, and suspension) were observed during

TABLE 3 Correlation between the total erodible particles collected by the sampler (TMC, kg·m^{-2}), rainfall (RF, mm), average wind speed (AWS, m·s^{-1}), maximum wind speed (MWS, m·s^{-1}), and soil water content (SWC, %) in NT and CT.

Tillage treatment	Correlation index					
NT		TMC (kg·m^{-2})	RF (mm)	AWS (m·s^{-1})	MWS (m·s^{-1})	SWC (%)
	TMC (kg·m^{-2})	1	0.164	0.416**	0.427**	−0.185
	RF (mm)		1	0.166	−0.115	0.523*
	AWS (m·s^{-1})			1	0.537**	−0.061
	MWS (m·s^{-1})				1	−0.298
	SWC (%)					1
CT		TMC (kg·m^{-2})	RF (mm)	AWS (m·s^{-1})	MWS (m·s^{-1})	SWC (%)
	TMC (kg·m^{-2})	1	0.198	0.382**	0.326**	−0.203
	RF (mm)		1	0.166	−0.115	0.591*
	AWS (m·s^{-1})			1	0.537**	−0.054
	MWS (m·s^{-1})				1	−0.296
	SWC (%)					1

* indicates a significant correlation ($p < 0.05$); ** indicates a very significant correlation ($p < 0.01$).

periods of higher wind speeds and lower soil moisture content (e.g., 1st to 13th April in 2016; third to fifth May in 2017; and 16th to 20th May in 2018), while the reverse was observed for periods of lower wind speeds and higher soil moisture content (e.g., second to sixth May in 2016; fifth to sixth May in 2017; and 15th to 21st April in 2018).

Table 3 reports the correlation between meteorological factors, soil water content, and sand transport under different tillage treatments. A significant positive correlation was observed between the total erodible particles collected by the sampler and both mean and maximum wind speeds under both the NT and CT treatments. In addition, wind erosion under the CT treatment exhibited a stronger relationship with rainfall and soil moisture than under the NT treatment.

Discussion

Affected by wind erosion and tillage, large quantities of soil particles are transported and lost from the surface of arable land each year during spring cultivation. Our results indicate surface creep as the major erosion type during the total transport of the Mollisol region in Northeast China. This is in agreement with Zobeck et al. (2003), who determined that creep transport accounted for 40% of total wind erosion. However, other studies have found saltation to be the dominant transport form of wind erosion, with the potential to provide power for creep and suspension (Martin and Kok, 2017; Liu and Bo, 2019). Under natural environments, a gradual transition is observed between the three erodible particles' movement patterns, and each transition mode is related to the surface shear stress and size of the erodible particles (Zhang et al., 2021). In general, the particle size cut-off points for suspension, saltation, and creep wind erosion are approximately 100 and 500 μm (Fattahi et al., 2020). Previous research has suggested that when erodible particles gain momentum and change their resting state, the majority experience creep motion prior to saltation (Jarrah et al., 2020; Swann et al., 2020). As the creeping motion of the particles continues, more particles collide with each other, leading to a gradual increase in the energy of some erodible particles. The particles move faster than their wind-up velocity, inducing the saltation motion of some of the small particles (Andreotti et al., 2002; Pähtz et al., 2020). In addition, erodible particles moving under saltation can continuously strike up fine particles during wind erosion, which are blown away in the form of suspension under high winds, eventually falling back to the land surface (Kheirabadi et al., 2018). Small diameter (<100 μm), long transport distances, and prolonged suspension of erodible particles under suspension can complicate the monitoring and collection of suspension, resulting in sand transport rates from suspension often being neglected in wind erosion field studies (Jarrah et al., 2020). Similar to many studies, only a small number of erodible particles under suspension was observed at the height of 2 m in our results. In addition, clear differences were observed in the number of erodible particles under saltation between heights (Figure 5). The vertical distribution of erodible particles under saltation is influenced by two major factors, namely, the wind speed and the number of erodible particles (Yang et al., 2019). A large number of erodible particles were observed in the soil surface layer. The high roughness value of the surface layer slowed down the wind speed at this layer, and thus there was not enough power to carry the erodible particles out of the farmland surface. This agrees with Yang et al. (2019), who suggested that the high roughness value of the surface layer

relative to other heights slowed down the wind speed and makes it less likely to erode particles, resulting in fewer erodible particles in the near-surface airflow relative to other heights in the vertical profile. The complex and microscopic exchanges of erodible particles and airflow increase with height (Tan et al., 2014). The current literature has not reached a consensus on the erodible particle distribution in the vertical profile of the saltation layers. Li et al. (2008) determined a relationship between the transport flux of erodible particles and the sand grain diameter from the soil surface to 20 cm height. The authors demonstrated that for erodible particles with diameters greater than 355 μm, the particle mass decreases with height according to a power law; otherwise, the mass decreases exponentially with height. Thus, the erodible particles must overcome the effects of gravity in order to maintain the mass in the saltation layer vertical profiles. Yang et al. (2019) identified a turning point for the vertical profile distribution of erodible particles. However, the number of erodible particles was observed to decrease, reducing the materials collected by the sampler. The launch velocities of erodible particles vary with their size (Li and Zhou, 2007), and thus the aeolian sand movement of the saltation layer fluctuates. This phenomenon is complex during the process of wind erosion. Our results are consistent with the work of Jia et al. (2015), who determined the wind erosion height of the wind-sand flow during wind erosion in black soil to be within 60 cm. This may be attributed to the similar grain-size fraction observed in both studies.

Different tillage treatments can produce highly variable results in terms of the wind erosion degree of agricultural soils. Our results agree with Xiao et al. (2021), who demonstrated that the sand transport of farmland under NT was significantly smaller than that under CT. Mozaffari et al. (2021) also reported wind erosion of tilled farmland to be more severe than untilled farmland, with the wind erosion rate of farmland soils exhibiting a decreasing trend as the no-tillage treatment duration increased. Agricultural soils affected by wind erosion can form a rough surface layer. When this occurs, the tillage treatment of the farmland can be a key factor influencing the further development of wind erosion. The NT treatment was observed to exert less damage to the surface soil. The surface stubble and crop straw mulch of NT may play a protective role on the surface, improving the surface aerodynamic roughness and weakening surface wind erosion (Asensio et al., 2015; Wang et al., 2019a). In addition, crop straw can effectively slow down soil evaporation, maintain soil moisture and increase the soil compactness, which is conducive to increasing the initial wind speed of eroded particles on the surface and strengthening the resistance of the soil surface to wind erosion (Shojaei et al., 2019; Xiao et al., 2021). However, the CT treatment requires frequent tilling of the surface layer of the farmland, which can create a ridge-like undulating terrain in the farmland and cause greater damage to the surface layer of the farmland soil. Thus, the CT treatment may increase the roughness of the soil surface, changing the airflow field structure and significantly affecting the magnitude and distribution of airflow-soil surface interaction forces (Yang et al., 2020; Carretta et al., 2021). Furthermore, the soil surface layer induced damage as the tillage process may have provided more erodible soil particles for wind erosion, promoting the occurrence of wind erosion on farmland and ultimately influencing the outcome of wind erosion on farmland (Labiadh, 2017; Pi et al., 2021). Thus, tillage treatment is a key anthropogenic influencing factor on wind erosion. The black soil region of Northeast China is an important commodity grain production base and its output is fundamental in ensuring national food security (Shen et al., 2020). As the tillage treatment is one of the most important factors affecting crop yield (Wang et al., 2019a), our research group also measured the annual output of the NT and CT treatments investigated in the current study. In particular, the yield from corn planted in 2018 under NT and CT was determined as 9,000 $kg{\cdot}hm^{-2}$ and 10,000 $kg{\cdot}hm^{-2}$, respectively. Although the crop yield of NT was lower than that of CT, which started in the year of 2007, the prevention effect of NT on wind erosion must be considered. Moreover, our research group also observed higher yields under NT compared to CT in the arable Mollisol region of Northeast China following 13 years of NT treatment (Guo et al., 2021). Therefore, NT can be potentially applied to enhance crop yield and effectively prevent wind erosion in the Mollisol region of Northeast China.

Zhang et al. (2019) determined wind erosion to be a result of a combination of factors. Our results suggest natural (wind speed and precipitation) and human (tillage management) factors to be the main influences behind wind erosion in arable land (Figure 6). We observed that the number of erodible particles on farmland increases with wind speed (e.g., 16th to 20th May in 2017 and 20th to 25th April in 2018) and decreases with increasing rainfall (e.g., 4th to 7th May in 2017 and 4th to 16th April in 2018). This has been confirmed in previous literature, whereby the amount of material accumulated each year by wind erosion was closely related to the wind speed and the rainfall amount in a given year (Pierre et al., 2018; de Oro et al., 2019; Pi et al., 2021). The soil particles begin to move when the wind speed is greater than the maximum threshold of frictional velocity between the soil particles and the surface of the farmland (Bergametti et al., 2016).

In addition to wind speed, differences in soil water content are also a major factor influencing wind erosion on agricultural soils. Our results reveal rainfall and soil moisture content to be maximized from 7 to 9 May in 2017 and from 19th to 21st April in 2018, corresponding to relatively lower levels of wind erosion (Figures 6b, Figures 6c).

This agrees with the work of Uzun et al. (2017), who reported the force required to separate soil particles to be greater at higher soil moisture content under the action of water in the film between the soil particles. Under wet conditions, the tension between water molecules and soil particles in the soil increases the cohesion between the particles, and thus an increase in soil moisture content enhances the cohesion and agglomeration of the soil, which ultimately increases the starting wind speed of the soil (Yuge and Anan, 2019; Wang et al., 2021). Therefore, when soil moisture content is high, it is difficult for soil particles to move even if the wind reaches the starting wind speed of the soil particles.

Conclusion

In the current study, we measured the three transport modes of wind erosion (i.e., creep, saltation, and suspension) under NT and CT on the arable Mollisol region in Northeast China during the years 2016–2018. The results identify creep as the dominant transport mode of wind erosion in the study region, causing 81.15% and 84.07% of the entire wind erosion under the NT and CT treatments. The most erodible particles by saltation were collected at 0.5 m above the ground (when comparing heights from 0.2 to 2 m). These observations can help our team to implement future prevention programs for the wind erosion of the arable Mollisol region in Northeast China.

Our results also reveal wind erosion on agricultural land to be influenced by tillage practices, rainfall, wind speed, and soil moisture content. We found a significant ($p \leq 0.05$) positive correlation between the total erodible particles collected by the sampler and both maximum and average wind speeds in the study area. Compared to the CT treatment, the NT treatment was more effective in reducing the erodible particles of creep and saltation in the surface soil of the cropland. This indicates the ability of mulching straw to effectively reduce wind erosion near arable soil surfaces. As the CT treatment lacked soil surface cover, wind erosion under the CT treatment was more susceptible to rainfall and soil moisture than that under the NT treatment. This may increase the occurrence of soil erosion on farmland.

This work concludes that the use of NT treatment can reduce soil loss by wind erosion on the farmland of Mollisols in Northeast China.

Data availability statement

The original contributions presented in the study are included in the article/Supplementary Material; further inquiries can be directed to the corresponding author.

Author contributions

SC designed the field observation and wrote the manuscript. XZ and WH conducted statistical analysis. JL and MG performed the observation and collected data. All authors contributed to the writing—reviewing and editing.

Funding

This research was funded by the projects of the National Key Research and Development Program of China (Grant No. 2021YFD1500700), the National Science Foundation of China (Grant No. 42177312), the project of Scientific and Technological Re-search Program of Chongqing Municipal Education Commission (Grant No. KJQN20200837), the project of Scientific Research Foundation of Chongqing Technology and Business University (Grant No. 1956027), and Major Theoretical Research Projects in Philosophy and Social Sciences of Chongqing Education Commission (Grant No. 19SKZDZX10) and Major Projects of Key Research Base of Humanities and Social Sciences of the Ministry of Education (Grant No. 16JJD790064).

Acknowledgments

The authors would like to thank the National Key Research and Development Program of China, Scientific and Technological Research Program of the Chongqing Municipal Education Commission, and Chongqing Technology and Business University for funding this research. They also wish to thank the Scientific Data Center of Northeast Black Soil, National Earth System Science Data Sharing Infrastructure, National Science and Technology Infrastructure of China (http://northeast.geodata.cn), for supporting the meteorological data.

Conflict of interest

The authors declare that the research was conducted in the absence of any commercial or financial relationships that could be construed as a potential conflict of interest.

Publisher's note

References

Andreotti, B., Claudin, P., and Douady, S. (2002). Selection of dune shapes and velocities Part 1: Dynamics of sand, wind and barchans. *Eur. Phys. J. B - Condens. Matter* 28 (3), 321–339. doi:10.1140/epjb/e2002-00236-4

Asensio, C., Lozano, F. J., Ortega, E., and Kikvidze, Z. (2015). Study on the effectiveness of an agricultural technique based on aeolian deposition, in a semiarid environment. *Environ. Eng. Manag. J.* 14 (5), 1143–1150. doi:10.30638/eemj.2015.125

Avecilla, F., Panebianco, J. E., Buschiazzo, D. E., and de, O. (2018). A study on the fragmentation of saltating particles along the fetch distance during wind erosion. *Aeolian Res.* 35, 85–93. doi:10.1016/j.aeolia.2018.10.003

Bagnold, R. (1941). *The physics of blown sand and desert dune*. London: Methuen, 34.

Bergametti, G., Rajot, J.-L., Pierre, C., Bouet, C., and Marticorena, B. (2016). How long does precipitation inhibit wind erosion in the Sahel? *Geophys. Res. Lett.* 43 (12), 6643–6649. doi:10.1002/2016gl069324

Blanco, H., and Lal, R. (2008). *Principles of soil conservation and management*. New York: Springer.

Carretta, L., Tarolli, P., Cardinali, A., Nasta, P., Romano, N., and Masin, R. (2021). Evaluation of runoff and soil erosion under conventional tillage and no-till management: A case study in Northeast Italy. *Catena* 197, 104972. doi:10.1016/j.catena.2020.104972

Chen, S., Burras, C. L., Lili, E., and Zhang, X. (2019a). Interrelationship among slope steepness, tillage practice and rainfall properties with surface runoff and soil loss on Mollisols in Northeast China. *Arch. Agron. Soil Sci.* 65 (13), 1860–1872. doi:10.1080/03650340.2019.1579310

Chen, S., Burras, C. L., and Zhang, X. (2019b). Soil aggregate response to three freeze-thaw methods in a northeastern China Mollisol. *Pol. J. Environ. Stud.* 28 (5), 3635–3645. doi:10.15244/pjoes/99205

Chen, S., Zhang, X., Hu, W., Yang, R., Li, H., and Zhai, X. (2019c). *Measurement device of soil wind erosion on arable Mollisols regionChnia. Patent No 2018219787883*. Beijing: China: China National Intellectual Property Administration.

Chen, Y., Liu, S., Li, H., Li, X., Song, C., Cruse, R., et al. (2011). Effects of conservation tillage on corn and soybean yield in the humid continental climate region of Northeast China. *Soil Tillage Res.* 115, 56–61. doi:10.1016/j.still.2011.06.007

Chi, W., Zhao, Y., Kuang, W., and He, H. (2019). Impacts of anthropogenic land use/cover changes on soil wind erosion in China. *Sci. Total Environ.* 668, 204–215. doi:10.1016/j.scitotenv.2019.03.015

Cornelis, W. M. (2006). *Hydroclimatology of wind erosion in arid and semiarid envirmonments, Dryland ecohydrology*. New York: Springer, 141–159.

de Oro, L. A., Colazo, J. C., Avecilla, F., Buschiazzo, D. E., and Asensio, C. (2019). Relative soil water content as a factor for wind erodibility in soils with different texture and aggregation. *Aeolian Res.* 37, 25–31. doi:10.1016/j.aeolia.2019.02.001

Fattahi, S. M., Soroush, A., and Huang, N. (2020). Biocementation control of sand against wind erosion. *J. Geotech. Geoenviron. Eng.* 146 (6), 04020045. doi:10.1061/(ASCE)GT.1943-5606.0002268

Feizi, Z., Ayoubi, S., Mosaddeghi, M. R., Besalatpour, A. A., Zeraatpisheh, M., and Rodrigo-Comino, J. (2019). A wind tunnel experiment to investigate the effect of polyvinyl acetate, biochar, and bentonite on wind erosion control. *Arch. Agron. Soil Sci.* 65 (8), 1049–1062. doi:10.1080/03650340.2018.1548765

Fryrear, D. W. (1986). A field dust sampler. *J. Soil Water Conserv.* 41 (2), 117–120.

Guo, M., Li, J., Li, J., and Zhang, X. (2021). Changes of soil structure and function after 16-year conservation tillage in black soil. *Trans. Chin. Soc. Agric. Eng.* 37 (22), 108–118. (In Chinese). doi:10.11975/j.issn.1002-6819.2021.22.012

Hong, C., Chenchen, L., Xueyong, Z., Huiru, L., Liqiang, K., Bo, L., et al. (2020). Wind erosion rate for vegetated soil cover: A prediction model based on surface shear strength. *Catena* 187, 104398. doi:10.1016/j.catena.2019.104398

Jarrah, M., Mayel, S., Tatarko, J., Funk, R., and Kuka, K. (2020). A review of wind erosion models: Data requirements, processes, and validity. *Catena* 187, 104388. doi:10.1016/j.catena.2019.104388

Jia, H., Wang, G., Guo, L., Zhuang, J., and Tang, L. (2015). Wind erosion control utilizing standing corn residue in Northeast China. *Soil Tillage Res.* 153, 112–119. doi:10.1016/j.still.2015.05.009

Jia, L., Zhao, W., Zhai, R., Liu, Y., Kang, M., and Zhang, X. (2019). Regional differences in the soil and water conservation efficiency of conservation tillage in China. *Catena* 175, 18–26. doi:10.1016/j.catena.2018.12.012

Kang, Y., He, Q., Yang, X., Yang, F., Ali, M., and Huo, W. (2017). Research on saltation and creeping laws of wind - blown currents based on field observations. *J. Arid. Land Resour. Environ.* 31 (5), 119–125. (In Chinese). doi:10.13448/j.cnki.Jalre.2017.154

Katra, I., Gross, A., Swet, N., Tanner, S., Krasnov, H., and Angert, A. (2016). Substantial dust loss of bioavailable phosphorus from agricultural soils. *Sci. Rep.* 6 (1), 24736–24737. doi:10.1038/srep24736

Kheirabadi, H., Mahmoodabadi, M., Jalali, V., and Naghavi, H. (2018). Sediment flux, wind erosion and net erosion influenced by soil bed length, wind velocity and aggregate size distribution. *Geoderma* 323, 22–30. doi:10.1016/j.geoderma.2018.02.042

Labiadh, M. (2017). *Impact of ploughing techniques on wind erosion: Field experiments assessment, euro-mediterranean conference for environmental integration*. New York: Springer, 1269–1270.

Li, W., and Zhou, Y. (2007). Statistical behaviors of different–sized grains lifting off in stochastic collisions between mixed sand grains and the bed in aeolian saltation. *J. Geophys. Res.* 112 (D22), D22106–D22456. doi:10.1029/2006JD007888

Li, Z., Feng, D., Wu, S., Borthwick, A. G. L., and Ni, J. R. (2008). Grain size and transport characteristics of non-uniform sand in aeolian saltation. *Geomorphology* 100 (3-4), 484–493. doi:10.1016/j.geomorph.2008.01.016

Liu, F., Hao, Y., Xin, Z., Chen, H., Xu, J., and Zhao, Y. (2014). The surface aeolian-sand flow structure in the noetheastern margin of the Ulanbuh Desert. *J. Desert Res.* 34 (5), 1200–1207. (In Chinese). doi:10.7522/j.issn.1000-694X.2014.00096

Liu, L., and Bo, T.-L. (2019). A study on the initiation of saltation in the model of wind-blown sand transport considering the effect of turbulence. *Granul. Matter* 21 (3), 78–15. doi:10.1007/s10035-019-0934-2

Liu, S., Zhang, X.-Y., Kravchenko, Y., and Iqbal, M. A. (2015). Maize (Zea mays L.) yield and soil properties as affected by no tillage in the black soils of China. *Acta Agric. Scand. Sect. B —. Soil & Plant Sci.* 65 (6), 554–565. doi:10.1080/09064710.2015.1036304

Liu, X., Li, H., Zhang, S., Cruse, R. M., and Zhang, X. (2019). Gully erosion control practices in Northeast China: A review. *Sustainability* 11 (18), 5065. doi:10.3390/su11185065

Lyu, X., Li, X., Wang, H., Gong, J., Li, S., Dou, H., et al. (2021). Soil wind erosion evaluation and sustainable management of typical steppe in Inner Mongolia, China. *J. Environ. Manage.* 277, 111488. doi:10.1016/j.jenvman.2020.111488

Martin, R. L., and Kok, J. F. (2017). Wind-invariant saltation heights imply linear scaling of aeolian saltation flux with shear stress. *Sci. Adv.* 3 (6), e1602569–10. doi:10.1126/sciadv.1602569

Mozaffari, H., Rezaei, M., and Ostovari, Y. (2021). Soil sensitivity to wind and water erosion as affected by land use in southern Iran. *Earth* 2 (2), 287–302. doi:10.3390/earth2020017

Pähtz, T., Clark, A. H., Valyrakis, M., and Durán, O. (2020). The physics of sediment transport initiation, cessation, and entrainment across aeolian and fluvial environments. *Rev. Geophys.* 58 (1), e2019RG000679. doi:10.1029/2019RG000679

Pi, H., Webb, N. P., Huggins, D. R., and Sharratt, B. (2021). Influence of physical crust cover on the wind erodibility of soils in the inland Pacific Northwest, USA. *Earth Surf. Process. Landf.* 46 (8), 1445–1457. doi:10.1002/esp.5113

Pierre, C., Kergoat, L., Hiernaux, P., Baron, C., Bergametti, G., Rajot, J. L., et al. (2018). Impact of agropastoral management on wind erosion in Sahelian croplands. *Land Degrad. Dev.* 29 (3), 800–811. doi:10.1002/ldr.2783

Sekaran, U., Sagar, K. L., and Kumar, S. (2021). Soil aggregates, aggregate-associated carbon and nitrogen, and water retention as influenced by short and long-term no-till systems. *Soil Tillage Res.* 104885, 104885. doi:10.1016/j.still.2020.104885

Shahabinejad, N., Mahmoodabadi, M., Jalalian, A., and Chavoshi, E. (2019). *In situ* field measurement of wind erosion and threshold velocity in relation to soil properties in arid and semiarid environments. *Environ. Earth Sci.* 78 (16), 501–522. doi:10.1007/s12665-019-8508-5

Shao, Y. (2001). A model for mineral dust emission. *J. Geophys. Res.* 106 (D17), 20239–20254. doi:10.1029/2001JD900171

Sharratt, B. S., Kennedy, A. C., Hansen, J. C., and Schillinger, W. F. (2018). Soil carbon loss by wind erosion of summer fallow fields in Washington's dryland wheat region. *Soil Sci. Soc. Am. J.* 82 (6), 1551–1558. doi:10.2136/sssaj2018.06.0214

Shen, H., Wang, D., Wen, L., Zhao, W., and Zhang, Y. (2020). Soil erosion and typical soil and water conservation measures on hillslopes in the Chinese Mollisol region. *Eurasian Soil Sc.* 53 (10), 1509–1519. doi:10.1134/S1064229320100178

Shojaei, S., Ardakani, M. A. H., Sodaiezadeh, H., jafari, M., and afzali, S. f. (2019). Optimization of parameters affecting organic mulch test to control erosion. *J. Environ. Manage.* 249, 109414. doi:10.1016/j.jenvman.2019.109414

Soil Survey Staff (2014). *Keys to soil Taxonomy*. 12th ed. Washington, DC: USDA-Natural Resources Conservation Service.

Swann, C., Sherman, D., and Ewing, R. (2020). Experimentally derived thresholds for windblown sand on Mars. *Geophys. Res. Lett.* 47 (3), e2019GL084484. doi:10.1029/2019GL084484

Tan, L., Zhang, W., Qu, J., Du, J., Yin, D., and An, Z. (2014). Variation with height of aeolian mass flux density and grain size distribution over natural surface covered with coarse grains: A mobile wind tunnel study. *Aeolian Res.* 15, 345–352. doi:10.1016/j.aeolia.2014.06.008

Uzun, O., Kaplan, S., Basaran, M., Deviren Saygın, S., Youssef, F., Nouri, A., et al. (2017). Spatial distribution of wind-driven sediment transport rate in a fallow plot in Central Anatolia, Turkey. *Arid Land Res. Manag.* 31 (2), 125–139. doi:10.1080/15324982.2016.1276487

Uzun, O., Kaplan, S., Ince, K., Basaran, M., and Erpul, G. (2020). Spatially and temporally assessing event-based wind erosion in adjacent plots of fallow and wheat cultivation in the Central Anatolia, Turkey. *Arch. Agron. Soil Sci.* 1-15, 661–675. doi:10.1080/03650340.2020.1849624

Wang, K., and Wang, H. (2022). Integrated cost dataset under the whole life cycle of biogas, straw and coal power generation. *J. Glob. Change Data Discov.* 1, 53–57. doi:10.3974/geodp.2022.01.07

Wang, X., Fan, J., Xing, Y., Xu, G., Wang, H., Deng, J., et al. (2019a). The effects of mulch and nitrogen fertilizer on the soil environment of crop plants. *Adv. Agron.* 153, 121–173. doi:10.1016/bs.agron.2018.08.003

Wang, X., Li, S., Sun, Y., Zhang, C., and Liu, G. (2021). Influence of freeze–thaw cycling on the soil mechanical properties of open-pit mine dump under different moisture contents. *Environ. Earth Sci.* 80 (7), 1–10. doi:10.1007/s12665-021-09592-9

Wang, X., Qi, J.-Y., Zhang, X.-Z., Li, S.-S., Virk, A. L., Zhao, X., et al. (2019b). Effects of tillage and residue management on soil aggregates and associated carbon storage in a double paddy cropping system. *Soil Tillage Res.* 194, 104339. doi:10.1016/j.still.2019.104339

Wassif, O. M., Meselhy, A. A., Sharkawy, S. F., and Ali, A. A. (2020). Quantify impact of wind erosion on organic matter content under management practices, Wadi El Raml, NWCZ, Egypt. Egypt. *Egypt. J. Desert Res.* 70 (1), 83–102. doi:10.21608/EJDR.2020.33688.1073

Xiao, L., Li, G., Zhao, R., and Zhang, L. (2021). Effects of soil conservation measures on wind erosion control in China: A synthesis. *Sci. Total Environ.* 778, 146308. doi:10.1016/j.scitotenv.2021.146308

Xie, Y., Lin, H., Ye, Y., and Ren, X. (2019). Changes in soil erosion in cropland in northeastern China over the past 300 years. *Catena* 176, 410–418. doi:10.1016/j.catena.2019.01.026

Xu, X., Zheng, F., Wilson, G., He, C., Lu, J., and Bian, F. (2018). Comparison of runoff and soil loss in different tillage systems in the Mollisol region of Northeast China. *Soil Tillage Res.* 177, 1–11. doi:10.1016/j.still.2017.10.005

Yang, C., Geng, Y., Fu, X. Z., Coulter, J. A., and Chai, Q. (2020). The effects of wind erosion depending on cropping system and tillage method in a semi-arid region. *Agron. (Basel).* 10 (5), 732. doi:10.3390/agronomy10050732

Yang, R. (2018). *Monitoring study on wind erosion in hailun of the typical Mollisols farmland in Northeast China*. China: Northeast Agricultural University. [master's thesis]. [Harbin (Hei Longjiang)](In Chinese).

Yang, Y., Liu, L., Li, X., Shi, P., Zhang, G., Xiong, Y., et al. (2019). Aerodynamic grain-size distribution of blown sand. *Sedimentology* 66 (2), 590–603. doi:10.1111/sed.12497

Yao, Q., Liu, J., Yu, Z., Li, Y., Jin, J., Liu, X., et al. (2017). Three years of biochar amendment alters soil physiochemical properties and fungal community composition in a black soil of northeast China. *Soil Biol. Biochem.* 110, 56–67. doi:10.1016/j.soilbio.2017.03.005

Yildiz, Ş., Enc, V., Kara, M., Tabak, Y., and Acet, E. (2017). Assessment of the potential risks of airbone microbial contamination in solid recovered fuel plants: A case study in istanbul. *Environ. Eng. Manag. J.* 16 (7), 1415–1421. doi:10.30638/eemj.2017.154

Yuge, K., and Anan, M. (2019). Evaluation of the effect of wind velocity and soil moisture condition on soil erosion in andosol agricultural fields (Model experiment). *Water* 11 (1), 98. doi:10.3390/w11010098

Zhang, H., Gao, Y., Sun, D., Liu, L., Cui, Y., and Zhu, W. (2019). Wind erosion changes in a semi-arid sandy area, Inner Mongolia, China. *Sustainability* 11 (1), 188. doi:10.3390/su11010188

Zhang, P., Sherman, D. J., and Li, B. (2021). Aeolian creep transport: A review. *Aeolian Res.* 51, 100711. doi:10.1016/j.aeolia.2021.100711

Zobeck, T. M., Sterk, G., Funk, R., Rajot, J. L., Stout, J. E., and Van Pelt, R. S. (2003). Measurement and data analysis methods for field-scale wind erosion studies and model validation. *Earth Surf. Process. Landf.* 28 (11), 1163–1188. doi:10.1002/esp.1033

frontiers | Frontiers in Environmental Science

TYPE Original Research
PUBLISHED 07 October 2022
DOI 10.3389/fenvs.2022.969898

OPEN ACCESS

EDITED BY
Huawei Pi,
Henan University, China

REVIEWED BY
Beatrice Moroni,
University of Perugia, Italy
Xiao-San Luo,
Nanjing University of Information Science and Technology, China

*CORRESPONDENCE
Roger Funk,
rfunk@zalf.de

SPECIALTY SECTION
This article was submitted to Drylands, a section of the journal Frontiers in Environmental Science

RECEIVED 15 June 2022
ACCEPTED 26 September 2022
PUBLISHED 07 October 2022

CITATION
Funk R, Busse J, Siegmund N, Sommer M, Iturri LA, Panebianco JE, Avecilla F and Buschiazzo DE (2022), Phytoliths in particulate matter released by wind erosion on arable land in La Pampa, Argentina.
Front. Environ. Sci. 10:969898.
doi: 10.3389/fenvs.2022.969898

Phytoliths in particulate matter released by wind erosion on arable land in La Pampa, Argentina

Roger Funk[1]*, Jaqueline Busse[1], Nicole Siegmund[1,2], Michael Sommer[1,2], Laura A. Iturri[3,4], Juan E. Panebianco[3], Fernando Avecilla[3] and Daniel E. Buschiazzo[3,4]

[1]Leibniz Centre for Agricultural Landscape Research (ZALF), Working Group Landscape Pedology, Müncheberg, Germany, [2]Institute of Environmental Science and Geography, University of Potsdam, Potsdam, Germany, [3]Institute of Earth and Environmental Sciences of La Pampa, National Council for Research and Technology (INCITAP CONICET-UNLPam), Santa Rosa, Argentina, [4]National University of La Pampa, Faculty of Agronomy (UNLPam), Santa Rosa, Argentina

Silicon (Si) is considered a beneficial element in plant nutrition, but its importance on ecosystems goes far beyond that. Various forms of silicon are found in soils, of which the phytogenic pool plays a decisive role due to its good availability. This Si returns to the soil through the decomposition of plant residues, where they then participate in the further cycle as biogenic amorphous silica (bASi) or so-called phytoliths. These have a high affinity for water, so that the water holding capacity and water availability of soils can be increased even by small amounts of ASi. Agricultural land is a considerable global dust source, and dust samples from arable land have shown in cloud formation experiments a several times higher ice nucleation activity than pure mineral dust. Here, particle sizes in the particulate matter fractions (PM) are important, which can travel long distances and reach high altitudes in the atmosphere. Based on this, the research question was whether phytoliths could be detected in PM samples from wind erosion events, what are the main particle sizes of phytoliths and whether an initial quantification was possible.

Measurements of PM concentrations were carried out at a wind erosion measuring field in the province La Pampa, Argentina. PM were sampled during five erosion events with Environmental Dust Monitors (EDM). After counting and classifying all particles with diameters between 0.3 and 32 µm in the EDMs, they are collected on filters. The filters were analyzed by Scanning Electron Microscopy and Energy Dispersive X-Ray analysis (SEM-EDX) to investigate single or ensembles of particles regarding composition and possible origins.

The analyses showed up to 8.3 per cent being phytoliths in the emitted dust and up to 25 per cent of organic origin. Particles of organic origin are mostly in the coarse dust fraction, whereas phytoliths are predominately transported in the finer dust fractions. Since phytoliths are both an important source of Si as a plant nutrient and are also involved in soil C fixation, their losses from arable land *via* dust emissions should be considered and its specific influence on atmospheric processes should be studied in detail in the future.

KEYWORDS

dust, dust composition, particulate matter, scanning electron microscope (SEM) analysis, phytolith

Introduction

Wind erosion is an important process contributing to soil formation and soil degradation in arid and semi-arid environments. Related dust emissions cause the loss of the most valuable parts of a soil, which not only reduce soil fertility but also influence physical and chemical processes in the atmosphere or remote deposition regions. About 2000 Mt of dust are emitted each year into the atmosphere, of which ¾ are deposited on land surfaces and ¼ on the oceans (Shao et al., 2011). Dust depositions may have an important role in the nutrient cycle of natural ecosystems or low input agriculture as shown from the Amazonas forests (Swap et al., 1992; Kaufmann et al., 2005; Koren et al., 2006) to the Sudan-Sahelian Zone (Jahn 1995; Stahr et al., 1996; Goudie and Middleton 2001). Dust depositions on the oceans activate the phytoplankton growth, which has a direct impact on the global carbon cycle and carbon sequestration as well, as stated by the "Iron hypothesis" of Martin and Fitzwater 1988 and the "Silica hypothesis" of Harrison 2000. Consequently, there is a close relationship between the cycles of dust (D-cycle), carbon (C-cycle) and energy (E-cycle) in the global context (Shao et al., 2011). In longer time-scales, dust has also modifying influences on the climate (Martínez-Garzia et al., 2011).

The sorting processes during a wind erosion event on agriculturally used soils are noticed most clearly in their physical effects, but have also consequences on the chemical composition of the dust and the depositions at the field site. Size, shape and density of single particles or aggregates are the determining criteria for their spread in the atmosphere and finally their transport distances. The contents of soil organic carbon (SOC) and nutrients in the dust fraction have been found to be many times greater than in the original soil. Iturri et al. (2017) found enrichment factors of about five for SOC in the PM_{10} fraction of the eroded material and Webb et al. (2012) reported factors up to seven for Australian dust. Also the nutrient contents of dust are greater with significant higher available P, organic matter and clay contents (Ramsperger et al., 1998; Iturri et al. 2021). Buschiazzo et al. (2007) have measured enrichment factors of two–five for nitrogen and of 1.5–eight for phosphorus for dust transported in 0.13 and 1.5 m height respectively. Measurements in Niger by Sterk et al. (1996) showed 17-times higher contents of K, C, N and P of the dust, trapped in a height of 2 m, than of the topsoil. Nerger et al. (2017) showed a general relationship between the measurement height and the enrichment ratio by summarizing results of different authors. Due to the low net primary production of most regions affected by wind erosion, removed nutrients and carbon can be regarded as irretrievable loss at the eroded site (Yan et al., 2005). Even at the landscape scale these losses are not balanced, because the finer and lighter fractions are transported over long distances and the depositions are spread at much larger areas than the eroded sites.

In addition to the well-studied macronutrients, more of the so-called beneficial elements have recently become into the focus of investigation. One of these elements is silicon (Si), which has a yield-stabilizing effect by increasing resistance to abiotic (drought, nutrient deficiency, metal toxicities) and biotic (fungal diseases, parasite infestation) stress factors, as well as providing culm stability in cereals and other grasses (Epstein, 1999). On a global scale, the Si budget affects the carbon cycle because CO_2 is consumed during silicate weathering (Amelung et al., 2018; Qi et al., 2020). Si is available for plants only as monomeric orthosilicic acid ($Si(OH_4)$), which is obtainable in soils from phytoliths. Phytoliths are amorphous silica particles embedded in plant tissues (biominerals), that remain in soils after decomposition of died plants or fallen leaves (Fernández Honaine et al., 2006). In soils, phytoliths may be found either within individual plant fragments or in the soil mass. The phytolith content varies in the soil horizons between 0.01 and 3% (Schaller et al., 2021) and is increased in the topsoil (Kaczorek et al., 2018). The size of the phytoliths varies from a few 100 nm up to 1 mm. The greatest importance of the phytoliths found in the soils seems to be attributed to the smallest phytogenic structures ($d < 5\,\mu m$). So, they are exactly in a size that makes them susceptible to become part of the suspended dust fraction once they are released from a soil by wind erosion. Latorre et al. (2012) described as first airborne phytoliths in dust in Argentina, whose concentrations are related to agricultural activities and dry weather conditions. The months with higher phytolith concentrations in the air coincided with periods when the soils were not covered with vegetation or when the soils were prepared for sowing. The aeolian release of phytoliths by agricultural activities or by wind erosion would not only reduce the silica content in the soil, but also cause possible undesirable inputs into other biotopes (e.g. eutrophication in water bodies, fertilization of the oceans). Even a small change in the silica content of a few percent would have considerable effects on the soil water holding capacity and so the plant-available water finally (Schaller et al., 2021). Thus, Si - losses in the form of phytoliths also represent a loss of soil quality that is worth investigating in more detail.

On the other hand, it has been demonstrated that dust from arable land has a much higher ice nucleation activity in the atmosphere compared to mineral dust (Conen and Leifeld 2014; Steinke et al., 2016). What causes this higher activity in detail is not yet clear, since soil dust consists of a large number of

components (Steinke et al. 2020). The high water absorption capacity of amorphous silica, to which the phytolites belong, could be a first hint that they might be involved in these processes.

Nevertheless, dust is a mixture of single or composed particles different in size, shape and density, and mineral or organic origin. Available measurement methods either examine a small portion of the airflow very accurately, or collect larger amounts of dust without examining it. Optical particle counters use light scattering to detect single particles passing a laser beam and count and classify all particles over certain ranges. They cannot be used to distinguish other important properties as the origin (mineral or organic), the composition (single or composed) or the huge variety of different shapes. Another disadvantage of event-based dust measurements is the often very small quantities that can be collected despite relatively high concentrations in the air. This means that methods that separate certain components from the total load cannot be used and the sample must be analyzed in its entirety. Scanning electron microscopy (SEM) can help to provide additional information about composition and properties of dust particles from samples of low quantities (Hinz et al., 1998; Edgerton et al., 2009; Tolis et al., 2014). Most studies were focused on specific components or elements in the dust, as soot, heavy metals or the mineral and microbiological composition for air quality reasons or source identification (Twiss et al. 1969; Falkovich et al., 2001; Tervahattu et al., 2004; Ramirez-Leal et al., 2014; Rout et al., 2014). Although phytoliths show a great variety of forms and surface structures, nomenclatures are available for their determination, in which they are described in detail (Gallego and Distel 2004; ICPT 2019), so that an identification by SEM should be possible.

Based on these already proven or suspected effects of phytoliths, the aim of our investigations was whether phytoliths could be detected in PM samples from wind erosion measurements at a field site, what are the main particle sizes of phytoliths and whether an initial quantification was possible, at least in a relative way.

Materials and methods

Site description

Wind, wind erosion and dust emissions were measured on a measuring field at the experimental Station of the National Institute for Agricultural Technology (INTA) in Anguil (63.9885°W and 36.577°S) in the Northeastern part of the province La Pampa. The measuring field was orientated along the main wind directions (N—S and S—N) with a size of 1.44 ha (240 × 60 m) and lies within other agricultural land. It was surrounded by pastureland in its immediate vicinity, so a direct input of saltating soil material from the adjacent fields could be excluded. Before the measuring campaign the field was tilled with a disc harrow to remove all vegetation cover. We made sure that the initial conditions at the beginning of the measurements were comparable. Tillage was done three times, before the measurements in August, in September and in November/December. The same tillage tool each time produced comparable roughness. The meteorological conditions led to a rapid drying of the soil surface after 1–2 days each time, so that the initial conditions of the measurements within this time span were similar.

The soils in this region developed from aeolian deposits of Holocene origin and are classified as Typic Ustipsamment with a sand content of 76%, a silt content of 17%, a clay content of 7%, and a carbon content of about 1.5%. The texture class is loamy sand resulting in a medium to high susceptibility to wind erosion. Despite the fairly balanced susceptibility to wind erosion derived from the soil data, there were a strong spatial differentiation in the transport processes due to low terrain structures, so that areas of soil erosion and deposition could be detected at the field immediately adjacent to each other (Siegmund et al., 2018).

Four Environmental Dust Monitors (EDM) were used to measure dust concentrations at heights of 1 and 4 m at two positions, two EDM164 and two EDM107 (GRIMM Aerosol Technique GmbH) (Figure 1). The EDM164 include All-in-One-weather stations (WS500-UMB, Lufft Mess-und Regeltechnik GmbH) to measure simultaneously wind velocity, wind direction, air temperature, air pressure and air humidity. Both positions were placed 40 m away from the field boundary on the longitudinal centerline, so we could define always one position representative for the incoming air and the other one for the outgoing air (Siegmund et al., 2022). The EDM measures the particle number concentrations for particles between 0.25 and 32 µm in diameter in 31 classes and the dust mass concentration of the fractions PM_{10}, $PM_{2.5}$ and $PM_{1.0}$. Air and dust are aspirated in a rate of 1.2 L min^{-1} and analyzed in an optical cell. Then the air is sucked through a PTFE filter with a diameter of 47 mm and a pore size of 1.5 µm, on which all particles are collected. After each wind erosion event the filters were changed. Since the air stream does not hit the filter concentrically, but close to the edge, this results in an uneven covering of the filter with particles. On the one hand, this affects the density of cover, but on the other hand, sorting also already takes place, since the coarser fractions settle close to the inlet and the finer fractions are distributed over the entire surface of the filter. Therefore we always choose two sections from each filter for our analyses, one from the immediate vicinity of the inflow and one that is opposite from the inlet with the largest distance. Our results presented in this study are based on six erosion events that occurred between August to December 2016 (Table 1). For the EDM, a relative humidity of <60% is specified as an operation limit. Otherwise, moisture-induced aggregation of the individual particles may occur. All measurements were below this value; on 12/12/2022 the air humidity was even <20%.

These erosion events were already the basis of other investigations. Details regarding the spatial variability of the

TABLE 1 Description of the erosion events of this study.

Date	Start-end of event hh:mm	u > 6 m s^{-1} (hh:mm)	Wind direction	Mean wind velocity (m s^{-1})	Wind force integral[a]	EF[b]	DAS[c]	Soil loss kg ha^{-1}
08/26/2016	09:52–15:10	04:47	SSW	8.0	23,049	n.d	n.d	244
09/13/2016	09:25–15:39	06:14	SSW	9.6	119,559	52	74	408
11/18/2016	09:20–14:40	04:51	N	8.1	39,510	60	71	-11
11/21/2016	10:50–17:40	06:03	SSE	7.1	34,154	54	81	3
12/04/2016	10:16–19:10	06:41	NNE	8.5	75,120	61	67	24
12/12/2016	14:52–19:10	04:14	WSW	8.6	56,630	60	69	443

[a]based on the equation to calculate the transport capacity of the wind with WFI = ∑((u-ut)u2), for ut > 6 m s-1.
[b]erodible fraction estimated by sieving through 0.84 mm mesh.
[c]dry aggregate stability calculated following Skidmore et al. (1994).

TABLE 2 Results of the visual analyses of filter loadings by particle counting.

Date	Total counted particles	Number of phytoliths	Number of particles with biological origin	Per cent of phytoliths	Per cent of particles with biological origin
08/26/2016 IN	511	25	69	4.9	13.5
08/26/2016 OUT	523	31	87	5.9	16.6
09/13/2016 IN	1,210	53	183	4.4	15.1
09/13/2016 OUT	1,171	132	133	11.3	11.4
11/18/2016 IN	1860	155	452	8.3	24.3
11/18/2016 OUT	673	56	136	8.3	20.2
11/21/2016 IN	709	10	7	1.4	1.0
11/21/2016 OUT	1,414	47	3	3.3	0.2
12/04/2016 IN	211	16	0	7.6	0.0
12/04/2016 OUT	550	13	1	2.4	0.2
12/12/2016 IN	493	23	0	4.7	0.0
12/12/2016 OUT	778	170	0	21.9	0.0

transport processes at the field, the horizontal and vertical fluxes of the dust fractions and the influence of wind fluctuations on the dust concentrations can be found in Siegmund et al., 2018, Siegmund et al., 2022a and Siegmund et al., 2022b.

Scanning Electron Microscopy und Energy Dispersive X-ray analysis

Scanning electron microscopy (SEM, ZEISS EVO MA10) and Energy Dispersive X-Ray analysis (EDX, Bruker XFlash Nano 5010) were used to investigate the sampled dust on the filters regarding its size distributions in forms of singular particles or as part of aggregations. The filters of the EDM from 1 to 4 m height, at the windward and leeward site and of each event were analyzed separately by cutting out parts of the filters or by picking up the dust from the filters with adhesive stubs. The coarse particles had to picked up mainly with the stubs, because they could become released in the SEM due to the electrical charge. All samples were coated with Au/Pd to make the sample surface conductive for better resolution.

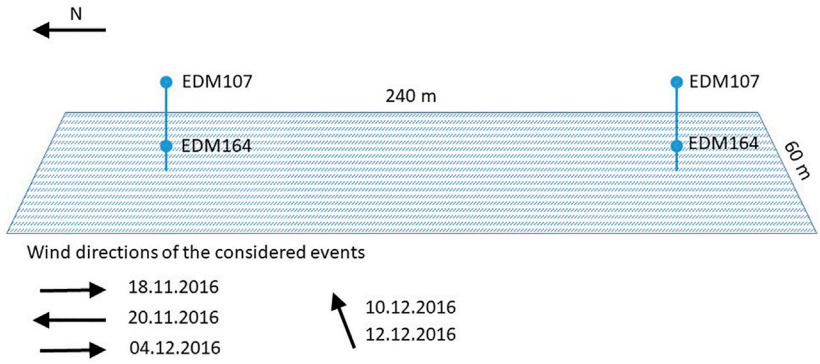

FIGURE 1
Setup of the dust measurements at the field site, arrows mark the wind directions of the regarded erosion events.

The classification was done visually by checking size and composition of the trapped particles. Image segments were selected that contained approximately 500 particles. After we could determine that a considerable part of the particles consisted of phytoliths, we compared identified phytoliths in the SEM images with similar already described morphotypes. For this purpose, the International Code for Phytolith Nomenclature (ICPN) 2.0 was used, which classifies opal phytoliths into 19 morphotypes defined by shape, size and surface ornamentation (Neumann et al., 2019). The particles identified as phytoliths were counted and set in proportion to the total number of particles of the image section. A distinction between the individual morphotypes was not made. Subsequently, single particles and image sections were analyzed by EDX, where matches with the visual analysis were checked.

Results and discussion

Generally the dust sampled at all days with wind erosion events shows great differences in the particle sizes and the particle composition. The EDM collected particles in a very wide size range, from diameters >100 µm to the sub-micron range of <1 µm in rounded, angular or elongated shapes. The number of particles increase exponentially with decreasing diameters. Particles of the PM_{10} -fraction were mostly below numbers of 10, while the EDM counted tens of thousands of particles of the 0.25 µm -fraction, which ultimately contribute little to the total mass. Thus, the comparative visual assessment can only be made within a size class by comparing the proportions of particles of approximately the same size. This is advantageously supported by the sorting processes during wind erosion. The particle size distributions of the filter loadings clearly reflect the different measurement heights. The larger particles with diameters around 100 µm, which are even outside the measuring range of the EDM of 0.25–32 µm, were predominantly transported in 1 m height (Figure 2, left). They are clear components of the saltation and short term suspension transport modes. At 4 m we could hardly find them on the filters and the particle sizes are smaller by one order of magnitude and more homogeneous (Figure 2, right). The differences in the concentrations of the different PM fractions are also reflected on the filter loading.

A closer look at the particles on the filters showed that a large part of them were of biological origin or possibly phytoliths. This was not surprisingly, since our measuring field was surrounded by other agricultural used areas, including pasture, reduced and conventional tilled fields, and the soils in La Pampa have developed under forest and grass steppes. Thus, the separate consideration of our pictures under this aspect was obvious. Table 2 summarizes the results of the visual analyses counting particles on the filters of the six erosion events.

It is noticeable that in the first three events the proportion of organic components is considerably higher than in the last three events. The proportion of phytoliths also tends to be lower. This can be explained by the fact that these three erosion events were always the first erosion events immediately following a tillage operation. These were carried out to remove vegetation at the plot and create a susceptible surface by breaking crusts. The last tillage occurred on 11/17/2016, and due to the persistently dry weather, no further tillage was necessary. The following erosion events consequently occurred on an already depleted soil surface, where especially the most easily erodible components were removed. These effect was also shown by Münch et al. (2022), who could prove that especially fresh applied or only slightly decomposed organic matter will be blown out by the wind at first.

As wind erosion is also a sorting process, its occurrence results in different particle size distributions of the eroded material in comparison to the original soil. Our studies show for the three erosion events with the initial field conditions,

10.3389/fenvs.2022.969898

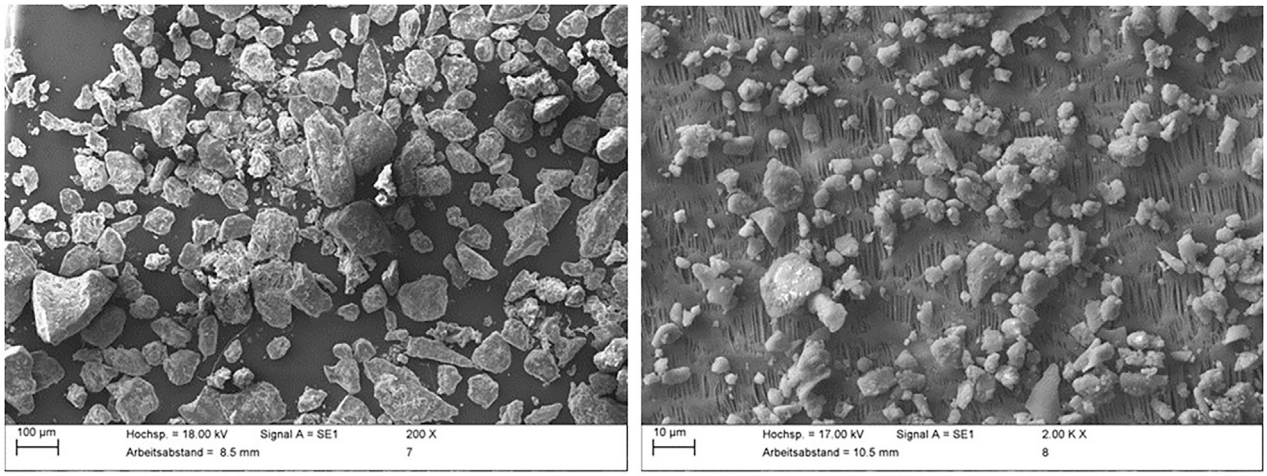

FIGURE 2
Overview of particles sampled on filters of the EDM in 1 m height (left, on an adhesive stub) and 4 m height (right, on a cut-out of the filter), scale bars in the lower left corner.

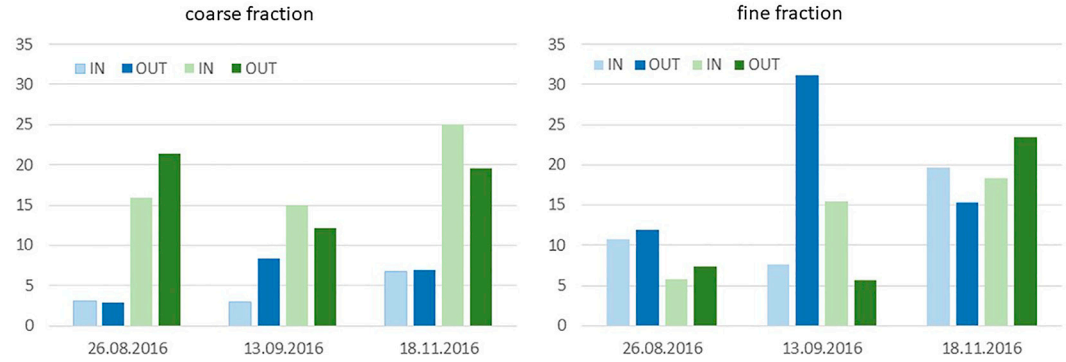

FIGURE 3
Percentage of phytoliths (blue bars) and particles of organic origin (green bars) in the coarse and fine fractions of the dust.

that there were differences in the composition between the coarse and fine fractions of the particulate matter. In the coarser fraction, particles of organic origin, as plant residues or residues in its early stage of decomposition, were more prevalent, while phytoliths were significantly less represented. In the finer fractions, the phytoliths were in the majority or at least at the same level (Figure 3, Figure 4). The proportion of phytoliths corresponds to those of other authors and ranges from 3 to 8.5% in the coarse particle fractions and from 10 to 31% in the fine particle fractions. This leads to a relative enrichment of the organic matter in the coarse dust fraction, since the sorting takes place only by aerodynamics of the very diverse shaped or composed particles. Thus, the enrichment of organic matter in the dust can be derived predominantly from the shift in size composition between organic and mineral particles. Phytoliths are much more similar to mineral particles in shape and density and are therefore subject to the same sorting and transport mechanisms.

Latorre et al. (2012) already pointed out that the majority of the windblown phytoliths in dust from the Pampean plains could be derived from grass species or other plant communities grown in the region, and that the highest concentrations could be found during periods of increased agricultural activity and bare soils. Thus, there should be a relationship between the releasing processes, such as wind erosion or tillage, and the amount of phytoliths. Since we had erosion events ranging from weak to medium intensity on our measurement field, we

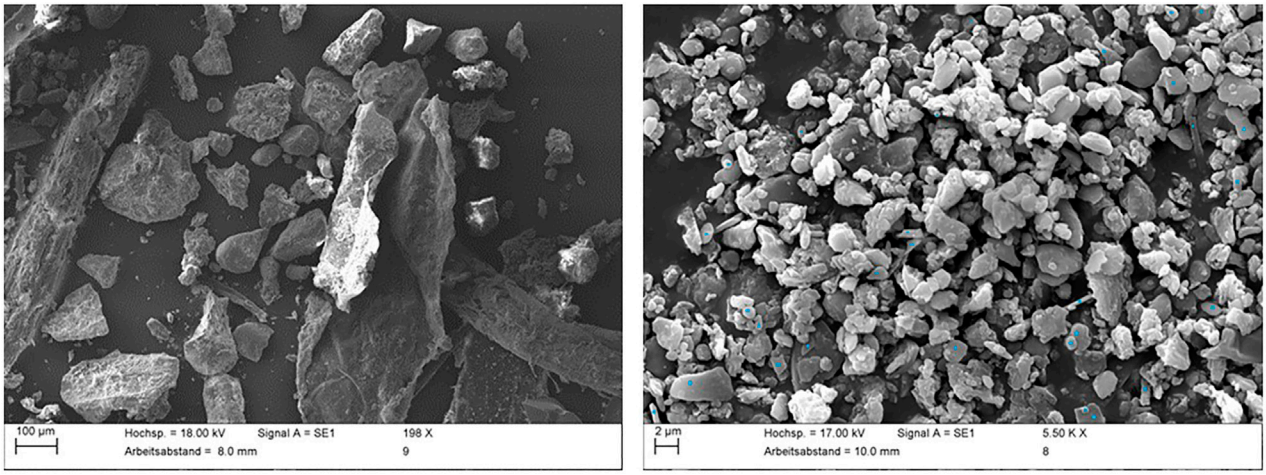

FIGURE 4
SEM images of the coarse and fine fractions of the sampled dust; left image shows big particles of organic origin, in the right image are phytoliths marked with blue dots.

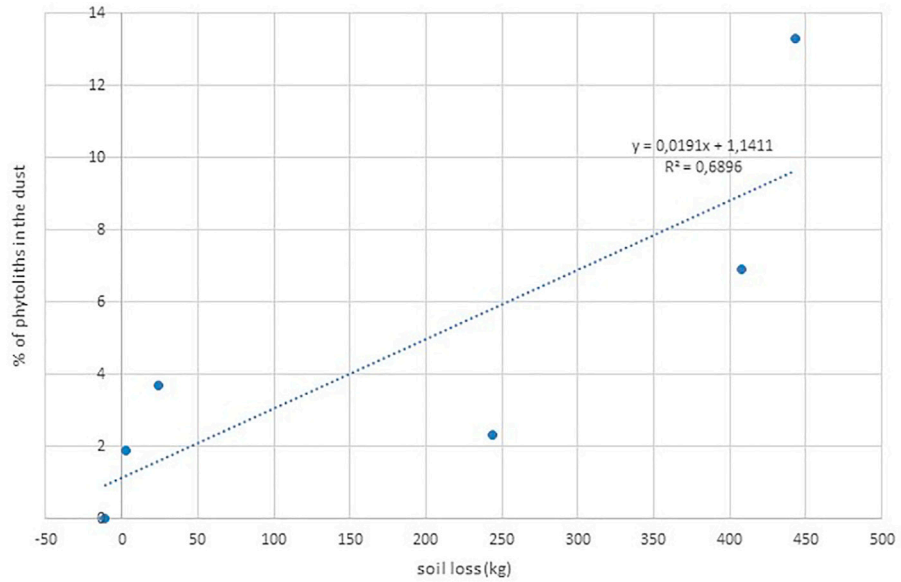

FIGURE 5
Percentage of phytoliths in the dust in dependence on wind erosion intensity.

combined the data from the wind erosion measurements with the phytolith estimation from the filters of each event. The relationship between the measured soil losses of all wind erosion events (Table 1) and the percentage of phytoliths in the dust shows a tendency of increasing shares of phytoliths with increasing soil losses (Figure 5). Thus, firstly an increasing ratio between emitted particles and the proportion of phytoliths can be derived and secondly it shows again that phytoliths are effected by the same sorting processes as mineral particles, because they are predominant in the finer dust fractions together with mineral particles of the same size. So, agriculturally used areas can be an important source for airborne phytoliths in the PM fractions which are released by wind erosion.

Since visual determination of the phytoliths in the total filter loading is despite the inclusion of determination keys subject to

subjectivity, we used EDX to try to eliminate this as much as possible, to identify more precisely the particles we refer to as phytoliths. Since only visual clues could be used for the phytolith classification, EDX can be used to validate these analyses. Since minerals also contain silicon, other elements must help to distinguish them from phytoliths. These can be aluminum, iron or sodium, which can be clearly assigned to mineral particles. Thus, in this case only one particle at the lower right edge of this image can be identified as phytolite origin by this exclusion method. Figure 6 shows an example of a larger section of a filter, where we counted about 140 particles and classified about 10% as phytoliths. Element mapping and applying the same exclusion methodology shows a quite good agreement between the classification and the verification. Thus, the purely visual assignment of phytoliths *via* the morphotypes can be considered sufficiently accurate. Problems arise mainly with the very small particles. Here, unfortunately, the EDX does not provide the same resolution as the SEM.

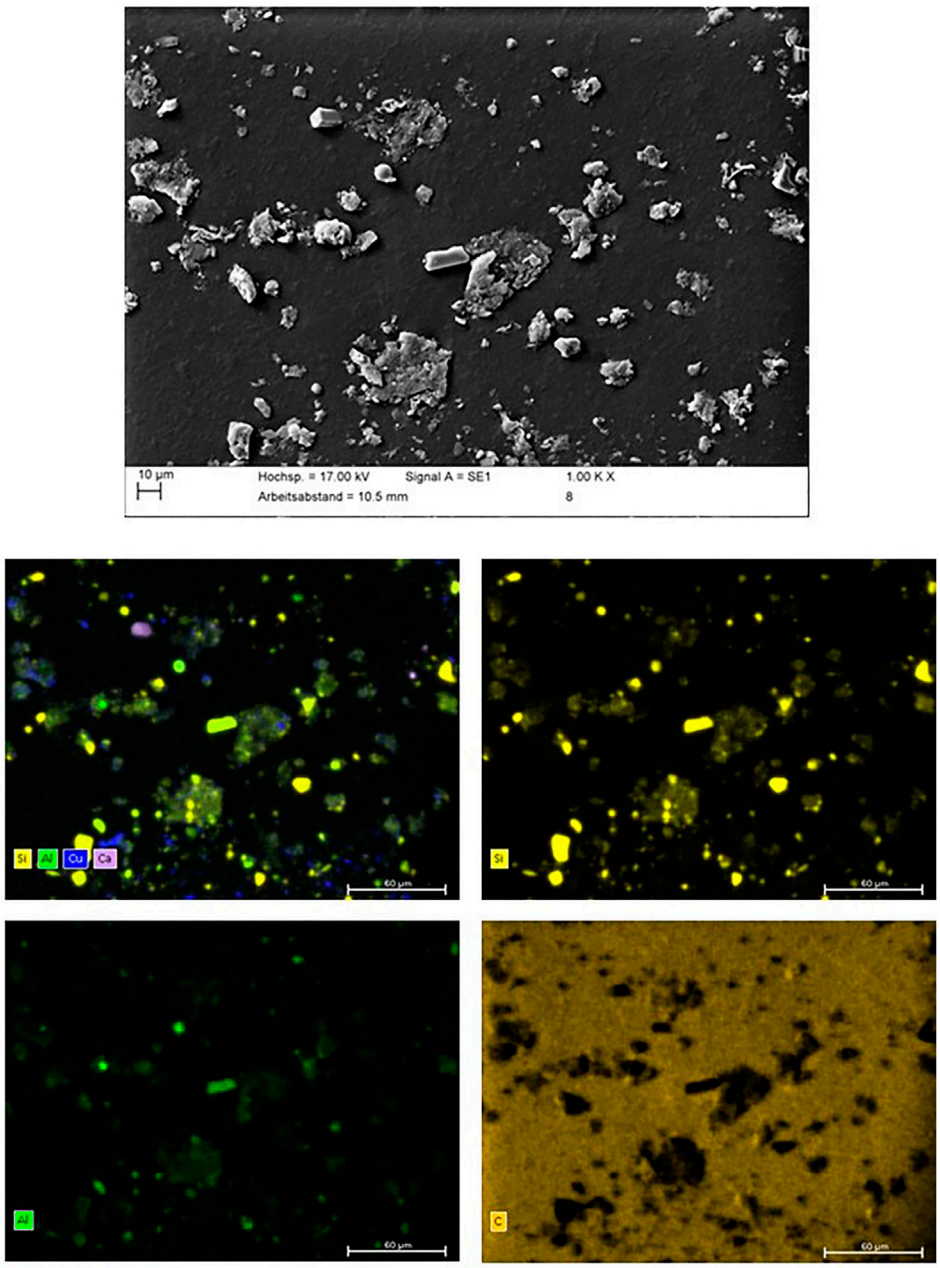

FIGURE 6
SEM and EDX analyses of a dust sample containing phytoliths.

Conclusion

SEM analyses provide extremely detailed insights into composition and shape diversity of dust samples. The complex composition of dust particles sampled during wind erosion events makes it difficult to assign them certain properties. Although a large number of studies have demonstrated an enrichment of organic matter as well as essential elements in suspended PM, there is still some uncertainty because a complete separation does not occur. The enrichment of organic matter can be clearly attributed to the shift in particle size composition after aeolian sorting if mineral and organic particles are defined by their aerodynamic diameter. Especially these larger particles of biological origin are also the carriers of mineral adhesions in the micro- and sub-micro scale. In the reverse case, mineral particles are known to carry "hitchhiking" microorganisms (Giongo et al., 2012; Favet et al., 2013). Thus, the emitted dust always reflects the diversity of properties of its origin and the special properties of agricultural dust, such as the higher ice nucleation activity, cannot be attributed to separated particles.

In our investigations, we were also able to detect phytoliths in the dust as well as their accumulation in the PM fractions. Since we could not separate the phytoliths by appropriate pretreatments, we had to identify them in the bulk sample. A check by means of elemental analysis with EDX showed only small deviations from our assignments, so we can conclude that most of the phytoliths were recognized by their morphotypes. Most recently, research has focused on silicon as being important for soil water holding capacity and water availability in soils (Schaller et al., 2020). The removal and transport by aeolian processes could be proven with our investigations. Therefore, particularly in the semi-arid arable areas, increased attention should be paid to any possibility of improving the water availability of the soils used there.

Data availability statement

The raw data supporting the conclusion of this article will be made available by the authors, without undue reservation.

Author contributions

Conceptualization, methodology, RF and MS; funding acquisition, RF, MS, and DB; investigation, NS, JP, FA, and LI; REM and EDX analyses, image processing JB and RF; writing—original draft RF; review and editing, all co-authors. All authors have read and agreed to the published version of the manuscript.

Funding

This study was supported by the joint project "Multiscale analysis of quantitative and qualitative fine particulate matter emissions from agricultural soils of La Pampa, Argentina" funded by the Deutsche Forschungsgemeinschaft (DFG) of Germany (DFG-GZ: Fu 247/10–1) and the National Council for Research and Technology of Argentina (CONICET).

Acknowledgments

The authors acknowledge the technical assistance and logistic support of the technicians at the INTA Station in Anguil, La Pampa, Argentina during our field experiments.

Conflict of interest

The authors declare that the research was conducted in the absence of any commercial or financial relationships that could be construed as a potential conflict of interest.

Publisher's note

References

Amelung, W., Blume, H.-P., Fleige, H., Horn, R., Kandeler, E., Kögel-Knabner, I., et al. (2018). "Böden als Pflanzenstandorte," in *Scheffer/schachtschabel lehrbuch der Bodenkunde*. Editors W. Amelung, H.-P. Blume, H. Fleige, R. Horn, E. Kandeler, I. Kögel-Knabner, et al. (Berlin, Heidelberg: Springer), 491–581. doi:10.1007/978-3-662-55871-3_9

Buschiazzo, D. E., Zobeck, T. M., and Abascal, S. A. (2007). Wind erosion quantity and quality of an Entic Haplustoll of the semi-arid pampas of Argentina. *J. Arid. Environ.* 69, 29–39. doi:10.1016/j.jaridenv.2006.08.013

Conen, F., and Leifeld, J. (2014). A new facet of soil organic matter. *Agric. Ecosyst. Environ.* 185, 186–187. doi:10.1016/j.agee.2013.12.024

Edgerton, E. S., Casuccio, G. S., Saylor, R. D., Lersch, T. L., Hartsell, B. E., Jansen, J. J., et al. (2009). Measurements of OC and EC in coarse particulate matter in the southeastern United States. *J. Air & Waste Manag. Assoc.* 59, 78–90. doi:10.3155/1047-3289.59.1.78

Epstein, E. (1999). Silicon. *Annu. Rev. Plant Physiol. Plant Mol. Biol.* 50, 641–664. doi:10.1146/annurev.arplant.50.1.641

Falkovich, A. H., Ganor, E., Levin, Z., Formenti, P., and Rudich, Y. (2001). Chemical and mineralogical analysis of individual mineral dust particles. *J. Geophys. Res.* 106 (18), 18029–18036. doi:10.1029/2000jd900430

Favet, J., Lapanje, A., Giongo, A., Kennedy, S., Aung, Y.-Y., Cattaneo, A., et al. (2013). Microbial hitchhikers on intercontinental dust: Catching a lift in Chad. *ISME J.* 7, 850–867. doi:10.1038/ismej.2012.152

Fernández Honaine, M., Zucol, A. F., and Osterrieth, M. (2006). Phytolith assemblages and systematic associations in grassland species of the South-Eastern Pampean Plains, Argentina. *Ann. Bot.* 98, 1155–1165. doi:10.1093/aob/mcl207

Gallego, L., and Distel, R. A. (2004). Phytolith assemblages in grasses native to Central Argentina. *Ann. Bot.* 94, 865–874. doi:10.1093/aob/mch214

Giongo, A., Favet, J., Lapanje, A., Gano, K. A., Kennedy, S., Davis-Richardson, A. G., et al. (2012). Microbial hitchhikers on intercontinental dust: High-throughput sequencing to catalogue microbes in small sand samples. *Aerobiologia* 29, 71–84. doi:10.1007/s10453-012-9264-0

Goudie, A., and Middleton, N. (2001). Saharan dust storms: nature and consequences. *Earth-Science Rev.* 56, 179–204. doi:10.1016/s0012-8252(01)00067-8

Harrison, K. G. (2000). Role of increased marine silica input on paleo-pCO2 levels. *Paleoceanography* 15, 292–298. doi:10.1029/1999pa000427

Hinz, K. P., Greweling, M., Iflseder, H., Trimborn, A., and Spengler, B. (1998). Source identification of single particles by on-line laser mass spectrometry. *J. Aerosol Sci.* 9, 1253–1254. doi:10.1016/s0021-8502(98)90809-6

Iturri, L. A., Funk, R., Leue, J., Sommer, M., and Buschiazzo, D. E. (2017). Wind sorting affects differently the organo-mineral composition of saltating and particulate materials in contrasting texture agricultural soils. *Aeolian Res.* 28, 39–49. doi:10.1016/j.aeolia.2017.07.005

Iturri, L. A., Funk, R., Sommer, M., and Buschiazzo, D. E. (2021). Elemental composition of wind-blown sediments from contrasting textured soils. *Aeolian Res.* 48, 100656. doi:10.1016/j.aeolia.2020.100656

Jahn, R. (1995). Ausmaß äolischer Einträge in circumsaharischen Böden und ihre Auswirkungen auf Bodenentwicklung und Standorteigenschaften, *Hohenh. Bodenkd. Hefte*, Stuttgart, Germany: Universität Hohenheim 23, 213.

Kaczorek, D., Puppe, D., Busse, J., and Sommer, M. (2019). Effects of phytolith distribution and characteristics on extractable silicon fractions in soils under different vegetation – an exploratory study on loess. *Geoderma* 356, 113917. doi:10.1016/j.geoderma.2019.113917

Kaufman, Y. J., Koren, I., Remer, L. A., Tanré, D., Ginoux, P., and Fan, S. (2005). Dust transport and deposition observed from the terra-moderate resolution imaging spectroradiometer (MODIS) spacecraft over the atlantic ocean. *J. Geophys. Res.* 110, D10S12. doi:10.1029/2003JD004436

Koren, I., Kaufman, Y., Washington, R., Todd, M., Rudich, Y. J., Vanderlei, M., et al. (2006). The bodele depression: A single spot in the sahara that provides most of the mineral dust to the amazon forest. *Environ. Res. Lett.* 1, 014005. doi:10.1088/1748-9326/1/1/014005

Latorre, F., Honaine, M. F., and Osterrieth, M. L. (2012). First report of phytoliths in the air of Argentina. *Aerobiologia* 28, 61–69. doi:10.1007/s10453-011-9211-5

Martin, J. H., and Fitzwater, S. E. (1988). Iron deficiency limits phytoplankton growth in the north-east Pacific subarctic. *Nature* 331, 341–343. doi:10.1038/331341a0

Martínez-Garzia, A., Rosell-Mele, A., Jaccard, S. L., Geibert, W., Sigman, D. M., and Haug, G. H. (2011). Southern ocean dust-climate coupling over the past four million years. *Nature* 476, 312–315. doi:10.1038/nature10310

Münch, S., Papke, N., Leue, M., Faust, M., Schepanski, K., Siller, P., et al. (2022). Differences in the sediment composition of wind eroded sandy soils before and after fertilization with poultry manure. *Soil Tillage Res.* 215, 105205. doi:10.1016/j.still.2021.105205

Nerger, R., Funk, R., Cordsen, E., and Fohrer, N. (2017). Application of a modeling approach to designate soil and soil organic carbon loss to wind erosion on long-term monitoring sites (BDF) in Northern Germany. *Aeolian Res.* 25, 135–147. doi:10.1016/j.aeolia.2017.03.006

Neumannn, K., Strömberg, C. A. E., Ball, T., Albert, R. M., Vrydaghs, L., and Cummings, L. S. (2019). International Code for phytolith nomenclature (ICPN) 2.0. *Ann. Bot.* 124, 189–199. International Committee for Phytolith Taxonomy (ICPT). doi:10.1093/aob/mcz064

Qi, L., Sun, T., Guo, X., Guo, Y., and Li, F. Y. (2020). Phytolith-occluded carbon sequestration potential in three major steppe types along a precipitation gradient in Northern China. *Ecol. Evol.* 11, 1446–1456. doi:10.1002/ece3.7155

Ramirez-Leal, R., Valle-Martinez, M., and Cruz-Campas, M. (2014). Chemical and morphological study of PM10 analysed by SEM-EDS. *Open J. Air Pollut.* 3, 121–129. doi:10.4236/ojap.2014.34012

Ramsperger, B., Peinemann, N., and Stahr, K. (1998). Deposition rates and characteristics of aeolian dust in the semi-arid and sub-humid regions of the Argentinean Pampa. *J. Arid. Environ.* 39, 467–476. doi:10.1006/jare.1997.0366

Rout, T. K., Masto, R. E., Padhy, P. K., George, J., Ram, L. C., and Maity, S. (2014). Dust fall and elemental flux in a coal mining area. *J. Geochem. Explor.* 144 C, 443–455. doi:10.1016/j.gexplo.2014.04.003

Schaller, J., Frei, S., Rohn, L., and Gilfedder, B. S. (2020). Amorphous silica controls water storage capacity and phosphorus mobility in soils. *Front. Environ. Sci.* 8, 94. doi:10.3389/fenvs.2020.00094

Schaller, J., Puppe, D., Kaczorek, D., Ellerbrock, R., and Sommer, M. (2021). Silicon cycling in soils revisited. *Plants* 10, 295. doi:10.3390/plants10020295

Shao, Y., Wyrwoll, K. H., Chappell, A., Huang, J., Lin, Z., McTainsh, G. H., et al. (2011). Dust cycle: An emerging core theme in Earth system science. *Aeolian Res.* 2, 181–204. doi:10.1016/j.aeolia.2011.02.001

Siegmund, N., Funk, R., Koszinski, S., Buschiazzo, D. E., and Sommer, M. (2018). Effects of low-scale landscape structures on aeolian transport processes on arable land. *Aeolian Res.* 32, 181–191. doi:10.1016/j.aeolia.2018.03.003

Siegmund, N., Funk, R., Sommer, M., Avecilla, F., Panebianco, J. E., Iturri, L. A., et al. (2022a). Horizontal and vertical fluxes of particulate matter during wind erosion on arable land in the province La Pampa, Argentina. *Int. J. Sediment Res.* 37, 539–552. doi:10.1016/j.ijsrc.2022.01.004

Siegmund, N., Panebianco, J. E., Avecilla, F., Iturri, L. A., Sommer, M., Buschiazzo, D. E., et al. (2022b). From gustiness to dustiness - the impact of wind gusts on particulate matter emissions in field experiments in La Pampa, Argentina. *Atmosphere* 13, 1173. doi:10.3390/atmos13081173

Skidmore, E. L., Hagen, L. J., Armburst, D. V., Durar, A. A., Fryrear, D. W., Potter, K. N., et al. (1994). "Methods for investigating basic processes and conditions affecting wind erosion," in *Soil erosion research methods*. Editor R. Lal (Ankeny, USA: Soil & W. Cons. Soc), 259–330.

Stahr, K., Herrmann, L., and Jahn, R. (1996). Long distance dust transport in the Sudano-Sahelian Zone and the consequences for soil properties. Proceedings of the international symposium 'wind erosion in west africa: The problem and its control, Germany, 5 – 7 Dec. 1994, Markgraf Verlag, Weikersheim: University of Hohenheim.

Steinke, I., Funk, R., Busse, J., Iturri, A., Kirchen, S., et al. (2016). Ice nucleation activity of agricultural soil dust aerosols from Mongolia, Argentina and Germany. *J. Geophys. Res. Atmos.* 121 (22), 13559–13576. doi:10.1002/2016jd025160

Steinke, I., Hiranuma, N., Funk, R., Höhler, K., Tüllmann, N., Umo, N. S., et al. (2020). Complex plant-derived organic aerosol as ice-nucleating particles - more than the sums of their parts? *Atmos. Chem. Phys.* 20 (19), 11387–11397. doi:10.5194/acp-20-11387-2020

Sterk, G., Herrmann, L., and Bationo, A. (1996). Wind-blown nutrient transport and soil productivity changes in southwest Niger. *Land Degrad. Dev.* 7, 325–335. doi:10.1002/(sici)1099-145x(199612)7:4<325::aid-ldr237>3.0.co;2-q

Swap, R., Garstang, M., Greco, S., Talbot, R., and Kallberg, P. (1992). Saharan dust in the Amazon basin. *Tellus B* 44, 133–149. doi:10.1034/j.1600-0889.1992.t01-1-00005.x

Tervahattu, H., Hongisto, M., Aarnio, P., Kupiainen, K., and Sillanpää, M. (2004). Composition and origins of aerosol during a high PM10 episode in Finland. *Boreal Environ. Res.* 9, 335–345.

Tolis, E. I., Gkanas, E. I., Pavlidou, E., Skemperi, A., Pey, J., Pérez, N., et al. (2014). Microstuctural analysis and determination of PM10 emission sources in an industrial Mediterranean city. *Open Chem.* 12 (10), 1081–1090. doi:10.2478/s11532-014-0549-8

Twiss, P. C., Suess, E., and Smith, R. M. (1969). Morphological classification of grass phytoliths. *Soil Sci. Soc. Am. J.* 33, 109–115. doi:10.2136/sssaj1969.03615995003300010030x

Webb, N. P., Chappell, A., Strong, C. L., Marx, S. K., and McTainsh, G. H. (2012). The significance of carbon-enriched dust for global carbon accounting. *Global Change Biology*. doi:10.1111/j.1365-2486.2012.02780.x

Yan, H., Wang, S., Wang, C., Zhang, G., and Patel, N. (2005). Losses of soil organic carbon under wind erosion in China. *Global Change Biology* 11, 828–840. doi:10.1111/j.1365-2486.2005.00950.x

Frontiers in
Environmental Science

Explores the anthropogenic impact on our natural world

An innovative journal that advances knowledge of the natural world and its intersections with human society. It supports the formulation of policies that lead to a more inhabitable and sustainable world.

Discover the latest Research Topics

See more →

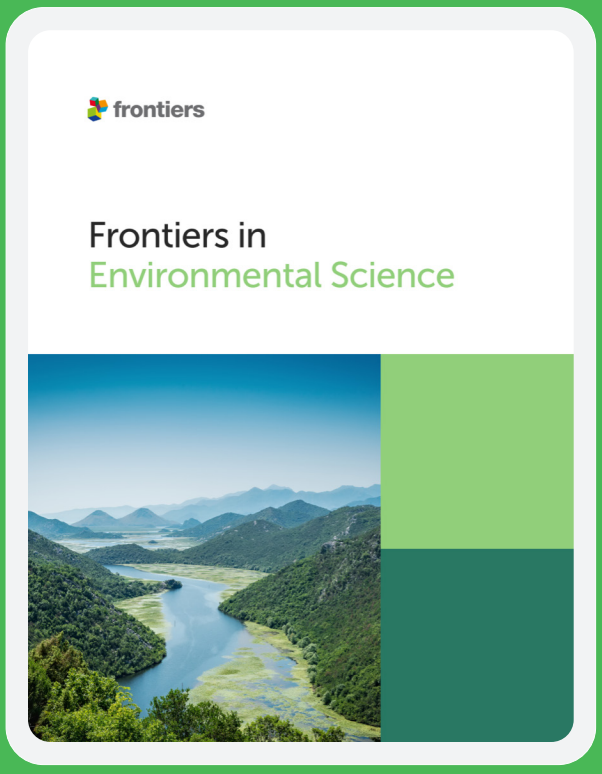

Frontiers

Avenue du Tribunal-Fédéral 34
1005 Lausanne, Switzerland
frontiersin.org

Contact us

+41 (0)21 510 17 00
frontiersin.org/about/contact